THE UNIVERSITY *of* EDINBURGH

THE UNIVERSITY of EDINBURGH

SCHOOL OF GEOSCIENCES
COLLEGE OF SCIENCE AND ENGINEERING

KU LEUVEN

ARENBERG DOCTORAL SCHOOL
FACULTY OF SCIENCE

The Atmospheric Chemistry of Earth-like Exoplanets: a 3D Perspective

Marrick Braam

Supervisors:
Prof. Dr. Paul Palmer
Prof. Dr. Leen Decin

Thesis submitted for the joint degree of
DOCTOR OF PHILOSOPHY
April 2024

The Atmospheric Chemistry of Earth-like Exoplanets: a 3D Perspective

Marrick Braam

This PhD thesis has been submitted in partial fulfillment of the requirements for the degree of Doctor of Philosophy (PhD) to the College of Science and Engineering, University of Edinburgh, Edinburgh, United Kingdom.

This PhD thesis has been submitted in partial fulfillment of the requirements for the degree of Doctor of Science (PhD): Astronomy and Astrophysics to Arenberg Doctoral School, Faculty of Science, KU Leuven, Leuven, Belgium.

Examination Committee:
Chair Edinburgh: Dr. Trent Dupuy (University of Edinburgh)
Chair Leuven: Prof. Dr. Christine Kirschhock (KU Leuven)
Supervisor: Prof. Dr. Paul Palmer (University of Edinburgh)
Supervisor: Prof. Dr. Leen Decin (KU Leuven)
Co-supervisor: Prof. Dr. Ken Rice (University of Edinburgh)
Co-supervisor: Prof. Dr. Jeremy Harvey (KU Leuven)
Examiner: Dr. Trent Dupuy (University of Edinburgh)
Examiner: Prof. Dr. Denis Defrère (KU Leuven)
Examiner: Dr. Paul Rimmer (University of Cambridge)

Funding acknowledgement: Marrick Braam is part of the CHAMELEON MC ITN EJD which received funding from the European Union's Horizon 2020 research and innovation programme under the Marie Sklodowska-Curie grant agreement no. 860470.

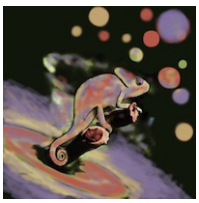

Cover art in collaboration with Pieter Steyaert

Abstract

Exoplanets or planets around other stars than the Sun are ubiquitous in the galaxy, with great diversity in stellar and planetary environments. The hundreds of known terrestrial exoplanets with mass and radius similar to Earth are preferentially found around M-dwarf stars. The James Webb Space Telescope (JWST) is providing the first glimpses into the atmospheres of these terrestrial exoplanets which is most easily achieved for planets on close-in orbits around a small and cool host star. The close-in orbits induce strong star-planet gravitational interactions that synchronize the planet's orbital and rotational velocity in a process called tidal locking, producing spin-orbit resonances akin to the Moon's 1:1 and Mercury's 3:2 spin-orbit resonance. Understanding the effects of spin-orbit resonances on atmospheric physics and chemistry is crucial to determine habitability, interpret spectroscopic observations, and put potential biosignatures (signs of biological processes in an atmosphere) into the environmental context.

Comprehensive 3D General Circulation Models (GCMs) that describe the physical processes in a planetary atmosphere have been employed to explore the habitability and observability of such exoplanets. The simulations show that heat transport from a permanent dayside to a permanent nightside prevents atmospheric collapse for 1:1 resonant exoplanets. The atmospheric circulation depends on the planet's rotation rate and orbital configuration and determines the distribution of clouds and hazes. A 3:2 resonant orbit with a theoretically predicted eccentricity of 0.3 changes the stellar irradiation pattern and generally warms the planetary climate. Besides heating and driving circulation, spatially asymmetric energetic radiation from the host star also photolyses molecules, driving the atmospheric composition out of thermochemical equilibrium and motivating the use of 3D coupled Climate-Chemistry Models (CCMs). For 1:1 resonant exoplanets of an Earth-like atmospheric composition, photochemistry driven by M-dwarf radiation can form a global ozone layer, with stellar flares affecting the chemistry and spatial distribution of ozone. The photochemistry is highly sensitive to the stellar flux distribution, in particular at ultraviolet (UV) wavelengths. Other drivers of disequilibrium chemistry such as lightning and circulation as well as the dependence of 3D atmospheric chemistry on the orbital configuration are, as of yet, underexplored. This thesis aims to build upon previous work and investigates the 3D coupled interactions between the physical and chemical processes that govern planetary atmospheres for tidally locked exoplanets around M-dwarfs.

I employ and further develop a 3D CCM – consisting of the Met Office Unified Model and the UK Chemistry and Aerosols framework – to simulate the physics and chemistry of exoplanet atmospheres. I configure two tidally locked exoplanets – nominally Proxima Centauri b and TRAPPIST-1 d – that are known to exhibit distinct circulation regimes, assuming 1:1 and eccentric 3:2 spin-orbit resonances and Earth-like atmospheric composition (N_2-O_2-CO_2-H_2O). The photochemical simulations consider the Chapman mechanism of ozone formation and the hydrogen oxide (HO_x) and nitrogen oxide (NO_x) catalytic cycles of ozone destruction. The CCM was previously used to simulate a 1:1 resonant exoplanet. For this study, I implement the calculation of varying stellar radiation with eccentricity and improve the photochemistry scheme to incorporate the latest stellar spectra in the calculation of spatially and temporally varying photolysis rates. At the time of writing, this is one of only four models able to do these calculations for exoplanets.

In Chapter 3, I demonstrate that using the latest stellar spectrum drives enhanced ozone formation on Proxima Centauri b in a 1:1 spin-orbit resonance with ozone column densities ten times higher than previously found. The global ozone layer shows significant longitudinal variations with an accumulation at the location of permanent nightside gyres. I then investigate the potential for lightning initiation on a tidally locked exoplanet, finding that vigorous convection on the dayside hemisphere results in lightning flash rates (LFR) of up to 0.16 flashes $km^{-2}yr^{-1}$, aligning with previously reported cloud coverage. The spatially asymmetric distribution of lightning flashes enhances the dayside hemisphere in NO_x, which is then advected to the nightside where it reacts to form more complex molecules in the absence of photochemistry. Lightning-induced chemistry is not sufficiently abundant and found too deep in the atmosphere to show detectable features in simulated transmission spectra.

Since the photochemical production of ozone is limited to the dayside hemisphere for 1:1 resonant exoplanets, a connection between the dayside ozone production region and the accumulation of ozone on the nightside has to exist. In Chapter 4, I investigate such dayside-nightside connections and how these explain the longitudinally varying ozone column densities. Transforming from the commonly used geographic to a tidally locked coordinate system to identify inter-hemispheric connections, I find that a stratospheric dayside-to-nightside circulation mechanism transports ozone from the dayside production regions to the nightside, where ozone-rich air then subsides and

accumulates at the locations of permanent gyres. With age-of-air tracer experiments, I demonstrate that this circulation mechanism also affects other tracers, as long as the dynamical timescales are shorter than chemical timescales and a stratospheric dayside production mechanism is present.

Chapter 5 compares Proxima Centauri b and TRAPPIST-1 d for both 1:1 and 3:2 spin-orbit resonances, the latter including an eccentricity of 0.3. These planets are known to exhibit distinct circulation regimes for a 1:1 resonance. Regardless of the resonance, TRAPPIST-1 d reaches the runaway greenhouse limit for its true irradiance within 1060 days of simulation. I artificially reduce the irradiance by 22% to ensure a stable climate for the 1:1 resonance, to still investigate the 3D atmospheric chemistry for a planet in this circulation regime. I report stable climates for Proxima Centauri b in both a 1:1 and 3:2 resonance. The 22% reduction in irradiance for TRAPPIST-1 d prevents the runaway greenhouse climate in the 1:1 resonant case. The atmospheric temperature of TRAPPIST-1 d in an eccentric 3:2 resonance increases significantly due to the eccentric orbit and a weaker stabilising cloud feedback, again driving the planet into a runaway greenhouse state. The distributions of ozone for the 3:2 resonant Proxima Centauri b and the 1:1 resonant TRAPPIST-1 d show latitudinal variations in ozone column densities, driven by an equator-to-pole circulation mechanism akin to the Brewer-Dobson circulation that controls the ozone distribution on Earth. Ozone production is stronger on Proxima Centauri b due to a higher UV flux. Ozone destruction is dominated by HO_x cycling on Proxima Centauri and by NO_x cycling on TRAPPIST-1 d, resulting from a much higher LFR (up to 1000 flashes $km^{-2}yr^{-1}$) for the latter.

I also demonstrate variability due to the rotation and eccentricity of Proxima Centauri b in a 3:2 spin-orbit resonance in Chapter 5. Especially prominent are the daytime-nighttime and periastron-apoastron cycles in water vapour (H_2O (g)) column densities at 48% and 12%, respectively. Surface temperature and ozone column densities have less pronounced cycles, but all show a brief time lag after periastron and apoastron passages, corresponding to the atmospheric response time. I use the 3D CCM data to generate synthetic emission spectra focusing on the mid-infrared (MIR) range (covered by JWST and also by the concept for the Large Interferometer For Exoplanets or LIFE). The 3D spatial variations and the observed geometry result in spectral fluctuations of up to 36 ppm for the 1:1 resonant exoplanets, depending on the orbital phase angle that we observe. The more homogeneous atmosphere of Proxima Centauri b in a 3:2 spin-orbit resonance lacks spectral fluctuations, presenting a discriminant from the 1:1 case and an important consideration for probing seasonally varying biosignatures.

The thesis highlights the complex 3D interplay in planetary atmospheres between stellar radiation, orbital configuration, atmospheric dynamics, hydrological cycles including cloud formation, lightning initiation, and (photo)chemistry. Chapters 3 and 5 illustrate how the magnitude of ozone production depends on the stellar UV irradiation, but that ozone destruction can be controlled by either the hydrological cycles (producing HO_x) or lightning initiation (producing NO_x) and the (photo)chemistry following these processes. Lightning initiation depends on the irradiation and thermodynamics, while orbital parameters like the planet's rotation rate and eccentricity determine the distribution of incoming stellar radiation, in turn also affecting the atmospheric circulation and chemistry. I also illustrate how age-of-air experiments and coordinate system transformations unveil the role of circulation-driven atmospheric chemistry in Chapters 4 and 5, paving the way for further discoveries in climate-dynamics-chemistry interactions as described in Chapter 6. Contrasting the simulations of TRAPPIST-1 d in Chapter 5 underscores the sensitivity of planetary climates to orbital configurations, with implications for habitability studies. Distinct 3D variations in ozone distributions affect potential biosignature interpretation on rocky exoplanets. The presence of spectral fluctuations for the 1:1 resonant cases and the constant spectra for the 3:2 resonant cases provide an important discriminant between both orbital configurations and needs to be considered when studying seasonally varying biosignatures.

I suggest various avenues for further research including 1) climate-dynamics-chemistry interactions, 2) additional disequilibrium chemical processes, 3) habitability for different spin-orbit resonances, 4) intercomparisons for models and (lightning) parametrizations, and 5) prebiotic chemistry in 3D. The 3D variations and potential spectral fluctuations can only be predicted and interpreted using complex 3D CCMs, emphasizing an important role for CCM simulations in developing the science objectives for observatories such as LIFE.

Lay Summary

The past three decades have seen numerous detections of planets outside of our Solar System or exoplanets. Hundreds of these are rocky exoplanets with a size similar to Earth orbiting around relatively small and cool stars known as M-dwarfs. The strong gravitational pull from the host star can lock the rotation and orbit of these planets into a specific ratio, resulting in so-called spin-orbit resonances. A 1:1 spin-orbit resonance means that the same side of the planet always faces the star, like the Moon around the Earth. In a 3:2 resonance, a planet rotates three times around its own axis for every two orbits around the star, like Mercury around the Sun.

We try to understand the effects of these resonances on the physical and chemical processes in exoplanet atmospheres, by applying complex computer models – like the ones used to simulate Earth's weather, climate, and atmospheric chemistry – to simulate exoplanet atmospheres. The simulations of exoplanet atmospheres help to 1) determine the habitability of exoplanets to understand whether they can support life and 2) how we might detect chemical species and potential signs of biological processes in their atmospheres.

Two of the main techniques to observe the temperature and chemical species in exoplanet atmospheres are transmission and emission spectroscopy. When we see a planet move in front of its host star, we observe a transmission spectrum of the stellar light passing through the planetary atmosphere. The intensity of the light varies with wavelength due to the interaction with molecules in the atmosphere, allowing astronomers to identify which molecules are present. Emission spectroscopy instead focuses on the light emitted by the planet, again varying with wavelength depending on the molecules present in the atmosphere.

In this thesis, I apply a computer model of an exoplanet atmosphere for different spin-orbit resonances. I aim to understand the effects on atmospheric chemistry and habitability and to interpret future observations with space telescopes. I focus on two distinct rocky planets, Proxima Centauri b and TRAPPIST-1 d. For these planets, I simulate the chemistry related to ozone, an interesting molecule since it is a sign of life on Earth and interacts strongly with stellar light. Because of this interaction, Earth's ozone layer protects the surface from harmful solar radiation. Ozone also forms due to

stellar light. I consider the three-dimensional structure of an atmosphere and simulate the chemistry driven by temperature, photodissociation, atmospheric circulation, and the presence of lightning flashes. These processes all depend on the planetary orbit and the spin-orbit resonance.

In the thesis, I show how stellar radiation from M-dwarfs drives the formation of a global ozone layer for both planets. The amount of ozone is much higher on Proxima Centauri b than on TRAPPIST-1 d because of more stellar radiation at ultraviolet (UV) wavelengths. I then study whether lightning occurs on exoplanets since lightning flashes can produce molecules that destroy ozone in chemical reactions. Persistent lightning storms cover the daysides of Proxima Centauri b and TRAPPIST-1 d in a 1:1 spin-orbit resonance. For TRAPPIST-1 d, the chemical effect of the storms is so strong that it destroys ozone. I predict that we are unlikely to see this chemical effect of lightning in transmission spectra.

The ozone on Proxima Centauri b shows spatial variations with large amounts on the permanent nightside. The production of ozone needs sunlight and is limited to the dayside. The thesis describes a specific circulation pattern transporting ozone from the dayside production regions to the nightside. It shows how circulation patterns affect the distribution of molecules in exoplanet atmospheres.

A comparison between the atmospheres of Proxima Centauri b and TRAPPIST-1 d for different spin-orbit resonances shows that both planets have habitable climates for a 1:1 resonance, although TRAPPIST-1 d requires an artificial reduction of the incoming stellar radiation. Distinct wind patterns on the planets result in different ozone distributions. TRAPPIST-1 d in a 3:2 resonance warms significantly due to a runaway greenhouse effect with very high surface temperatures. Proxima Centauri b still shows habitable surface temperatures in a 3:2 resonance. The resonance leads to day-night cycles accompanied by time variations in surface radiation, temperature, water vapour, and ozone. Emission spectra show signatures of molecules like ozone, water vapour, and carbon dioxide. The spectra vary with time for exoplanets in a 1:1 resonance but not for a 3:2 resonant planet since the atmosphere is more uniform. This distinction is crucial in our search for seasonally varying signs of biological processes on exoplanets.

The thesis shows the intricate interactions between stellar radiation, planetary orbit, atmospheric circulation, lightning, and atmospheric chemistry within planetary atmospheres. All of these processes are affected by spin-orbit resonances and the associated day-night cycles. The interactions between these processes determine the habitability of a planet and our ability to interpret molecules and potential signs of biological processes in their atmospheres.

Beknopte Samenvatting

Sinds de eerste detectie in 1995 van een exoplaneet is een grote hoeveelheid planeten buiten ons Zonnestelsel ontdekt. Honderden zijn rotsplaneten, vergelijkbaar in grootte met de Aarde. De rotsplaneten worden vooral gevonden rondom relatief koele en kleine sterren die we rode dwergen noemen. De sterke zwaartekracht van de moederster kan de spin en de baan van een planeet vastzetten in een bepaalde verhouding, resulterend in een zogenaamde spin-baan resonantie. Een 1:1 resonantie betekent dat dezelfde kant van de planeet altijd gericht is naar de ster en leidt tot een permanente dag- en nachtzijde. Dit is vergelijkbaar met de baan van de Maan rondom de Aarde. In een 3:2 resonantie draait een planeet drie keer om de eigen as voor iedere twee banen rondom de ster, zoals Mercurius rondom de Zon.

Het is belangrijk dat wij deze resonanties en hun invloed op atmosferen begrijpen, omdat deze gevolgen hebben voor dag en nacht cycli, temperaturen aan het oppervlak van de planeet, atmosferische circulatie, en atmosferische chemie. Wetenschappers gebruiken geavanceerde computer modellen om de fysische en chemische processen in de atmosferen van exoplaneten te bestuderen. Dezelfde modellen worden ook gebruikt in de voorspellingen van het weer, klimaat, en de atmosferische chemie op Aarde. De simulaties van exoplanetaire atmosferen helpen ten eerste om vast te stellen wat de leefbaarheid van een exoplaneet is en ten tweede hoe we moleculen en mogelijk tekenen van biologische processen kunnen waarnemen in de atmosfeer.

Astronomen gebruiken voornamelijk twee manieren om de temperatuur en moleculen in exoplanetaire atmosferen te ontdekken: transmissie en emissie spectroscopie. In transmissie beweegt de planeet voor de moederster langs en zien we een kleine dip in de hoeveelheid sterlicht die we ontvangen. De sterkte van de dip hangt af van de golflengte waarin we observeren door de interactie met moleculen in de atmosfeer. Hierdoor kunnen we bepalen welke moleculen zich in de atmosfeer bevinden. In emissie spectroscopie nemen we het licht waar dat wordt uitgezonden door de planeet. Ook dit licht varieert met de golflengte door de aanwezigheid van moleculen in de atmosfeer.

In deze thesis gebruik ik een computer model van een exoplanetaire atmosfeer voor verschillende spin-baan resonanties. Het doel is om de gevolgen voor atmosferische chemie en leefbaarheid te bepalen en om toekomstige observaties met ruimtetelescopen te verklaren. De modellen simuleren de chemie gerelateerd aan ozon op twee rotsplaneten, Proxima Centauri b en TRAPPIST-1 d. Ozon is een interessant molecuul

omdat het een gevolg is van leven op Aarde en veel interacties heeft met sterstraling. Deze interacties zorgen bijvoorbeeld voor de bescherming tegen schadelijke ultraviolette zonnestraling op Aarde. Ik beschouw de driedimensionale structuur van een atmosfeer en simuleer de chemie ten gevolge van temperatuur, fotodissociatie, atmosferische circulatie, en de aanwezigheid van bliksemschichten. Deze processen hangen sterk af van de planetaire baan en spin-baan resonanties.

In de thesis toon ik aan hoe sterstraling van rode dwergen de formatie van een globale ozonlaag kan aandrijven op beide planeten. De relatief sterke sterstraling produceert meer ozon op Proxima Centauri b dan op TRAPPIST-1 d. Hierna onderzoek ik of bliksem kan ontstaan op exoplaneten, aangezien bliksem moleculen kan produceren die ozon vernietigen in chemische reacties in de atmosfeer. Aanhoudend onweer bedekt de dagzijde van planeten in een 1:1 resonantie. Voor TRAPPIST-1 d is het chemische effect van onweer zo sterk dat ozon wordt vernietigd. Voorspelde transmissie spectra voor Proxima Centauri b tonen geen merkbaar direct effect van de moleculen die geproduceerd of vernietigd worden door bliksem.

De ozonlaag op Proxima Centauri b in een 1:1 resonantie toont ruimtelijke variaties, met een grote hoeveelheid ozon op de nachtzijde van de planeet. De productie van ozon hangt af van sterstraling en vindt alleen plaats op de dagzijde. De thesis beschrijft hoe de atmosferische circulatie zorgt voor transport van ozon van de dag- naar de nachtzijde. Dit toont aan hoe atmosferische circulatie de distributie van moleculen in een atmosfeer kan beïnvloeden.

Een vergelijking tussen de atmosferen van Proxima Centauri b en TRAPPIST-1 d voor verschillende resonanties toont dat beide planeten leefbare klimaten hebben voor een 1:1 resonantie, hoewel TRAPPIST-1 d een kunstmatige reductie van de hoeveelheid sterstraling nodig heeft. Diverse windpatronen resulteren in verschillende ruimtelijke distributies van de ozonlaag. TRAPPIST-1 d in een 3:2 resonantie laat een dramatische opwarming zien door een op hol geslagen broeikaseffect met zeer hoge temperaturen aan het oppervlak. Proxima Centauri b heeft nog steeds leefbare temperaturen voor een 3:2 resonantie. De resonantie brengt dag en nacht cycli met variaties in de sterstraling, temperatuur, waterdamp, en ozon. Emissie spectra bevatten indicaties van moleculen als ozon, waterdamp, en koolstofdioxide. De spectra variëren met de tijd voor exoplaneten in een 1:1 resonantie terwijl de spectra voor een 3:2 resonantie constant zijn door een meer homogene atmosfeer. Dit onderscheid is cruciaal voor de zoektocht naar seizoensgebonden tekenen van biologische processen op exoplaneten.

De thesis toont de ingewikkelde interacties in planetaire atmosferen, tussen sterstraling, planeetbaan, atmosferische circulatie, bliksem, en atmosferische chemie. Al deze processen worden beïnvloed door spin-baan rotaties en de bijkomende of afwezige dag- en nacht-cycli. De interacties tussen deze processen bepalen de leefbaarheid van exoplaneten en ons perspectief om de kenmerken van moleculen en mogelijke tekenen van biologische processen in observaties van een atmosfeer te verklaren.

Koarte Gearfetting

Sûnt de earste deteksje yn 1995 bin der hast 6,000 planeten bûten ús Sinnestelsel ûntdekt, saneamde eksoplaneten. Hûnderten binne rotsplaneten, ferlykber yn grutte mei de Ierde. De rotsplaneten wurde foaral fûn rûnom relatyf kâlde en lytse stjerren dy 't wy reade dwergen neame. De sterke swiertekrêft fan de memmestjer kin de ferhâlding tusken de spin en de omgong fan in planeet fêstsette, resultearjend yn in saneamde spin-omgong resonânsje. In 1:1 resonânsje betsjut dat deselde kant fan 'e planeet altyd rjochte is nei de stjer en resultearred yn in permaninte dei- en nachtside. Dit is fergelykber mei de omgong fan de Moanne om de Ierde. Yn in 3:2 resonânsje draait in planeet trije kear om de eigen as foar elke twa omgongen om de stjer hinne, lykas Mercurius om de Sinne.

It is wichtich dat wy dizze resonânsjes en harren ynfloed op atmosfearen begripe, omdat dy gefolgen hawwe foar de dei en nacht syklus, temperatueren oan it oerflak fan de planeet, atmosfearyske sirkulaasje, en atmosfearyske gemy. Wittenskippers brûke komplekse kompjûtermodellen om de fysyske en gemyske prosessen yn 'e atmosfearen fan eksoplaneten te bestudearjen. Deselde modellen wurde ek brûkt yn de foarsizzingen fan it waar, it klimaat, en de atmosfearyske gemy op Ierde. Earst, helpe de simulaasjes fan eksoplanetêre atmosfearen om fêst te stellen wat de leefberens fan in eksoplaneet is. Twads, helpe de simulaasjes fêst te stellen hoe 't wy moleculen en mooglik tekenjen fan libjen waarnimme kinne yn 'e atmosfear.

Astronomen brûke benammen twa wizen om de temperatuer en molekulen yn eksoplanetêre atmosfearen te ûntdekken: transmisje en emisje spektroskopy. Yn transmisje beweecht de planeet foar de memmestjer del en sjogge wy in lytse dip yn hoefolle stjerljocht wy ûntfange. De grutte fan 'e dip hinget ôf fan 'e golflingte dêr 't wy yn observearje troch de ynteraksje mei molekulen yn 'e atmosfear. Dêrtroch kinne wy bepale hokker moleculen oft der yn 'e atmosfear binne. Yn emisje spektroskopy observearje wy it ljocht dat útstjoerd wurdt troch de planeet. Dit ljocht fariearret ek mei de golflingte troch de oanwêzigens fan molekulen yn 'e atmosfear.

Yn dizze skripsje brûk ik in kompjûtermodel fan in eksoplanetêre atmosfear foar ferskillende spin-baan resonânsjes. Ik stribje dernei om de gefolgen foar atmosfearyske gemy en leefberens te bepalen en om takomstige observaasjes mei romteteleskopen te ferklearjen. De modellen simulearje de gemy relatearre oan oazon op twa planeten, Proxima Centauri b en TRAPPIST-1 d. Oazon is in ynteressant molekuul omdat it in gefolch is fan libben op Ierde en in soad ynteraksjes hat mei stjerstrieling. Dy

ynteraksjes soargje ek foar de beskerming tsjin skealik ultrafiolette sinnestrieling op Ierde. Ik beskôgje de trijediminsjonale struktuer fan in atmosfear en simulearje de gemy as gefolch fan temperatuer, fotodissosjaasje, atmosfearyske sirkulaasje, en de oanwêzigens fan bliksemskichten. Dizze prosessen hingje sterk ôf fan 'e planetêre omgong en spin-omgong resonânsjes.

Stjerstrieling fan reade dwergen kin de formaasje fan in globale oazonlaach oandriuwe. De relatyf sterke stjerstrieling produsearret mear oazon op Proxima Centauri b. Hjirnei ûndersykje ik oft bliksem ûntstean kin op eksoplaneten, om't bliksem molekulen produsearje kin dy 't oazon ferneatigje yn gemyske reaksjes yn de atmosfear. Oanhâlden ûnwaar bedekt de side fan planeten yn in 1:1 resonânsje. Foar TRAPPIST-1 d is it gemyske effekt fan ûnwaar sa sterk dat it oazon ferneatiget. Foarseine transmisje spektra fan Proxima Centauri b litte gjin merkber direkt effekt sjen fan de molekulen dy 't produsearre wurde troch bliksem.

De oazonlaach op Proxima Centauri b yn in 1:1 resonânsje lit romtlike feriaasjes sjen, mei in grutte hoemannichte oazon op 'e nachtside fan 'e planeet. De produksje fan oazon hinget ôf fan stjerstrieling en is allinich op 'e deiside. De skripsje beskriuwt hoe 't de atmosfearyske sirkulaasje soarget foar transport fan oazon fan de deiside nei de nachtside. Dat lit sjen hoe 't atmosfearyske sirkulaasje molekulen yn in atmosfear kin distribuearre.

In ferliking tusken de atmosfearen fan Proxima Centauri b en TRAPPIST-1 d foar 1:1 en 3:2 resonânsjes lit sjen dat beide planeten leefbere klimaten hawwe foar in 1:1 resonânsje, al hat TRAPPIST-1 d in keunstmjittige reduksje fan de sterstrieling nedich. In ûnderskied yn wynpatroanen resultearret yn ferskillende romtlike distribúsjes fan de oazonlaach. TRAPPIST-1 d yn in 3:2 resonânsje lit in dramatyske opwaarming sjen troch in broeikaseffekt mei tige hege temperatueren oan it oerflak. Proxima Centauri hat lykwols noch leefbere temperatueren foar in 3:2 resonânsje. De resonânsje bringt dei en nacht sykly mei fariaasjes yn 'e stjerstrieling, temperatuer, wetterdamp, en oazon. Emisje spektra befetsje yndikaasjes fan molekulen as oazon, wetterdamp, en koalstofdiokside. De spektra fariearje mei de tiid foar eksoplaneten yn in 1:1 resonânsje wylst de spektra foar in 3:2 resonânsje konstant binne troch in mear homogene atmosfear. Dit ûnderskied is krúsjaal foar de syktocht nei seizoensbûne tekens fan libben op eksoplaneten.

De skripsje analysearret de yngewikkelde ynteraksjes yn planetêre atmosfearen, tusken stjerstrieling, planeetomgong, atmosfearyske sirkulaasje, bliksem, en atmosfearyske gemy. Al dizze prosessen wurde beynfloede troch spin-omgong resonânsjes en de bykommende of ôfwêzige dei en nacht sykly. De ynteraksjes tusken dizze prosessen bepale de leefberens fan eksoplaneten en ús perspektyf om de tekens fan molekulen en mooglike tekens fan libben yn observaasjes fan in atmosfear te ferklearjen.

Acknowledgements

First, I would like to thank my supervisors for giving me the fantastic opportunity to work on the boundary between Earth and exoplanetary science. Paul and Leen, I could not have asked for better preparation for the next steps in my academic career. Thank you for all the guidance, support, and insightful meetings whilst allowing substantial independence in the research and its dissemination. Paul, sometimes I wonder how you do it, but your dedication to helping your students is inspiring. You will somehow make time for science, discussing model crashes, administrative matters, group trips, or even walks in the Meadows (when we were all working from home). Leen, our scientific discussions always encouraged a deep understanding of fundamental physical concepts, in my case until the final days before submission! You have a great ability to help others achieve this understanding and it always results in fascinating meetings and insights.

I also thank my co-supervisors, Ken and Jeremy, for interesting scientific discussions and for ensuring adequate progression in the PhD. Having different viewpoints on the research has helped me a lot. The technical assistance, support, and collaborations with Nathan Mayne and all the members of the Exeter Exoplanet Theory Group were invaluable in achieving the work in this thesis. I am glad I managed to visit Exeter twice but it is impressive how well you can make remote participants feel part of EETG. Being a member of the CHAMELEON network allowed me to become part of an amazing ESR community: I am proud of what we achieved with our ESR retreats. I would like to thank Ludmila Carone for her continuous support and interesting scientific discussions throughout the PhD. A European joint PhD degree hosted in a non-EU country comes with its challenges and I would like to thank all the people who helped to make this possible, and particularly Sophie Ramette and Brendan Martin for always helping me with questions. With limited knowledge of written Frisian, I decided to write a Frisian summary of this thesis, which I could not have done without the help of Andries and Wietske Jongbloed.

To all who made the Crew Attic such a wonderful place to spend many days, although depending on the season the presence of heating or the absence of countless wasps would have made for slight improvements... Thank you to those who were there from start to finish, Carla, Maureen, Hannah, and Callum; to those who spent their secondment here, Fran and Linus; and to those who joined in recently, Gergely and Kalyani. Thank you, Timothy, Luca, Tinne, Nicholas, and Marc-Antoine, for kindly

welcoming me into your offices at the IvS. To the past and present members of Geovil Town, for a mixture of great and not-so-great football games, that were nevertheless always fun. Every conference I have attended involved reunions with old friends or the creation of new friendships. Even though the reunions can be infrequent, they form a source of inspiration in my academic journey.

The first two weeks of 'confinement' in David Horn House resulted in lasting friendships and a headstart to my time in Edinburgh. To the wonderful people that I met in university accommodation at Buccleuch Place. Sen Sen, Jay, and Chen, random chance brought together such great flatmates and you truly broadened my horizon. Thank you to those people who shared adventures in the Highlands with me, particularly Memo and Xixi. Even just going to the Pentlands always ends up being a bigger adventure than intended! I am very grateful for all the friends who came to visit me in Edinburgh, Leuven, or in some cases even both. Thank you, Arjen, Boyd, Chris, Dennis, Laura, Martin, Pieter, Radu, Sjoerd, Thomas, Tom R., Tom V., Ype, Yvette.

Thank you, Jamie, for all your support over these years, for the (at least) weekly taco night and so many creative recipes, for coping with my fascination for camping trips in Scotland, and for always being excited to explore together. Meeting each other in Edinburgh meant a start in English for us. With both of us leaving the UK, will it now transition to Dutch or German?

Finally, to my family. Thank you, Sander and Lisa, for dealing with a brother across the Channel during good and more challenging times and for taking the time to visit. Pap en mam, thank you for continuous support, lending an ear and giving life advice whenever required, and for allowing and encouraging me to figure out my own path in life. With excitement, you made numerous visits to Scotland and Belgium, to the extreme case that a specific birthday on October 7th in 2022 was enough reason for a day trip from Friesland to Leuven. I could not have made it this far without you and I hope this thesis also makes you proud.

Declaration

I declare that this thesis was composed by myself, that the work contained herein is my own except where explicitly stated otherwise in the text, and that this work has not been submitted for any other degree or professional qualification except as specified.

The outcomes of this work have been published in or will be submitted to academic journals:

The research presented in Chapter 3 has been published in Monthly Notices of the Royal Astronomical Society (Braam et al., 2022).

The research presented in Chapter 4 has been published in Monthly Notices of the Royal Astronomical Society (Braam et al., 2023).

The research presented in Chapter 5 will be submitted for publication in The Planetary Science Journal.

I am a co-author on two other papers that were published during my PhD. We investigate flare-induced chemistry for tidally locked M-star planets (Ridgway et al., 2023), where I contributed to the development of the (photo)chemical network, the deposition parametrizations, and to the analysis of 3D data. Recently, we combined 3D simulations of atmospheric chemistry with dynamical systems theory to analyse the compound dynamics of temperature, wind speeds, and ozone columns on tidally locked exoplanets (De Luca et al., 2024). For this project, I performed the 3D simulations and contributed significantly to the analysis and interpretation of the results. Both of these works are referred to in the thesis but will not be described in detail.

Marrick Braam

Contents

Figures and Tables

Figures

Tables

List of Abbreviations

ASAD	A Self-contained Atmospheric chemistry coDe
CAPE	Convective Available Potential Energy
CCM	Coupled Climate-chemistry Model
CG	Cloud-to-Ground
DD	Dry deposition
DU	Dobson Unit
ELT	Extremely Large Telescope
FUV	Far-Ultraviolet
GCM	General Circulation Model
HST	Hubble Space Telescope
HWO	Habtable Worlds Observatory
HZ	Habitable Zone
IC	Intracloud
JWST	James Webb Space Telescope
LASO	Latitudinally Asymmetric Stratospheric Oscillation
LFR	Lightning flash rate
LIFE	Large Interferometer For Exoplanets
LW	Longwave
MIR	Mid-infrared
MMR	Mass Mixing Ratio
NUV	Near-ultraviolet
ODE	Ordinary Differential Equation
PAL	Present Atmospheric Level
PC2	Prognostic Cloud and Condensate scheme
PIE	Photochemical Intercomparison for Exoplanets
PSG	Planetary Spectrum Generator
SED	Spectral Energy Distribution
SOCRATES	Suite of Community Radiative Transfer codes based on Edwards and Slingo
SW	Shortwave
THAI	TRAPPIST-1 Habitable Atmosphere Intercomparison
TOA	Top of the atmosphere
UKCA	UK Chemistry and Aerosols
UM	Unified Model
UV	Ultraviolet

VMR	Volume mixing ratio
WD	Wet deposition
XUV	Extreme-ultraviolet

Chapter 1

Introduction

1.1 Planets Near and Far

Amongst the first discoveries of planets around other stars than the Sun were the discovery of exoplanets orbiting a neutron star (Wolszczan & Frail, 1992) and a Sun-like (G-type) star (Mayor & Queloz, 1995). About three decades later, the count of confirmed exoplanets has now reached 5,602[1]. These exoplanets provide interesting opportunities to investigate whether the Solar System is unique and, ultimately, whether Earth is unique. Simply considering bulk planetary parameters, Solar System planets seem to fall into a relatively tight temperature range of $\sim$70–700 K, for Neptune and Venus, respectively. The Solar System demonstrates three tight ranges of planetary mass and radius (see e.g. de Pater & Lissauer, 2015, Chapter 1, for an overview): 0.05–1 $M_\oplus$ and 0.38–1 $R_\oplus$ for the rocky planets, 14.5–17.2 $M_\oplus$ and 3.9–4.0 $R_\oplus$ for the ice giants, and 95.2–317.8 $M_\oplus$ and 9.4–11.2 $R_\oplus$ for the gas giants. Our current sample of confirmed exoplanets already reveals an astonishingly wide parameter space compared to this, with a much more continuous distribution of equilibrium temperatures ranging from 55–4000 K, masses ranging from 10^{-2}–10^4 $M_\oplus$, and radii between 0.27–24 $R_\oplus$. One of the many fascinating discoveries is the common existence of exoplanets with sizes between Earth and Neptune that have no counterpart in the Solar System (see the review by Bean et al., 2021). The definition of a rocky or terrestrial planet is commonly based on the bulk composition that follows from constraints on mass and radii (e.g. Rogers, 2015). Upper limits to be consistent with rocky compositions are $R<1.6$ $R_\oplus$ (Rogers, 2015) or $M<10$ $M_\oplus$ (e.g. Stevens & Gaudi, 2013). For a larger radius (>2 $R_\oplus$) or mass a planet will become gaseous due to rapid gas accretion (e.g. Ida & Lin, 2004), leaving the radius gap in between (Fulton et al., 2017). The confirmed exoplanets include 1,052 planets with mass and radius consistent with a rocky composition[1]. The occurrence rate of rocky exoplanets is estimated at 0.15 planet per FGK star (Howard et al., 2012; Fressin et al., 2013; Petigura et al., 2013; Kunimoto & Matthews, 2020) and increases to 0.46 planet per M-dwarf stars (Dressing & Charbonneau, 2013, 2015).

1. As of 05/04/2024, from the NASA Exoplanet Archive (https://exoplanetarchive.ipac.caltech.edu)

Despite the tight ranges in bulk planetary parameters, the Solar System planets (and their moons) exhibit a great diversity in their atmospheres. This diversity includes (but is by no means limited to) atmospheric pressures ranging from 92 bar on Venus to a seasonally variable 4–9 mbar Mars (Hess et al., 1980), persistent giant storms and lightning on Jupiter (Vasavada & Showman, 2005), sulfuric acid clouds (Young, 1973) and reportedly phosphine (Greaves et al., 2021) on Venus, variable methane levels on Mars (Webster et al., 2018), complex organic chemistry on Titan (Yung et al., 1984), and seasonal hazes on Pluto (Gladstone et al., 2016). Earth's oxygen-rich atmosphere has been altered significantly by biological processes on the planet, and these indications of biological processes in Earth's atmosphere are known as biosignatures. However, we also know that the atmospheric composition of Earth has evolved considerably over geological timescales and only became rich in oxygen after the Oxidation Events $\sim$2.5 and 0.54 Gyr ago (e.g. Lyons et al., 2014). Rocky planet atmospheres are generally depleted in volatile elements as compared to the Sun due to a range of atmospheric formation and loss processes (Wordsworth & Kreidberg, 2022). The diversity in Solar System atmospheres provides a glimpse of the atmospheric diversity that we may expect and are beginning to uncover for the diverse set of exoplanets.

1.2 The Formation of Atmospheres

The Solar System shows a distinction between hydrogen-dominated atmospheres for the giant planets and atmospheres of three rocky planets (Earth, Mars, Venus) dominated by high mean molecular weight gases. Planetary atmospheres can form through 1) the accretion of nebular gas from the protoplanetary disk (primordial), 2) release of gas following the accretion of planetesimals (primary), or 3) outgassing from the planetary interior (secondary). Several geological and atmospheric processes can modify the atmospheres of rocky exoplanets to evolve from primordial or primary to secondary atmospheres, see Lichtenberg et al. (2023) for a comprehensive overview.

Particularly important is the tendency of young rocky planets to lose their primordial atmospheres through hydrodynamical escape processes, with light species such as hydrogen particularly affected. This escape can be driven by XUV radiation (X-ray and extreme-ultraviolet or $\lambda <$121.6 nm), which has affected Earth's atmosphere during stages of enhanced XUV luminosity of the Sun (e.g. Zahnle & Walker, 1982; Ribas et al., 2005). After the loss of hydrogen, atmospheres are more stable against escape due to a higher mean molecular mass. In the context of exoplanets, both XUV-driven hydrodynamic escape (Lopez & Fortney, 2013; Owen & Wu, 2013) and core-powered mass loss (Ikoma & Hori, 2012; Gupta & Schlichting, 2019) can explain the radius gap between 1.6 and 2.0 $R_\oplus$. Since M-dwarfs have a relatively long phase of enhanced luminosity in their early lifetime (Baraffe et al., 2015) and emit a relatively large fraction of their radiation in the XUV (France et al., 2016; Ribas et al., 2017), planets around M-dwarfs will be particularly susceptible to these escape processes.

After the disk phase, planetary atmospheres will be strongly affected by interior-atmosphere interactions and geochemical cycles along with impact degassing (Chyba, 1990). The formation of such secondary atmospheres is complex and depends on volatile abundances in the mantle, the redox state, and the degassing pressure (Lichtenberg et al., 2023). The redox state is an important chemical principle in this context: a system is reducing if it contains relatively high amounts of reducing species such as H or Fe^0 that donate electrons, whereas a system is oxidizing if it contains high amounts of species like O that accept electrons. For Venus, Earth, and similarly sized exoplanets we expect an oxidized interior with CO_2 and H_2O as dominant outgassed volatiles and for more reduced planets we expect an atmosphere rich in hydrogen (Gaillard et al., 2021; Lichtenberg et al., 2023). The solubility of volatiles in magma determines what is outgassed (Sossi et al., 2020) and the solubility of volatiles in water controls weathering rates on planets with oceans and thus affects the atmospheric content of volatiles, as shown by Earth's carbonate-silicate cycle (see e.g. Pierrehumbert, 2010b, Chapter 8). Hence, given the range of possible outgassing rates and interior-atmosphere interactions, atmospheric compositions may vary considerably across terrestrial exoplanets.

1.3 Observing Exoplanet Atmospheres

Several techniques exist to probe the signals of exoplanet atmospheres and distinguish them from a much brighter star nearby. Figure 1.1 illustrates the techniques that rely on measurements of the combined star-planet flux (Seager & Sasselov, 2000). Due to the varying geometry of the star-planet system as seen from Earth, we observe variations in the brightness or flux. For a transiting exoplanet (left in Figure 1.1), we measure a transmission spectrum when the planet passes in front of its host star. The stellar flux that is transmitted through the limb of the planetary atmosphere is affected by absorption and scattering due to constituents of the planetary atmosphere. At a phase of 180° later in the orbit, the planet passes behind the host star in the secondary eclipse. In this case, the missing thermal emission from the planet can be used to infer planet properties such as the temperature. For the rest of this orbit and for the full orbit of the non-transiting exoplanet (right), we can probe the thermal emission from the planet, given sufficient sensitivity and angular resolution of a telescope. Probing the thermal emission in a specific wavelength band as a function of the orbital phase will result in a phase curve, with a signal varying as a function of the orbital phase. Other ways to observe exoplanet atmospheres include high-resolution spectroscopy in which we resolve individual absorption lines (e.g. Snellen et al., 2010) and direct imaging techniques that block out the stellar light using coronography, a promising approach to future characterisation of terrestrial exoplanets on wide orbits around Sun-like (G-type) stars (like the Earth) (Feng et al., 2018).

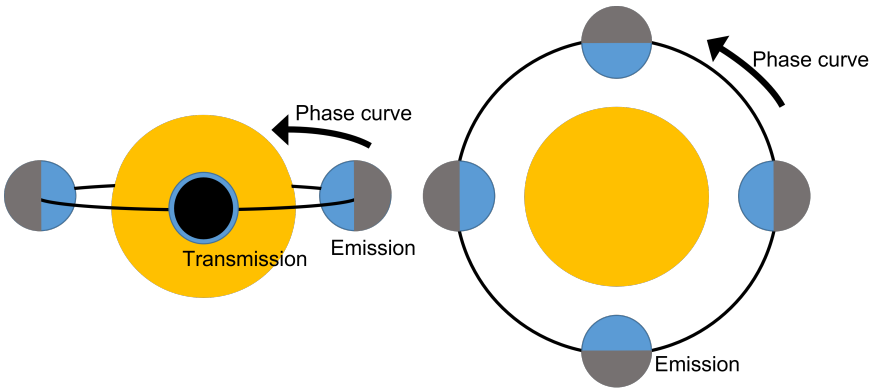

Figure 1.1: Geometries of two exoplanet orbits as seen from Earth: for a transiting planet on the left and a non-transiting planet on the right. For a transiting-planet (as seen from Earth), we can infer planet properties when the planet moves in front or behind of its host star. In the former case, we probe the transmission of stellar light through the limb of the atmosphere in a transmission spectrum. In the latter case, we can learn about the planetary atmosphere due to the absence of the planet's thermal emission in the combined star-planet flux. With enough sensitivity and angular resolution, we can measure the emission spectrum for the rest of the orbit of a transiting planet and for a non-transiting exoplanet during the full orbit, probing the thermal emission from the planet. When probing the thermal emission at a specific wavelength as a function of orbital phase we obtain a planet's phase curve.

Focusing on the methods that observe combined star-planet fluxes, the main challenge is to separate a planet from its host star that is at least a million times brighter. Terrestrial exoplanets around M-dwarfs provide an opportunity since they are: 1) the most commonly found stellar type, 2) relatively small stars, making exoplanet atmospheric signatures easier to detect, and 3) relatively cool stars, meaning that temperate terrestrial exoplanets have a close-in orbit with an enhanced probability to transit. Table 1 of Wordsworth and Kreidberg (2022) lists the most promising transiting exoplanets. Of particular interest here is the system of seven rocky exoplanets orbiting the cool M-dwarf TRAPPIST-1 (Gillon et al., 2017). On the other hand, Proxima Centauri b (Anglada-Escudé et al., 2016) presents the most promising non-transiting target to probe thermal emission.

The Hubble Space Telescope (HST) has observed twelve terrestrial planets orbiting M-dwarfs, finding featureless spectra and ruling out H_2-dominated atmospheres for LHS 1140 b (Edwards et al., 2020), TRAPPIST-1 b–h (de Wit et al., 2016, 2018; Garcia et al., 2022), L 98-59 b–d (Zhou et al., 2022, 2023), Kepler-138 d (Piaulet et al., 2023), and GJ 1132 b (Libby-Roberts et al., 2022). For GJ 1132b b, this put earlier reported detections into question (Southworth et al., 2017; Swain et al., 2021). LHS 1140 b reportedly had water features but these might also be explained by stellar contamination (Edwards et al., 2020). Therefore, it seems that planets have atmospheres with a high mean molecular weight, clouds or hazes blocking the spectral features, or no atmosphere at all. More recently, observations with JWST have been published for five planets, generally also finding featureless spectra for LHS 475 b

(Lustig-Yaeger et al., 2023), TRAPPIST-1 b (Lim et al., 2023), GJ 1132 b (May et al., 2023), GJ 486 b (Moran et al., 2023), and GJ 341 b (Kirk et al., 2024). Water features due to stellar contamination are commonly observed in these transmission spectra, specifically due to the relatively low temperatures in stellar atmospheres of M-dwarfs (Rackham et al., 2018).

Thermal emission measurements offer a complementary view since they probe the global temperatures and heat circulation of a planet (e.g. Selsis et al., 2011). Additionally, since emission spectra originate in the part of the atmosphere that is optically thick at particular wavelengths, emission spectra are sensitive to the vertical atmospheric structure (Madhusudhan & Seager, 2009). Using Spitzer at 4.5 μm, Kreidberg et al. (2019) probed the thermal emission for LHS 3844 b, finding a large dayside-nightside temperature gradient and thus an absence of an atmosphere with strong heat circulation. By measuring the thermal emission from TRAPPIST-1 b and c, both Greene et al. (2023) and Zieba et al. (2023) report high dayside temperatures with little heat redistribution and thus rule out CO_2-rich atmospheres. The coming years will see more discoveries by JWST in rocky exoplanet atmospheres, potentially confirming an atmosphere for the first time.

Soon, ground-based instruments such as the Extremely Large Telescope (ELT) will provide high spectral and angular resolution, which can be used to characterise rocky exoplanet atmospheres and search for biosignatures using high-resolution spectroscopy (Snellen et al., 2013) and high-contrast imaging (Vaughan et al., 2024). Furthermore, the search for biosignatures has motivated the conceptualization of the next-generation space missions. The Habitable Worlds Observatory (HWO) is a planned NASA mission focusing on direct detection of reflected lights from temperate exoplanets, making use of a coronograph. The Large Interferometer For Exoplanets (LIFE) mission concept instead focuses on the detection of thermal emission from a range of temperate exoplanets (Quanz et al., 2022). Hence, detailed characterisation of rocky exoplanet atmospheres is on the doorstep.

1.4 Terrestrial Atmospheric Structure

The vertical distribution of the temperature in a planetary atmosphere differs significantly from planet to planet, and may even show substantial spatial and temporal variations on a single planet. Nevertheless, as shown in Figure 1.2, some general processes apply to all atmospheres (Wordsworth & Kreidberg, 2022). As a function of increasing altitude (or decreasing pressure), Figure 1.2 shows that the planetary boundary layer is a highly turbulent and therefore well-mixed region connected to the surface, which is also where interior-atmosphere interactions will occur. The troposphere is dominated by convection (Sergeev et al., 2020) driving an upward vertical flux of water vapour following the evaporation from the surface oceans. The pressure in the rising air parcel decreases to match that of the surrounding air, which is accompanied by expansion and thus cooling of the parcel. The

saturation threshold decreases with this cooling, causing an enhanced relative humidity. Once the relative humidity passes 100%, clouds start to form. A convective cloud deck over the substellar point of 1:1 resonant exoplanets can provide a stabilizing climate feedback by reflecting incoming stellar radiation (Yang et al., 2013; Kopparapu et al., 2016). Additionally, most of the heat transport happens in the troposphere (Showman et al., 2013). Due to the cold trap at the tropopause (or the boundary between the troposphere and stratosphere), there is only a small amount of exchange between these regions. The stratosphere is in radiative balance with little vertical mixing. On Earth, oxygen molecules in the stratosphere absorb incoming UV radiation and form ozone at these altitudes (Chapman, 1930). Consequently, the stratosphere will be important for the production of photochemical gaseous species and hazes on exoplanets. The presence of a strong UV absorber such as ozone can lead to stratospheric heating and result in a temperature inversion (Godolt et al., 2015), though the extent of heating will depend on the stellar flux distribution. For Earth, the next layer is the mesosphere in which temperature decreases with altitude until the coldest point in the atmosphere (Seinfeld & Pandis, 2016). Above the mesosphere we find the thermosphere, absorbing stellar XUV radiation and therefore reaching high temperatures (Seinfeld & Pandis, 2016) with the potential for atmospheric escape (Wordsworth & Kreidberg, 2022). Most atmospheres are transparent to the incoming visible radiation, which heats the planetary surface. Subsequently, the surface emits radiation at infrared (IR) wavelengths, which is absorbed by molecules such as CO_2, CH_4, N_2O, thereby heating the planet through the greenhouse effect (Pierrehumbert, 2010b).

1.5 Terrestrial Exoplanets: Orbits

Terrestrial exoplanets are exciting opportunities to test the uniqueness of Earth, motivating considerable effort into studying their habitability around different stellar types (e.g. Shields et al., 2016). The current concept of habitability revolves around the availability of liquid water and is summarized in the concept of the Habitable Zone (HZ; Kasting et al., 1993; Kopparapu et al., 2013), the circumstellar zone in which liquid water can exist on a planetary surface. At the inner edge of the HZ, the high surface temperatures cause the evaporation of water vapour, with subsequent water photolysis and hydrogen escape leading to the loss of a planet's water inventory (Kasting, 1988). Before this would happen, the lower atmosphere becomes opaque to outgoing radiation and thus surface temperatures will increase in a runaway greenhouse (Simpson, 1928; Ingersoll, 1969; Nakajima et al., 1992; Goldblatt & Watson, 2012; Chaverot et al., 2022). The radiation limit or Simpson-Nakajima limit in outgoing radiation is 282 W m^{-2}. The outer edge is defined by CO_2 condensation resulting in the weakening of the greenhouse effect due to CO_2. To first order, the HZ boundaries can be based on the stellar flux and orbital distance, conveniently the parameters that we know best

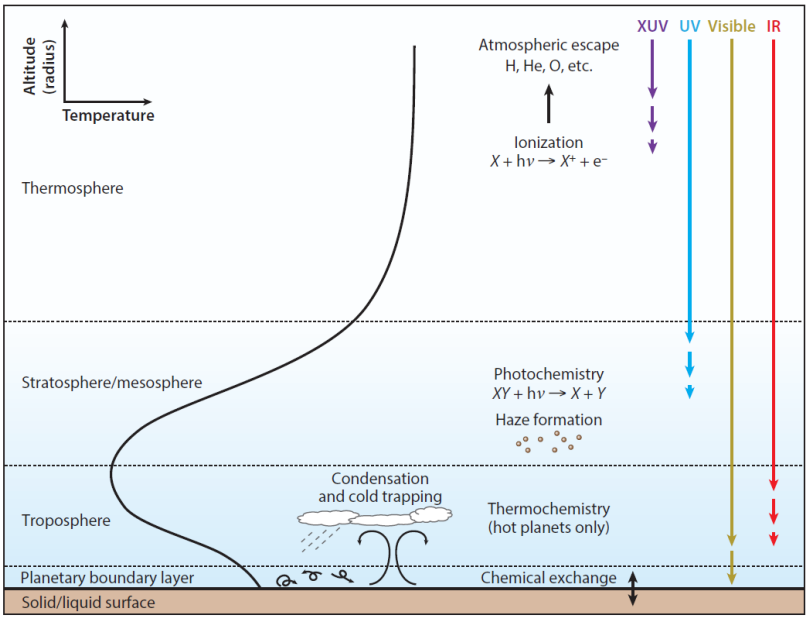

Figure 1.2: Illustration of the simplified vertical temperature distribution on rocky exoplanet atmospheres, along with key physical and chemical processes and the transparancy to light at different wavelengths. As a function of increasing altitude (or decreasing pressure), atmospheres are generally divided in the planetary boundary layer, troposphere, stratosphere, mesosphere, and thermosphere. Figure taken from Wordsworth and Kreidberg (2022).

for exoplanets. Therefore, despite the limitations and the many additional factors determining planetary habitability (e.g. Meadows & Barnes, 2018), the HZ remains a very useful concept. Out of the currently confirmed exoplanets, 106 orbit inside the HZ of their host star (Childs et al., 2022).

Due to the relatively low temperatures of M-type stars, the circumstellar HZ is located close to the host star. Consequently, an exoplanet orbiting in the HZ will experience a differential gravitational field from the host star which induces strong tidal torques on the planet (Barnes, 2017). These torques affect the planet's angular momentum, producing specific frequencies between a planet's orbital and spin velocity in a process called tidal locking (e.g. Barnes, 2017; Pierrehumbert & Hammond, 2019). These frequencies are known as spin-orbit resonances, given by $p=\omega/n$ where ω is the planet's spin velocity and $n=2\pi/P$ the orbital angular velocity for a planet of orbital period P. Nearby examples of spin-orbit resonances include the Moon's 1:1 spin-orbit resonance around the Earth and Mercury's 3:2 spin-orbit resonance around the Sun. Besides planets orbiting M-dwarfs, tidal locking can also occur for planets around K- and G-type stars or those in multiplanet systems (Barnes, 2017).

Following Goldreich and Soter (1966) and Pierrehumbert and Hammond (2019), the time (in years) for a planet on a circular orbit at an orbital distance r (AU) and with an initial spin velocity Ω_0 (in units of present Earth's spin $\Omega_\oplus$) to become tidally locked is given by:

$$t_{lock} = 3.01 \times 10^8 \frac{\rho \Omega_0 r^6}{M_*^2} \frac{Q}{k_2}, \tag{1.1}$$

for a mean planet density ρ (in units of Earth's density $\rho_\oplus$) and stellar mass M_* (in $M_\odot$). Hence, the prefactor accounts for the unit conversions and the conversion from seconds to years. Q is a measure of tidal dissipation and depends on the rheology of the planet and the Love number k_2 depends on a planet's rigidity. These parameters are uncertain, but t_{lock} is mainly driven by the r^6 dependence. Following Pierrehumbert and Hammond (2019), we use an estimated Q/k_2=1000 for rocky planets, whereas Q/k_2=$10^5/0.3 = 3.3 \times 10^6$ for gaseous planets (e.g., Goldreich & Soter, 1966; Kramm et al., 2012). Assuming an initial spin velocity equal to Earth's angular velocity (7.292$\times 10^{-5}$ rad s^{-1}) and known values for ρ, r, and M_* [2], we can estimate the tidal locking timescale for exoplanets. Figure 1.3 shows the exoplanet population in terms of orbital period (P_{orb}) and planetary mass (M_p). Simply looking at the distribution in P_{orb}–M_p space already shows the wide diversity in exoplanet parameters as mentioned in Section 1.1 and confirms the continuous mass range between 10^{-2}–10^4 $M_\oplus$. Compared to Solar System planets (as indicated by the letters), we indeed see that the current exoplanet population is found on relatively close-in orbits, partly due to the observational bias (e.g. Mordasini et al., 2009). Such close-in orbits are particularly prominent when we consider planets that could be rocky, using an approximate upper limit of 10 $M_\oplus$ (the dashed horizontal line in Figure 1.3) following Stevens and Gaudi (2013). For all exoplanets in Figure 1.3 that have the relevant parameters available, I use Equation 1.1 to calculate their tidal locking timescale and indicate planets with $t_{lock}>1$ Gyr as blue dots and planets with $t_{lock}<1$ Gyr as orange dots. Compared to planetary lifetimes, 1 Gyr is a short amount of time. Since Figure 1.3 indicates that most exoplanets can be tidally locked within only 1 Gyr, I argue that we need to understand tidally locked exoplanets in the context of exoplanet habitability.

The final planetary spin states resulting from the process of tidal locking depend on the orbital eccentricity of a planet (Goldreich, 1966; Goldreich & Peale, 1966; Dobrovolskis, 2007; Makarov, 2012; Noyelles et al., 2014; Barnes, 2017). For planets with a low eccentricity ($e\leq$0.2), planets are highly likely captured in a 1:1 spin-orbit resonance or synchronous rotation. For a slightly higher eccentricity between $\sim$0.2–0.35, planets are likely captured in a 3:2 spin-orbit resonance or sesqui-synchronous rotation. Higher-order resonances are possible for higher eccentricities (see Figure 6 of Dobrovolskis, 2007), such as a 2:1 resonance for $e\sim$0.4 or even a 10:1 resonance for $e\sim$0.77. Given Mercury's e=0.2056, the entrapment in a 3:2 resonance is a likely outcome of its orbital evolution (Dobrovolskis, 2007; Makarov,

2. Using data in the NASA Exoplanet Archive on 05/04/2024 (https://exoplanetarchive.ipac.caltech.edu)

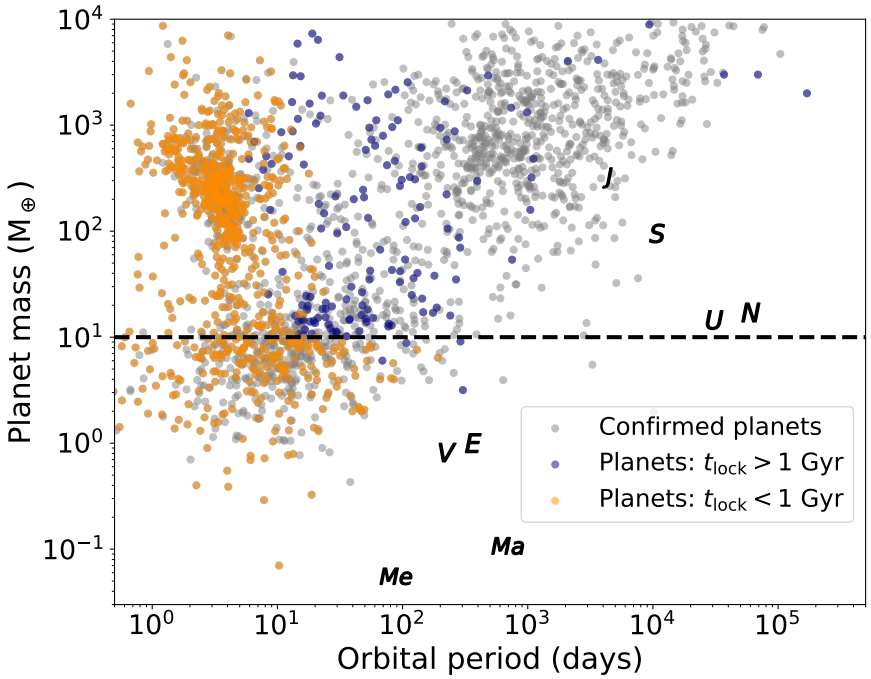

Figure 1.3: Orbital period versus planetary mass for confirmed exoplanets (grey dots). Blue dots denote planets with a calculated tidal locking timescale longer than 1 Gyr, and orange dots are planets with a tidal locking timescale shorter than 1 Gyr. Data was taken from the NASA Exoplanet Archive. Solar System planets are also shown according to their first one or two letters, and the black dashed line indicates an approximate distinction between terrestrial planets and gas giants.

2012; Noyelles et al., 2014). A planet can go through different resonance states during its evolution, as Makarov et al. (2018) suggest for TRAPPIST-1 b, d, and e. The 1:1 spin-orbit resonance presents the most extreme case of tidal locking and will lead to a permanent dayside and nightside hemisphere, with dramatic consequences for the planet's irradiation pattern (Dobrovolskis, 2015), affecting the planetary atmosphere, climate, and habitability. For a 3:2 resonance, a 360° shift in the substellar point – thus defining a day and night for every location on the planet – will take two orbits around the host star, since the substellar point shifts 180° in longitude for every orbit. Therefore, the daytime hemisphere changes with every orbit for a planet in a 3:2 spin-orbit resonance. Higher-order resonances will have a more frequent change of the daytime hemisphere: for example, a 2:1 resonant planet will have a full day-night cycle globally for every orbit and a 10:1 resonant planet will have nine day-night cycles. The resulting instellation patterns will have more subtle changes (Dobrovolskis, 2015) compared to the 3:2 resonant planets and therefore have less dramatic consequences for planetary atmospheres and habitability.

1.6 Exoplanet Habitability

As said, a first-order approximation of the planetary climate and therefore its habitability can be based on the incident stellar flux and orbital configuration, but many more factors play a role (see Figure 2 of Meadows & Barnes, 2018, for an overview). A holistic approach is the ultimate goal but by isolating a number of these factors we are starting to understand their effects on potential habitability. The state and composition of an atmosphere, if it exists, is an essential factor in habitability studies. The atmosphere can serve as a protective layer, for example via the absorption of UV radiation by ozone (e.g. Seinfeld & Pandis, 2016), and its composition determines the amount of greenhouse warming, energy (re)distribution and part of the planetary albedo (Pierrehumbert, 2010b; Kaltenegger, 2017). The possible existence of clouds and hazes (aerosols) can further influence the climate of terrestrial planets by scattering incident stellar light and trapping outgoing thermal radiation, motivating a range of exoplanet studies (e.g. Yang et al., 2013; Yang & Abbot, 2014; Arney et al., 2016; Kopparapu et al., 2016; Arney et al., 2017; Mak et al., 2024). Kasting et al. (1993) assume Earth-like N_2-CO_2-H_2O atmospheres, but a wide variety of atmospheric compositions may produce appropriate surface temperatures for liquid water, e.g. N_2-, CO_2- and H_2-dominated atmospheres (Seager, 2013). The latter of these would, for example, greatly extend the HZ outer edge due to the greenhouse effect from collision-induced absorption by H_2-H_2 pairs (Seager et al., 2013). Another important role is played by climate feedbacks, which can maintain habitable environments despite changes in stellar flux and atmospheric compositions. On Earth, an example of such a process is the carbonate-silicate cycle, which in turn depends on the presence of plate tectonics (Walker et al., 1981). The spectral type of the host star is of key importance: firstly, the spectral energy distribution varies per spectral type, affecting the

climate and photochemistry (e.g. Segura et al., 2003; Rugheimer et al., 2013; Godolt et al., 2015; Rugheimer et al., 2015a). Besides that, the more luminous O- and B-type stars have relatively short lifetimes while the faint M-type stars have long lifetimes but can showcase variability in their energy output (France et al., 2016; Loyd et al., 2016; Youngblood et al., 2016).

1.6.1 Climate Modeling

The initial determinations of the HZ used 1D radiative-convective climate models (Kasting et al., 1993; Kopparapu et al., 2013). These models simplify the planetary atmosphere and climate system to a single column from the surface to the top of the atmosphere. The passage of (stellar) radiation, convection, temperature, and humidity are simulated through the column, given the star-planet configuration and the background atmospheric composition. Moving beyond 1D, the key processes acting in a climate system include (Forget & Leconte, 2014):

- Radiative transfer through the atmosphere
- Large-scale atmospheric circulation, primarily forced by temperature differences
- Vertical mixing and transport due to convection and turbulence
- Phase changes of volatiles
- Photochemistry, affecting the atmospheric composition and driving aerosol formation
- Surface thermal properties and potentially plate tectonics.

Most of these processes can not be accurately accounted for in 1D models. Moreover, given the variations in instellation patterns for different planetary orbits, we need to understand the atmosphere in 3D, including spatial and temporal variations in instellation, atmospheric dynamics, and cloud formation. To this end, several studies have adapted 3D GCMs – initially developed to simulate Earth's weather and climate – to the study of exoplanets and their habitability. GCMs are based on the conservation of momentum and energy and, starting from some initial condition, the equations of motions are solved on discrete timesteps to simulate the evolution of circulation. The GCM divides the atmosphere up into a spherical grid of longitude, latitude, and height or pressure. For each model grid point, the dynamical core can be coupled to, for example, a radiative transfer solver, parametrizations of turbulence and convection, cloud models, modelled surface properties, and a chemical network (Forget & Leconte, 2014). In this way, GCMs study many physical processes in a planetary atmosphere in a self-consistent manner.

For planets in 1:1 resonances, GCM simulations were first performed by Joshi et al. (1997), showing distinct conditions and large temperature differences between the dayside and night-side hemispheres. Initially, it was thought that the nightside hemisphere might be so cold that the bulk species of the atmosphere condense out, cold-trapping the volatiles and reducing the atmospheric pressure, a process known as atmospheric collapse. A (partly) collapsed atmosphere is present on Mars, Triton, and Pluto (Wordsworth & Kreidberg, 2022). Joshi et al.

(1997) and Joshi (2003) showed that heat transport can prevent atmospheric collapse on 1:1 resonant exoplanets around M-dwarfs, opening up investigations into their habitability. The atmospheric circulation of such exoplanets exhibits distinct regimes depending on a planet's rotation rate and radius (e.g. Merlis & Schneider, 2010; Edson et al., 2011; Carone et al., 2014, 2015, 2016; Kopparapu et al., 2017; Noda et al., 2017; Carone et al., 2018; Haqq-Misra et al., 2018). Furthermore, Sergeev et al. (2022a) show that a single planet close to a regime transition in terms of its rotation rate can fall in two circulation regimes, depending on initial conditions and model parametrizations. Haqq-Misra et al. (2018) investigate the circulation regimes and the transitions between them using the Rossby deformation radius (indicating the maximum extent of the mean zonal circulation from the dayside to the nightside) and the Rhines length (denoting the latitudinal scale at which turbulent flow can organise into zonal jets). For Earth-size planets with a 1 bar N_2-H_2O atmosphere, they denote planets in the different circulation regimes as fast or rapid rotators (for orbital periods $<$5 days) and slow rotators (for orbital periods $>$20 days), with the planets in the transition regime between the two known as Rhines rotators (for orbital periods 5–20 days). In this thesis, I will investigate two distinct circulation regimes, that have also been assigned other names:

- The first regime exhibits weak superrotation with a single equatorial jet. This is known as the 'Rhines rotator' (Haqq-Misra et al., 2018), 'Type II circulation' (Noda et al., 2017), and the 'single jet' regime (Sergeev et al., 2022a). Proxima Centauri b is thought to fall in this regime.
- The second regime exhibits superrotation in a pair of midlatitude jets. This is also known as the 'fast rotator' (Haqq-Misra et al., 2018), 'Type IV circulation' (Noda et al., 2017), and the 'double jet' regime (Sergeev et al., 2022a). TRAPPIST-1 d is thought to fall in this regime.

Like on Earth, non-uniform instellation is the driver of atmospheric circulation. The emergence of superrotation is described by Showman et al. (2013). The dayside-nightside contrast on 1:1 resonant exoplanets leads to an overturning circulation, with upwelling on the dayside and downwelling on the nightside (Showman et al., 2013). This vertical motion results in a superposition of planetary-scale Rossby and Kelvin waves, which drives eddy momentum equatorward (Showman & Polvani, 2010). A typical part of this wave structure is a pair of quasi-stationary cyclonic gyres on the nightside (Showman & Polvani, 2010). The equatorward momentum feeds the superrotating jet (Showman & Polvani, 2011). The overturning circulation is a dominant component of the dayside-to-nightside heat transport (Hammond & Lewis, 2021).

The dayside of 1:1 resonant exoplanets may be covered by thick convective clouds, resulting from near-surface convergence and convection at the substellar point (Yang et al., 2013), which is similar to the development of the intertropical convergence zone (ITCZ) on Earth (Faulk et al., 2017). The fact that these clouds are found at exactly the substellar point reduces the incoming radiation and leads to a relatively high albedo, providing a negative

climate feedback and enhancing the habitability of 1:1 resonant exoplanets (Yang et al., 2013; Kopparapu et al., 2016). The cloud albedo feedback is sensitive to the planet's orbital period (Yang et al., 2013; Carone et al., 2016; Kopparapu et al., 2016; Carone et al., 2018). Different stellar fluxes affect the climates of rapidly rotating terrestrial planets in the Habitable Zone of FGK stars (Wolf et al., 2017) and synchronously rotating exoplanets around GM stars (Eager et al., 2020). While most studies to date consider aquaplanets (i.e. planets without any continents), other important influences on the climate are the presence and composition of landmasses due to the impact on convection and water evaporation, which can lead to a wider HZ (Abe et al., 2011; Lewis et al., 2018; Rushby et al., 2020), and/or ocean heat transport (Hu & Yang, 2014; Del Genio et al., 2019). Furthermore, 3D simulations have shown the effect of varying background abundances on climate (Pierrehumbert, 2010a; Turbet et al., 2016). Remarkable planet candidates for surface habitability include Proxima Centauri b (Turbet et al., 2016; Boutle et al., 2017) and TRAPPIST-1 e (Wolf, 2017; Turbet et al., 2018; Sergeev et al., 2022a; Turbet et al., 2022).

As opposed to the dayside-nightside (or zonal) contrasts of an exoplanet in a 1:1 resonance, a 3:2 resonance results in a changing daytime hemisphere for the planet and exhibits meridional (equator-to-pole) gradients in atmospheric quantities (e.g. Turbet et al., 2016; Boutle et al., 2017; Del Genio et al., 2019). Therefore, Del Genio et al. (2019) suggest that – at least in the absence of eccentricity – the circulation is more like that of a slowly rotating Earth (see also Del Genio & Suozzo, 1987), with a meridional circulation including Hadley cells and westward jets over the midlatitudes. As mentioned before, including eccentricity will cause an insolation pattern and associated heating concentrated in two hot spots, one for each hemisphere (Dobrovolskis, 2015; Boutle et al., 2017; Colose et al., 2021). Additionally, an eccentric orbit will produce an increase in the mean flux over one orbit as compared to the circular case (Williams & Pollard, 2002; Dressing et al., 2010; Bolmont et al., 2016). In this way, spin-orbit resonances may affect the inner edge of the HZ, as defined by the moist greenhouse limit of the maximum stratospheric water vapour abundances to retain the Earth's oceans (Kasting, 1988) or the Simpson-Nakajima limit in outgoing longwave radiation (e.g. Goldblatt et al., 2013). However, Colose et al. (2021) find that higher-order resonances have little effect on the inner edge since the warming of the planet is accompanied by a drier stratosphere.

For both resonances, the atmospheric dynamics controls the distribution of atmospheric tracers such as clouds and chemical species. Previous work has shown that the distribution of clouds depends on the rotation rate and circulation regime of 1:1 resonant planets (e.g. Komacek & Abbot, 2019; Sergeev et al., 2022a), but for temperate rocky exoplanets generally follows the strong dayside convection and thus shows zonal gradients (Yang et al., 2013). For 3:2 resonant planets, the cloud cover follows the hot spots in temperature or show banded structures but demonstrates mainly meridional gradients (Boutle et al., 2017; Colose et al., 2021).

1.7 Exoplanet Atmospheric Chemistry

The chemical composition of an atmosphere affects the radiative balance of the planet through the scattering and absorption of incoming and outgoing radiation (Pierrehumbert, 2010b). Static chemical compositions have been investigated (Pierrehumbert, 2010a; Turbet et al., 2016; Boutle et al., 2017), but ultimately the atmospheric chemistry is in a coupled balance with the incoming stellar flux and atmospheric dynamics. A hierarchy of chemical principles helps to uncover atmospheric chemistry systematically. The redox state (as defined in Section 1.2) broadly classifies the atmospheric composition. For example, Titan's H_2- and CH_4-rich atmosphere is highly reducing whereas Earth's O_2-rich atmosphere is oxidizing (Yung & DeMore, 1999). The redox state already tells us something about habitability and the potential to form prebiotic compounds (Rimmer & Rugheimer, 2019). If we know the bulk composition, we can use equilibrium chemistry to determine the atmospheric composition as a function of pressure, temperature, and initial abundances via minimization of Gibbs free energy (e.g. Burrows et al., 1999; Heng et al., 2016; Woitke et al., 2018). For high pressures and temperatures, such as the deep atmospheres of hot Jupiters, equilibrium chemistry is justified since chemical timescales are very short (Moses, 2014; Drummond et al., 2018b). The relatively cool environments of temperate rocky exoplanets lead to longer chemical timescales. The photodissociation timescale in the upper atmosphere and dynamical timescales in the presence of strong transport processes may then be shorter than the chemical timescale and, consequentially, these processes can drive disequilibrium chemistry.

On Earth, a significant driver of disequilibrium chemistry is the presence of life (Krissansen-Totton et al., 2018), leaving chemical traces in the atmosphere that are known as biosignatures (Schwieterman et al., 2018). An example of such a biosignature is the combined presence of O_2 and CH_4, including ozone as the photochemical byproduct of molecular oxygen (Lovelock, 1965; Sagan et al., 1993; Des Marais et al., 2002; Schwieterman et al., 2018). However, various processes can drive disequilibrium chemistry, such as photochemistry driven by UV radiation, stellar flares, lightning, atmospheric dynamics, volcanism, and meteorite impacts (e.g. Owens et al., 1985; Zahnle, 1986; Segura et al., 2010; Rugheimer et al., 2015a; Airapetian et al., 2016; Rimmer & Helling, 2016; Ardaseva et al., 2017; Zahnle et al., 2020).

The most important driver of disequilibrium chemistry is photolysis and therefore the incoming stellar radiation. To investigate the impact of such disequilibrium processes, 1D photochemical kinetics models have been employed for a range of exoplanet conditions. These models simulate interactive photo- and kinetic chemistry in a single atmospheric column – given P, T, vertical mixing, and incoming stellar radiation – by solving for the coupled 1D continuity equations (e.g. Kasting & Donahue, 1980; Yung et al., 1984; Owens et al., 1985; Zahnle, 1986; Rimmer & Helling, 2016; Tsai et al., 2021). Key findings include the discovery of an abiotic pathway to O_2 driven by photochemistry for CO_2-rich planets around M-dwarfs (Hu et al., 2012; Domagal-Goldman et al., 2014; Tian et al., 2014; Wordsworth & Pierrehumbert, 2014;

Gao et al., 2015; Harman et al., 2015; Luger & Barnes, 2015) and accumulation of O_2 following the photolysis of H_2O and subsequent H escape (e.g. Tian, 2015b; Wordsworth et al., 2018; Lincowski et al., 2019), presenting false positives scenarios in the search for biosignatures like O_2 and O_3. Kozakis et al. (2022) focus on the usage of O_3 as a proxy for O_2 and find variations in the O_2–O_3 relationship as a function of the host star and initial conditions, affecting the reliability of O_3 as a biosignature. Energetic processes such as stellar flares (Segura et al., 2010) and lightning (Chameides et al., 1977; Ardaseva et al., 2017; Harman et al., 2018) can destroy strong molecular bonds (such as those of molecular nitrogen), opening up ozone production mechanisms (Haagen-Smit, 1952) or catalytic cycles that destroy ozone (Crutzen, 1970), further affecting the reliability of these species as biosignatures. Additionally, these energetic processes may have been important drivers of prebiotic chemistry in planetary atmospheres (Miller, 1953; Chameides & Walker, 1981; Airapetian et al., 2016; Rimmer & Helling, 2016), beyond the role of photochemistry (Zahnle, 1986; Rimmer & Rugheimer, 2019; Pearce et al., 2022), affecting the potential for the origin of life on other planets. Clearly, not all biosignatures originate exclusively from biological sources and need to be understood in their environmental context, especially for the variety of potential exoplanet environments.

As discussed in Section 1.6, these environmental conditions can vary spatially and temporally and fundamentally depend on 3D processes in the planetary atmosphere. Additionally, atmospheric circulation controls the distributions of tracers such as clouds and chemical compounds. In turn, the tracers themselves are radiatively active (e.g. the greenhouse gases or stratospheric warming by ozone, see Section 1.4) and affect the climate and dynamical state of the atmosphere (Godolt et al., 2015; Hochman et al., 2022, 2023). Hence, many potential climate-chemistry interactions exist, motivating the development of coupled CCMs or even Earth System Models (ESMs; e.g. Ramanathan et al., 1987; Isaksen et al., 2009; Archibald et al., 2020), also as part of the Intergovernmental Panel for Climate Change reports (Masson-Delmotte et al., 2021). CCMs consist of a GCM coupled with a photochemical network and allow the exploration of the intricate relationships between (photo)chemistry, atmospheric dynamics, and the thermal structure of the atmosphere, to understand mechanisms like the Brewer-Dobson Circulation (Brewer, 1949; Dobson, 1956; Butchart, 2014) as illustrated in Figure 1.4. The Brewer-Dobson circulation controls the distribution of ozone and water vapour on Earth, following the photochemical production of ozone through the Chapman mechanism (Chapman, 1930) which is strongest at the tropical latitudes (see the yellow square). The Brewer-Dobson circulation then describes the ascent of ozone-rich air to the upper troposphere and stratosphere (the white arrows), followed by equator-to-pole transport and subsidence at the higher latitudes. Mixing barriers (thick green lines) are bypassed and, in this way, the thickness of the ozone layer on Earth varies meridionally, with a relatively enhanced ozone layer at higher latitudes.

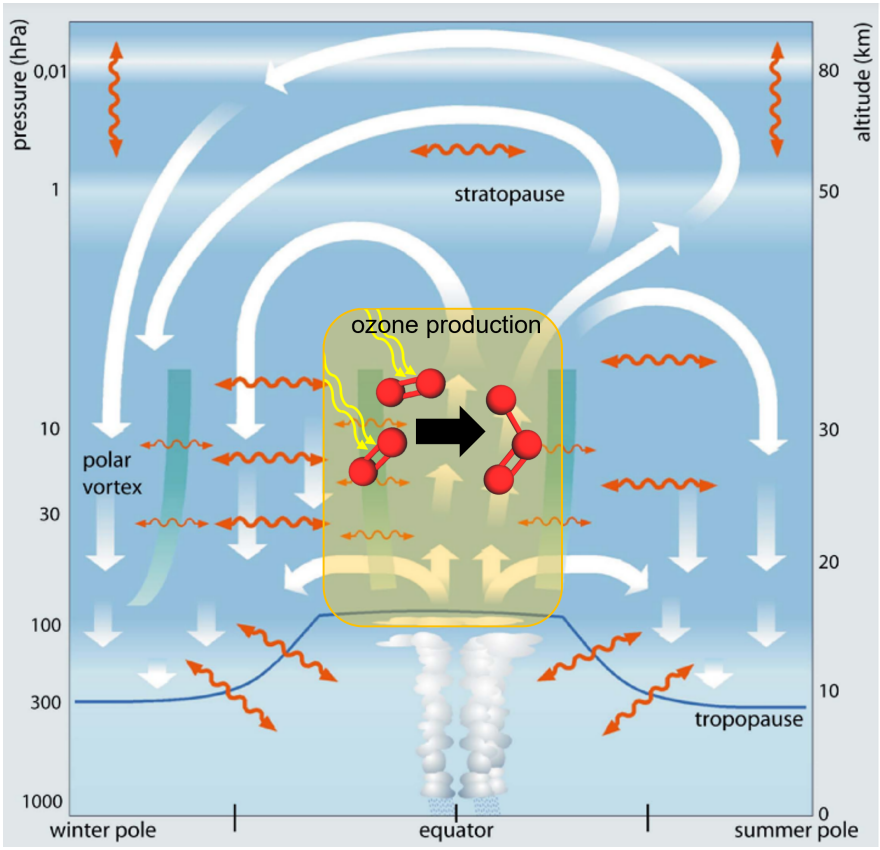

Figure 1.4: Illustration of the Brewer-Dobson circulation on Earth. White and orange wavy arrows represent atmospheric transport and mixing processes, whereas the thick green lines indicate barriers for stratospheric transport and mixing. The main photochemical production region of ozone is indicated by the yellow square, with wavy yellow arrows denoting incoming stellar radiation driving ozone production. The Brewer-Dobson circulation transports ozone from its tropical production regions to higher latitudes. Figure adapted from original version in Bönisch et al. (2011), with credit to Dr. U. Schmidt.

A few studies have applied CCMs to the study of HZ exoplanets to investigate their atmospheric chemistry in 3D, mainly focusing on planets in 1:1 spin-orbit resonances and for Earth-like atmospheric composition. For a tidally locked Earth around the Sun, a breakdown of the Brewer-Dobson circulation is reported (Proedrou & Hocke, 2016; Proedrou et al., 2016). Instead, ozone accumulates on the nightside of a tidally locked Earth, where it has a comparatively long chemical lifetime. Carone et al. (2018) investigate the stratospheric dynamics for a large set of exoplanets in terms of orbital period and radius, using a GCM without interactive chemistry but providing detailed discussions on the effects for tracer distributions. For planets on orbital periods between 6–25 days, they report the development of tropical Rossby waves that induce equatorial jets in the stratosphere and facilitate pole-to-equator transport, confining tracers to the equatorial regions in an 'anti-Brewer-Dobson circulation' (Carone et al., 2018), assuming shallow stratosphere wind breaking (waves break in the lower stratosphere). Chen et al. (2019) demonstrate variations in the meridional distribution of ozone using a CCM and confirm the confinement of ozone to the equatorial regions for such short orbital period planets. However, the presence of extratropical Rossby waves or deep stratosphere wind breaking (when waves can break high up in the stratosphere) prevents this equatorial confinement and instead support equator-to-pole transport (Carone et al., 2018). For planets on orbital periods $<$6 days, thermally-driven equator-to-pole circulation supports the accumulation of tracers at higher latitudes (Carone et al., 2018; Chen et al., 2019). For tidally locked M-dwarf planets, Chen et al. (2018) show that the shifts in stellar flux distribution, illumination geometry and rotationally-induced circulation can affect the distribution of chemical species, although the day-to-nightside variation in mixing ratio stays below 20% for the majority of biosignatures. Simulations of synchronously rotating exoplanets predict significant zonal variations in the ozone layer for planets around M-dwarfs like Proxima Centauri b (Yates et al., 2020) and in the haze distribution for hot Jupiter atmospheres (Parmentier et al., 2013; Steinrueck et al., 2021). Yates et al. (2020) report extended chemical lifetimes for ozone on the nightside of synchronously rotating exoplanets, leading to an enhanced nightside ozone layer following photochemical production on the dayside. Chen et al. (2021) study the influence of flares (through enhanced UV activity and proton events) on N_2-dominated atmospheres orbiting around G, K, and M-dwarfs. The combination of a magnetic field, radiation environment and atmospheric circulation determines the extent of chemical perturbations, which is seen especially in the NO, OH, and O_3 distributions for unmagnetized, tidally-locked planets around K and M-dwarfs. Fast rotation and magnetic fields seem to counteract the effect of flares, but it shows that space weather plays an important role for atmospheric chemistry, influencing the habitability and detectability of atmospheric constituents (Chen et al., 2021).

The complex 3D interplay between stellar radiation, planetary orbit, atmospheric dynamics, and (photo)chemistry determines the planetary climate and habitability as well as potential spectroscopic observations. In emission, reflection, or transmission, each of these observations will be affected by 3D spatial and temporal variations (Turbet et al., 2016; Boutle

et al., 2017; Cooke et al., 2023a). For hot Jupiters, fluctuations in temperature and chemical composition between the dayside and nightside (Nixon & Madhusudhan, 2022; Pluriel, 2023), alongside 3D wind-driven chemistry (Zamyatina et al., 2023) significantly impact the synthetic spectra. On rocky planets, the spatial and temporal variability in water clouds introduces internal atmospheric variability in observations (Komacek & Abbot, 2019; May et al., 2021; Cohen et al., 2023b), whereas stratospheric wind oscillations have been identified by Cohen et al. (2022). Additionally, fluctuations in the distribution of gaseous chemical species, both spatially and temporally, induce spectroscopic variations across orbital phases or observational angles (Olson et al., 2018; Cooke et al., 2023a). Planets with obliquity or an eccentric orbit will show seasonal effects in the atmosphere (Olson et al., 2018), with the variations following passage through periastron and apoastron for a planet in an eccentric higher-order spin-orbit resonance of particular importance for exoplanets. The ongoing discoveries of JWST and potential discoveries with future observatories like the ELT, HWO, and LIFE (see Section 1.3) highlight the need for comprehensive 3D simulations that describe the physical and chemical properties of exoplanet atmospheres to understand habitability, interpret spectroscopic observations, put biosignatures into environmental context, and determine the potential for life on exoplanets.

1.8 Thesis Aims

The overarching goal of this thesis is to perform 3D simulations and provide an in-depth investigation of the 3D coupled interactions between stellar radiation, orbital configuration, atmospheric dynamics, cloud formation, lightning, and (photo)chemistry for terrestrial exoplanets in tidally locked orbits. I focus on specific known planets orbiting M-dwarf stars but emphasize that the results are more generally applicable to planets in similar orbits and around similar host stars. I apply and further develop a state-of-the-art 3D CCM – currently one of only four that can do these calculations for exoplanet atmospheres – to simulate the 3D spatial and temporal evolution, essentially making it a 4D exploration of exoplanet atmospheres. I use the CCM simulations to determine the effect of various drivers of disequilibrium atmospheric chemistry and the consequences for habitability, observability, and potential abiotic pathways to false positive biosignatures.

The following questions will be investigated in the thesis as part of this overarching goal:

1. How do variations in quiescent stellar spectra drive 3D photochemistry in the atmospheres of tidally locked exoplanets?
2. What is the potential for lightning formation on tidally locked exoplanets, and how does this energetic (disequilibrium) process affect atmospheric chemistry in 3D?
3. How do 3D circulation patterns affect the atmospheric chemistry on tidally locked exoplanets and can these explain spatially varying ozone layers as previously predicted?

4. What are the effects of distinct spin-orbit resonances on planetary climate and atmospheric chemistry?
5. How does 3D atmospheric chemistry evolve for an eccentric orbit and does this produce any variability?
6. What traces do these 3D effects in atmospheric chemistry leave in synthetic spectra and will they be tractable in future observations?

In Chapter 2, I briefly introduce the underlying modelling frameworks that are used in this thesis. Chapter 2 discusses the key components required for the adaptation of a comprehensive Earth System Model to the study of exoplanets and introduces the development that I performed on the side of atmospheric chemistry modelling. Chapter 3 presents my findings on the 3D atmospheric chemistry of Proxima Centauri b, using the latest observed stellar spectrum as a driver of photochemistry. Proxima Centauri b is also the main target for my investigation into the initiation and subsequent chemical effect of lightning, the first time this is explored in 3D for exoplanets. Hence, Chapter 3 revolves around disequilibrium chemistry resulting from photolysis and lightning. In Chapter 4 I focus on wind-driven disequilibrium chemistry and investigate the spatially varying ozone layer that is predicted in Chapter 3 and also found in earlier work by Yates et al. (2020). By transforming from the commonly used geographic coordinate system to a tidally locked coordinate system, I identify the existence of a stratospheric dayside-to-nightside circulation that drives ozone from the photochemically active dayside to the inactive nightside. In Chapter 5, I compare simulations of two planets, Proxima Centauri b and TRAPPIST-1 d, that are known to exhibit distinct circulation regimes for 1:1 spin-orbit resonances. I compare the resulting 3D chemical distributions and add simulations of both planets in a 3:2 resonance including the effect of orbital eccentricity. These represent the first simulations of 3D exoplanet chemistry in higher-order spin-orbit resonances. Finally, in Chapter 6, I summarise the main findings of this work along with its implications and suggestions for future research.

Chapter 2

Modelling Atmospheric Chemistry in 3D

In this Chapter, I provide a general overview of the modeling framework that has been used to model the atmospheric chemistry of rocky exoplanets in 3D. First, I will introduce the GCM used (the Met Office Unified Model or UM) in Section 2.1, followed by a description of the CCM (the UM coupled with the UK Chemistry and Aerosols framework or UM-UKCA) along with required model developments in the adaptation to exoplanets. Figure 2.1 illustrates the different model components and guides this Chapter. Chapters 3, 4, and 5 all have a Methods Section describing the specific model setup used for the simulations in that Chapter.

2.1 The Unified Model

The UM is a GCM that simulates the 3D flow of the atmosphere and has been in continuous development for almost 30 years, a general description of the model can be found in Walters et al. (2019). The UM simulates the atmosphere of Earth over a wide range of temporal and spatial scales and is commonly used for regional weather predictions over days to weeks and for climate predictions over decades to centuries.

The UM has been adapted and applied to the simulation of a diverse set of exoplanets, including terrestrial planets (e.g. Mayne et al., 2014a; Boutle et al., 2017; Lewis et al., 2018; Eager et al., 2020; Joshi et al., 2020; Sergeev et al., 2020; Yates et al., 2020), sub-Neptunes (Drummond et al., 2018a; Mayne et al., 2019), and hot Jupiters (Amundsen et al., 2014; Mayne et al., 2014b; Amundsen et al., 2016; Drummond et al., 2016, 2018b; Lines et al., 2018; Drummond et al., 2020). In this thesis, the UM is used in its Global Atmosphere 7.0 (GA7.0) configuration (Walters et al., 2019). As shown in Figure 2.1, I configure exoplanets as aquaplanets with a slab of ocean covering the full surface. The mixed-layer ocean has a heat capacity of 10^7 J K^{-1} m^{-2} and does not include any horizontal transport, following the definition by Frierson et al. (2006). It would take an energy of 10^7 J to heat the mixed-layer ocean by 1 K, which corresponds to a slab of depth 2.4 m (Boutle et al., 2017). In this way, the heat capacity determines the change in surface temperature (due to the net surface

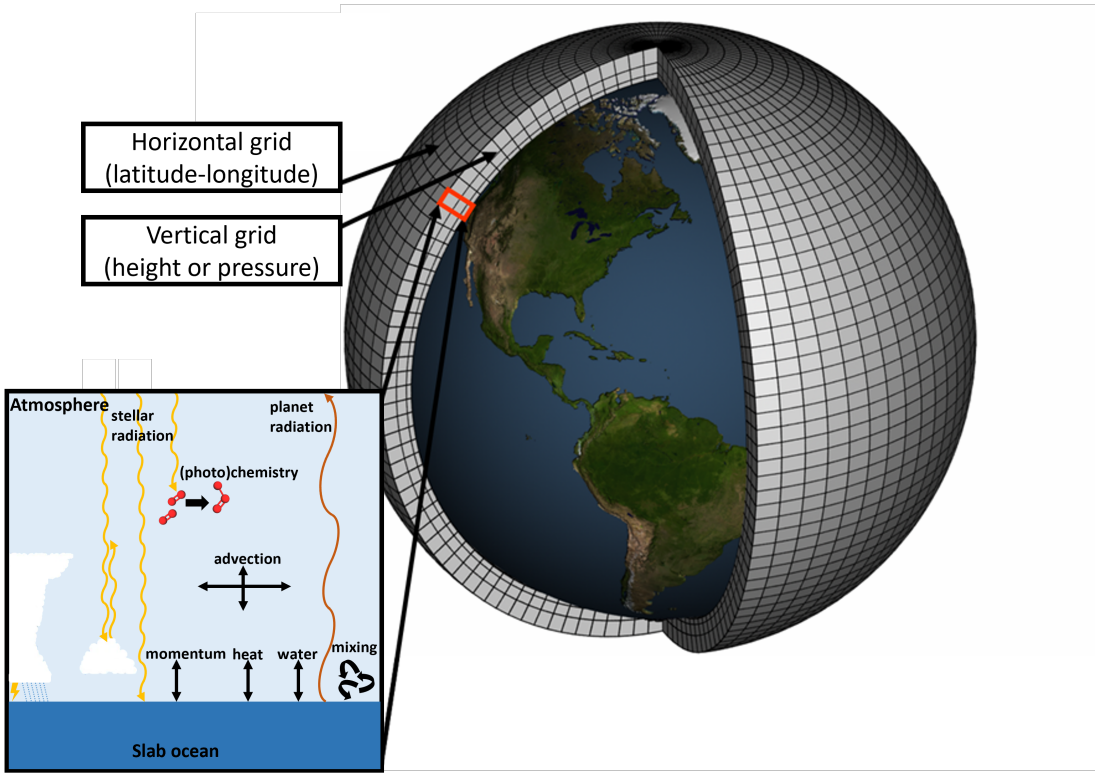

Figure 2.1: Illustration of the horizontal (latitutde-longitude) and vertical (height or pressure) grid used in the UM. In every gridbox, the model simulates a range of physical and chemical processes including radiative transfer, atmospheric dynamics, cloud formation, (photo)chemistry, and lightning generation. Note that the Earth's continents are removed in the aquaplanet setup. Figure was adapted from NOAA[1].

irradiance, the latent heat of vaporization, and the sensible heat flux or the loss of energy due to heat transfer to the atmosphere). Since we run the models to equilibrium, this will not affect the mean temperatures, but is an important consideration for variability. In all simulations, I assume a surface pressure of 10^5 Pa, thus determining the thickness of the atmosphere.

1. Source: https://celebrating200years.noaa.gov/breakthroughs/climate_model/modeling_schematic.html.

2.1.1 The Equations of Motion

The dynamical core of the model (ENDGame) solves the equations of motion (Vallis, 2017) to describe the fluid flow on a rotating sphere (Wood et al., 2014), with a horizontal grid based on latitude (ϕ) and longitude (λ) in degrees, and vertical levels corresponding to altitude z in m. The formalism is semi-Lagrangian by using a Lagrangian approach on an Eulerian grid to enhance stability, allow for wave propagation, and be able to apply damping (Wood et al., 2014). ENDGame solves for the full equations of motion but is also able to apply commonly used simplifications in GCMs such as (White et al., 2005; Mayne et al., 2014a; Mayne et al., 2014b; Heng & Showman, 2015):

- The shallow-fluid approximation, which assumes that the atmosphere is thin as compared to the planetary radius (the ratio is $\sim 10^{-3}$ for Earth but 0.1 for hot Jupiters).
- The traditional approximation, which neglects several metric and rotation terms such as the $\cos\phi$ Coriolis terms (defined below). To ensure conservation of energy, angular momentum, and potential vorticity, the shallow-fluid and traditional approximations need to be applied together (White & Bromley, 1995). The violation is mainly due to the height variation of angular momentum in the equation of motion relating to the Coriolis force for the meridional direction, which will be introduced below.
- Constant gravity with altitude, which assumes that there is no contribution from the atmosphere to the gravity.
- Vertical hydrostatic balance, which assumes that the gravitational force and pressure term balance.

Using the first three assumptions results in the shallow-water equations and adding in the fourth assumption gives the primitive equations. Below, I will describe the equations of motion as used in this work, several previous papers provide a detailed description of the full and primitive equations along with the effects of each of the potential approximations focused on the UM (White & Bromley, 1995; White et al., 2005; Mayne et al., 2014a, 2019).

ENDGame can solve for the full equations of motion, but in our case still includes simplifications in the form of a constant gravity g_p and spherical symmetry as explained by Mayne et al. (2014a). The conservation of momentum describes how the velocity or momentum of a fluid react to internal and external forces and is described for the meridional (u), zonal (v), and vertical (w) wind in m s^{-1}:

$$\frac{Du}{Dt} = \frac{uv\tan\phi}{r} - \frac{uw}{r} + fv - f'w - \frac{c_p\theta}{r\cos\phi}\frac{\partial\Pi}{\partial\lambda} + D(u), \tag{2.1}$$

$$\frac{Dv}{Dt} = -\frac{u^2\tan\phi}{r} - \frac{vw}{r} - fu - \frac{c_p\theta}{r}\frac{\partial\Pi}{\partial\phi} + D(v). \tag{2.2}$$

$$b\frac{Dw}{Dt} = \frac{u^2+v^2}{r} + uf' - g_p - c_p\theta\frac{\partial\Pi}{\partial r}, \tag{2.3}$$

along with the conservation of mass or continuity equation:

$$\frac{D\rho}{Dt} = -\rho \left[\frac{1}{r\cos\phi}\frac{\partial u}{\partial \lambda} + \frac{1}{r\cos\phi}\frac{\partial (v\cos\phi)}{\partial \phi} + \frac{1}{r^2}\frac{\partial (r^2 w)}{\partial r} \right], \tag{2.4}$$

and the thermodynamic equation, associated with conservation of energy:

$$\frac{D\theta}{Dt} = \frac{Q}{\Pi} + D(\theta), \tag{2.5}$$

and finally, the equation of state describing the properties of a fluid:

$$\Pi^{\frac{1-\kappa}{\kappa}} = \frac{R^* \rho \theta}{P_0}. \tag{2.6}$$

In the set of equations, the material derivative is used due to the Lagrangian formalism:

$$\frac{D}{Dt} \equiv \frac{\partial}{\partial t} + \frac{u}{r\cos\phi}\frac{\partial}{\partial \lambda} + \frac{v}{r}\frac{\partial}{\partial \phi} + w\frac{\partial}{\partial r}. \tag{2.7}$$

The zonal, meridional, and vertical wind flow in the longitudinal (λ, in rad), latitudinal (ϕ, in rad), and radial (r, in m) direction, respectively. Both the specific heat capacity c_p (J K^{-1} kg^{-1}) and specific gas constant R^* (J K^{-1} kg^{-1}) depend on the chemical composition of the atmosphere, with the unitless ratio between them κ=c_p/R^*. P_0 is the reference (here surface) pressure in Pa, Q the heating rate in K s^{-1} (following from the radiative transfer, see Section 2.1.2), and $D(X)$ the diffusion operator relating to the quantity X. The diffusion operator $D(X)$ represents unresolved subgrid-scale mixing processes and transfer of kinetic energy from large-scale flows to smaller scales (Mayne et al., 2014b) and is applied to the conservation of momentum for u and v winds (ms^{-2}) as well as the thermodynamic equation (Ks^{-1}). This horizontal diffusion complements the inclusion of vertical boundary-layer diffusion following Lock et al. (2000) and Brown et al. (2008). b represents a switch (1 or 0) to the (quasi-)hydrostatic equations, depending on whether one also uses the assumptions for the shallow-water equations. The density is given by ρ (kg m^{-3}) and for these planets we assume constant gravity g_p in m s^{-2} (Mayne et al., 2014a). f and f' represent the Coriolis parameters for the planetary rotation rate Ω in rad s^{-1}:

$$f = 2\Omega \sin\phi, \tag{2.8}$$

$$f' = 2\Omega \cos\phi. \tag{2.9}$$

The potential temperature θ (in K) is given by:

$$\theta = T\left(\frac{P_0}{P}\right)^{R/c_p}, \tag{2.10}$$

and the dimensionless Exner pressure Π by:

$$\Pi = \left(\frac{P}{P_0}\right)^{R/c_p} = \frac{T}{\theta}. \tag{2.11}$$

Hence, the Coriolis term $f'w$ in Equation 2.1 represents the height variation of angular momentum, which would be suppressed if we assume the shallow-fluid approximation (White & Bromley, 1995). Therefore, we have to make the traditional approximation as well to ensure conservation of angular momentum. For simulations of extended atmospheres (such as those of hot Jupiter Mayne et al., 2014b), the UM is thus particularly suitable since it has the ability to solve for the full equations of motion. Equations 2.1–2.6 are used for the simulations in this thesis.

2.1.2 Radiative Transfer

The radiative transfer in the UM is described by the Suite of Community Radiative Transfer codes based on Edwards and Slingo or SOCRATES (Edwards & Slingo, 1996; Manners et al., 2021), using the two-stream approximation. The shortwave (SW) spectral bands in SOCRATES treat the incoming stellar radiation that is absorbed and reflected in the atmosphere and at the surface, this energy drives the atmospheric circulation. The longwave (LW) spectral bands treat the radiation emitted from the planet, which interacts with the atmosphere and redistributes heat, before the remainder is emitted to space. The spectral bands for Proxima Centauri are distributed over non-overlapping wavelength regions following the Global Atmosphere 7.0 configuration described by Walters et al. (2019), with 6 bands describing the SW radiation from 0.2 – 10 μm and 9 bands the LW radiation from 3.3 - 10000 μm (see their Table 2). For TRAPPIST-1, a higher number of 21 SW (0.2–20 μm) and 12 LW (3.3–10000 μm) bands are used (Sergeev et al., 2022b; Turbet et al., 2022). Line-by-line opacities for each species are treated in a smaller number of k-coefficients, with O_2, CO_2, H_2O, N_2O, and O_3 as radiatively active species. For overlapping species in a spectral band, SOCRATES determines the dominant absorber in each model grid cell. For the dominant absorber, the full k-distribution within the spectral band is used, whereas minor species are then treated as gray opacities. A detailed description of this method known as equivalent extinction can be found in Amundsen et al. (2017). A spectral file contains all the information on the stellar radiation, absorbing gases, continua, collision-induced absorption, and potential aerosol scattering and absorption parameters (Manners et al., 2021). The number and the distribution of spectral bands depends on the atmospheric composition and the stellar spectral energy distribution. A comparison of 1D radiative transfer models by Yang et al. (2016) shows the sensitivity of climate to both the treatment of water vapour opacities and the choice of spectral bands (see their figure 2), finding radiative fluxes that differ by up to 10 Wm^{-2}. The distribution of the spectral bands will affect the inner edge of the Habitable Zone (Kopparapu et al., 2017). Wolf et al. (2022) show use the ExoCAM GCM – including SOCRATES to

describe the radiative transfer – to show that the sensitivity to band choices is especially prominent for CO_2-dominated atmospheres, and less so for N_2-dominated atmospheres like the ones simulated in this thesis (as further described in Section 2.2.5). The key output from the radiative transfer calculations are the heating rates Q (K s^{-1}) in each model grid cell, as used in the thermodynamic equation (Equation 2.5).

The incoming stellar radiation and its passage through the atmosphere as well as the photolysis rates of chemical species will change over time with a dependence on the orbital parameters. The inclusion of positional astronomy within SOCRATES (Edwards & Slingo, 1996; Manners et al., 2021) is based on the description in Smart (1944). For an eccentric Keplerian orbit, the true anomaly $\nu_A(t)$ represents the angle (in radians) between the direction of periastron from the barycenter and the position of a planet at time t. The mean anomaly $M_A(t)$ (in radians) is the fictitious angle from periastron for a planet on a circular orbit at the same time t, assuming the same semi-major axis as for the true elliptical orbit. Hence, the mean anomaly concerns the mean motion $2\pi/P$ where P is the orbital period in seconds. The mean anomaly at time $(t-t_p)$ after periastron is given by:

$$M_A(t) = \frac{2\pi(t-t_p)}{P}. \tag{2.12}$$

Here, t indicates the current time, t_p the time when the planet is at periastron, and P the length of a year or orbital period (all in seconds). For a Keplerian orbit of eccentricity e, $M_A(t)$ can be used to calculate the true anomaly $\nu_A(t)$, or the angular distance of a planet on an eccentric orbit from periastron. In SOCRATES, $\nu_A(t)$ is represented as the third-order approximation of a series expansion known as the equation of the center, following the derivation by Smart (1944):

$$\nu_A(t) = M_A(t) + \left(2e - \frac{e^3}{4}\right)\sin(M_A(t)) + \frac{5}{4}e^2\sin(2M_A(t)) + \frac{13}{12}e^3\sin(3M_A(t)). \tag{2.13}$$

Using Kepler's second law, ν_A is then used to calculate the normally incoming stellar radiation or irradiance at the top of the planetary atmosphere (S_{TOA}) in W m^{-2}:

$$S_{TOA}(t) = S_0\left(\frac{1+e\cos(\nu_A(t))}{1-e^2}\right)^2, \tag{2.14}$$

where S_0 is the stellar constant, the normally incoming stellar radiation at the mean star-planet distance a in W m^{-2}. S_0 can be calculated from the stellar radiant flux density F:

$$S_0 = \frac{4\pi R_*^2 F}{4\pi a^2}, \tag{2.15}$$

where R_* is the stellar radius. $4\pi R_*^2 F$ represents the integration over wavelength of the spectral stellar radiant flux density $F(\lambda)$ at the surface of the star (ranging from 0 to 10 μm in SOCRATES):

$$F = \int_{0\ \mu m}^{10\ \mu m} F(\lambda) d\lambda. \tag{2.16}$$

The incoming radiation will, however, depend on the local stellar zenith angle (ζ). To determine ζ, we use the orbital parameters to calculate the stellar declination δ, denoting the latitude at which the star is vertically overhead:

$$\sin(\delta) = \sin(\varepsilon)\sin(\alpha). \tag{2.17}$$

The declination depends on the obliquity ε (0 in our case) and angular distance of the planet relative to vernal equinox α (or right ascension).

Additionally, we need to know the hour angle HA of the star, denoting the angle (in radians) through which a planet has rotated since stellar noon or the angle of the star from the local meridian:

$$HA = \lambda + \pi\left(\frac{2t}{T_D} - 1\right), \tag{2.18}$$

where T_D is the length of the day and for longitude λ. If we consider the astronomical measurement of time on Earth based on the Earth's rotation, the solar day represents the length of time between two successive returns of the Sun to some meridian. The time system based on the solar day is the apparent solar time. However, the apparent solar day has a variable length with seasonal deviations of up to 16 minutes, due to: 1) the Earth's eccentricity, which causes variations in the Earth's orbital velocity as it speeds up close to periastron and slows down close to apoastron, and 2) the Earth's obliquity, meaning that the Sun's annual motion lies in the ecliptic which is tilted to the Earth's celestial equator. The mean solar time follows a theoretical motion of the mean sun moving at a uniform rate along the equator. The mean solar day then represents the average of the apparent solar days in a year. The discrepancy between the apparent and mean solar time is described by the equation of time. Two formulations of the equation of time exist in the UM, based on Smart (1944) and Mueller (1995). The equation of time derived by Mueller (1995) contains higher-order terms and therefore is more appropriate for the relatively high eccentricity considered in this thesis.

Using the local hour angle HA as a function of time allows us to calculate ζ at latitude ϕ and longitude λ (through HA):

$$\cos(\zeta) = \cos(\phi)\cos(\delta)\cos(HA) + \sin(\phi)\sin(\delta). \tag{2.19}$$

The incoming stellar radiation S can then be calculated at any location as:

$$S(t) = S_{TOA}(t) \times \cos(\zeta). \tag{2.20}$$

2.1.3 Parametrizations of Small-scale Processes

Parametrizations are required to describe sub-gridscale processes in the model. Convection in the simulations is based on a mass-flux approach following Gregory and Rowntree (1990). The parametrization decomposes the atmospheric column into updrafts, downdrafts, and a subsiding environment (Arakawa, 2004; Rio et al., 2019; Sergeev et al., 2020). The surface buoyancy flux then triggers convection and the ascent of an undilute parcel (so no mixing or interaction with the surroundings). This undilute parcel ascends to the level of neutral buoyancy, from which either deep, mid-level, or shallow convection is diagnosed, based on the height of the levels of neutral buoyancy and that of strong vertical updrafts (Walters et al., 2019; Sergeev et al., 2020). The closure determines the balance between the generation of convective energy (e.g., heating at the surface, advection of warm air aloft) and dissipation of convective energy (e.g., precipitation, downdrafts, mixing). Convective cloud formation drives a bulk vertical flux of heat, moisture, and momentum, and is accompanied by entrainment and detrainment of background air in and out of the convective plume, as illustrated by the convective cloud in Figure 2.1. Turbulent mixing in the atmosphere follows the implementations by Lock et al. (2000) and Brown et al. (2008).

Large-scale clouds are described by the Prognostic Cloud and Prognostic Condensate (PC2) scheme (Wilson et al., 2008) with additional parametrizations for cloud erosion and the critical relative humidity. The scheme calculates increments to the prognostic variables of liquid, ice, and total cloud fractions and the mixing ratios of water, liquid, and ice clouds based on the physical processes in the model (e.g., advection, radiation, convection, microphysics, boundary layer processes, adiabatic expansion). The parametrization determines both the amount of condensate in one gridbox and the fractional cloud coverage in the box. Precipitation resulting from the large-scale clouds is described by Wilson and Ballard (1999) and Boutle et al. (2014). The formation of lightning flashes in the atmosphere fundamentally depends on the cloud formation processes. The model uses parametrizations of lightning flash rates (LFRs) in terms of the cloud-top height, that were derived from the laws of electricity and have been empirically tested (Vonnegut, 1963; Williams, 1985; Price & Rind, 1992; Luhar et al., 2021). The parametrization of LFRs will be described in more detail in Chapter 3 for its application to exoplanet simulations.

2.2 UK Chemistry and Aerosols

UKCA is a framework to model global atmospheric composition, which includes aerosol and gas-phase chemistry and is coupled to the UM for large-scale advection, convective transport, and boundary layer mixing of its aerosol and chemical tracers (Morgenstern et al., 2009; O'Connor et al., 2014; Archibald et al., 2020). In this thesis, I will only use the UKCA description of gas-phase chemistry.

2.2.1 Chemical Kinetics

To predict the evolution of atmospheric chemistry, UKCA explicitly simulates the effect of individual chemical reactions using the A Self-contained Atmospheric chemistry coDe (ASAD) chemical solver (Carver et al., 1997; Wild & Prather, 2000). A chemical network is a collection of all the known reactions required to solve for the chemistry of a particular atmosphere (or part of an atmosphere). To predict their temporal evolution, a description of chemical kinetics is required. Behind the field of chemical kinetics lies the conservation of mass or continuity equation. For chemical species j=$1,...,J$ with J the number of species in a system, the continuity equation reads as:

$$\frac{\partial n_j}{\partial t} = P_j - L_j - \nabla\Psi_j + E_j - DD_j - WD_j. \tag{2.21}$$

P_j and L_j denote the chemical production and loss of the species j, respectively. E_j denotes emissions (a source) and DD_j and WD_j denote the sinks due to dry and wet deposition, respectively. The net change due to transport of a species is given by $\nabla\Psi_j$ and follows the large-scale flow in the atmosphere. All right-hand terms have units of molecules cm^{-3}s^{-1}, giving the rate of change in species concentrations in molecules cm^{-3}s^{-1}. Chemical species are treated as tracers with mixing ratios q_j and follow the conservation of mass as shown in Equation 2.4. The UM uses an Eulerian grid but a Lagrangian approach to track where a tracer comes from (the departure point), signifying the semi-Lagrangian approach. For every species, q_j at the departure point is interpolated and used to determine the advected abundances to the arrival point or current position. The scheme is described in detail by Davies et al. (2005) and Wood et al. (2014). For the P_j and L_j terms in Equation 2.21, UKCA considers unimolecular, bimolecular, termolecular, and photolysis reactions.

For a standard bimolecular reaction A + B $\longrightarrow$ C + D, the rate of change or reaction rate (molecules cm^{-3}s^{-1}) is calculated as follows:

$$\frac{dn_A}{dt} = \frac{dn_B}{dt} = -kn_An_B \tag{2.22}$$

for number densities n_A and n_B in molecules cm^{-3}. The rate constant k (cm^3 molecules^{-1} s^{-1}) is given by the modified Arrhenius equation:

$$k = A\left(\frac{T}{300}\right)^{\alpha} e^{(-E_a/RT)}, \tag{2.23}$$

with A the pre-exponential factor (depending on the frequency of suitable collisions), α denoting the temperature dependence, and E_a giving the activition energy of a chemical reaction.

In a termolecular reaction, two species collide with sufficient energy to provide an intermediate compound. The presence of a third body M to take up excess energy can prevent the intermediate compound from decomposing and instead stabilize to be the reaction product. The standard reaction is A + B + M $\longrightarrow$ AB + M and the reaction rate is given by:

$$\frac{dn_{AB}}{dt} = -kn_A n_B n_M, \tag{2.24}$$

with k now the three-body rate constant (cm^{6}molecules^{-2}s^{-1}). Due to the dependence on the third body, the reaction rate depends on the pressure, giving separate rate constants for low (k_0) and high (k_∞) pressure:

$$k_0 = A_1\left(\frac{T}{300}\right)^{\alpha_1} e^{(-E_{a1}/RT)}, \tag{2.25}$$

$$k_\infty = A_2\left(\frac{T}{300}\right)^{\alpha_2} e^{(-E_{a2}/RT)}. \tag{2.26}$$

UKCA uses the Troe formalism to describe the three-body rate constant at any pressure:

$$k = \left(\frac{k_0 n_M}{1 + k_0 n_M / k_\infty}\right) F_c^{\left(1+[\log(\frac{k_0 n_M}{k_\infty})]^2\right)^{-1}}, \tag{2.27}$$

with F_c following from the Troe formalism, typically reported as a species-dependent constant and sometimes including a significant temperature dependence (Carver et al., 1997). Unimolecular reactions also follow a varying order depending on pressure (Carver et al., 1997), since the theory of unimolecular rates involves a second-order bimolecular activation step (A + M $\longrightarrow$ A* + M with rate constant k_1) followed by a rate-limiting unimolecular step (A* $\longrightarrow$ B + C with rate constant k_2). At low pressures, the reaction rate follows:

$$\frac{dn_A}{dt} = -k_1 n_A n_M, \tag{2.28}$$

and at high pressures:

$$\frac{dn_A}{dt} = -k_2 n_A. \tag{2.29}$$

The pressure-dependent rate constants for unimolecular reactions are again calculated using the Troe formalism as specified in Equations 2.25–2.27.

2.2.2 Photolysis

As described in Section 1.7, stellar radiation is the most important driver of atmospheric chemistry. It affects the atmospheric temperature (see Section 2.1.2) and drives changes in humidity, precipitation, pressure, and lightning, which all affect atmospheric chemistry in turn. However, the primary effect is the process of photolysis or photodissociation. For the standard reaction AB + hν $\longrightarrow$ A + B, the photolysis reaction rate is given by:

$$\frac{dn_{AB}}{dt} = -J_{AB}n_{AB} = -n_{AB}\int_{\lambda_{\min}}^{\lambda_{\max}} \sigma_{AB}(\lambda)\Phi_{AB}(\lambda)I(\lambda)d\lambda, \tag{2.30}$$

where J_{AB} denotes the photolysis rate constant (s^{-1}), $\sigma_{AB}(\lambda)$ the absorption cross section or probability for photon absorption (cm^2 $molecules^{-1}$), and $\Phi_{AB}(\lambda)$ the quantum yield or the number of molecules photolysed per absorbed photon (molecules $photon^{-1}$). $I(\lambda)$ represents the stellar actinic flux or the radiative flux on a volume of air from all directions (photons $cm^{-2}s^{-1}nm^{-1}$). Within UKCA, the Fast-JX photolysis scheme interactively calculates photolysis rate constants J_{AB} of chemical species in the atmosphere (Wild et al., 2000; Bian & Prather, 2002; Neu et al., 2007; Telford et al., 2013). The stellar radiation at the top-of-the-atmosphere is distributed over 18 wavelength bins covering 177–850 nm (Wild et al., 2000; Bian & Prather, 2002). Fast-JX uses multi-scattering eight-stream radiative transfer to calculate the passage of the actinic flux through the atmosphere, using the UM output to account for the local stellar zenith angle and the varying optical depths of Rayleigh scattering, absorbing gases, clouds, and aerosols. The local solar zenith angle affects $I(\lambda)$ and the temperature dependence of both $\sigma_{AB}(\lambda)$ and $\Phi_{AB}(\lambda)$ also follow from the UM simulations. In this way, Fast-JX interactively determines photolysis rate constants which are then fed to the ASAD chemical solver (Telford et al., 2013).

In adapting the photolysis calculations to exoplanets, we need to account for the changes in incoming stellar radiation. For Proxima Centauri, I use the composite spectrum from the MUSCLES spectral survey (France et al., 2016; Loyd et al., 2016; Youngblood et al., 2016). TRAPPIST-1 was part of the follow-on Mega-MUSCLES survey and its spectrum is taken from Wilson et al. (2021). In Figure 2.2, I show the stellar spectral radiant flux density $F(\lambda)$ (panel a) and spectral actinic flux $I(\lambda)$ (panel b) that are received by Proxima Centauri b (blue) and TRAPPIST-1 d (red), as compared to that received by Earth around the Sun (black). Figure 2.2a shows that the spectral radiant flux density received by Earth peaks at much shorter wavelengths than that received by Proxima Centauri b and TRAPPIST-1 d, with instead more infrared flux received by the latter two (as expected for planets around M-dwarfs). This will drive the radiative transfer as described in Section 2.1.2. Focusing on the photolysis

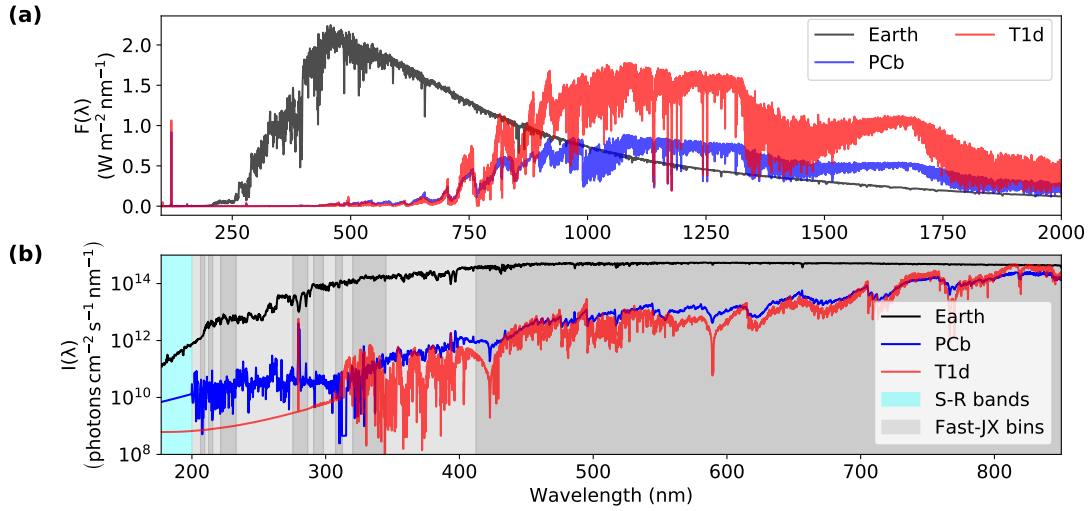

Figure 2.2: The stellar spectra showing (a) the spectral radiant flux density in units of W m^{-2}nm^{-1} and (b) the spectral actinic flux in photons cm^{-2}s^{-1}nm^{-1}, as received by planets on a circular orbit for the Earth at 1 AU, Proxima Centauri b at 0.0485 AU, and TRAPPIST-1 d at 0.0223 AU. Panel (b) focuses on the wavelengths used to calculate photolysis rates (see Equation 2.30), with the different Fast-JX wavelength bins indicated by grey patches. The Schuman-Runge (S-R) bands are covered by wavelength bins of enhanced resolution.

region in Figure 2.2b, Proxima Centauri b and TRAPPIST-1 d receive significantly lower total actinic flux in the 177–850 nm region than the Earth. The alternating grey patches indicate the Fast-JX wavelength bins. The Schuman-Runge (S-R) bands, important for O_2 photolysis, fall into the cyan region and are covered by wavelength bins of enhanced resolution (Bian & Prather, 2002). The division of stellar actinic flux along with $\sigma_{AB}(\lambda)$ and $\Phi_{AB}(\lambda)$ over these wavelength bins determine the flexible calculation of photolysis rates through Equation 2.30. The calculation of these photolysis rates will be further described in Section 3.2.3 for the case study of Proxima Centauri b.

2.2.3 Deposition and Emissions

Dry deposition is the removal of atmospheric chemical species by turbulent transfer and uptake at the Earth's surface, occurring in the planetary boundary layer (see Figures 1.4 and 2.1). UKCA has different options for the inclusion of dry deposition (O'Connor et al., 2014), in this thesis I use the tabulated dry deposition velocities (v_D, in m s^{-1}). Per species, v_D depends on the particular surface type but I only consider their deposition onto water surfaces due to the aquaplanet model configurations (Section 2.1). Values for v_D are given at 1 m above the surface for O_3, NO_2, NO_3, N_2O_5, HNO_3, HO_2NO_2, and H_2O_2 (Ganzeveld & Lelieveld, 1995; Sander & Crutzen, 1996) and extrapolated to the mid-point of the lowest model layer following Sorteberg and Hov (1996). The deposition rate is then calculated as $DD_j = (n_j \times v_D)/h$ with number density n_j in molecules m^{-3} and h the height of the lowest model layer in m.

Wet deposition is parametrized as a first-order loss rate following the convective and large-scale precipitation in the UM (O'Connor et al., 2014), as described in Section 2.1.3. The wet deposition rate in each model grid box is calculated using:

$$WD_j = n_j \times \Lambda_j \times p(l), \tag{2.31}$$

where Λ represents the scavenging coefficient (based on removal by Brownian diffusion, interception, and inertial impaction) for species j (m^{-1}) and $p(l)$ the precipitation rate from model level l ($m\ s^{-1}$). The scheme calculates scavenging rates for each species for convective and large-scale precipitation separately, following the fraction of each species in aquaeous phase as described by Henry's Law. A detailed description is given by O'Connor et al. (2014).

UKCA has a variety of options to include both natural and anthropogenic emissions that affect atmospheric chemistry (O'Connor et al., 2014; Archibald et al., 2020). For the work in this thesis I limit myself to only one emission source, the emissions of nitric oxide (NO) due to the presence of lightning flashes (see Section 2.1.3). The emissions in UKCA are set at 216 moles NO per flash to match the global lightning-NO production on Earth (Archibald et al., 2020; Luhar et al., 2021). The emitted NO is added to the NO tracer as shown in Equation 2.21. In Chapter 3, I will present a detailed discussion on the lightning parametrization and its subsequent impact on atmospheric chemistry.

2.2.4 Chemical Solver

Simulating the temporal evolution of the chemical kinetics then involves solving the system of nonlinear Ordinary Differential Equations (ODEs) such as Equation 2.21, with one ODE for each species involved. Atmospheric chemistry involves stiff ODEs due to reaction timescales that vary by orders of magnitude. Within UKCA, the ASAD chemical package performs the time integration for the gas-phase chemistry (Carver et al., 1997; Wild & Prather, 2000; Esentürk et al., 2018). It uses a backward Euler implicit numerical scheme to integrate the ODEs. The implicit scheme provides enhanced stability over explicit schemes and is thus particularly suited to solve for stiff systems (Esentürk et al., 2018).

Given the standard Equation 2.21, we follow Esentürk et al. (2018), and write:

$$y_j(n_j) = \frac{\partial n_j}{\partial t}, \tag{2.32}$$

and take $n_j(0)$=$n_{j,0}$ as the initial concentration of species j. We can then discretise the time variable into timesteps Δt:

$$\frac{n_j(t_* + \Delta t) - n_j(t_*)}{\Delta t} = y_j(n_j(t_* + \Delta t)), \tag{2.33}$$

where t_* represents the current time. The species concentrations at the next timestep ($n_j(t_* + \Delta t)$) appears on both sides of the nonlinear equation, and y_j is dependent on the state of the system at both the current and nex timestep, making it implicit. This can be solved for by using Newton-Raphson iteration. The first step is to rewrite Equation 2.33:

$$Y_j(n_j(t)) = \frac{n_j(t) - n_j(t_*)}{\Delta t} - y_j(n_j(t)) = 0, \tag{2.34}$$

using $t = t_* + \Delta t$. The Jacobian matrix **J** is built from the system of ODEs and nonlinear reaction rates. Given the Jacobian, the Newton-Raphson iteration starts with an initial guess for $n_j(t)$ (calculated based on the chemical concentrations from the previous timestep) and iteratively solves for:

$$\mathbf{J}(n_j^k)(\Delta n_j^k) = -Y_j(n_j^k), \tag{2.35}$$

where $\mathbf{J}(n_j^k)$ represents the Jacobian at the kth iteration and the increment $\Delta n_j^k = n_j^{k+1} - n_j^k$. The initial guess is improved for every iteration and will approach the solution to Equation 2.34. Once the increment falls below the tolerance limit (10^{-4}, Esentürk et al., 2018), the model will output the concentrations at the next timestep. If the solver fails to converge, the timestep is halved and the routine repeated. The Newton-Raphson iteration method was further updated using the Quasi-Newton method by Esentürk et al. (2018), speeding up the processes of finding the roots of a nonlinear function as shown in Equation 2.34.

2.2.5 Chemical Network

In this thesis, I mainly use UKCA's Stratospheric-Tropospheric (StratTrop, Archibald et al., 2020) chemistry scheme. Originally, StratTrop includes 75 chemical species that are connected by 283 reactions (Archibald et al., 2020). I use a reduced version of the StratTrop scheme, to better identify the impact of the different chemical mechanisms on the atmospheric chemistry of exoplanets. In Table 2.1, I show the 21 species included along with their initial abundances. The other 54 species in StratTrop are shown for completeness but with zero abundance. The 21 species are connected by 71 reactions that are shown in Table 2.2. The network includes a description of the Chapman mechanism of ozone formation (Chapman, 1930), following Yates et al. (2020). Additionally, I simulate the reactive hydrogen (HO_x) catalytic cycle, where HO_x denotes the ensemble of atomic hydrogen (H), the hydroxyl radical (OH) and the hydroperoxy radical (HO_2), to account for ozone destruction following the oxidation and photolysis of water vapour. Lastly, I add the nitrogen oxide (NO_x) catalytic cycle, including NO and nitrogen dioxide (NO_2), to the network. More complex oxidised nitrogen species, such as nitrate (NO_3), nitrous oxide (N_2O), and the reservoirs nitric acid (HNO_3) and dinitrogen pentoxide (N_2O_5), are also simulated. Following the Earth-like atmospheric setup from Boutle et al. (2017), the initialisation of N_2, O_2 and CO_2 is based on pre-industrial Earth abundances and an atmospheric pressure of 1 bar. These species are assumed to be well-mixed and constant as a function of altitude (see Table 2.1). Initial values for H_2O are based

on evaporation from the slab ocean. As described in Section 1.7, abiotic pathways to oxygen-rich conditions similar to the pre-industrial Earth exist (e.g. Hu et al., 2012; Domagal-Goldman et al., 2014; Luger & Barnes, 2015; Tian, 2015a). The 1 bar atmospheric pre-industrial Earth composition was chosen as a starting point for the 3D simulations in this thesis as this is the situation we know best. In doing so, we also build upon many 3D GCM studies (e.g. Joshi et al., 1997; Merlis & Schneider, 2010; Turbet et al., 2016; Boutle et al., 2017) including model intercomparisons (Fauchez et al., 2022; Sergeev et al., 2022b; Turbet et al., 2022) as well as CCM studies (Chen et al., 2018, 2019; Yates et al., 2020; Chen et al., 2021).

To avoid the impact of initial conditions that are far from steady-state values, the remainder of the HO_x and the NO_y species are initialised at mass mixing ratios of 10^{-9} and 10^{-15}, respectively. All the other species are initially set to zero and do not participate in the subsequent atmospheric chemistry. Table 2.1 also shows which species are active in the SOCRATES radiation scheme and/or result from lightning emissions. The lightning-induced species will be further discussed in Section 3.2.4.

2.2.6 Nomenclature

Throughout this thesis, several measures of atmospheric composition will be used by considering the atmosphere as a chemical mixture. The mass mixing ratio q_j of a species j is defined as the mass of one constituent m_j (in kg) compared to that of all other constituents in an atmosphere:

$$q_j = \frac{m_j}{m_{tot} - m_j}. \tag{2.36}$$

The mass mixing ratio becomes huge when considering bulk species and using mass fraction is more sensible. When species j is a trace gas in the atmosphere, $m_j \ll m_{tot}$ and thus the mass mixing ratio is equivalent to the mass fraction:

$$w_j = \frac{m_j}{m_{tot}}. \tag{2.37}$$

The mole fraction (χ_j), equivalent to volume mixing ratio (VMR) for trace gases, denotes the amount of a constituent divided by the total amount in a chemical mixture:

$$\chi_j = \frac{n_j}{n_{tot}}, \tag{2.38}$$

with n denoting number densities in molecules m^{-3}. In an atmosphere, we can convert between w_j and χ_j with the help of the molar mass M_j and M_{tot} (or the mean molecular weight μ of the atmosphere), in units kg mol^{-1}:

$$\chi_j = \frac{m_j}{m_{tot}} \frac{\mu}{M_j} = w_j \frac{\mu}{M_j}. \tag{2.39}$$

The mean molecular weight is calculated as the sum of all species j that make up the atmosphere:

$$\mu = \sum_j M_j w_j. \tag{2.40}$$

The concentration of a species represents the amount of substance per unit volume and can be expressed as number density n_i in and mass density ρ_i in kg m^{-3}. Integrating the number density over the vertical extent of the atmosphere results in the column density in molecules m^{-2}.

Species	Initial w	Notes
N_2	0.78084	Uniform
O_2	0.2314	Uniform, rad active
CO_2	5.941×10^{-4}	Uniform, rad active
H_2O	N/A[a]	Rad active
N_2O	(1×10^{-15})	Lightning-induced, rad active
CH_4	0.0	
CFCs	0.0	
Cl-bearers[b]	0.0	
Br-bearers[c]	0.0	
H_2	1×10^{-9}	
O_3	1×10^{-9}	Rad active
$O(^3P)$	1×10^{-9}	
$O(^1D)$	1×10^{-9}	
H_2O_2	1×10^{-9}	
H	1×10^{-9}	
OH	1×10^{-9}	
HO_2	1×10^{-9}	
NO	(1×10^{-15})	Lightning-induced
NO_2	(1×10^{-15})	Lightning-induced
NO_3	(1×10^{-15})	Lightning-induced
N_2O_5	(1×10^{-15})	Lightning-induced
HONO	(1×10^{-15})	Lightning-induced
HNO_3	(1×10^{-15})	Lightning-induced
HO_2NO_2	(1×10^{-15})	Lightning-induced
N	(1×10^{-15})	Lightning-induced
CO	0.0	
HCHO	0.0	
MeOO	0.0	
MeOOH	0.0	
H_2S	0.0	
SO_3	0.0	
DMS	0.0	
SO_2	0.0	
H_2SO_4	0.0	
MSA	0.0	
CS_2	0.0	
NH_3	0.0	

Table 2.1: Abundances used for the chemistry initialisation. 'Rad active' indicates that a species is used in the UM radiative transfer. The ozone abundance is fed back from UKCA to the UM for this radiative transfer. [a] H_2O follows from evaporation from the slab ocean; [b]Cl-bearers include Cl, ClO, Cl_2O_2, OClO, BrCl, HOCl, $ClONO_2$, $CFCl_3$, CF_2Cl_2, HCl; [c]Br-bearers include Br, BrO, BrCl, $BrONO_2$, HBr, HOBr, MeBr

	Reaction	Scheme
1	$O(^1D) + O_2 \longrightarrow O(^3P) + O_2$	Chapman
2	$O(^1D) + N_2 \longrightarrow O(^3P) + N_2$	Chapman
3	$O(^1D) + CO_2 \longrightarrow O(^3P) + CO_2$	Chapman
4	$O(^1D) + O_3 \longrightarrow O_2 + O(^3P) + O(^3P)$	Chapman
5	$O(^1D) + O_3 \longrightarrow O_2 + O_2$	Chapman
6	$O(^3P) + O_3 \longrightarrow O_2 + O_2$	Chapman
7	$O(^3P) + O_2 + M \longrightarrow O_3 + M$	Chapman
8	$O_2 + h\nu \longrightarrow O(^3P) + O(^3P)$	Chapman
9	$O_2 + h\nu \longrightarrow O(^3P) + O(^1D)$	Chapman
10	$O_3 + h\nu \longrightarrow O_2 + O(^3P)$	Chapman
11	$O_3 + h\nu \longrightarrow O_2 + O(^1D)$	Chapman
12	$H_2O + O(^1D) \longrightarrow 2OH$	HO_x
13	$HO_2 + O(^3P) \longrightarrow OH + O_2$	HO_x
14	$HO_2 + O_3 \longrightarrow OH + 2O_2$	HO_x
15	$OH + HO_2 \longrightarrow H_2O + O_2$	HO_x
16	$OH + O_3 \longrightarrow HO_2 + O_2$	HO_x
17	$H + HO_2 \longrightarrow H_2 + O_2$	HO_x
18	$H + HO_2 \longrightarrow O(^3P) + H_2O$	HO_x
19	$H + HO_2 \longrightarrow OH + OH$	HO_x
20	$H + O_3 \longrightarrow OH + O_2$	HO_x
21	$HO_2 + HO_2 \longrightarrow H_2O_2 + O_2$	HO_x
22	$O(^1D) + H_2 \longrightarrow OH + H$	HO_x
23	$O(^3P) + H_2 \longrightarrow OH + H$	HO_x
24	$O(^3P) + H_2O_2 \longrightarrow OH + HO_2$	HO_x
25	$O(^3P) + OH \longrightarrow O_2 + H$	HO_x
26	$OH + H_2 \longrightarrow H_2O + HO_2$	HO_x
27	$OH + H_2O_2 \longrightarrow HO_2 + H_2O$	HO_x
28	$OH + OH \longrightarrow H_2O + O(^3P)$	HO_x
29	$H + O_2 + M \longrightarrow HO_2 + M$	HO_x
30	$HO_2 + HO_2 + M \longrightarrow H_2O_2 + O_2 + M$	HO_x
31	$OH + OH + M \longrightarrow H_2O_2 + M$	HO_x
32	$H_2O + h\nu \longrightarrow OH + H$	HO_x
33	$H_2O_2 + h\nu \longrightarrow OH + OH$	HO_x
34	$H + NO_2 \longrightarrow OH + NO$	NO_x
35	$HNO_3 + OH \longrightarrow NO_3 + H_2O$	NO_x

Table 2.2: Reactions included in the different chemical networks. The associated rate constants can be found in Archibald et al. (2020). Continues on next page.

	Reaction	Scheme
36	$HO_2 + NO \longrightarrow OH + NO_2$	NO_x
37	$HO_2 + NO_3 \longrightarrow OH + NO_2 + O_2$	NO_x
38	$N + NO \longrightarrow N_2 + O(^3P)$	NO_x
39	$N + NO_2 \longrightarrow N_2O + O(^3P)$	NO_x
40	$N + O_2 \longrightarrow NO + O(^3P)$	NO_x
41	$N_2O_5 + H_2O \longrightarrow HONO_2 + HONO_2$	NO_x
42	$NO + NO_3 \longrightarrow NO_2 + NO_2$	NO_x
43	$NO + O_3 \longrightarrow NO_2 + O_2$	NO_x
44	$NO_2 + NO_3 \longrightarrow NO + NO_2 + O_2$	NO_x
45	$NO_2 + O(^3P) \longrightarrow NO + O_2$	NO_x
46	$NO_2 + O_3 \longrightarrow NO_3 + O_2$	NO_x
47	$O(^1D) + N_2O \longrightarrow N_2 + O_2$	NO_x
48	$O(^1D) + N_2O \longrightarrow NO + NO$	NO_x
49	$O(^3P) + NO_3 \longrightarrow O_2 + NO_2$	NO_x
50	$OH + HO_2NO_2 \longrightarrow H_2O + NO_2 + O_2$	NO_x
51	$OH + HONO \longrightarrow H_2O + NO_2$	NO_x
52	$OH + NO_3 \longrightarrow HO_2 + NO_2$	NO_x
53	$HO_2 + NO_2 + M \longrightarrow HO_2NO_2 + M$	NO_x
54	$HO_2NO_2 + M \longrightarrow HO_2 + NO_2 + M$	NO_x
55	$NO + NO + O_2 \longrightarrow NO_2 + NO_2$	NO_x
56	$NO_2 + OH + M \longrightarrow HNO_3 + M$	NO_x
57	$NO_3 + NO_2 + M \longrightarrow N_2O_5 + M$	NO_x
58	$N_2O_5 + M \longrightarrow NO_2 + NO_3 + M$	NO_x
59	$O(^1D) + N_2 + M \longrightarrow N_2O + M$	NO_x
60	$O(^3P) + NO + M \longrightarrow NO_2 + M$	NO_x
61	$O(^3P) + NO_2 + M \longrightarrow NO_3 + M$	NO_x
62	$OH + NO + M \longrightarrow HONO + M$	NO_x
63	$HNO_3 + h\nu \longrightarrow NO_2 + OH$	NO_x
64	$HONO + h\nu \longrightarrow OH + NO$	NO_x
65	$HO_2NO_2 + h\nu \longrightarrow HO_2 + NO_2$	NO_x
66	$NO + h\nu \longrightarrow N + O(^3P)$	NO_x
67	$NO_2 + h\nu \longrightarrow NO + O(^3P)$	NO_x
68	$NO_3 + h\nu \longrightarrow NO + O_2$	NO_x

Table 2.2: Reactions included in the different chemical networks. The associated rate constants can be found in Archibald et al. (2020). Continues on next page.

	Reaction	Scheme
69	$NO_3 + h\nu \longrightarrow NO_2 + O(^3P)$	NO_x
70	$N_2O + h\nu \longrightarrow N_2 + O(^1D)$	NO_x
71	$N_2O_5 + h\nu \longrightarrow NO_3 + NO_2$	NO_x

Table 2.2: Reactions included in the different chemical networks. The associated rate constants can be found in Archibald et al. (2020).

Chapter 3

Lightning-induced chemistry on tidally locked exoplanets

This Chapter is based on the publication:

Lightning-induced chemistry on tidally locked Earth-like exoplanets

Marrick Braam, Paul I. Palmer, Leen Decin, Robert J. Ridgway, Maria Zamyatina, Nathan J. Mayne, Denis E. Sergeev, and N. Luke Abraham

Monthly Notices of the Royal Astronomical Society, Volume 517, Issue 2, September 2022, Pages 2383–2402, DOI: https://doi.org/10.1093/mnras/stac2722

Author contributions: Marrick Braam, Paul Palmer, and Leen Decin conceived the science questions. Marrick Braam led the research, performed the simulations, analysed the model results, and wrote the manuscript. Paul Palmer and Leen Decin supervised the work and edited the manuscript. Robert Ridgway, Maria Zamyatina, Nathan Mayne, Denis Sergeev, and Luke Abraham contributed to the model development and provided feedback on the manuscript.

3.1 Introduction

We know that exoplanets are ubiquitous in the galaxy (e.g. Kopparapu et al., 2013; Hsu et al., 2019), but for those that support an atmosphere, we know little about the associated physical and chemical properties. This gap in our knowledge has implications for understanding whether these planets are potentially habitable and whether they could present false-positive biosignatures (e.g. Scalo et al., 2007; Schwieterman et al., 2018). With the successful launch of the James Webb Space Telescope (JWST) in late 2021 and the construction of new ground-based facilities (such as the Extremely Large Telescope, ELT), we can expect the first insights into the atmospheres of some observationally favourable and potentially habitable exoplanets (e.g. Lustig-Yaeger et al., 2019). Simulating the physical and chemical properties of these

atmospheres is essential to interpreting the observations. Here, I focus on understanding the atmospheric composition of an Earth-like exoplanet orbiting an M-dwarf star, which is likely to sustain habitable surface conditions for a range of atmospheric compositions (Turbet et al., 2016; Boutle et al., 2017; Yates et al., 2020).

Earth-size planets are preferentially discovered in close-in orbits around M-dwarf stars (Dressing & Charbonneau, 2015) and their potential habitability is an active area of research (e.g. Shields et al., 2016). M stars are cooler and smaller compared to other types of stars. Consequently, the circumstellar Habitable Zone (HZ) (Kasting et al., 1993; Kopparapu et al., 2013) moves inward. A planet orbiting in this HZ is likely to be tidally locked (e.g. Barnes, 2017), which results in large temperature differences between the dayside and nightside of a planet. Proxima Centauri b (Anglada-Escudé et al., 2016) is a nearby example of a planet orbiting in the HZ of an M star. Assuming the planet has an atmosphere, hemispheric mean temperatures from simulations can differ by $\sim$60 K for Proxima Centauri b (Boutle et al., 2017; Sergeev et al., 2020), and the planet is a candidate for surface habitability (see also Ribas et al., 2016; Turbet et al., 2016; Lewis et al., 2018). The tidally locked configuration has implications for winds and vertical transport that require an understanding of the full three-dimensional circulation including clouds. This motivates the adaptation of general circulation models (GCMs), used for weather and climate predictions for Earth, to exoplanets. The Met Office Unified Model (UM) has been adapted and applied to a wide range of exoplanets (e.g. Mayne et al., 2014a; Mayne et al., 2014b; Boutle et al., 2017; Drummond et al., 2018a; Drummond et al., 2020) and was also included in the recent THAI project (Fauchez et al., 2022; Sergeev et al., 2022b; Turbet et al., 2022), an intercomparison of GCM outputs for potentially habitable atmospheres on TRAPPIST-1 e.

The main driver of atmospheric circulation on terrestrial exoplanets is the incoming stellar irradiation. The impact of different spectral energy distributions has been studied for fast-rotating exoplanets (Shields et al., 2013; Wolf et al., 2017) and for tidally locked planets (Eager et al., 2020). For tidally locked planets, the day-night contrast in stellar radiation results, in many cases, in the development and maintenance of equatorial jets that redistribute heat to the nightside (Showman & Guillot, 2002; Showman & Polvani, 2011; Koll & Abbot, 2016). This redistribution can help to prevent atmospheric collapse on the nightside (Joshi et al., 1997; Turbet et al., 2018). Besides the jet, many 3D GCM simulations show stationary gyres at mid-latitudes and moderate divergence at the substellar point (e.g. Carone et al., 2014, 2015; Hammond et al., 2020; Hammond & Lewis, 2021). The circulation regime also varies with orbital period (e.g. Merlis & Schneider, 2010; Edson et al., 2011; Carone et al., 2015, 2018) and time-dependent wave phenomena can further impact our ability to interpret observations (Cohen et al., 2022). Yang et al. (2013) show that the dayside is covered by a thick cloud deck, resulting from vigorous convection centred at the substellar point. This results in a cloud albedo feedback that is also sensitive to the orbital period (Yang et al., 2013). For Proxima

Centauri b, nightside Rossby gyres develop on either side of the equatorial jet (Turbet et al., 2016; Boutle et al., 2017). These gyres trap air, that experiences extensive radiative cooling (Yang & Abbot, 2014), as described by Boutle et al. (2017) and Yates et al. (2020). As a consequence, the atmospheric pressure decreases locally and atmospheric constituents such as ozone are drawn downwards to lower altitudes thereby increasing local ozone column abundances (Yates et al., 2020). Most GCM studies assume aquaplanets with a slab ocean, but ocean heat transport can also increase the habitable area of a (tidally locked) planet (Hu & Yang, 2014; Del Genio et al., 2019). The existence and distribution of landmasses further influence the planetary climate through changes in convection and water evaporation (e.g. Abe et al., 2011; Lewis et al., 2018; Rushby et al., 2020). Finally, the chemical composition of the atmosphere also affects the radiative balance of the planet through scattering and absorption of incoming and outgoing radiation. Static chemical compositions have been investigated (e.g. Pierrehumbert, 2010a; Turbet et al., 2016; Boutle et al., 2017), but there is a balance between the irradiation, the atmospheric physics and chemistry (in particular constituents that have significant opacities under the incident stellar radiation).

This balance motivates the need for coupled climate-chemistry models (CCMs) to study the relationships between radiatively active atmospheric constituents (gases and aerosols) and the atmospheric dynamics of the planet. There is a growing body of work investigating 3D atmospheric photochemistry on exoplanets orbiting in the HZ, from understanding the impact of tidal locking on Earth's ozone distribution (Proedrou & Hocke, 2016) to understanding how the stellar flux distributions of M-dwarfs influence both the magnitude and distribution of atmospheric biosignature gases (Chen et al., 2018) and an ozone layer on Proxima Centauri b through changes in chemical production and loss rates (Yates et al., 2020). Perturbations in the incident stellar radiation will influence the planetary atmospheric chemistry and physics. The magnitude of chemical perturbations due to stellar flares (through enhanced UV activity and proton events), for example, is determined by a combination of the planetary magnetic field, radiation environment and atmospheric circulation (Chen et al., 2021). Perturbations are seen especially in distributions of NO, OH, and ozone for unmagnetized, tidally locked planets around K and M stars. Planets that have protective magnetic fields are able to (partially) counteract the effect of flares (Chen et al., 2021), emphasizing the potential role of stellar activity in determining the habitability of a planet. Furthermore, both inter-annual and seasonal variations in clouds and chemistry can impact the observability of spectral features on Earth-analogue exoplanets (Cooke et al., 2023b).

On Earth, the presence of lightning discharges can lead to local perturbations in atmospheric chemistry. Lightning has sufficient energy to thermally decompose molecular nitrogen and oxygen to form an abiotic source of nitrogen oxides (NO_x=NO+NO_2, Crutzen 1970; Schumann and Huntrieser 2007). Through atmospheric chemistry, NO_x can influence the distribution of atmospheric ozone. Ozone is the photochemical byproduct of molecular oxygen and thus

depends on oxygen levels, as is shown by the 3D CCM simulations of Cooke et al. (2022) for various epochs in Earth's history. Furthermore, the nonlinear oxygen-ozone relationship depends on the host star's UV spectrum (Kozakis et al., 2022). Since oxygen on Earth is largely produced by sources of biological origin (Schwieterman et al., 2018), its photochemical product ozone can be seen as a potential biosignature. However, pathways to false positives for abiotic oxygen and ozone on planets orbiting M-dwarfs exist, including accumulation of O_2 following the photolysis of H_2O and subsequent H escape (e.g. Tian, 2015b; Wordsworth et al., 2018; Lincowski et al., 2019) and CO_2 photolysis releasing oxygen atoms (e.g. Kasting & Catling, 2003; Domagal-Goldman et al., 2014; Harman et al., 2015). Understanding these abiotic influences is essential for the interpretation of spectral signatures (Schwieterman et al., 2018).

Studies using 1-D photochemical models have considered the impact of global thunderstorms on exoplanetary atmospheric chemistry (Rimmer & Helling, 2016; Ardaseva et al., 2017; Harman et al., 2018). It was found that the chemical effect of lightning would be hard to detect on Earth-like exoplanets (Ardaseva et al., 2017). Harman et al. (2018) showed that catalytic cycles following NO production from lightning enhance the reliability of O_2 as a biosignature, assuming Earth-like chemical composition. However, just like planetary atmospheres and climates, the emergence of lightning is a 3D process, that depends on a combination of cloud formation, particle charging and charge separation (Helling, 2019). In GCMs of Earth, lightning is usually parametrized in terms of convective parameters, such as cloud-top height (Price & Rind, 1992; Luhar et al., 2021), convective precipitation and mass flux (Allen & Pickering, 2002), and upward cloud ice flux (Finney et al., 2014). Lightning has already been observed on the giant planets in the Solar System (e.g. Aplin, 2006; Hodosán et al., 2016), but is yet to be detected on exoplanets. However, GCMs predict a thick and convective cloud deck to cover the dayside of tidally locked planets (e.g. Yang et al., 2013) and the first evidence for clouds on exoplanets is being obtained (Pont et al., 2013; Kreidberg et al., 2014; Diamond-Lowe et al., 2018). Therefore, lightning on exoplanets is a reasonable expectation (Helling, 2019), leading to potentially important disruptions of the atmospheric chemistry.

Here, I investigate the impact of lightning-induced chemistry on a tidally locked exoplanet in the HZ. I use the UM in the configuration of a planet orbiting an M-dwarf star, nominally Proxima Centauri b, building on previous studies (Boutle et al., 2017; Yates et al., 2020). I also use the UK Chemistry and Aerosol framework (UKCA), coupled with the UM, to describe gas-phase chemistry, with lightning as the main source of nitric oxide (NO). In Section 3.2, I describe the model setup, the process of making UKCA compatible with the M-dwarf setup and the choice of lightning parametrization. In Section 3.3 I present the results, briefly dis-

cussing the planetary climate before presenting the emergence of lightning and the resulting atmospheric chemistry. I discuss the importance of stellar fluxes, comparison to other results and potential observability in Section 3.4. Finally, I present the conclusions of the study in Section 3.5.

3.2 Methods

In this Section, I describe the different components of the CCM, the lightning parametrization, and, lastly, I specify the experimental setup of these simulations.

3.2.1 Unified Model

I use the UM, a 3D GCM, in its Global Atmosphere 7.0 configuration (Walters et al., 2019), as introduced in Section 2.1. The ENDGAME dynamical core solves the non-hydrostatic fully compressible deep-atmosphere equations of motion (Wood et al., 2014). Parametrized sub-grid scale processes include convection that is described using a mass flux-based approach (Gregory & Rowntree, 1990), water cloud physics that is described using a prognostic condensate scheme (Wilson et al., 2008), and turbulent mixing (Lock et al., 2000; Brown et al., 2008). The atmospheric radiative transfer is described by the Suite of Community Radiative Transfer codes based on Edwards and Slingo (SOCRATES) scheme, which uses the correlated-k method (Edwards & Slingo, 1996; Manners et al., 2021). The UM is typically used to study Earth's weather and climate but recently has been adapted to study different types of exoplanets (e.g Mayne et al., 2014a; Mayne et al., 2014b; Boutle et al., 2017; Mayne et al., 2017; Drummond et al., 2018a; Lewis et al., 2018; Drummond et al., 2020; Eager et al., 2020; Sergeev et al., 2020; Yates et al., 2020).

Here, I adapt the UM to investigate the climate dynamics and atmospheric chemistry of Proxima Centauri b (Anglada-Escudé et al., 2016), in a circular, tidally locked orbit around its host star following previous studies (Boutle et al., 2017; Yates et al., 2020). The stellar, orbital and planetary parameters are listed in Table 3.1. The horizontal resolution is 2 by 2.5° in latitude and longitude, respectively. The atmosphere is divided into 60 vertical levels extending from the surface to 85 km, with quadratic stretching to enhance resolution near the surface, following Yates et al. (2020). To describe stellar radiation, I use the composite spectrum at version 2.2 as presented by the MUSCLES spectral survey (France et al., 2016; Loyd et al., 2016; Youngblood et al., 2016). This spectral energy distribution was created from archival data of XMM-Newton and the Hubble Space Telescope (HST) and covers wavelengths from 0.5 nm to 5.5 μm. Since the 6 'shortwave' bands of SOCRATES treat incoming radiation up to 10 μm, I extended the spectrum by using the spectrum presented by Ribas et al. (2017) for wavelengths between 5.5 and 10 μm. This final composite spectrum was used to recalculate correlated-k absorption coefficients. Previous UM studies of Proxima Centauri

b used a synthetic BT-Settl spectrum, appropriate for the host star properties (Boutle et al., 2017; Yates et al., 2020). I assume an aquaplanet covered by a 2.4 m slab ocean mixed layer with a total heat capacity of 10^7 J K^{-1} m^{-2}. Sea ice formation is not included in these simulations, but the associated ice-albedo feedback is weak for planets around M-dwarfs (Joshi & Haberle, 2012; Shields et al., 2013).

I assume a surface pressure of one bar for these simulations, building on previous work with the UM as well as other GCM studies (e.g. Joshi, 2003; Merlis & Schneider, 2010; Yang et al., 2013; Carone et al., 2014; Kopparapu et al., 2016; Boutle et al., 2017; Rushby et al., 2020; Sergeev et al., 2022b; Turbet et al., 2022). One bar of surface pressure is also a common assumption for many other photochemical models, ranging from 1-D (e.g. Domagal-Goldman et al., 2014; Tian et al., 2014; Harman et al., 2015, 2018) to global 3D CCM studies (Chen et al., 2018, 2019; Yates et al., 2020; Chen et al., 2021). I acknowledge that stellar activity can potentially have detrimental effects on the atmospheric mass and thus surface pressure of Proxima Centauri b, as shown by Garraffo et al., 2016; Airapetian et al., 2017; Garcia-Sage et al., 2017; Airapetian et al., 2020. For this first investigation of lightning-induced chemistry, I opted for the case of a 1 bar surface pressure, since 1) we are currently unable to constrain any particular value of the surface pressure as the best value, so a sensible starting point for this first study is to use the atmospheric parameters that we understand in the greatest detail, and 2) the results apply more generally for tidally locked planets that reside in the HZ of their M-dwarf host star. This may include planets with the potential to sustain a 1 bar N_2-dominated atmosphere, for example the outer planets of the TRAPPIST-1 system (Turbet et al., 2020).

In this work, I focus on the impacts of lightning and use a time-averaged stellar spectrum. However, this work has been performed in close collaboration with a complementary study, using the UM but including the impact of stellar activity while omitting lightning. This study, Ridgway et al. (2023), is also based on Proxima Centauri b, but uses SOCRATES to calculate the photolysis rates and a simplified idealised chemistry scheme to capture the ozone interactions (Drummond et al., 2016; Drummond et al., 2020). The complementarity of these two studies has provided an excellent opportunity for mutual testing and development.

3.2.2 UK Chemistry and Aerosol Framework

The UK Chemistry and Aerosol (UKCA) model (Morgenstern et al., 2009; O'Connor et al., 2014; Archibald et al., 2020) is a framework to describe the global atmospheric chemical composition of the simulated exoplanet. A detailed description of the UKCA framework is given in Section 2.2, here I will provide a brief overview. UKCA includes aerosol and gas-phase chemistry and is coupled to the UM dynamics. It uses the UM components for large scale advection, convective transport and boundary layer mixing of its aerosol and chemical tracers (O'Connor et al., 2014; Archibald et al., 2020). UKCA contains a large number of gas-phase and heterogeneous chemical reactions, some of which I have included in the

Table 3.1: Orbital and planetary parameters for the Proxima Centauri b setup, following Boutle et al. (2017).

Parameter	Value
Semi-major axis (AU)	0.0485
Stellar Irradiance (W m^{-2})	881.7
Orbital Period (days)	11.186
Rotation rate (rad s^{-1})	6.501×10^{-6}
Eccentricity	0
Obliquity	0
Radius ($R_\oplus$)	1.1
Surface gravity (m s^{-2})	10.9

chemical network. Furthermore, the chemistry schemes in UKCA describe wet and dry deposition (Giannakopoulos et al., 1999). In this study, I use the Stratospheric (Strat, Morgenstern et al., 2009) and Stratospheric-Tropospheric (StratTrop, Archibald et al., 2020) chemistry schemes. Originally, StratTrop includes 75 chemical species that are connected by 283 reactions (Archibald et al., 2020). I used a reduced version of the UKCA chemistry schemes (Table 3.2), to quantify the impact of the different chemical mechanisms on the atmospheric chemistry of a tidally locked exoplanet. First, I use a simple network that describes the Chapman mechanism of ozone formation (Chapman, 1930), following Yates et al. (2020). Second, I add the reactive hydrogen (HO_x) catalytic cycle, where HO_x denotes the ensemble of atomic hydrogen (H), the hydroxyl radical (OH) and the hydroperoxy radical (HO_2). I include this cycle to account for ozone chemistry following the oxidation and photolysis of water vapour. Lastly, I add the nitrogen oxide (NO_x) catalytic cycle, including NO and nitrogen dioxide (NO_2), to the network. I also include other oxidised nitrogen species, such as nitrate (NO_3), nitrous oxide (N_2O), and the reservoirs nitric acid (HNO_3) and dinitrogen pentoxide (N_2O_5). Collectively, these nitrogen species belong to the NO_y family and can also influence ozone chemistry. In these simulations, lightning is the main source of NO that initiates further NO_y chemistry, as described in Section 3.2.4. In the upper atmosphere, the slow termolecular reaction between N_2 and $O(^1D)$ provides another source of NO_y, but this does not impact the lightning-induced chemistry that occurs at altitudes below 20 km.

The complete list of species, reactions, initial conditions and details about deposition states in each of the 3 reduced schemes can be found in Tables 2.1 and 2.2, respectively. I also note which species are active in the SOCRATES radiation scheme. Following the Earth-like atmospheric setup from Boutle et al. (2017), the initialisation of N_2, O_2 and CO_2 is based on pre-industrial Earth abundances, and these species are assumed to be well-mixed. Initial values for H_2O are based on evaporation from the slab ocean. To avoid the impact of initial conditions that are far from steady-state values, the remainder of the HO_x and the NO_y species are initialised at mass mixing ratios of 10^{-9} and 10^{-15}, respectively. All the other species are initially set to zero and do not participate in the subsequent atmospheric

Table 3.2: Specifications of the different chemistry schemes that were used in this study. The schemes presented are reduced versions of UKCA's Strat (Morgenstern et al., 2009) and StratTrop chemistry schemes (Archibald et al., 2020). Each row also includes the chemistry from the rows above, hence '+NO_x' means NO_x-chemistry added to HO_x and the Chapman mechanism. Tables 2.1 and 2.2 give a full overview of the chemical species and reactions included in each scheme.

Chemistry	Species	Bimolecular Reactions	Termolecular Reactions	Photolysis Reactions	Total Reactions	Chemistry Scheme	Lightning-NOx
Chapman	6	6	1	4	11	Strat	No
+HO_x	12	23	4	6	33	StratTrop	No
+NO_x	21	42	14	15	71	StratTrop	Yes

chemistry. UKCA also includes surface emissions, but I set them to zero. Lightning discharges produce atmospheric emissions of NO, which I describe in Section 3.2.4. Since lightning is the only source of NO in the lower 20 km of the atmosphere, this initiates the subsequent NO_y chemistry.

3.2.3 Fast-JX Photolysis Code

Besides participating in chemical reactions, atmospheric species can be photolysed by the interaction with ultraviolet (UV) and visible radiation (Bian & Prather, 2002). To describe atmospheric photolysis, UKCA uses the Fast-JX photolysis scheme (Wild & Prather, 2000; Bian & Prather, 2002; Neu et al., 2007; Telford et al., 2013). Fast-JX is an efficient photolysis scheme that takes into account the varying optical depths of Rayleigh scattering, absorbing gases, clouds and aerosols. In this way, Fast-JX provides an interactive treatment of photolysis in modelling (3D) atmospheric compositions. The radiation is divided over 18 wavelength bins, with 11 bins covering 177–291 nm and seven bins covering 291–850 nm. These bins group regions of similar absorption as specified by Bian and Prather (2002). Fast-JX calculates how many photons of each wavelength are absorbed and/or scattered as light passes through the plane-parallel atmosphere (Telford et al., 2013). Photolysis rates are then calculated from the actinic flux, cross-sections and quantum yields in each bin.

For Fast-JX, I extract the radiation between 177 and 850 nm from the MUSCLES spectrum for Proxima Centauri. To describe non-Earth orbits in UKCA, I follow Yates et al. (2020) and scaled the M-dwarf fluxes to find the top-of-the-atmosphere (TOA) flux received by a planet at 1 AU. A synchronization to the orbital distance of Proxima Centauri b is added to UKCA to determine the TOA flux received by the planet. This is shown in Figure 3.1, along with the TOA flux for Earth.

I regroup the fluxes over the wavelength bins, following Bian and Prather (2002), to produce the TOA fluxes at 1 AU as shown in Table 3.3 (and as the horizontal black lines in Figure 3.1). Precursor work by Yates et al. (2020) using the BT-Settl spectrum did not include this regrouping and instead erroneously divided the fluxes over 18 bins in terms of increasing wavelength

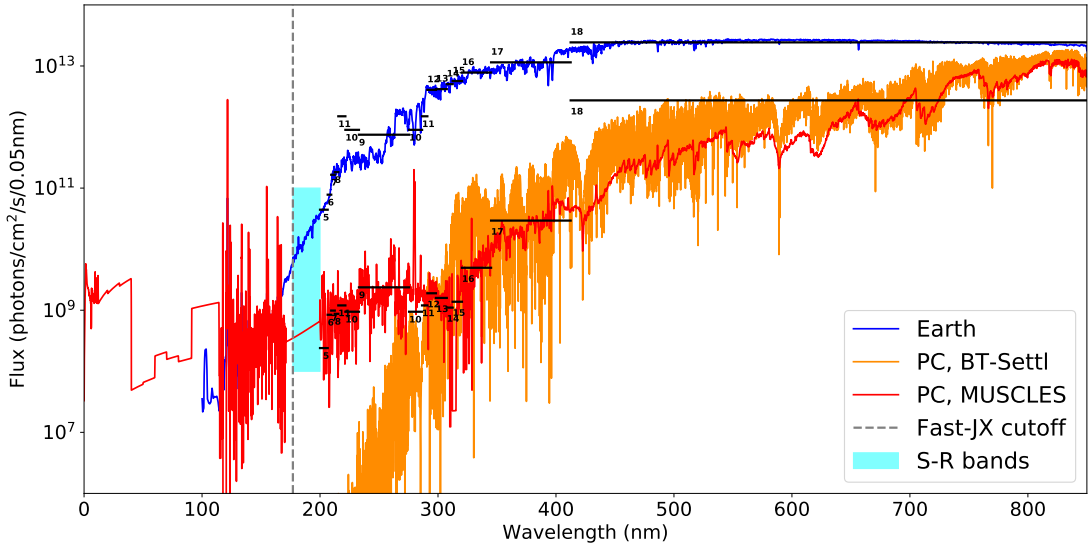

Figure 3.1: Top-of-the-atmosphere fluxes received on Earth and Proxima Centauri b. The red line shows the flux for the composite MUSCLES spectrum of Proxima Centauri, as used in this study; and the orange line denotes the stellar flux generated by the BT-Settl spectrum that was used by Boutle et al. (2017) and Yates et al. (2020). Fast-JX treats fluxes at wavelengths between 177 (the dashed vertical line) and 850 nm. The solid horizontal black lines denote the flux per bin for Fast-JX bins 5–18 and are numbered accordingly. Bins 1–4 and part of bin 5 contain a combination of the Schumann-Runge (S-R) bands (Bian & Prather, 2002) and treat the fluxes falling in the shaded rectangular patch, or between 177 and 202.5 nm.

Table 3.3: Top-of-the-atmosphere flux for a planet orbiting at 1 AU around Proxima Centauri.

Bin #	TOA flux at 1 AU (photons $s^{-1}cm^{-2}$)
1	1.091×10^{8}
2	1.011×10^{8}
3	9.240×10^{7}
4	4.550×10^{7}
5	3.301×10^{8}
6	1.189×10^{8}
7	1.392×10^{8}
8	1.371×10^{8}
9	4.739×10^{9}
10	5.773×10^{9}
11	5.922×10^{8}
12	6.467×10^{8}
13	6.881×10^{8}
14	2.596×10^{8}
15	5.086×10^{8}
16	5.761×10^{9}
17	9.321×10^{10}
18	5.625×10^{13}

(see Table 1 of Yates et al., 2020). Comparing my results with those from Yates et al. (2020) highlights significant differences between most of the bins, such as bin 18, for which the flux from Yates et al. (2020) is $\sim$2 orders of magnitude higher than either the BT-Settl or MUSCLES spectra. This is due to lumping together fluxes up to 2150 nm, beyond the 850 nm upper limit for Fast-JX. This affects, for example, ozone absorption in the Chappuis bands (Burrows et al., 1999) to produce molecular oxygen and O(^{3}P); correcting this error reduces photolysis rates for this reaction by a factor of 20. Hence, this removes the destruction of ozone due to unphysical reasons. As is also seen from Figure 3.1, the MUSCLES spectrum is stronger by up to 8 orders of magnitude at shorter wavelengths ($\lambda <$300 nm). This UV radiation plays an essential role in atmospheric chemistry by driving the photolysis of molecular oxygen ($\lambda <$240 nm and ozone ($\lambda <$320 nm).

3.2.4 Emissions of NO from Lightning

I use a lightning parametrization based on simple scaling relations between the size of a thundercloud and the electrical power output (Vonnegut, 1963). The scaling relations are derived from the laws of electricity, assuming a thunderstorm as an electric dipole separated by a distance characterised by the cloud dimension. Since the number of lightning flashes depends on the electrical power, the lightning flash rates (LFR) in flashes min^{-1} can be described in terms of the cloud-top height H (Williams, 1985; Price & Rind, 1992; Boccippio, 2002; Luhar et al., 2021). Parametrizations are derived for continental and oceanic LFRs.

Since I assume an aquaplanet, I only use the oceanic parametrization:

$$LFR_O = 2.0 \times 10^{-5} H^{4.38}. \tag{3.1}$$

The flash rates are calculated at locations where the convective cloud depth exceeds 5 km, and the cloud depth is based on the base and top convective cloud heights from the convection scheme. The threshold of 5 km follows from the range of data used to develop the parametrization (Price & Rind, 1994). The flash rates are subsequently apportioned into cloud-to-ground (CG) and intracloud (IC) flashes, based on an empirical ratio between the two (Price & Rind, 1993). Extending the parametrization to extraterrestrial environments, justified by the assumption of an Earth-like atmosphere and thus a similar process of charging and charge separation on Proxima Centauri b, I can provide a first assessment of the spatial and temporal distributions of lightning flashes in tidally locked environments and study the relation to the planet's convective activity.

Atmospheric electric discharges (including lightning) provide high-temperature channels of up to 30,000 K. In these channels, new trace molecules can be produced from the ambient atmospheric constituents (Rakov & Uman, 2003). In Earth's atmosphere, the production of NO affects ozone photochemistry (Crutzen, 1970) and the lifetimes of a range of other gases, e.g. CO and nitrous oxide (N_2O) (Rakov & Uman, 2003; Brune et al., 2021; Mao et al., 2021). As the air cools rapidly, the abundances from the high-temperature reactions are 'frozen in' via the so-called Zel'dovich mechanism (Zeldovich et al., 1947). The exact consequences for the atmospheric composition depend on the lightning flash rates and the amount of NO that is produced per flash, terrestrial constraints on the amount of NO per flash are presented by Schumann and Huntrieser (2007).

I use the UKCA emission formulation to describe emissions of NO from individual flashes (Luhar et al., 2021). The production of NO per flash is a key uncertainty, ranging from $\sim$33–700 moles NO per flash with averages of 250 (Schumann & Huntrieser, 2007) and 180 moles NO per flash (Bucsela et al., 2019). To match the global lightning-NO_x production on Earth, NO production rates are scaled to 216 moles NO per flash (Archibald et al., 2020; Luhar et al., 2021). Furthermore, I do not distinguish between CG and IC flashes in the NO production rate. The emitted NO is redistributed vertically, between 500 hPa (or $\sim$4.4 km) and the cloud top for IC flashes and between the surface and 500 hPa for CG flashes, and added to the NO concentration in the chemistry scheme. With a global mean surface pressure equal to 1000 hPa, the midpoint in terms of atmospheric mass is at $\sim$500 hPa.

3.2.5 Experimental Setup

To ensure model stability and to avoid violating the Courant-Friedrichs-Lewy conditions for strong high-altitude winds, I ran the simulations at timesteps of four minutes for atmospheric dynamics. The chemical timestep was left at the default of one hour, as in Yates et al. (2020). From the initial conditions, as described in Sections 3.2.1 and 3.2.2, I run the simulations to a steady state as determined by the balance of incoming and outgoing TOA radiation fluxes and the stabilisation of the surface temperature. I find that the steady state for Proxima Centauri b is generally reached by $\sim$1000 Earth days. I also check that chemical steady state is reached by examining the stabilisation of the total ozone column density and volume mixing ratio of ozone, since ozone is a long-lived species. For Proxima Centauri b, this is typically reached within 15 Earth years, depending on the complexity of the chemical network being used and subject to stochastic changes in atmospheric dynamics. Following Yates et al. (2020), I run for 5 more years to a total of 20 years of spin-up time and report the results as the mean of the following 120 days (or $\sim$10 orbits of Proxima Centauri b).

3.3 Results

This section starts with a description of the planetary climate, followed by the distribution of lightning flashes. Then I discuss the resulting atmospheric chemistry, first focusing on ozone chemistry and, finally, on lightning-induced chemistry.

3.3.1 Background Climate

The overall climate resulting from the simulations is largely similar to that presented in Boutle et al. (2017), which is unsurprising given the similarity in the model configurations. Here I include a description of the main climate elements relevant to this study and refer the reader to Boutle et al. (2017) for a more complete description.

A clear dayside-nightside contrast in surface temperature is simulated, with time-mean temperatures ranging from a maximum of 291 K on the dayside to as low as 157 K over two nightside Rossby gyres on either side of the equator, due to persistent radiative cooling. In terms of sustaining liquid water on the planetary surface, $\sim$45% of the planet's dayside remains at habitable surface temperatures ($>$273.15 K). Generally, I find much higher atmospheric specific humidity on the dayside, due to evaporation (higher overall temperatures) and convection, than on the nightside (Boutle et al., 2017; Yates et al., 2020). Clouds and radiatively active gases such as ozone impede the penetration of UV radiation to the surface so that levels are lower than those found on Earth (e.g. O'Malley-James & Kaltenegger, 2017). The dayside hemispheric mean level of UV surface radiation ($\lambda<$320 nm) is reduced to 15% of the TOA value. This is about 0.2% of the level on Earth's surface (Segura et al., 2003), comparable to the findings of Segura et al. (2005) for planets orbiting M-dwarfs.

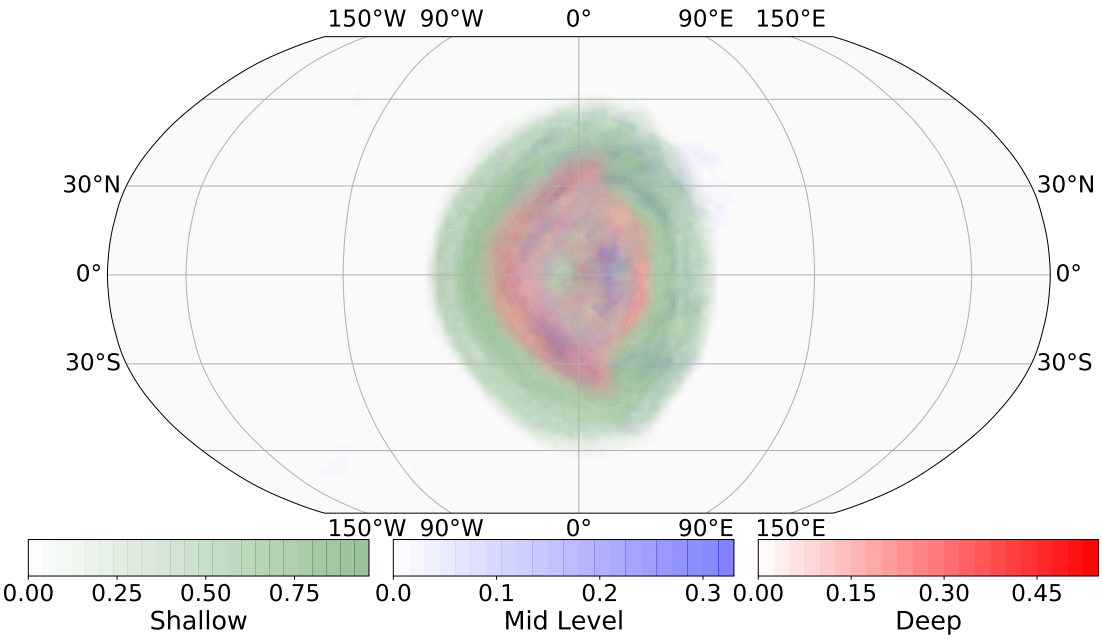

Figure 3.2: Time-mean (120 days) indicator of shallow, mid-level and deep convection over the planetary surface. The indicator is equal to 1 if a convection type is diagnosed or 0 if not, and the diagnosis of convection is based on undilute parcel ascent from the near surface, for grid boxes where the surface buoyancy flux is positive (Walters et al., 2019).

The distribution of clouds is influenced by the zonally asymmetric stellar heating of the planet due to the assumed tidally locked configuration in this study. Intense heating at the substellar point drives deep convection and consequently water and ice cloud formation, resulting in a thick cloud deck that covers a large fraction of the dayside hemisphere centred on the substellar point (e.g. Yang et al., 2013; Boutle et al., 2017; Sergeev et al., 2020). The equatorial jet advects the high clouds downstream, creating an asymmetry in the high-cloud cover that impacts the vertical extent of convective clouds (Boutle et al., 2017). Figure 3.2 shows that deep convection occurs around the substellar point and falls off radially. Furthermore, deep convective mixing tends to occur more intensely westward of the substellar point, coincident with a source of gravity waves (Cohen et al., 2022). Due to a decreasing depth of convection as a function of radial distance from the substellar point, lower-altitude clouds become more frequent (Boutle et al., 2017; Sergeev et al., 2020).

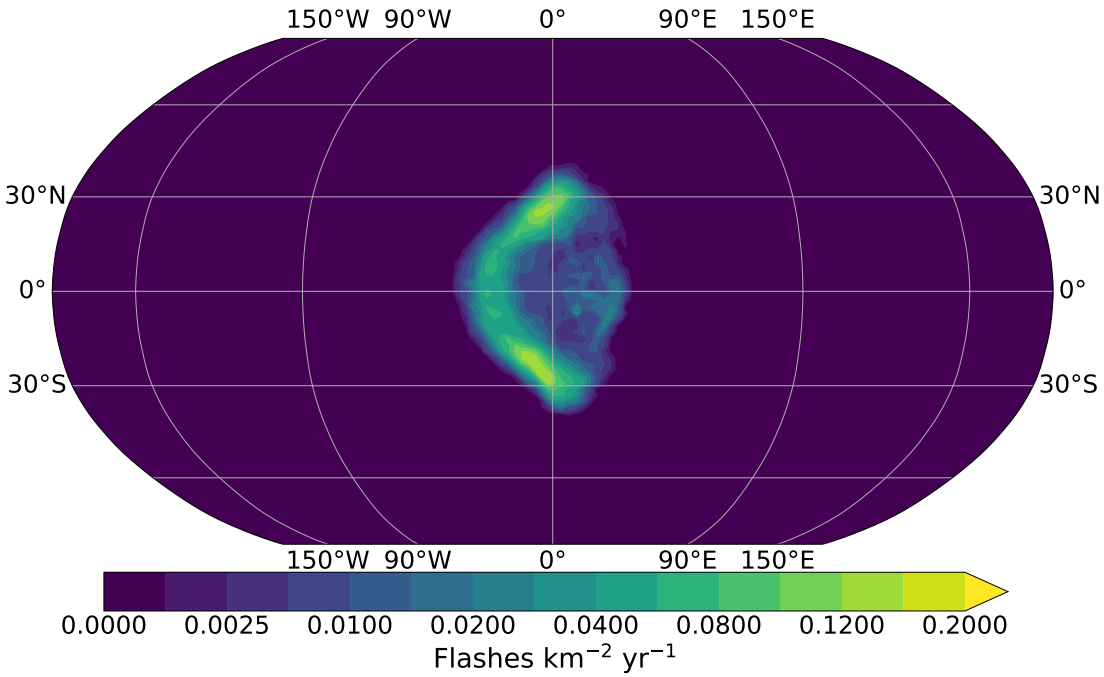

Figure 3.3: Annual lightning flash rates on Proxima Centauri b, following parametrizations shown in Equation 3.1 (Price & Rind, 1992; Luhar et al., 2021). The mean of 120 days was taken from the high-frequency flash rate output and subsequently scaled to annual rates.

3.3.2 Lightning Flash Rate Estimates

From Earth, we expect lightning flashes to occur mainly in regions of vigorous convective activity and hence where high clouds develop, as is also evident from Equation 3.1. Figure 3.3 shows that, using the parametrization in terms of cloud-top height, lightning flashes are indeed concentrated around the region of deep convective activity, associated with surface heating over the substellar point. The asymmetry in the vertical extent of convective cloud cover results in a crescent-like shape with rates of up to 0.16 flashes km^{-2}yr^{-1}. This LFR is generally lower than observed values over the Earth's oceans, where LFRs reach values of up to $\sim$0.01 flashes km^{-2}day^{-1} (or $\sim$3.65 flashes km^{-2}yr^{-1}; Han et al. 2021). Accounting for the impacts of coastal regions and islands on oceanic flash rates on Earth (e.g. Williams et al., 2004; Liu et al., 2012), I retrieved the original LIS/OTD datasets on observed LFRs on Earth (Cecil et al., 2014). This was used to determine LFRs over parts of the oceans that are island-free, and resulted in LFRs between 0.11–0.57 flashes km^{-2}yr^{-1}. Hence, my findings for Proxima Centauri b fall into the lower end of this range.

To understand why LFRs for Proxima Centauri b are at the lower end of oceanic flash rates on Earth, I plot the convective cloud depths for Proxima Centauri b in Figure 3.4. The convective cloud depths are based on the analysis of output at a high temporal resolution (4 minutes) for 10 days of the simulation, giving us over 4×10^6 data points over the entire planetary surface. Cloud depths extend up to 15.7 km in altitude for Proxima Centauri b. For the oceanic

regions in the tropics on Earth, clouds extend up to 17 km (Dessler et al., 2006; Bacmeister & Stephens, 2011). This suggests that the convection driving the formation of these clouds is weaker on Proxima Centauri b, resulting in a lower LFR. Besides that, Proxima Centauri b (T_{surf}∼291 K) is generally cooler than Earth, even without the continents (T_{surf}∼300 K). Atmospheric temperatures are generally also lower, resulting in a drier atmosphere and thereby limiting cloud formation and the initiation of lightning. As discussed below, the flash rates and the extended structures we see around the substellar point have a significant effect on the atmospheric chemistry of Proxima Centauri b, and more generally on similar tidally locked planets.

3.3.3 Ozone Chemistry

I use the refined spectral flux distribution as shown in Table 3.3 to simulate the atmospheric chemistry of Proxima Centauri b, and report the results as 120-day means after 20 years of spin-up from initial conditions. Figure 3.5 shows the hemispheric mean volume mixing ratios (VMR) of ozone as a function of altitude, corresponding to the three different chemistry schemes described in Table 3.2. In all three cases, incoming stellar radiation is sufficient to establish and maintain an ozone layer, initiated by the Chapman mechanism (Chapman, 1930). This mechanism can be summarized by five chemical reactions:

$$O_2 + h\nu \longrightarrow O(^3P) + O(^3P), \quad \text{(R1)}$$
$$O(^3P) + O_2 + M \longrightarrow O_3 + M, \quad \text{(R2)}$$
$$O_3 + h\nu \longrightarrow O_2 + O(^3P), \quad \text{(R3)}$$
$$O_3 + h\nu \longrightarrow O_2 + O(^1D), \quad \text{(R4)}$$
$$O_3 + O(^3P) \longrightarrow O_2 + O_2. \quad \text{(R5)}$$

Reaction R1 initiates the production of ozone and R5 represents the termination step for the Chapman mechanism. Reactions R2–4 describe the rapid interchange between $O(^1D)$, $O(^3P)$, O_2 and O_3. Furthermore, $O(^1D)$ is de-excited following the interaction with N_2, O_2 and CO_2.

Figure 3.5 shows that the Chapman mechanism results in the thickest ozone layer, peaking at 40–60 km with VMRs of 43 and 47 ppm on the dayside and nightside, respectively. The dayside ozone profile peaks at a lower VMR and a lower altitude (∼48 km) compared to the nightside peak at ∼60 km due to active photochemistry on the dayside. $O(^3P)$ is still transported to the nightside with the prevailing high-altitude horizontal winds. Combined, there is less photolysis of ozone through reactions R3 and R4 and the shifted balance between R2 and R5 determine the higher nightside VMR at altitudes above ∼50 km. Compared to Yates et al. (2020), the refined bin distribution of the stellar spectra, described above, generally results in an increase in radiation with wavelengths <240 nm and consequently a twenty-fold increase in O_2 photolysis rates and increased ozone VMRs. Further details of this comparison

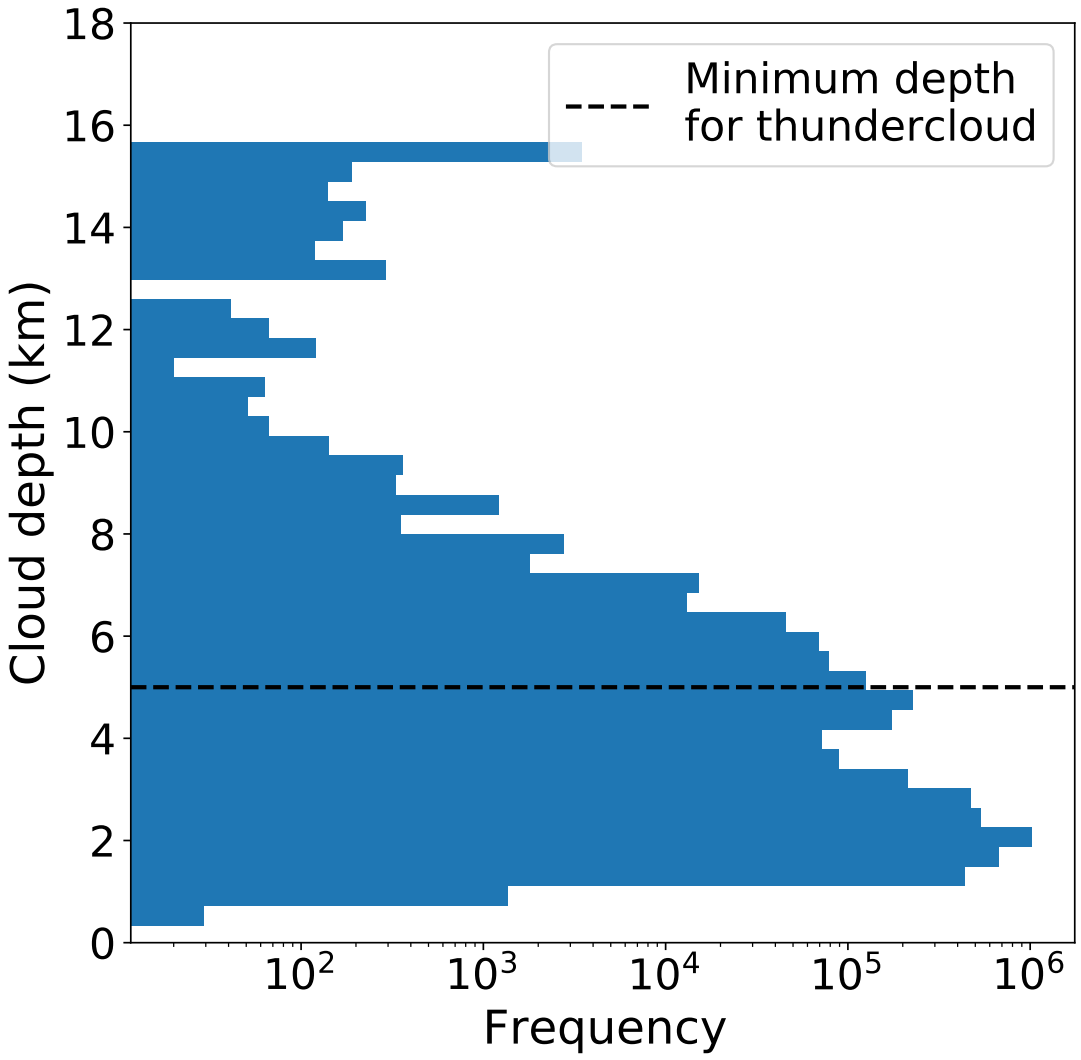

Figure 3.4: Convective cloud depths for Proxima Centauri b from 10 days of simulation at a high temporal resolution of 4 minutes. Depths were calculated as the difference between the convective cloud top and convective cloud base. Also indicated is the threshold for the classification of a thundercloud in the lightning scheme, as described in Section 3.2.4.

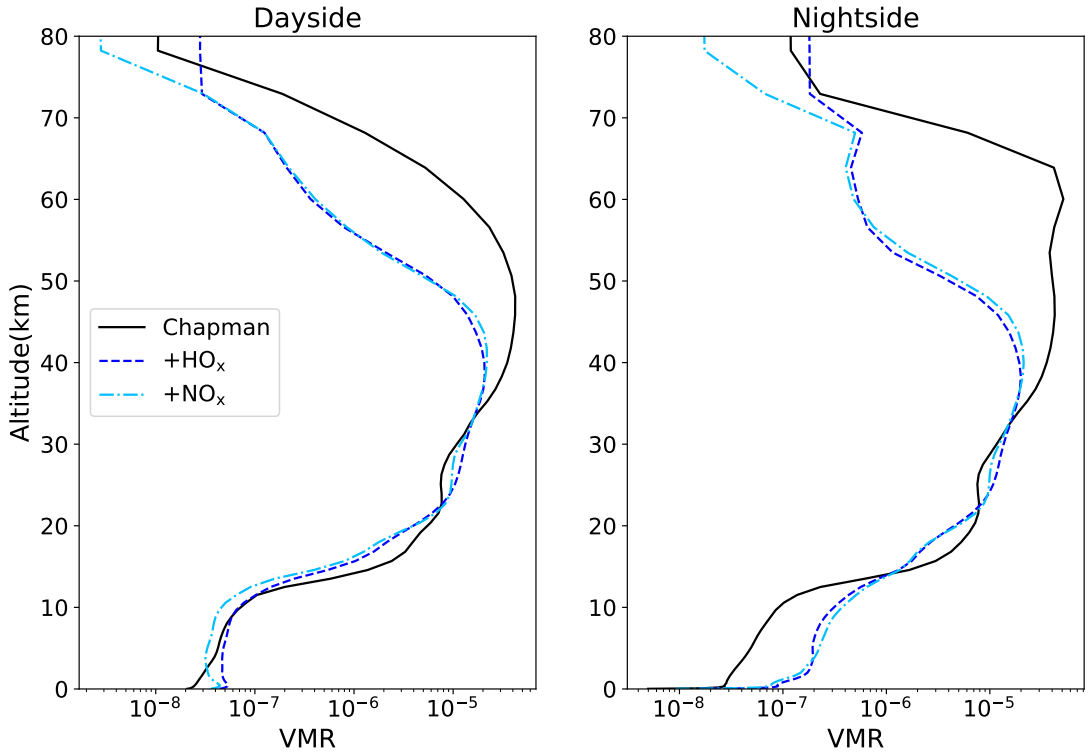

Figure 3.5: Hemispheric mean vertical ozone VMR profiles (mole mole^{-1}) for different chemical schemes (Table 3.2). The left and right panels show the day- and nightside hemisphere respectively.

are described in Section 3.3.4. The relatively high ozone VMR enhances transport of heat to the nightside, which increases the nightside surface temperature especially at the location of the cold traps, consistent with Yang and Abbot (2014) and the simulations from Boutle et al. (2017) for an Earth-like atmospheric composition. The increased nightside temperatures result in similar dayside and nightside ozone vertical profiles.

On Earth, several catalytic cycles destroy stratospheric ozone (e.g. Grenfell et al., 2006). In this study, I consider two cycles that involve HO_x and one that involves NO_x driven by lightning. The two HO_x cycles are:

HO_x cycle 1:

$$H_2O + O(^1D) \longrightarrow 2OH, \quad \text{(R10)}$$

$$OH + O_3 \longrightarrow HO_2 + O_2, \quad \text{(R11)}$$

$$HO_2 + O_3 \longrightarrow OH + 2O_2, \quad \text{(R12)}$$

$$OH + HO_2 \longrightarrow H_2O + O_2, \quad \text{(R13)}$$

and

HO_x cycle 2:

$$H_2O + h\nu \longrightarrow OH + H, \quad \text{(R14)}$$

$O(^3P) + OH \longrightarrow O_2 + H,$ (R15)

$H + O_2 + M \longrightarrow HO_2 + M,$ (R16)

$HO_2 + O(^3P) \longrightarrow OH + O_2$ (R17)

$H + O_3 \longrightarrow OH + O_2,$ (R18)

$OH + HO_2 \longrightarrow H_2O + O_2.$ (R13)

These catalytic cycles are a consequence of water vapour in the atmosphere. Following $O(^1D)$ production from the photolysis of ozone in reaction R4, the oxidation of water vapour in reaction R10 initiates HO_x cycle 1 describing OH-HO_2 cycling, as previously studied by Yates et al. (2020). The second HO_x cycle is initiated by the photolysis of water vapour and describes H-OH-HO_2 cycling.

Figure 3.6 shows hemispheric mean reaction rates (molecules cm^{-3} s^{-1}) as a function of altitude on the dayside and nightside of the planet, for the Chapman+HO_x+NO_x chemistry scheme. Using these rates, we can identify which reactions are most important throughout the atmosphere. The initiation (R1) and termination (R5) reactions of the Chapman mechanism are shown as solid lines. The reaction rate associated with oxygen photolysis (R1) mostly occurs on the dayside (nightside rates reflect those determined by scattered daytime radiation at the terminators) and falls off rapidly with decreasing altitude after the maximum in the ozone layer at 40 km. The peak rate of R5 between $\sim$19 km and $\sim$50 km reflects the coincident altitude of the simulated ozone layer (Figure 3.5) and a peak in $O(^3P)$ production from ozone and oxygen photolysis. On the dayside between $\sim$19 and $\sim$38.5 km, I find that ozone loss is dominated by reaction R5. The lower nightside rate of R5 follows from the dependence on photolysis reactions producing $O(^3P)$. Generally, nightside mean reaction rates are weaker than dayside mean reaction rates (Figure 3.6) due to the absence of stellar radiation and due to the slower progression of chemical reactions in the lower temperatures of the nightside hemisphere.

Including the HO_x catalytic cycles decreases the dayside and nightside peaks in the ozone layer to 21 and 20 ppm, respectively (Figure 3.5), and moves them to lower altitudes. Both HO_x cycles lead to the consumption of odd oxygen molecules ($O(^3P)$ and/or O_3), resulting in a significant depletion of the ozone layer above $\sim$38.5 km compared to the Chapman-only scheme (Figure 3.5). The reaction rate of R1 increases between $\sim$20–30 km when adding in the HO_x chemistry, due to lower overhead ozone abundances and thus less UV shielding, resulting in a higher ozone VMR at these altitudes. The dotted lines in Figure 3.6 correspond to HO_x cycle 1, for which R10 is the initiation reaction. Reactions R11 and R12 denote the propagation steps responsible for the catalytic destruction of ozone, and reaction R13 denotes the termination step. The net effect of this OH-HO_2 cycling is the consumption of two ozone molecules. I find that this catalytic cycle dominates ozone loss in the lower atmosphere of this tidally locked M-dwarf planet, in agreement with previous studies (Yates et al., 2020).

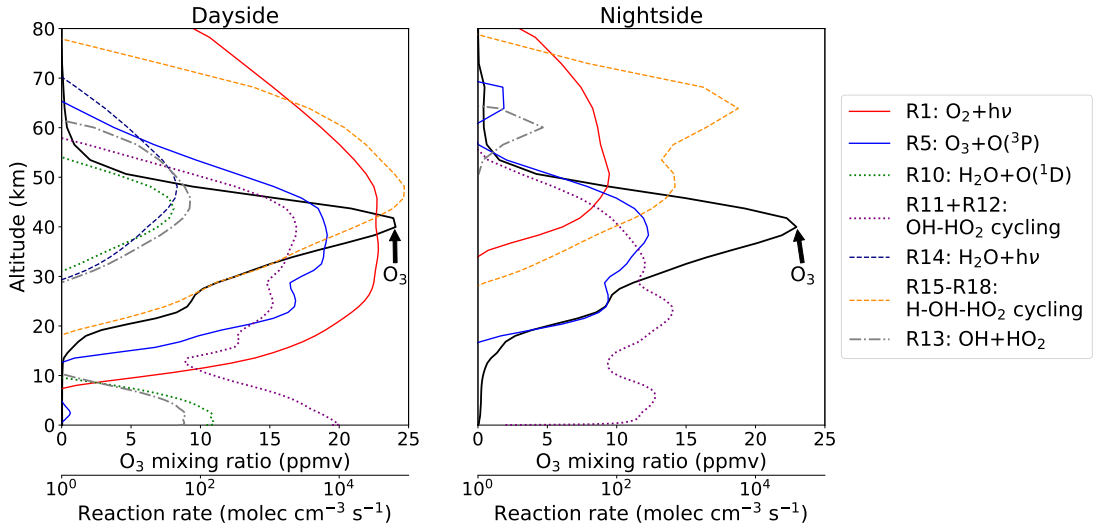

Figure 3.6: Dayside and nightside reaction rates (molecules cm^{-3} s^{-1}) and the corresponding ozone profile (VMR) in black using the improved spectral flux distribution. Results are from my third experiment, including the Chapman mechanism and HO_x and NO_x chemistry. Solid, dotted, and dashed lines denote reaction rates relevant to the Chapman mechanism, HO_x cycle 1, and HO_x cycle 2, respectively. The common termination reaction (R13) for both HO_x cycles is plotted as a dash-dotted line.

From the purple dotted line in Figure 3.6, I find that the propagation reactions R11 and R12 dominate below ∼19 and ∼30 km on the dayside and nightside, respectively. As described above, the termination step from the Chapman mechanism dominates ozone loss between ∼19 and ∼38.5 km on the dayside.

Above ∼38.5 km, HO_x cycle 2 begins to dominate, as can be seen from the dashed lines in Figure 3.6. In terms of increasing altitude, HO_x production is initially a combination of the oxidation (R10) and photolysis (R14) of water vapour. Above ∼44 km, H_2O photolysis dominates. In this cycle, both reactions R15 and R16 have to happen to convert OH into HO_2, and the cycle will then be completed by reaction R17 converting HO_2 back into OH. Another pathway is R15 for the conversion of OH to H followed immediately by R18 to return OH, completing the H-OH-HO_2 cycling. For the sake of readability, I combine these steps by plotting the sum of reactions R15, R16, R17 and R18 in Figure 3.6. I find that the propagation steps for H-OH-HO_2 cycling dominate above ∼38.5 km on the dayside. The common termination step for the two HO_x cycles is R13 (Figure 3.6). The reaction rates associated with the propagation reactions from both cycles can be up to 1000 times higher than the termination or the initiation steps (e.g. at 55 km). This means that one OH molecule can participate in these ozone-depleting catalytic cycles as many as 1000 times, before being removed by the termination step.

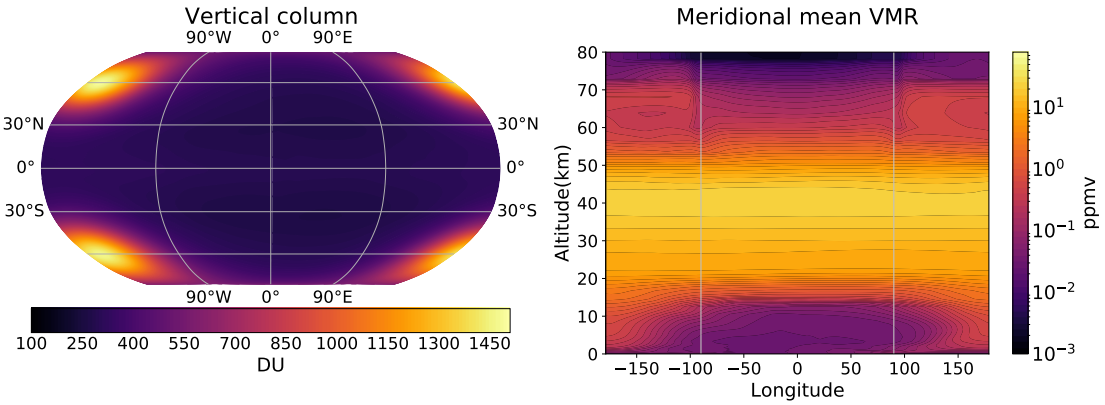

Figure 3.7: Spatial distribution of O_3 around the planet, for my third experiment in Table 3.2. The panel on the left shows the vertical column densities in DU. Right-hand side panels show the meridional mean VMR (mean over latitude) as a function of longitude and altitude. Relative depletion on the dayside and accumulation of O_3 in the nightside cold traps (centred at ∼150°W) is clearly seen.

On the nightside, the weak O_2 (see R1 in Figure 3.6) and O_3 photolysis resulting from scattered radiation at the terminator limit the formation of atomic oxygen. Consequently, advection from the dayside determines the abundance of $O(^3P)$ and OH, leading to significantly smaller nightside abundances. As a result, reaction rates can be decreased by a factor of 100 (e.g. the HO_x propagation steps, R11, R12, R15-R18) to 100,000 (R10). Below ∼20 km, only small amounts of ozone (tens of ppbs) are found, resulting from relatively weak oxygen photolysis, losses due to deposition, and the effectiveness of HO_x cycle 1 in the troposphere (0–20 km).

The net result of the Chapman mechanism and HO_x cycles is a 3D ozone distribution similar to previous work (Yates et al., 2020), shown in Figure 3.7. However, the corrected spectral distribution of stellar radiation leads to larger ozone production across the planet. Ozone column densities are as thin as 269 Dobson Units (DU, where 1 DU$=2.687 \times 10^{20}$ molecules m^{-2}) on the dayside and peak at 1490 DU over the nightside Rossby gyres located at midlatitudes and centred at ∼150°W (Figure 3.7). This increased thickness is caused by the Rossby gyres trapping air, which is subsequently exposed to extensive radiative cooling (so-called cold traps). Due to this cooling, the atmosphere reduces in thickness locally, transporting the ozone in the column down to the troposphere thereby increasing the column abundance (Yates et al., 2020). The mean reaction rates associated with the HO_x cycle are up to 100 times smaller on the nightside below ∼20 km. Combined, these two effects lead to higher nightside ozone abundances at these altitudes (Figure 3.5).

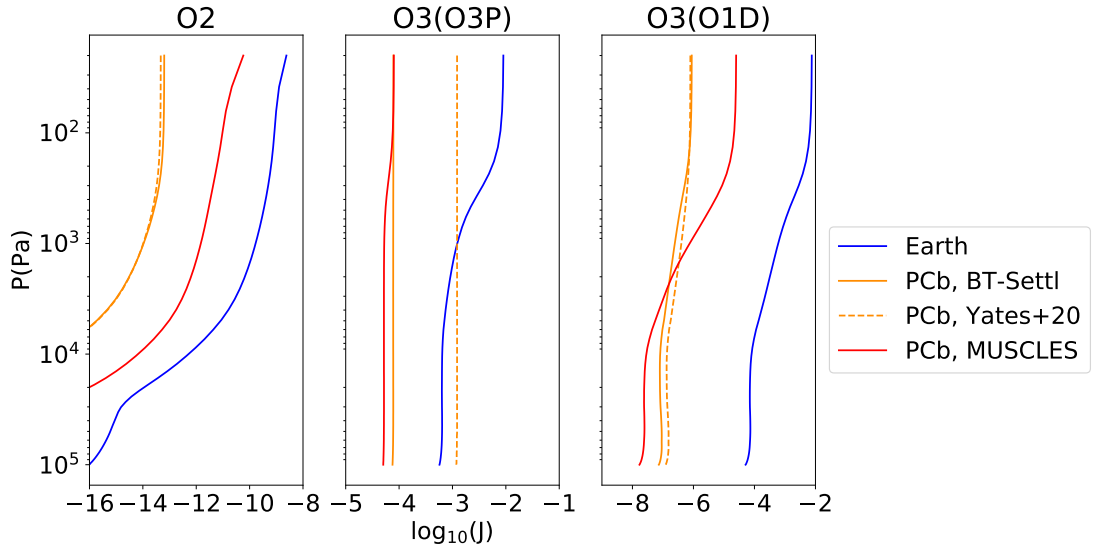

Figure 3.8: Photolysis rates (J, in s^{-1}) as computed with Fast-JX offline runs. Every run corresponds to 1-D column in an atmosphere assuming Earth-like conditions (e.g. O_3 layer, P-T structure, etc.). The only change between the runs is the stellar flux distribution.

3.3.4 Sensitivity of Ozone Chemistry to Stellar Spectra

The application of different stellar spectral energy distributions in this study (see Figure 3.1) and the comparison with Yates et al. (2020) allow for an assessment of the sensitivity of ozone chemistry to stellar spectra. As can be seen in Figure 3.1, the BT-Settl spectrum represents a quiescent M-dwarf with minor UV output. The MUSCLES spectrum provides a better representation of the UV output from M-dwarfs, though it does not account for time-dependent stellar activity. To quantify the impact of UV fluxes on the ozone distribution, Figure 3.8 shows the photolysis (or J-) rates as calculated by Equation 2.30 for reactions R1 (O_2 photolysis), R3 (O_3 photolysis into O(^{3}P)) and R4 (O_3 photolysis into O(^{1}D)). The photolysis rates have been calculated using the offline version of Fast-JX (Wild & Prather, 2000; Bian & Prather, 2002), under the assumption of an Earth-like atmosphere (O_3 layer, P-T structure, cloud distributions, etc.). The Earth-like parameters were kept unchanged for the sake of comparison as well as computational efficiency, while only changing the stellar flux distributions according to the spectra shown in Figure 3.1. The photolysis rate is calculated in each of the 18 wavelength bins, with a λ_{min} and λ_{max} corresponding to each of the bins, as described in Bian and Prather (2002) and shown for most bins in Figure 3.1.

First, the blue lines indicate the J-rates for the flux that Earth receives, and have been validated in intercomparison studies (e.g. Chipperfield et al., 2010). The two orange lines in Figure 3.8 both correspond to BT-Settl spectra for Proxima Centauri b. The dotted line shows the photolysis rates for the rebinning of fluxes by Yates et al. (2020), while the solid line shows the improved rebinning for BT-Settl. The J-rates for O_2 and O_3(O^1D) are similar between the

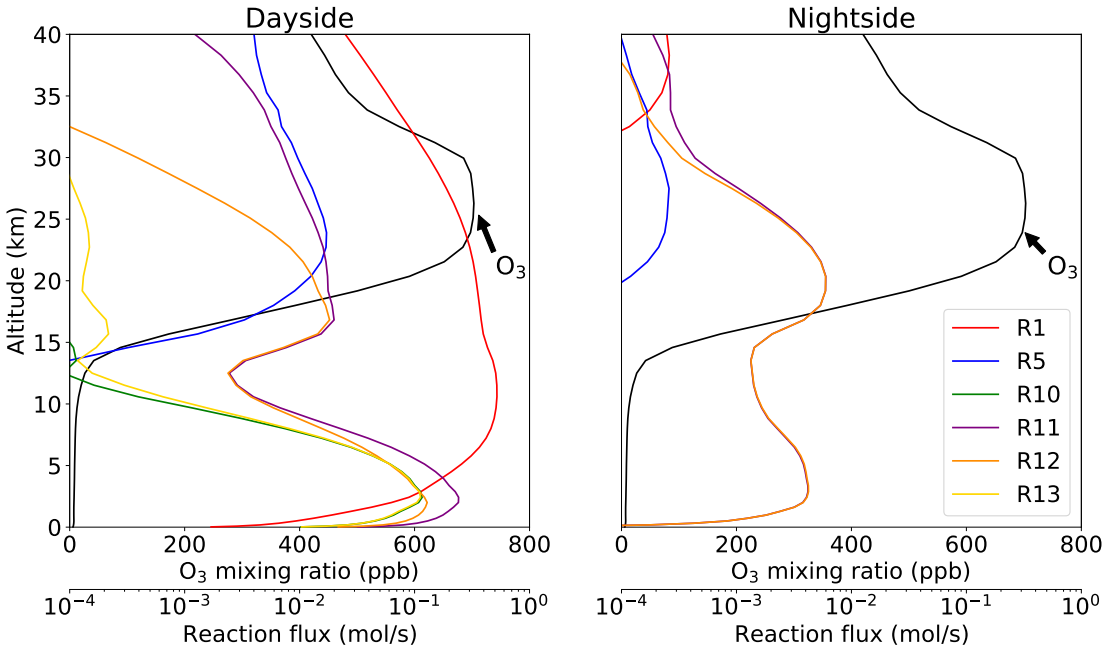

Figure 3.9: Reaction rates and ozone profile using the spectral flux distribution as presented in Table 2 of Yates et al. (2020). Can be compared to the lower row of their figure 2. Note that the numbering of chemical reactions is different.

two cases, but $O_3(O^3P)$ photolysis was a factor 10 stronger in the models from Yates et al. (2020). As described in Section 3.2.3, this is caused by their extension of the upper limit of bin 18. The improved BT-Settl spectrum results in an ozone layer peaking at ∼1360 ppb (see Figure 3.10), two times as high as the value found by Yates et al. (2020) (see Figure 3.9).

Basing the approach on observations, substituting the MUSCLES spectrum provides us with more flux in the UV regions important for O_2 photolysis. Consequently, the red line in Figure 3.8 shows that $J(O_2)$ is ∼100–1000 times higher than for the BT-Settl spectrum, still falling short by a factor of ∼100 as compared to a solar spectrum at Earth's orbit. O_2 photolysis for the MUSCLES spectrum is mainly driven by the stellar flux in the Schumann-Runge bands through bins 3 and 5 and the flux in bin 10 at wavelengths of 221.5–233 nm (see Figure 3.1). For both the BT-Settl and a Solar spectrum, fluxes at wavelengths of 215.5–240 nm are predominantly driving O_2 photolysis. This illustrates the impact of the relatively flat MUSCLES spectrum as seen in Figure 3.1. Nevertheless, the ozone layer of Proxima Centauri b peaks at a higher VMR (∼21 compared to ∼12 ppm on Earth: Seinfeld and Pandis (2016)), since O_3 photolysis rates are significantly lower. $J(O_3)$ is lower than the BT-Settl values for $P < 10^2$ Pa, which is caused by the respective flux distributions in bins 12–15. For MUSCLES, the flux in bin 12 (291–298.3 nm) is higher, whereas the fluxes in BT-Settl bins 13–15 (298.3–320.3 nm) are higher. The impact on the O_3 layer is in broad agreement with the results from Chen et al. (2019), who also find a thinner O_3 layer for a quiescent M-dwarf as compared to UV irradiation from an active M-dwarf and enhanced Solar spectrum.

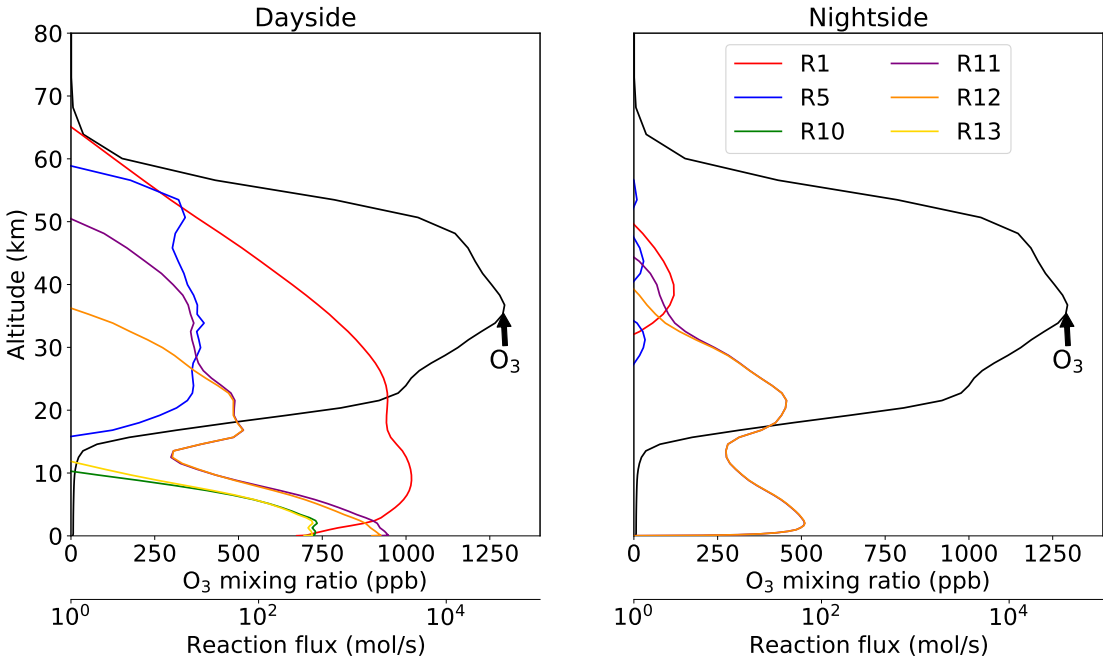

Figure 3.10: Reaction rates and ozone profile using the improved spectral flux distribution (Bian & Prather, 2002) for the BT-Settl spectrum. Results shown are from using the Chapman mechanism and basic HO_x chemistry. Can be compared to Figure 3.9 and the bottom panels of figure 2 in Yates et al. (2020).

3.3.5 Lightning-induced NO_y Chemistry

The third experiment focuses on NO_y chemistry in the lower atmosphere (<20 km), where lightning is the only source of NO at 216 moles NO per flash, and is denoted 'NO_x' in Table 3.2 and Figure 3.5. The magnitude and distribution of these flash rates are described in Section 3.3.2 and shown in Figure 3.3. The resulting distribution of lightning-produced NO can initiate catalytic cycles that result in the loss of ozone and consist of the following reactions:

$$NO + O_3 \longrightarrow NO_2 + O_2 \quad \text{(R19)}$$

$$NO_2 + h\nu \longrightarrow NO + O(^3P) \quad \text{(R20)}$$

$$NO_2 + O_3 \longrightarrow NO_3 + O_2 \quad \text{(R21)}$$

$$NO_3 + h\nu \longrightarrow NO_2 + O(^3P) \quad \text{(R22)}$$

$$NO_3 + h\nu \longrightarrow NO + O_2. \quad \text{(R23)}$$

NO quickly reacts with O_3 to form NO_2 (R19). On the dayside, NO_2 can be photolysed back into NO again (R20). Together, they form a first catalytic cycle leading to the destruction of one ozone molecule. With a relatively small abundance of $O(^3P)$ below 20 km, NO_2 is likely to react with O_3 again through reaction R21 to produce NO_3 that is subsequently photolysed to NO_2 (R22) or NO (R23). The photolysis rate for reaction R22 (flux at λ>345 nm) is ~8 times higher than R23 (flux at λ>412.5 nm) for the spectral flux distributions of the Sun and Proxima Centauri. The net result of this second catalytic cycle is the destruction of two ozone

molecules. The termination step in the NO_x is the oxidation of NO_2 by OH:

$$NO_2 + OH + M \longrightarrow HNO_3 + M. \quad \text{(R24)}$$

The reaction rates of R10 and R14 (Figure 3.6) show that OH (and thus HNO_3) production occurs predominantly on the dayside. NO_2 can further react with the NO_3 produced through reaction R21 to form N_2O_5:

$$NO_3 + NO_2 + M \longrightarrow N_2O_5 + M. \quad \text{(R25)}$$

The species HNO_3 and N_2O_5 are more stable and therefore have a relatively long lifetime against chemical loss. Eventually, they are converted back into NO_x, for example, via:

$$HNO_3 + h\nu \longrightarrow NO_2 + OH \quad \text{(R26)}$$
$$N_2O_5 + h\nu \longrightarrow NO_3 + NO_2. \quad \text{(R27)}$$

In the presence of water, N_2O_5 is also converted into HNO_3:

$$N_2O_5 + H_2O \longrightarrow 2\,HNO_3. \quad \text{(R28)}$$

Furthermore, HNO_3 is subject to removal by deposition. On the nightside, the absence of stellar radiation further enhances the lifetime of NO_3, HNO_3 and N_2O_5. Therefore, these species serve as reservoirs for NO_x. The reservoirs and NO_x together form the NO_y family. The tidally locked configuration of Proxima Centauri b provides distinct radiation environments on the dayside and nightside, which leads to a dayside-nightside contrast in NO_x and its reservoirs. A schematic summary of the mechanism that is initiated by NO produced from lightning is shown in Figure 3.11, indicating chemical reactions that only occur on the dayside hemisphere in red.

The dayside-nightside contrast in atmospheric chemistry involving nitrogen species is explored using the hemispheric-mean reaction rates in Figure 3.12. Following the production of NO by lightning, NO_2 is predominantly formed on the dayside of the planet, with the reaction rate that describes the conversion from NO to NO_2 (R19) being about 200 times higher on the dayside than on the nightside. The photolysis of NO_2 (R20) also peaks on the dayside and is smaller by a factor of $\sim$2000 on the nightside. Hence, NO_2 is available for nightside NO_y chemistry, initiated by R21. I also find a strong decrease (10^3–10^4) in nightside rates that describe the photolysis of HNO_3 (R26) and N_2O_5 (R27). Notably, the reaction rate associated with the photolysis of NO_3 in R22 and R23 only triples on the dayside. This is because NO_3 mainly absorbs radiation at wavelengths between $\sim$550 and $\sim$700 nm, which is more likely to be scattered in the planet's atmosphere than shorter wavelength radiation. The reaction rate

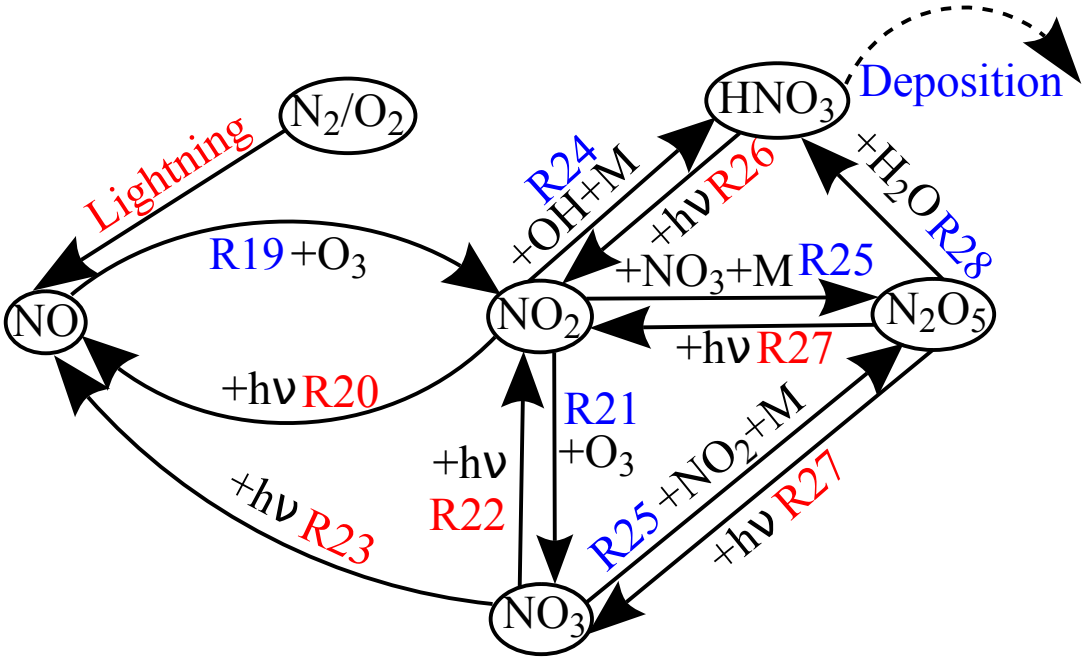

Figure 3.11: Overview of the main chemical reactions that are initiated by lightning-induced NO. Arrows run from the reactant to the product. The chemical reaction is numbered as RXX, corresponding to the main text. Reactions in red only occur on the dayside of the planet, reactions in blue can occur on both hemispheres. HONO, HO_2NO_2, and N_2O are omitted in this diagram but also included in the network.

of R21 is twice as large on the dayside, and oxidation (by O(^{3}P) and OH) further destroys dayside NO_3. The production of N_2O_5 through R25 is $\sim$700 times larger on the nightside. The reaction with water vapour through R28 can again lead to the production of HNO_3. HNO_3 is rapidly removed by dry deposition (DD) and wet deposition (WD), which is stronger on the dayside of the planet due to a higher precipitation rate. Figure 3.12 shows that wet deposition provides a loss term for HNO_3 up to 12 km and dry deposition is limited to the surface. These combined effects of chemistry and deposition on the NO_x reservoirs indicate an accumulation on the nightside.

Figure 3.13 shows the resulting spatial distribution of these important NO_x and NO_y species. Left-hand side panels show the vertically integrated column densities (in molec m^{-2}) of each species, with the wind vectors at an altitude of 6850 m, where the superrotating jet speed is the largest (up to 40 km s^{-1}). The column densities are calculated as the pressure-weighted sum of the number densities in each vertical layer. Right-hand side panels show the meridional mean VMR for each of the species. The first row of Figure 3.13 shows that lightning-induced NO is produced on the dayside, most strongly in the crescent shape determined by the lightning flashes in convective clouds (Figure 3.3). To quantify hemispheric differences, I define a day-to-nightside contrast following Chen et al. (2018) and Koll and Abbot (2016). However, instead of using mean mixing ratios, I use hemispheric mean vertical column densities of species to calculate the relative difference between hemispheres:

$$r_{\mathrm{diff}} = \frac{r_{\mathrm{day}} - r_{\mathrm{night}}}{r_{\mathrm{global}}}, \tag{3.2}$$

where r_{day}, r_{night} and r_{global} are the dayside, nightside and global mean vertical column densities (in molec m^{-2}) of a chemical species, respectively. There is enhanced NO on the dayside of the planet (Figure 3.13) with an associated r_{diff} value of 198%. NO is most abundant between 5.5 and 15 km, with a maximum of 0.117 ppt at 12.5 km. This is a consequence of the parametrization of NO emissions per lightning flash: emitted NO is distributed between 500 hPa and the cloud top, as described in Section 3.2.4. Furthermore, the tidally locked orbit, NO lifetime and wind structure allow for a maximum near the NO emission source. Differences in NO at the eastward terminator between 12–14 km are due to eastward advection and subsequent photolysis of NO_2 lower in the atmosphere (R20). The balance of chemical reactions R19-R23 in a tidally locked configuration determines the vertical column densities of NO, NO_2 and NO_3 (first three rows of Figure 3.13). The lightning-produced NO leads to NO_2 and subsequently NO_3 that spread around the dayside of the planet, following atmospheric transport. NO_3 is rapidly photolysed, releasing NO_2 back. Consequently, NO_2 (r_{diff}=80%) has the largest vertical column densities, peaking at 6.2×10^{16} molecules m^{-2}, westward of the substellar point. We know from reaction R24 that the production of HNO_3 occurs

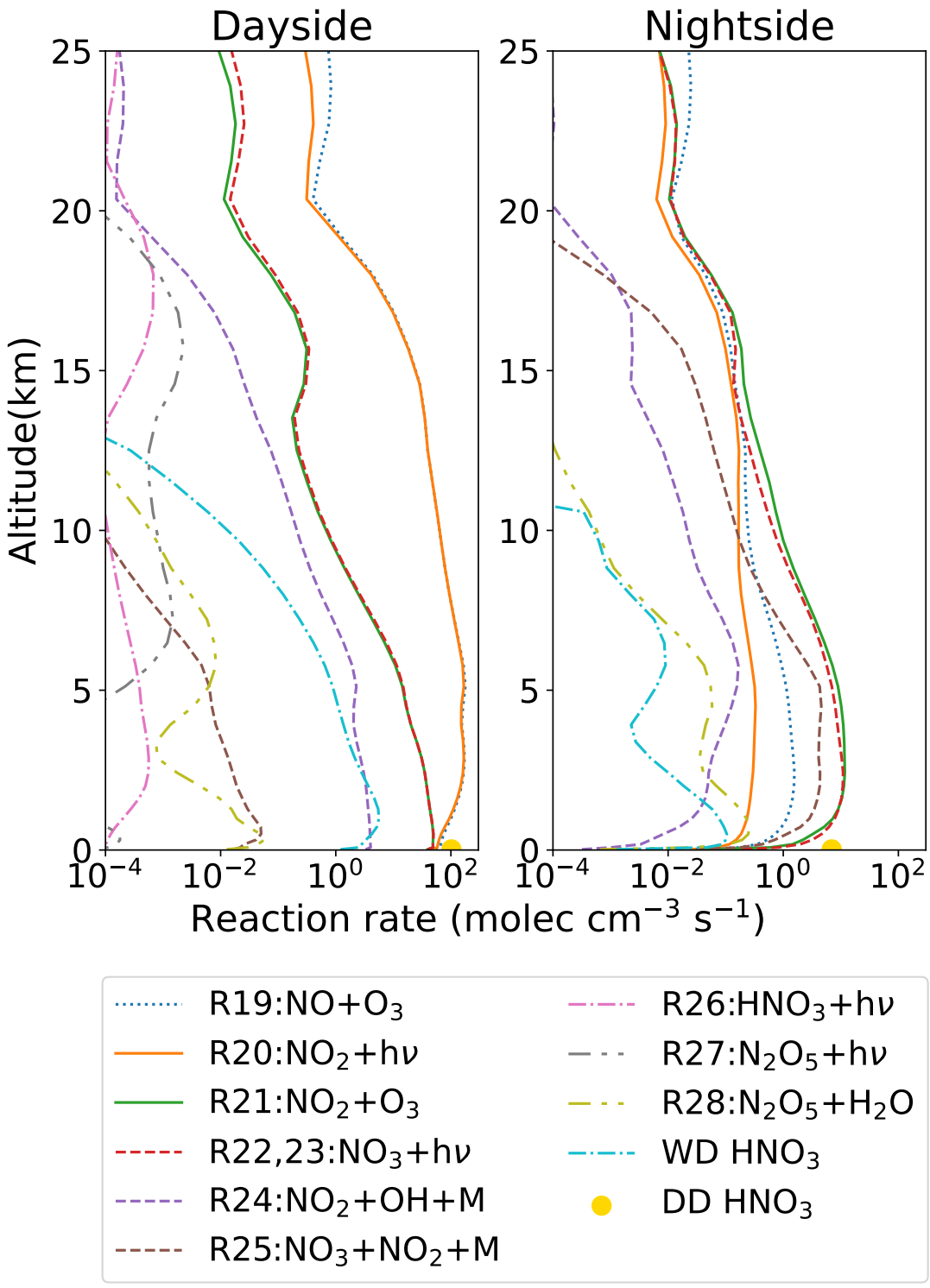

Figure 3.12: Hemispheric mean reaction rates (molecules cm^{-3} s^{-1}) for nitrogen chemistry, below altitudes of 40 km. Reaction numbers are explained in Section 3.3.5 and Figure 3.11. The wet (WD) and dry deposition (DD) of HNO_3 are also shown. Wet deposition occurs up to altitudes of ∼12 km and dry deposition is limited to the surface.

predominantly on the dayside. The decrease in the column density of HNO_3 in Figure 3.13, towards the minimum value of 3.0×10^{15} molecules m^{-2} close to the substellar point, shows that HNO_3 is susceptible to photolysis as well as to wet deposition following cloud formation and precipitation.

In the absence of stellar radiation and lightning flashes, atmospheric chemistry is different on the nightside. Here, the chemistry depends exclusively on the advection of chemical species from the dayside of the planet. This can be seen from the NO_2 and HNO_3 columns aligning with the wind vectors in Figure 3.13, as these species are advected from the dayside to the nightside. This dayside-to-nightside transport of chemical species was also discussed in previous work on terrestrial exoplanets (Chen et al., 2018; Yates et al., 2020) and hot Jupiters (e.g. Drummond et al., 2020). NO column densities are much smaller on the nightside because the source is found on the dayside and because of the absence of photolysis of the other nitrogen-bearing species. Without stellar radiation and with relatively low nightside $O(^3P)$ abundances, the dominant loss pathways for nightside NO_2 result in the production of NO_y reservoir species. The oxidation by O_3 (R21) still produces a significant amount of NO_3. In the absence of stellar radiation, NO_3 and HNO_3 are no longer efficiently destroyed. This results in a much thicker nightside NO_3 column, evident from the r_{diff} of -200% for NO_3, and a slightly thicker mean HNO_3 column on the nightside, with r_{diff}=-8%. HNO_3 has a smaller r_{diff} since it depends on dayside production and is subject to deposition. Nightside NO_2 and NO_3 are sufficiently abundant to initiate the production of N_2O_5 (R25). The fifth row in Figure 3.13 shows that, following the nightside production, N_2O_5 is advected towards the dayside. In doing so, N_2O_5 passes across the western terminator after which it is rapidly destroyed due to photolysis or the reaction with water vapour. The relative depletion of N_2O_5 in the equatorial regions between 90 and 180°E is linked to the same reaction with water vapour (transported from the dayside). The tendency of N_2O_5 to accumulate on the nightside can also be seen from its r_{diff} of -95%. Since the conversion from NO_3, HNO_3 or N_2O_5 back into NO_x involves either photolysis or the interaction with OH, the nitrogen reservoirs (NO_3, HNO_3 and N_2O_5) have an extremely long lifetime on the planet's nightside. It is this accumulation of the reservoir species that is seen by the contrasting dayside and nightside vertical columns in the last three rows of Figure 3.13. It should be stated that while the day-to-night contrasts are big in relative terms, they are small in absolute terms.

Combined, lightning-induced NO_y chemistry and the configuration of a tidally locked M-dwarf planet lead to dayside-nightside distinctions. The chemical mechanism in Figure 3.11 summarizes the main reactions responsible for these distinctions as well as where they occur on the planet, initiated by lightning flashes that produce NO. Lightning and chemical reactions that are limited to the dayside of the planet are shown in red and indicate why the accumulation of reservoir species on the nightside occurs.

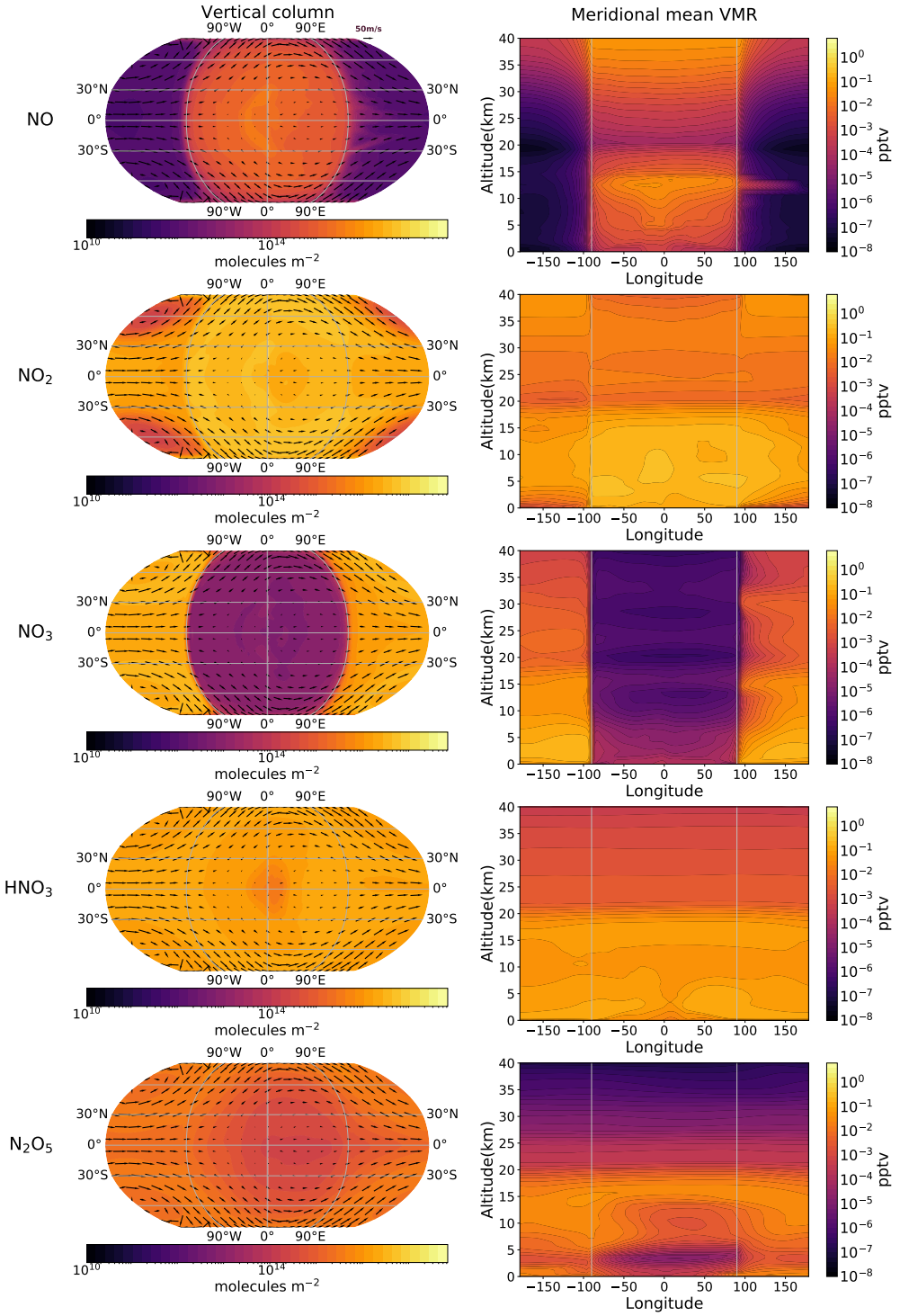

Figure 3.13: Spatial distributions of NO, NO_2, NO_3, HNO_3, and N_2O_5. Left-hand side panels show the vertical column densities calculated from a mass-weighted vertical integral. Furthermore, they show the wind vectors at altitudes of 6850 m, where the superrotating jet speed is the largest. Right-hand side panels show the meridional mean VMR (mean over latitude) as a function of longitude and altitude.

3.4 Discussion

Here I reflect on key uncertainties associated with this study, including 1) the importance of stellar radiation, particularly the UV wavelengths; 2) describing the distribution of LFRs, including the thermal decomposition of chemical species; and 3) the prospects of observing the changes in atmospheric chemistry predicted by these simulations using observations from the James Webb Space Telescope.

3.4.1 The Importance of Photochemistry

Photolytic reactions are the main driver of atmospheric chemistry on M-dwarf planets. The host stars irradiate a large UV contribution to the bolometric flux compared to other stars (Figure 3.1), and therefore many chemical reactions on the orbiting planets are driven by UV radiation.

I use the Fast-JX model to describe photolysis in the 177–850 nm region. The upper limit is based on photons being sufficiently energetic to break molecular bonds (Bian & Prather, 2002). Fast-JX is optimized for the calculation of photolysis rates in the troposphere and stratosphere on Earth, motivating the lower cutoff at 177 nm. Radiation with lower wavelengths is attenuated above the mesosphere (except for O_2 Lyman α absorption at 121 nm). Furthermore, the solar flux falls off precipitously for wavelengths shorter than 177 nm (Figure 3.1). The current assumption of an Earth-like atmosphere on Proxima Centauri b intrinsically assumes attenuation of incoming radiative fluxes at these lower wavelength regions. The MUSCLES spectrum that I use is based on observations, but uncertainties remain. First, the region between 175–200 nm is based on a quadratic fit to the surrounding continuum (Loyd et al., 2016). Besides that, MUSCLES continuum fluxes are often based on the photon-limited noise floor of the data rather than actual measurements of the stellar output, because of the intrinsic faintness of UV radiation from M-dwarfs (Loyd et al., 2016). Future measurements will help to improve the quality and range of the spectra being used, as well as help test the assumption about using an Earth-like atmosphere.

The relation between UV fluxes and photochemistry in 3D simulations of exoplanets has been explored across a range of stellar energy distributions (Chen et al., 2018, 2019) and for time-dependent stellar activity (Chen et al., 2021; Ridgway et al., 2023). Furthermore, 1-D photochemical models have been used to quantify the amount of ozone resulting from different stellar UV distributions (e.g. Segura et al., 2005, 2010; Domagal-Goldman et al., 2014; O'Malley-James & Kaltenegger, 2017; Teal et al., 2022) and alongside varying molecular oxygen abundances (Kozakis et al., 2022). The results in Section 3.3.4 complement these findings by comparing photolysis rates on Proxima Centauri b driven by the MUSCLES and BT-Settl spectra of the host star. I find that the stronger UV flux from the MUSCLES spectrum leads to ozone mixing ratios that are enhanced by a factor of 15. The distinct responses of photolysis rates for O_2 and O_3 (see Figure 3.8) indicate the complexity of these calculations.

As described in Section 3.3.3, the 3D spatial distribution of ozone is broadly similar to Yates et al. (2020). The similarities include a lower dayside mean ozone column (302 DU) as compared to the nightside (483 DU) and a buildup of ozone at the locations of the nightside Rossby gyres, as is also shown in Figure 3.7. Nevertheless, the magnitude of ozone column densities and mixing ratios differs significantly depending on the stellar spectrum used. Therefore, in the case of ozone and agreeing with the findings from Chen et al. (2018), I conclude that the magnitudes of volume mixing ratios are controlled by a balance of photochemical production and destruction. On the other hand, the chemical lifetime of ozone is long enough for the spatial distribution to be controlled by transport processes.

In agreement with Boutle et al. (2017), I find a substantial fraction of the planetary surface on the dayside to be potentially habitable ($\sim$45%), with a temperature exceeding 273.15 K. This fraction could change with the inclusion of ocean heat transport (Hu & Yang, 2014) or ice-albedo feedback, though the latter is shown to play only a marginal role for M-dwarf planets (Shields et al., 2013). Furthermore, a thick ozone layer increases the likelihood that any surface life is protected from harmful UV radiation (e.g. Shields et al., 2016). To quantify this, I compare the UV flux ($\lambda <$320 nm) at 51 km (just above the ozone layer) with the flux at the surface. I find that only 15% reaches the surface levels, after being attenuated by the ozone layer (and water clouds closer to the surface). As mentioned in Section 3.3.1, this amounts to about 0.2% of Earth's surface UV radiation levels. Hence, in line with the results from O'Malley-James and Kaltenegger (2017) for a 1-D model of an 'active' M-dwarf spectrum, the thick ozone layer provides sufficient protection against harmful UV radiation. This ozone layer can also protect against enhanced UV irradiation during stellar flares, although strong flares and the absence of a magnetic field might also produce strong perturbations of the ozone layer (Chen et al., 2021). The perturbing of atmospheric chemistry by the enhanced UV flux and stellar energetic particles from flares is further explored in a separate publication (Ridgway et al., 2023). Lightning may also have played a role in the origin of life, which was shown by the production of amino acids in a reducing atmosphere following electrical discharges in the Miller-Urey experiment (Miller, 1953). However, the formation of organic molecules following lightning is more likely in a reducing atmosphere (e.g. Chameides & Walker, 1981), which would require starting conditions that differ from the assumed oxygen-rich composition.

The motivation for assuming Earth-like atmospheric chemistry in this study was the aim of studying ozone chemistry and the impact of lightning-induced species. The addition of atmospheric chemistry to a 3D GCM significantly increases the computational expense, particularly if, as done here, it is considered self consistently with the radiative transfer and dynamics. Therefore, I have included only the most essential chemical reactions (based on our broader knowledge of the reactions occurring in an Earth-like atmosphere). Moving away from this photochemical regime involves a significant increase in the size of the associated

chemical network that would consequently be difficult to run in a 3D CCM. As such, for this initial study, I used Earth-like atmospheric chemistry. Including accurate and sufficiently small chemical networks that support other photochemical regimes is an important topic for future investigation.

3.4.2 CCM Comparisons

The previous CCM studies of terrestrial exoplanets made use of the CAM-Chem 3D model (Chen et al., 2018) for an atmosphere with 26 levels extending up to 50 km and WACCM (Chen et al., 2019, 2021) for an atmosphere up to 145 km in 66 levels, thus including the thermosphere. The UM-UKCA CCM falls in between this range with 60 levels describing an atmosphere up to 85 km. Other differences in the previous studies include landmasses in the form of Earth's continental distribution (though with the substellar point in the middle of the Pacific Ocean) that can impact the climate (Lewis et al., 2018; Rushby et al., 2020). Chen et al. (2018) use a stellar insolation of 1360 W m^{-2}, compared to 881.7 W m^{-2} used here. The insolation is varied in Chen et al. (2019, 2021), but not to values as low as ours. This study uses a reduced description of atmospheric chemistry, focusing on individual processes, whereas theirs include 97 species connected by 196 reactions (Chen et al., 2018) and 58 species connected by 217 reactions (Chen et al., 2019, 2021). I turned off surface emissions and, as opposed to the earlier work, included wet deposition, potentially further impacting the atmospheric composition. Finally, the aforementioned differences in UV fluxes play a major role in the chemical abundances.

The vertical distribution of ozone in Figure 3.5 can be directly compared to the previous studies. As mentioned before, the observation of a thinner O_3 layer for a weaker stellar UV irradiation is in agreement with Chen et al. (2019). Furthermore, the influence of the HO_x catalytic cycle 1 as a sink for O_3 on tidally locked, Earth-like exoplanets was also found by Yates et al. (2020) and Chen et al. (2018), though not extensively elaborated on in the latter study. The finding of the O_3 sink due to H_2O photolysis and the resulting HO_x catalytic cycle 2 in the upper stratosphere, as described in Section 3.3.3, further expands our knowledge of the impact of HO_x catalytic cycles on tidally locked, Earth-like exoplanets. Chen et al. (2018) find an O_3 layer that peaks at $\sim$10 ppm above altitudes of 30 km (see their figure 3), which agrees roughly with the findings of this study for the HO_x and NO_x cases in Figure 3.5. One notable difference is the decrease that can be seen upwards of 45 km in the simulation of this study, whereas their O_3 abundance seems to stay constant. This difference can be caused by stronger O_3 photolysis in these atmospheric layers and above, in this case. The inactive stellar spectra in Chen et al. (2019) result in more reduced ozone at $\sim$0.1 ppm (see their figure 5). A potential cause of this is the increase of the model-top to 145 km (Chen et al., 2019). The ozone abundance for a planet orbiting a pre-flare M star in Chen et al. (2021) peaks at a few ppm again.

As discussed in Section 3.2.1 I performed this study, focusing on lightning and the time-averaged irradiation, alongside a complementary study focusing on stellar flares (Ridgway et al., 2023). These two studies used the same underlying model, the UM, but differing photolysis and chemistry schemes which provided an excellent mechanism to increase confidence in the robustness of the model setups.

Inter-model differences can have a wide range of causes. Firstly, the exact impact of photochemistry is influenced by the choice of stellar spectra, the extent of wavelength ranges and the specific distribution of fluxes over wavelength bins. Next to that, the complexity of the chemical network (as well as reaction rate constants), initial chemical abundances, treatment of dry and/or wet deposition and the potential inclusion of surface emissions can alter the resulting atmospheric composition. Finally, the vertical extent of the atmosphere and the possible inclusion of landmasses affect dynamics and thus the chemistry directly and indirectly. The inter-model differences and variety of potential causes motivate the need for further model intercomparisons for CCMs, as mentioned by (Cooke et al., 2023b) and following those done for 3D GCM simulations of TRAPPIST-1e assuming static atmospheric compositions (the THAI project, Fauchez et al., 2022; Sergeev et al., 2022b; Turbet et al., 2022).

3.4.3 Parametrizing Lightning

Atmospheric lightning is a complex physical phenomenon that is observed on Earth and other Solar System planets (e.g. Aplin, 2006; Hodosán et al., 2016), but is difficult to model explicitly, partly due to the uncertainties associated with the small-scale processes that initiate lightning. To keep the process tractable within a GCM, lightning parametrizations have been developed in terms of different convection parameters (e.g. Allen & Pickering, 2002; Finney et al., 2014; Etten-Bohm et al., 2021; Stolz et al., 2021), but the parametrization in terms of cloud-top height remains the most used in CCMs for Earth (Luhar et al., 2021).

The occurrence of lightning on Earth is generally higher than on the giant planets or Venus (Hodosán et al., 2016). Nevertheless, the processes of charging of cloud particles, charge separation due to gravitational settling and the buildup of electrostatic potential differences that lead to discharges are expected to remain the same, and the electric field breakdown does not strongly depend on the chemical composition of the atmosphere (Helling et al., 2013; Helling, 2019). Simulating an Earth-like atmosphere on a tidally locked exoplanet further supports the assumption of a similar process for the emergence of lightning discharges. The lightning parametrization I use in terms of cloud-top height (Equation 3.1) is evaluated successfully for Earth and based on the fundamental laws of electricity (Vonnegut, 1963; Williams, 1985), as described in Section 3.2.4. Therefore, it is reasonable that this parametrization will also deliver reasonable LFRs for an Earth-like exoplanet, although I acknowledge that the coefficients used in Equation 3.1 have been tuned to match observed LFRs on Earth (Price &

Rind, 1992; Luhar et al., 2021) and therefore could represent a potential error. Nevertheless, the distribution of LFRs on the tidally locked exoplanet (Figure 3.3) makes physical sense and is consistent with the predictions of a thick convective cloud deck covering the dayside of the planet (see e.g. Yang et al. 2013; Boutle et al. 2017; Sergeev et al. 2020 and Figure 3.2).

The effect of decreasing LFR with lower atmospheric temperature was described in Section 3.3.2. To predict the effects of climate change on the initiation of lightning, several studies have investigated the effects of a higher atmospheric temperature, but no consensus has been reached based on the different parametrizations (Clark et al., 2017). On the one hand, a higher temperature leads to fewer ice clouds and therefore fewer mixed-phase collisions, limiting the number of lightning flashes and NO_x produced by them (e.g. Finney et al., 2018). On the other hand, the depth of convection and precipitation rate increase in a warming climate, potentially increasing the number of lightning flashes (e.g. Banerjee et al., 2014). The response of lightning initiation to changes in the atmospheric pressure is complex due to the competing effects of clouds, pressure broadening, heat capacity, lapse rate, and relative humidity, as shown by Zhang and Yang (2020) for a tidally locked planet. To build upon these results, further simulations of the initiation of lightning are currently being conducted, in a range of atmospheric conditions and using an improved description of the electrification process, following the high-resolution simulations of tidally locked exoplanets by Sergeev et al. (2020).

Another factor of uncertainty is the thermal decomposition of chemical species following a lightning discharge. The species affected by thermal decomposition will depend on the ambient atmospheric composition (Harman et al., 2018; Helling, 2019). This is further illustrated by studies of lightning-induced chemistry on Venus and Mars (Nna Mvondo et al., 2001) and Early Earth (Chameides & Walker, 1981; Navarro-González et al., 2001; Ardaseva et al., 2017). Since I simulate a background composition dominated by N_2 and O_2, thermal decomposition of these species and subsequent NO production, following the Zel'dovich mechanism (Zeldovich et al., 1947), is a reasonable expectation. The exact amount of NO produced per flash is uncertain on Earth (e.g. Schumann & Huntrieser, 2007; Miyazaki et al., 2014; Bucsela et al., 2019; Allen et al., 2021a; Allen et al., 2021b), and is related to unknowns in the distinction between CG and IC flashes and dependencies on e.g. peak current, channel length, rate of energy dissipation and the number of strokes per flash (Murray, 2016; Luhar et al., 2021). I performed a sensitivity calculation in which the NO production was increased to 830 moles NO per flash, which did not result in significant changes to the spatial distribution of NO_y as shown in Figure 3.13. Harman et al. (2018) show that NO production rates from lightning on temperate terrestrial planets with N_2-O_2-CO_2 atmospheres will stay within an order of magnitude of the rate on Earth. Other sources of NO include stellar flares and coronal

mass ejections through enhanced UV flux and energetic particles (Segura et al., 2010; Chen et al., 2021; Ridgway et al., 2023), volcanic eruptions (von Glasow et al., 2009), and cosmic rays (Scalo et al., 2007), and their combined effects alongside lightning have to be studied in future work.

Comparing my results to the 1-D models of Ardaseva et al. (2017) and Harman et al. (2018), I find a much smaller impact of lightning-induced NO_x on atmospheric chemistry, explained by three major differences. First, flash rates up to 5×10^4 flashes $\mathrm{km^{-2}hr^{-1}}$ are used by Ardaseva et al. (2017) and both 1-D models assume global thunderstorms emitting NO throughout the atmosphere, resulting in an increased magnitude and spatial extent of flash rates. Second, I find NO from lightning confined to the lower 20 km of the atmosphere, whereas NO has a strong impact up to $\sim$80 km for Ardaseva et al. (2017) and Harman et al. (2018). Lastly, the effect of lightning-induced NO on the distribution of O_2 and ozone strongly depends on catalytic cycles following the photolysis of CO_2 (Harman et al., 2018), and future work will be directed to analysing these effects in a 3D CCM. This will be part of a wider investigation of exoplanet atmospheric chemistry and physics such as lightning in the context of different atmospheric composition and mass, following GCM simulations such as Turbet et al. (2016) and Paradise et al. (2021). Through the variation of atmospheric mass, we can take into account the potential effects of stellar wind-driven escape (Airapetian et al., 2020).

3.4.4 Observational Prospects

Lightning discharges are known to emit both optical (e.g. Borucki et al., 1985) and radio signals (e.g. Zarka et al., 2004). Our limited knowledge of lightning across the Solar System indicates the difficulties of detecting this phenomenon on other planets. Therefore, direct detection of exoplanetary lightning will be difficult with current observing technology. However, as described in Section 3.3.5, lightning produces NO that will subsequently result in a cascade of perturbed chemical reactions. Among the lightning-induced chemical species, NO, NO_2, N_2O and HNO_3 are known to have absorption features (e.g. Tabataba-Vakili et al. 2016; Kopparapu et al. 2021) in the spectral range that will be observed by JWST. The presence of high disequilibrium abundances of N_2O has also been proposed as a potential biosignature since N_2O in Earth's atmosphere is mainly produced by biotic sources (e.g. Sagan et al., 1993; Schwieterman et al., 2018). The possibility of lightning on exoplanets broadens the observational context of trace gases, and ignoring this may result in a false positive in the search for biosignatures.

I use the NASA Planetary Spectrum Generator (PSG) (Villanueva et al., 2018) to test whether the combined UM-UKCA model can potentially result in atmospheric phenomena that would be observable via transmission spectroscopy. The PSG is a radiative transfer model suite for forward modelling and retrievals of planetary spectra. For the purpose of this study, I generate transmission spectra for the UM-UKCA description of Proxima Centauri b (assuming

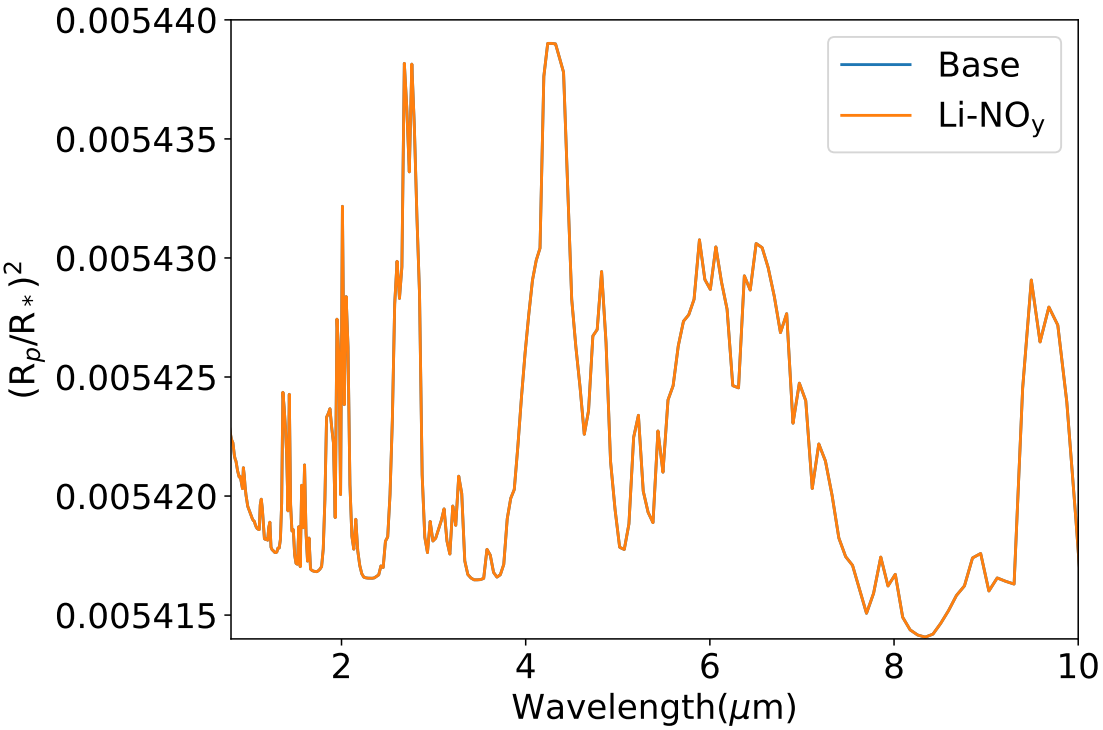

Figure 3.14: Transmission spectra for this setup of Proxima Centauri b, assuming it transits. Spectra are shown with and without lightning-induced NO_y present in the atmosphere.

it transits), using pressure, temperature, altitude and abundances of N_2, H_2O, CO_2, O_3, NO, NO_2, N_2O, and HNO_3. Recognising that transmission spectra will observe the atmosphere in the terminator regions, I extract model values for 1) all latitudes at longitudes between 75–105°E and 75–105°W and 2) all longitudes at latitudes between 85–90°N and 85–90°S. After that, I calculate the zonal and meridional mean to find a mean vertical profile for the terminator regions.

As shown in Figure 3.14, I find that lightning-induced NO_y species are not sufficiently abundant to leave detectable signals in the transmission spectrum, which agrees with previous 1-D model results (Ardaseva et al., 2017). Although Proxima Centauri b does not transit, the spectra are shown to be illustrative for other M-dwarf orbiting planets that do transit. I acknowledge that extending this study to exoplanets that support larger-scale and more vigorous convective updrafts and/or different chemical composition may result in large chemical perturbations that could be observable.

3.5 Conclusions

I used a 3D CCM (Met Office Unified Model coupled to the UK Chemistry and Aerosol framework) to study the emergence of lightning, driven by vigorous convection over and around the substellar point, and the subsequent impact on atmospheric chemistry on an Earth-like, tidally locked exoplanet. Building on previous work (Yates et al., 2020) I have: 1) updated the treatment of photochemistry, by including the MUSCLES spectrum for Proxima Centauri in the Fast-JX photolysis code that provides more UV flux than a previous study (Yates et al., 2020) with implications for ozone chemistry, and by correcting the distribution of these fluxes over different wavelength bins; and 2) expanded the atmospheric chemistry to improve the description of ozone chemistry, including a more comprehensive description of the HO_x catalytic cycle and NO_y chemistry that is initiated by lightning as the source of NO.

I find that the incoming stellar flux supports an ozone layer across the planet, with a spatial distribution determined by atmospheric dynamics. The distribution is dominated by the substellar point and two local ozone hotspots on the nightside driven by two cyclonic Rossby gyres. The ozone column ranges from values found on Earth ($\sim$300 DU) on the dayside to values that are five times higher over the nightside cold traps. For the Earth-like exoplanet, I parametrize lightning flashes as a function of cloud-top height, using parametrizations widely applied to modelling lightning on Earth. The flashes result in the production of NO from the thermal decomposition of N_2 and O_2 in the lightning channel. I find that:

- Lightning flash rates peak at 0.16 flashes $km^{-2}yr^{-1}$, concentrated in a crescent-like shape westward of the substellar point, coinciding with regions of vigorous dayside convection.
- Lightning flashes result in a dayside atmosphere that is rich in $NO_x(=NO+NO_2)$ due to the rapid interconversion between the species in the presence of stellar radiation. The lightning-induced NO_x is found below altitudes of 20 km and thus is vertically separated from the peak ozone layer at 40 km. The ozone profile is determined mainly by the Chapman mechanism and the HO_x catalytic cycle resulting from the oxidation and photolysis of water.
- Following strong eastward winds that result from thermal gradients between the day- and nightside of the planet, NO_x is advected to the nightside. Here, the absence of stellar radiation allows NO_x to be stored in reservoir species such as NO_3, HNO_3, and N_2O_5.

I find that part of the planetary surface is potentially habitable in terms of the surface temperature and absorption of harmful UV radiation by the ozone layer, in agreement with Boutle et al. (2017) and Yates et al. (2020). However, the amount of ozone and thus surface habitability of a planet strongly depend on the amount of UV flux, illustrating the need for a systematic characterisation of host star spectra (such as the MUSCLES spectral survey). Given the large range of causes for inter-model variability, exoplanetary CCMs would greatly benefit

from further model intercomparisons. Furthermore, the emergence and chemical effects of lightning can be further explored in convection resolving models (Sergeev et al., 2020) and in different atmospheric compositions (e.g. Chameides & Walker, 1981; Ardaseva et al., 2017), to further assess observability and potential relevance in the search for biosignatures. The development of accurate chemical networks describing non-Earth-like regimes is essential in understanding exoplanet atmospheric chemistry.

Chapter 4

Stratospheric dayside-to-nightside circulation drives the 3D ozone distribution on synchronously rotating rocky exoplanets

This Chapter is based on the publication:

Stratospheric dayside-to-nightside circulation drives the 3D ozone distribution on synchronously rotating rocky exoplanets

Marrick Braam, Paul I. Palmer, Leen Decin, Maureen Cohen, and Nathan J. Mayne

Monthly Notices of the Royal Astronomical Society, Volume 526, Issue 1, November 2023, Pages 263–278, DOI: https://doi.org/10.1093/mnras/stad2704

Author contributions: Marrick Braam conceived the science question, performed the simulations and analyses, and wrote the manuscript. All co-authors contributed via regular discussions and advice and provided feedback on the manuscript.

4.1 Introduction

The past two decades have seen the discovery of numerous Earth-size exoplanets, with a substantial fraction of them orbiting in the circumstellar Habitable Zone (Kasting et al., 1993). Earth-size planets are preferentially discovered around M-dwarf stars (Dressing & Charbonneau, 2015), because they are the most abundant stellar type, have relatively small radii, and are relatively cool, allowing for exoplanets in short-period orbits. The habitability of such exoplanets has been debated in light of the stellar and planetary environments (Shields et al., 2016). Comprehensive numerical simulations that describe the physical and chemical properties of a planetary atmosphere in such environments are essential to understanding habitability and interpreting spectroscopic observations.

Since M stars are cooler and smaller than other stellar types, a planet in the Habitable Zone orbits at a small orbital distance and feels a strong gravitational pull from the host star. This can lead to spin-orbit resonances for the planet, so-called tidal locking, of which the most extreme case is the 1:1 resonant orbit or synchronous rotation (e.g. Barnes, 2017; Renaud et al., 2021). Simulations with General Circulation Models (GCMs) help us understand how synchronous rotation affects the planetary atmosphere and surface habitability. First, synchronous rotation creates distinct hemispheric environments and a large temperature difference between the dayside and nightside (e.g. Joshi et al., 1997). Second, synchronous rotation leads to distinct photochemical environments, with strong photochemical production and destruction on the dayside and an absence of photochemistry on the nightside, as shown in Chapter 3 (see also Proedrou & Hocke, 2016; Chen et al., 2018; Yates et al., 2020; Ridgway et al., 2023). Depending on the rotation period, synchronous rotation can also lead to atmospheric circulation that is characterised by thermally direct circulation for slowly rotating planets (e.g. Merlis & Schneider, 2010; Edson et al., 2011; Heng et al., 2011; Koll & Abbot, 2016; Haqq-Misra et al., 2018). The existence of this large-scale circulation requires the Rossby deformation radius to exceed the planetary radius (Carone et al., 2014, 2015; Noda et al., 2017; Haqq-Misra et al., 2018), which is the case for planets like Proxima Centauri b, Trappist-1 e to h, LHS-1140 b and GJ 667 C c, assuming an Earth-like atmosphere. The dayside-nightside contrast leads to an overturning circulation, with upwelling on the dayside and downwelling on the nightside (Showman et al., 2013). This vertical motion results in a superposition of planetary-scale Rossby and Kelvin waves, which drives eddy momentum equatorward (Showman & Polvani, 2010). A typical part of this wave structure is a pair of quasi-stationary cyclonic gyres on the nightside (Showman & Polvani, 2010). The equatorward momentum feeds the superrotating jet (Showman & Polvani, 2011). The overturning circulation is a dominant component of the dayside-to-nightside heat transport (Hammond & Lewis, 2021).

Atmospheric circulation impacts the spatial and temporal distribution of chemical species and other tracers such as clouds (e.g. Boutle et al., 2017; Komacek & Abbot, 2019; Sergeev et al., 2020) and photochemical hazes (Parmentier et al., 2013; Steinrueck et al., 2021). On Earth, the Brewer-Dobson circulation controls the large-scale distribution of chemical tracers such as ozone (O_3) and water vapour in the atmosphere (Brewer, 1949; Dobson, 1956; Butchart, 2014). Ozone formation is initiated by photochemistry through the Chapman mechanism (Chapman, 1930), which is strongest at tropical latitudes. The Brewer-Dobson circulation describes the ascent of ozone-rich air in the tropics, followed by equator-to-pole transport and descending air motions at high latitudes, leading to meridional variations with a relatively enhanced ozone layer at high latitudes. The production of ozone depends on the presence of molecular oxygen, which has been at a mole fraction of $\chi_{O2}{=}21\%$ for the past $\sim$0.5 Gyr but was substantially less abundant for most of Earth's history (e.g. Lyons et al., 2014). Oxygen levels during the Proterozoic (2.4–0.54 Gyr ago) were likely between 0.01 and 0.001 times the

present atmospheric level (PAL) (Lyons et al., 2014; Cooke et al., 2022). Decreasing oxygen levels down to 0.001 PAL leads to a thinner ozone layer, from a present-day global average ozone column density of 279 DU (DU: 1 DU$=2.687 \times 10^{20}$ molecules m^{-2}) to 66 DU for a 0.01 PAL case (Cooke et al., 2022). Nevertheless, the Brewer-Dobson circulation and the associated meridional variability seem to persist (see Figure 4 in Cooke et al., 2022).

Proedrou and Hocke (2016) simulated a tidally-locked Earth using a 3D climate-chemistry model (CCM), which consists of a GCM coupled to a photochemical network to study the relation between (photo)chemistry, atmospheric dynamics and the thermal structure of the atmosphere. They find a breakdown of the Brewer-Dobson circulation, and instead predict that ozone accumulates on the nightside, where it has a long lifetime (Proedrou & Hocke, 2016). Carone et al. (2018) investigated stratospheric circulation on tidally-locked exoplanets and the potential impact on the distribution of chemical species. For planets with short orbital periods (<25 days), tropical Rossby waves can induce strong equatorial jets in the stratosphere with pole-to-equator transport of airmasses (Carone et al., 2018). Chen et al. (2019) showed the meridional distribution of ozone from CCM simulations, confirming that this pole-to-equator circulation essentially confines photochemical species such as ozone to the equatorial regions. The existence of extratropical Rossby waves or damping of tropical Rossby waves prevents this equatorial confinement. Instead, a thermally-driven overturning circulation can drive equator-to-pole transport of photochemical species (Carone et al., 2018; Chen et al., 2019), leading to meridional structure with enhanced ozone at high latitudes. For planets like Proxima Centauri b, Carone et al. (2018) find a relatively weak tropical Rossby wave, with a thermally-driven equator-to-pole circulation existing in the stratosphere (see their Figure 12). For such planets, the enhanced ozone abundances at high latitudes were later also simulated by Chen et al. (2019).

The distribution of radiatively active species such as ozone impacts habitability (e.g. Ridgway et al., 2023), and will determine what spectroscopic observations of the planetary atmosphere will look like. For hot Jupiters, dayside-nightside variations in temperature and chemical abundances (Nixon & Madhusudhan, 2022; Pluriel, 2023) and 3D transport-induced quenching (Zamyatina et al., 2023) both affect the appearance of synthetic spectra. For rocky planets, the spatial and temporal variation of water clouds causes variability in observations (May et al., 2021; Cohen et al., 2023a). Moreover, spatial and temporal variability of gaseous chemical species can manifest itself in spectroscopic variations over the orbital phase or observing geometry (Cooke et al., 2023b). Despite reporting a non-detection for the atmosphere, the observation of TRAPPIST-1 b illustrates the capability of JWST to characterise Earth-size exoplanets (Greene et al., 2023).

For the exoplanets that have an atmosphere, we need to understand their 3D nature, including circulation, clouds, and atmospheric chemistry, which motivates the application of 3D CCMs to exoplanetary environments. Such simulations of synchronously rotating exoplanets predict a significant zonal structure in the ozone layer for planets around M dwarfs like Proxima Centauri b (as shown in Chapter 3, see also Yates et al., 2020) and haze distribution for hot Jupiters (Parmentier et al., 2013; Steinrueck et al., 2021). Yates et al. (2020) found that ozone has a much longer chemical lifetime on the nightside as compared to the dayside of M-dwarf exoplanets. These long nightside lifetimes lead to the accumulation of ozone in the nightside gyres, despite the absence of stellar radiation needed to initiate the relevant photochemistry. This spatially variable ozone layer indicates a connection between the photochemically active dayside regions and nightside gyres, which is currently not understood.

In this study, I aim to understand the dayside-nightside connection and identify the physical and chemical mechanism that drives the spatially variable ozone layer on synchronously rotating exoplanets around M-dwarf stars. I use a 3D CCM to investigate the spatial and temporal structure of atmospheric ozone, in a configuration for Proxima Centauri b. In Section 4.2, I briefly describe the CCM and introduce metrics used to diagnose atmospheric circulation. This will be followed by a description of the ozone distribution and its relation to atmospheric circulation in Section 4.3, mainly focusing on 1 PAL O_2 and then testing the mechanism for a 0.01 PAL O_2 atmosphere. In Section 4.4, I identify a possible driver of the circulation, investigate variability in our simulations and discuss the potential observability. Finally, I present the conclusions of this study in Section 4.5.

4.2 Methods

This section starts with a description of the 3D coupled climate-chemistry model. This is followed by the introduction of useful metrics to diagnose atmospheric circulation and its impact on chemistry in Section 4.2.2. Finally, I summarize the experimental setup in Section 4.2.3.

4.2.1 Coupled Climate-Chemistry Model

The 3D CCM consists of the Met Office Unified Model (UM) as the GCM coupled with the UK Chemistry and Aerosol framework (UKCA), in the configuration described in Chapter 2 and Section 3.2. UM-UKCA is used to simulate the atmospheric dynamics and chemistry for Proxima Centauri b, but the results apply to other planets in similar orbits around M-dwarf stars. Like for Chapter 3, I simulate an aquaplanet with 1 bar or 1000 hPa surface pressure and use a horizontal resolution of 2° by 2.5° in latitude and longitude, respectively. The atmosphere extends up to 85 km in 60 vertical levels. I assume that Proxima Centauri b is in a 1:1 resonant orbit around its M-dwarf host star and use the orbital parameters as shown in Table 4.1. The substellar point is located at 0° latitude (ϕ) and 0° longitude (λ).

Table 4.1: Orbital and planetary parameters for the Proxima Centauri b setup, following Boutle et al. (2017).

Parameter	Value
Semi-major axis (AU)	0.0485
Stellar Irradiance (W m^{-2})	881.7
Orbital Period (days)	11.186
Rotation rate (rad s^{-1})	6.501×10^{-6}
Eccentricity	0
Obliquity	0
Radius ($R_\oplus$)	1.1
Surface gravity (m s^{-2})	10.9

The UM is used in the Global Atmosphere 7.0 configuration (Walters et al., 2019), including the ENDGame dynamical core to solve the non-hydrostatic fully compressible deep-atmosphere equations of motion (Wood et al., 2014). A detailed description can be found in Section 2.1. Parametrized sub-grid processes include convection (mass-flux approach, based on Gregory and Rowntree 1990), water cloud physics (Wilson et al., 2008), turbulent mixing (Lock et al., 2000; Brown et al., 2008) and the generation of lightning as described in Chapter 3 (see also Price & Rind, 1992; Luhar et al., 2021). The incoming stellar radiation for 0.5 nm to 5.5 μm is described by the v2.2 composite spectrum for Proxima Centauri from the MUSCLES spectral survey (France et al., 2016; Loyd et al., 2016; Youngblood et al., 2016) and extended to 10 μm using the spectrum from Ribas et al. (2017). Radiative transfer through the atmosphere is treated by the Suite of Community Radiative Transfer codes based on Edwards and Slingo (SOCRATES) scheme (Edwards & Slingo, 1996). The UM is one of the leading models in predicting the Earth's weather and climate and has been adapted for the study of several types of exoplanets, including terrestrial planets (e.g. Mayne et al., 2014a; Boutle et al., 2017; Lewis et al., 2018; Eager et al., 2020; Yates et al., 2020; Ridgway et al., 2023, Chapter 3) but also Mini-Neptunes (e.g. Drummond et al., 2018a) and hot Jupiters (e.g. Mayne et al., 2014b, 2017). Furthermore, the UM was part of the TRAPPIST-1e Habitable Atmosphere Intercomparison (THAI) project (Fauchez et al., 2021, 2022; Sergeev et al., 2022b; Turbet et al., 2022).

I use UKCA to simulate the 3D atmospheric chemical composition, by including its description of gas-phase chemistry and following the detailed descriptions of UKCA in Sections 2.2 and 3.2.2. UKCA is fully coupled to the UM for large-scale advection, convective transport and boundary layer mixing of the chemical tracers (Morgenstern et al., 2009; O'Connor et al., 2014; Archibald et al., 2020). The Fast-JX photolysis scheme is implemented within UKCA, to calculate photolysis rates of chemical species in the atmosphere (Wild et al., 2000; Bian & Prather, 2002; Neu et al., 2007; Telford et al., 2013). By taking into account the varying optical depths of Rayleigh scattering, absorbing gases, and clouds from the UM, Fast-JX provides an interactive treatment of photolysis in calculating the 3D distribution of chemical

species in the atmosphere. I distribute the stellar flux from Proxima Centauri over the 18 wavelength bins of Fast-JX, as shown in Sections 2.2.2 and 3.2 (specifically Figure 3.1). These fluxes are synchronised to the orbital distance of Proxima Centauri b which provides an interactive calculation of photolysis rates over the planetary orbit. The chemistry included is a reduced version of UKCA's Stratospheric-Tropospheric scheme (StratTrop, Archibald et al., 2020), including the Chapman mechanism of ozone formation, and the hydrogen oxide (HO_x=H+OH+HO_2) and nitrogen oxide (NO_x=NO+NO_2) catalytic cycles. This results in 21 chemical species that are connected by 71 reactions, describing the main mechanisms that control the abundance of ozone in an Earth-like atmospheric composition. A full list of species and reactions can be found in Tables 2.1 and 2.2.

4.2.2 Metrics

The meridional circulation is diagnosed using the mean meridional mass streamfunction (in kg s^{-1}), which calculates the northward mass flux above pressure P:

$$\Psi_m = \frac{2\pi R_p \cos\phi}{g} \int_0^P \bar{v} dP, \tag{4.1}$$

with R_p as the planetary radius, g as the gravitational acceleration and $\bar{v}$ as the zonal and temporal mean of the northward velocity component at latitude ϕ. Earlier studies using this metric for synchronously rotating exoplanets (e.g. Merlis & Schneider, 2010; Edson et al., 2011; Carone et al., 2015; Haqq-Misra & Kopparapu, 2015; Carone et al., 2018) showed 1) the existence of tropospheric Hadley and Ferrel cells transporting heat and mass from the equatorial to polar regions and 2) the impact of orbital configuration on the Brewer-Dobson circulation in the stratosphere (Carone et al., 2018).

However, with the fixed substellar point of synchronously rotating planets, the mean meridional circulation varies depending on the position relative to the substellar point: for example, the hemispheric mean meridional circulation can vary significantly between the dayside and nightside. The zonal circulation is analogous to the Walker circulation cells on Earth, with rising motion at the location of the heat source, followed by eastward and westward flow aloft and, after descending on the nightside, a return flow along the surface back to the heat source (Geisler, 1981). The mean zonal mass streamfunction can be used to calculate the eastward mass flux above pressure P:

$$\Psi_z = \frac{2\pi R_p}{g} \int_0^P \bar{u} dP, \tag{4.2}$$

where $\bar{u}$ is the meridional mean of the zonal velocity component. For slow rotators, the mean zonal circulation connects the substellar and antistellar points (Gill, 1980; Merlis & Schneider, 2010; Edson et al., 2011; Heng et al., 2011; Showman & Polvani, 2011; Haqq-Misra & Kopparapu, 2015; Haqq-Misra et al., 2018). The substellar-antistellar circulation also consists of a cross-polar flow (Haqq-Misra & Kopparapu, 2015).

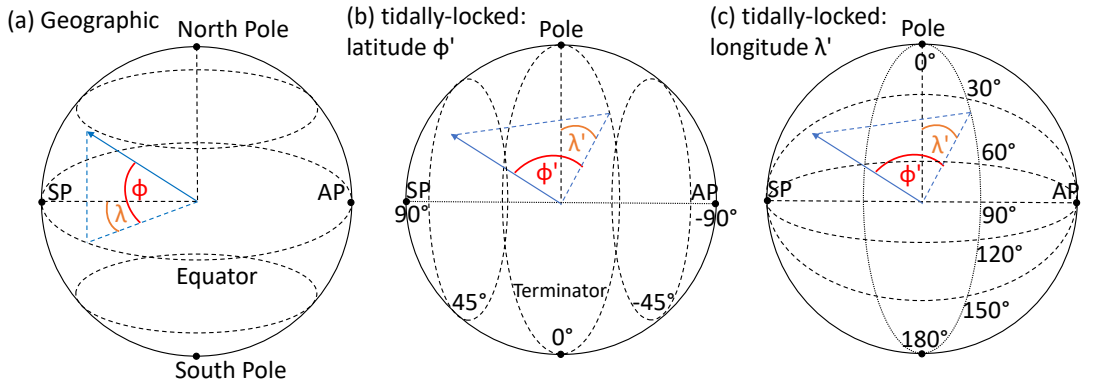

Figure 4.1: Geographic coordinate system (a) showing latitude ϕ and longitude λ, with the substellar point (SP) located at (0°,0°). In the tidally-locked coordinate system, I use tidally-locked latitude ϕ' and tidally-locked longitude λ'. Panel b illustrates tidally-locked latitudes, with the substellar point located at ϕ'=90°, the terminator at ϕ'=0°, and the nightside corresponding to negative ϕ'. Panel c shows tidally-locked longitudes, illustrating how lines of constant tidally-locked longitude connect the substellar and antistellar (AP) points. Figures based on Koll and Abbot (2015).

As elaborated in Section 4.1, the total wind flow on synchronously rotating exoplanets consists of several components. I perform a Helmholtz decomposition of the total wind flow, following Hammond and Lewis (2021). This decomposes the total wind flow into its rotational, eddy rotational, and divergent components. The divergent wind mainly drives the substellar-antistellar overturning circulation (Hammond & Lewis, 2021; Sergeev et al., 2022b). Since the divergent component is roughly isotropic around the substellar point, we can move from the usual latitude-longitude or geographic coordinate system to a tidally-locked coordinate system (Koll & Abbot, 2015; Hammond & Lewis, 2021). The transformation between geographic coordinates and tidally-locked coordinates is illustrated in Figure 4.1. The tidally-locked latitude ϕ' is measured as the angle from the terminator (at ϕ'=0, see Figure 4.1b) and the tidally-locked longitude λ' is the angle about the substellar point (see Figure 4.1c), with the geographic North Pole located at (ϕ', λ')=$(0, 0)$ in tidally-locked coordinates. The substellar point and antistellar point correspond to ϕ'=90° and $-90°$, respectively. In representing a sphere on a 2-D plot, the geographic coordinate system stretches the poles and thereby emphasizes meridional gradients (e.g. equator-to-pole temperature gradients). Meridional gradients are especially pronounced when the axial rotation is substantially faster than the orbital rotation. For synchronously rotating planets, the rotation periods are the same, giving the strongest gradients between the substellar and antistellar points. Therefore, the tidally-locked coordinate system stretches the substellar and antistellar points as the extrema in ϕ'. As illustrated in Figure 4.1c, every line of constant λ' corresponds to a line connecting the substellar point and antistellar point, in every direction over the sphere. Hence, cross-polar flow in geographic coordinates is automatically taken into account in the tidally-locked coordinate system and was found to be an important contribution to the tropospheric dayside-to-nightside circulation

(Hammond & Lewis, 2021). It was shown by Hammond and Lewis (2021) that integrating the continuity equation in tidally-locked coordinates over λ' leads to the tidally-locked mean meridional mass streamfunction:

$$\Psi'_m = \frac{2\pi R_p \cos\phi'}{g} \int_0^P \bar{v'} dP, \tag{4.3}$$

where $\bar{v'}$ is the zonal mean of the meridional velocity component at tidally-locked latitude ϕ'. In this system, the meridional mass streamfunction calculates the mass flux toward the antistellar point (along lines of constant λ'), connecting the substellar and antistellar points whilst covering the whole planet.

To better identify the transport of ozone around the planet, I weight the stream functions using the ozone mass mixing ratio (w_{O_3}), which is measured as the mass of ozone per unit mass of air in a parcel. This gives us the ozone mass streamfunction:

$$\Psi'_{m,O_3} = \Psi'_m \times w_{O_3}, \tag{4.4}$$

which can be applied generally using any of the streamfunctions in Equations 4.1, 4.2 or 4.3 to give the ozone-weighted meridional, zonal, or the tidally-locked meridional mass streamfunction.

In assessing the impact of atmospheric dynamics on chemical abundances, it is important to make a comparison between the timescales of processes that can control the ozone abundance. The dynamical lifetimes include the zonal (τ_u), meridional (τ_v), and vertical components (τ_w), and are calculated following Drummond et al. (2018b):

$$\tau_u = \frac{L}{u} = \frac{2\pi R_p}{u}, \tag{4.5}$$

$$\tau_v = \frac{L}{v} = \frac{\pi R_p}{v}, \tag{4.6}$$

$$\tau_w = \frac{H}{w}, \tag{4.7}$$

with L the relevant horizontal scale in terms of the planetary radius R_p, and H the vertical scale height. The zonal (u), meridional (v), and vertical (w) wind components are all in m s^{-1}. For the chemical lifetimes I use:

$$\tau_{chem} = \frac{n_{O_3}}{R_x}, \tag{4.8}$$

where n_{O_3} denotes the ozone number density (molecules m^{-3}) and R_x the loss of ozone (in molecules m^{-3} s^{-1}) due to reaction x, following the dominant chemical reactions of Section 3.3. Specifically, I use the termination reaction of the Chapman mechanism (Chapman, 1930):

$O_3 + O(^3P) \longrightarrow O_2 + O_2,$ (R1)

and the rate-limiting step of the dominant HO_x catalytic cycle (Yates et al., 2020):

$HO_2 + O_3 \longrightarrow OH + 2O_2.$ (R2)

A detailed overview of the chemical reactions in the chemical mechanisms can be found in Section 3.3. I calculate the lifetimes for sets of gridpoints centred at four distinct locations in the ozone distribution (see Figure 4.3), and subsequently take the meridional and zonal mean. These locations cover the substellar point (10 latitudes $\times$ 8 longitudes = 80 grid points), the nightside jet ($10\times7=70$ points), and the two nightside gyres with $5\times7=35$ points each.

4.2.3 Experimental Setup

I use the final state of the 'Chapman+HO_x+NO_x' simulation from Chapter 3 for the analysis. The atmosphere was initialized at an Earth-like atmospheric composition, using pre-industrial values of N_2, O_2 and CO_2 (see also Boutle et al., 2017). Water vapour profiles are interactively determined by evaporation from the slab ocean. The HO_x and NO_x species are initialized at mass mixing ratios of 10^{-9} and 10^{-15}, respectively. To test the results for an atmosphere of lower oxygen content, I initialize a second simulation with 0.01 PAL O_2 and an increased amount of N_2 to maintain a surface pressure of 1000 hPa. This decrease in oxygen is informed by the fact that for most of Earth's history, the atmosphere contained lower O_2 levels than we presently see (Lyons et al., 2014).

I report results from these simulations as 600-day mean of the CCM output (equal to $\sim$50 orbits of Proxima Centauri b) after spinning up to ensure the simulations have reached a dynamical and chemical steady state. The dynamical steady state was determined by the stabilisation of the surface temperature and radiative balance at the top of the atmosphere. The chemical steady state was determined by the stabilisation of ozone as a long-lived species, through the total column density and mole fraction χ_{O_3}. In diagnosing the impact of dynamical processes on the ozone distribution, parts of the spin-up period have also been used to plot the evolution of chemically inert tracers (see e.g. Figure 4.7 below). The analysis of temporal variability in Section 4.4.3 is based on a 6-day output over 900 days of simulation after reaching a steady state, to ensure the inclusion of potential variability at longer timescales.

4.3 Results

In this section, I start with a brief description of the planetary climate and ozone layer, focusing on the 1 PAL O_2 atmosphere. After that, I discuss the atmospheric circulation followed by its impact on the distribution of ozone around the planet, elaborating on the stratospheric overturning circulation. I then perform a comparison of relevant lifetimes in the atmosphere and investigate the implications of the stratospheric overturning circulation for lightning-induced chemistry. I end with testing how a 0.01 PAL O_2 atmosphere affects the stratospheric overturning circulation and ozone distribution.

4.3.1 Planetary Climate and Atmospheric Ozone

The simulated climate of Proxima Centauri b is broadly similar to that described by Boutle et al. (2017) and described in Section 3.3. Furthermore, the formation of an ozone layer under quiescent stellar radiation is explained in detail by Yates et al. (2020) and in Section 3.3. Here, I give a brief description of the details essential for this study. The simulated surface temperature of Proxima Centauri b is shown in Figure 4.2, using a geographic coordinate system in panel (a) and a tidally-locked coordinate system in panel (b). Both panels show the dayside-to-nightside contrast characteristic of synchronous rotation, with dayside maxima in surface temperature of up to 289 K and minima of 157 K over the nightside Rossby gyres. Figure 4.2b demonstrates the usefulness of the tidally-locked coordinate system in identifying the dayside-to-nightside contrasts, with the terminator located at $\phi'=0^{\circ}$. The horizontal wind vectors are shown at P$\approx$400 hPa, illustrating the tropospheric jet as well as the Rossby gyres on the nightside. The dayside-to-nightside circulation is part of an overturning circulation across multiple pressure levels that will be described in more detail in Section 4.3.2. At the locations of the nightside Rossby gyres (Showman & Polvani, 2010), the coldest areas on the planetary surface are found with air that is trapped and subject to radiative cooling. The atmospheric pressure in the gyres is relatively low, like the eye of tropical cyclones (Schubert et al., 2007). The gyres are relatively isolated from the rest of the hemisphere and their edges act as mixing barriers (Vallis, 2017). The gyres are a general feature of slowly rotating exoplanets in a synchronous orbit with a single equatorial jet in the troposphere (Sergeev et al., 2022a).

I find a spatially variable distribution of ozone in Figure 4.3a, with a relatively thin dayside ozone layer and accumulation of ozone on the nightside. Typical values for the vertically-integrated ozone column densities on Earth are 200–400 DU, with lower values over the equatorial regions and ozone hole and higher values over high-latitude regions (Eyring et al., 2013). For synchronously rotating planets, most of the dayside ozone column density falls within this range. The locations of the nightside Rossby gyres correspond to the maxima in the thickness of the ozone column, reaching up to 1401 DU. The gyres are not fully symmetric, evident from slightly different shapes and the average ozone columns: the area-

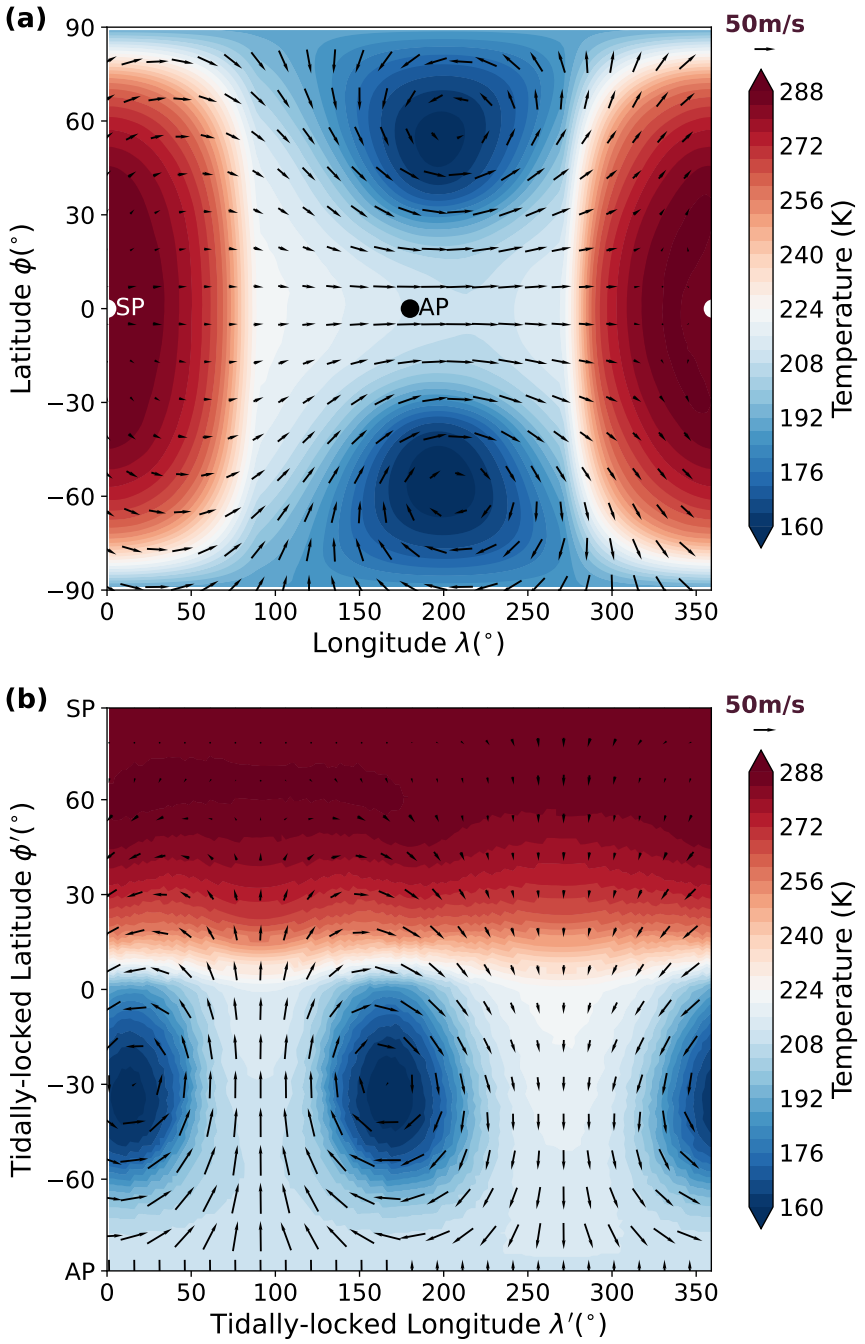

Figure 4.2: Temporal mean surface temperature over 50 orbits of Proxima Centauri b, using (a) the geographic coordinate system and (b) the tidally-locked coordinate system (Koll & Abbot, 2015). The substellar point (SP) is transformed from $(\phi,\lambda)=(0°,0°)$ in geographic coordinates (white dot) to $\phi'=90°$ in tidally-locked coordinates, as also shown in Figure 4.1. Overplotted are the horizontal wind vectors at P$\approx$400 hPa, showing both the tropospheric jet and the existence of the Rossby gyres on the nightside. The plots also show the location of the antistellar point (AP).

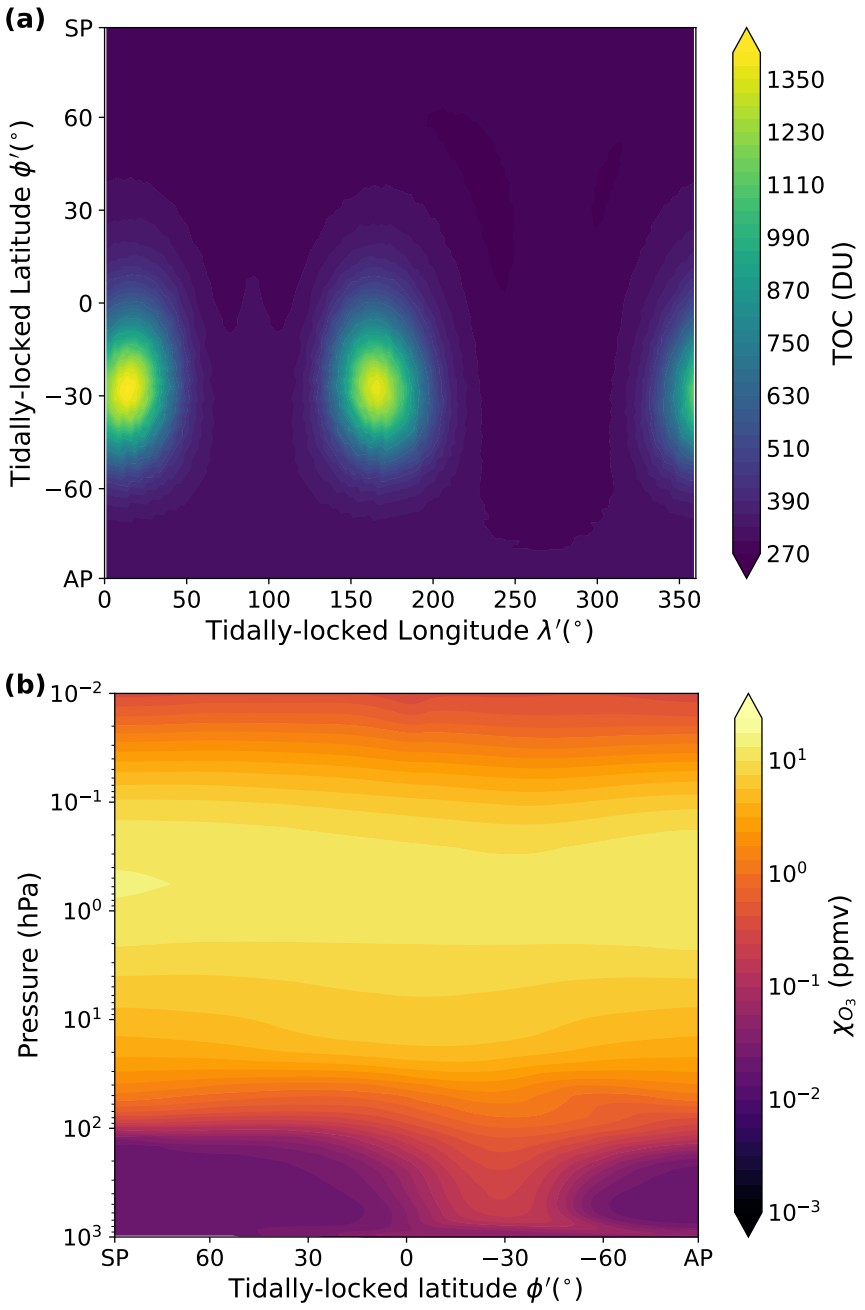

Figure 4.3: (a) Total ozone column density and (b) mole fraction χ_{O_3}, both taking means over 50 orbits of Proxima Centauri b. Both plots illustrate the spatially variable ozone layer with accumulation at the locations of the nightside Rossby gyres ($-60<\phi'<0$). The substellar and antistellar point are denoted as SP and AP, respectively.

weighted mean column density of the low-λ' gyre (for $\lambda' \leq 70$ and $\lambda' > 320°$) is equal to 626 DU and of the mid-λ' gyre ($110 < \lambda' \leq 220°$) to 601 DU, both confined between tidally-locked latitudes $-60 < \phi' < 0°$. Figure 4.3b shows that the accumulation of ozone at the gyre locations mostly occurs in the lower atmosphere, at pressure levels corresponding to the troposphere (< 100 hPa). The highest χ_{O_3} are found between 10 and 0.1 hPa and form a significant contribution to the planetary ozone layer, especially on the dayside.

The existence of such a spatially variable ozone layer depends on a complex interplay between photochemistry and atmospheric dynamics and changes as a function of incoming stellar radiation and planetary rotation state (Chen et al., 2019, 2021). The production mechanisms for atmospheric ozone are relatively well-understood and due to photochemistry: in the presence of stellar radiation molecular oxygen will dissociate and form ozone through the Chapman mechanism (Chapman, 1930). The 3D impact of M-dwarf radiation on the Chapman mechanism has been explored by previous studies, both in quiescent (Yates et al., 2020, Chapter 3) and flaring conditions (Ridgway et al., 2023). In all cases, an ozone layer develops around the planet. As such exoplanets are likely to rotate synchronously around their host star (Barnes, 2017), stellar radiation and the photochemical production of ozone are limited to the planetary dayside. This is illustrated in Figure 4.4, showing the time-averaged chemical tendency of ozone. The tendency denotes the balance between the production and loss of ozone due to chemical processes. I find that ozone production mainly occurs on the dayside and is particularly strong at high $\phi' > 45°$ (i.e., close to the substellar point), whereas ozone production is practically absent at the locations of the nightside gyres ($-60 < \phi' < 0°$) and more generally the nightside troposphere (below ~ 100 hPa) and stratosphere (between $\sim 100 - 0.1$ hPa). Hence, another mechanism must be driving the relatively enhanced ozone abundances at the locations of the nightside Rossby gyres. In the upper atmosphere (above ~ 0.1 hPa), atomic oxygen is quickly advected to the nightside where it forms ozone and thus gives net ozone production. The ozone is subsequently advected back to the dayside, where it is destroyed by the photochemical loss processes that are particularly strong in these top layers of the atmosphere.

4.3.2 Overturning Circulations

The relationship between the ozone distribution in Figure 4.3 and the global atmospheric circulation becomes clear through the mass streamfunctions, as defined in Section 4.2.2. From left to right, Figure 4.5 shows the mean meridional mass streamfunctions Ψ_m, Ψ'_m and $\Psi'_{m,\mathrm{O_3}}$ that have been calculated from the divergent wind component. A positive streamfunction (red contours) indicates clockwise circulation, and a negative streamfunction (blue) indicates anticlockwise circulation.

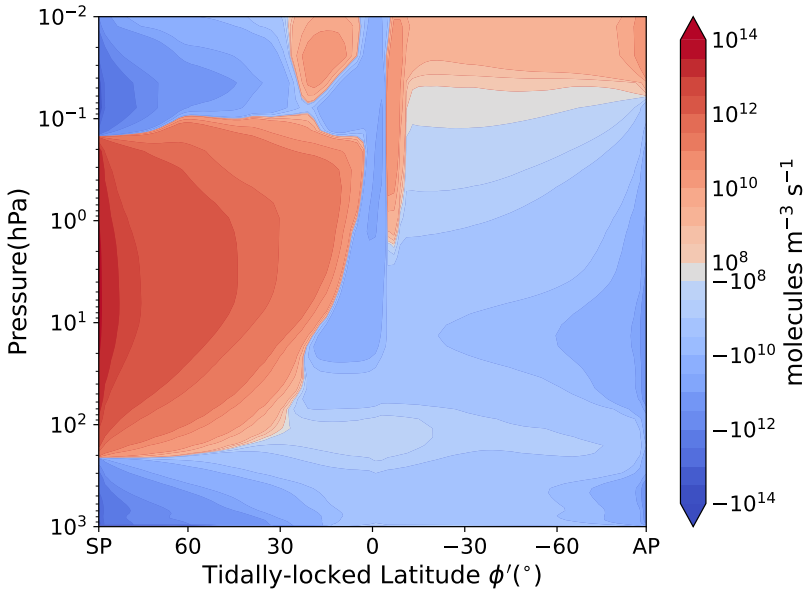

Figure 4.4: Meridional mean ozone chemical tendency (production-loss) in tidally-locked coordinates, showing that ozone production is limited to the planet's dayside.

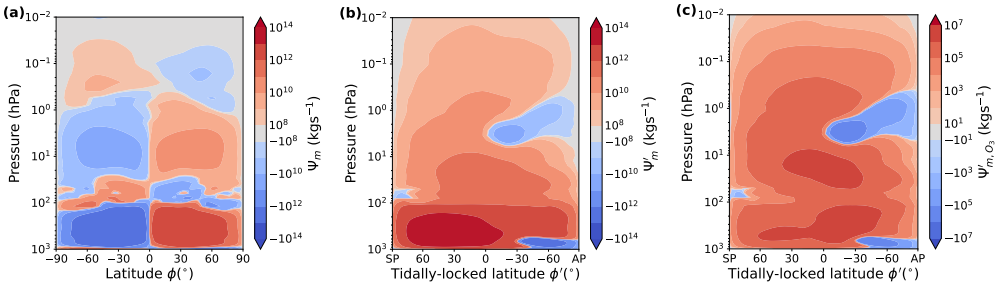

Figure 4.5: Zonal mean meridional mass streamfunctions illustrating different aspects of atmospheric circulation. Positive values (red) indicate clockwise and negative values (blue) anticlockwise motion. (a) The meridional mass streamfunction in geographic coordinates Ψ_m (Equation 4.1) shows equator-to-pole stratospheric transport like the Brewer-Dobson circulation. (b) The meridional mass streamfunction in tidally-locked coordinates Ψ'_m (Equation 4.3) shows an overturning dayside-to-nightside circulation including a strong stratospheric component (above $\sim$100 hPa). (c) The meridional ozone mass streamfunction $\Psi'_{m,\mathrm{O_3}}$ (Equation 4.4) shows that this stratospheric component is significant in terms of transporting ozone from the dayside to the nightside.

From Figure 4.5a, I find strong poleward transport of air at tropospheric pressures (>100 hPa) in a single thermally driven circulation cell (Merlis & Schneider, 2010; Edson et al., 2011). Moving up into the stratosphere, I find stacked layers of clockwise and anticlockwise circulation. The existence of poleward transport between ~ 50 and ~ 1.5 hPa indicates additional thermally-driven circulation cells. These cells transport aerosols and chemical tracers such as ozone from the equator to the poles through the stratosphere (Carone et al., 2018; Chen et al., 2019). This equator-to-pole transport leads to an enhanced high latitude ozone layer on the dayside in geographic coordinates, with mean ozone column densities of $\sim$490 DU above 80° North and South as compared to a mean of $\sim$290 DU between 10° North and 10° South (see also Yates et al., 2020, Chapter 3). Since the stellar radiation at the poles is too weak to initiate the photochemistry responsible for ozone production, this polar enhancement has to be due to the poleward transport of ozone produced in the equatorial regions.

Moving to tidally-locked coordinates using Ψ'_m in Figure 4.5b, I find a single overturning circulation cell that dominates the troposphere and transports air and heat from the dayside towards the nightside. A weaker anticlockwise circulating cell is present between the anti-stellar point and $\phi' \approx -30°$, induced by the temperature gradient between those two points. The absence of anticlockwise motion when moving to lower pressure levels in Figure 4.5b indicates that a connection between the tropospheric cell and the stratospheric circulation exists. An overturning circulation covers essentially all of the stratosphere, connecting the dayside and nightside. Air ascends in the ozone production regions (between 0.2 and 100 hPa, see Figure 4.4) and moves through the stratosphere towards the nightside, where it subsides at the locations of the nightside gyres and thus the locations of ozone accumulation as shown in Figure 4.3.

To quantify the impact of this mass transport on the distribution of ozone, I calculate the tidally-locked ozone-weighted mass streamfunction $\Psi'_{m,\mathrm{O_3}}$ (Equation 4.4) as shown in Figure 4.5c. The ozone mass streamfunction demonstrates that the circulation of ozone through the stratosphere provides a significant contribution to the dayside-to-nightside transport. The downward ozone transport at the ϕ' of the Rossby gyres ($-60 < \phi' < 0°$) indicates that this stratospheric dayside-to-nightside circulation drives ozone-rich air into the Rossby gyres and thus leads to ozone maxima on the nightside.

Figure 4.6 again shows $\Psi'_{m,\mathrm{O_3}}$, now separated into 4 ranges of λ'. Each of these λ' ranges corresponds to a distinct feature of the ozone distribution in Figure 4.3a. Figure 4.6a shows the λ'-range that contains the low-λ' gyre ($\lambda' > 320°$ and $\lambda' \leq 70°$), illustrating the dayside-to-nightside transport of ozone-rich air, followed by descending motion at ϕ' corresponding to the location of the Rossby gyres. The ozone is supplied from part of its production region (see Figure 4.4) between pressures of 0.2 hPa and 20 hPa. Figure 4.6b shows the low-λ'-range that does not contain the gyres and instead includes the nightside-to-dayside component of the equatorial jet. $\Psi'_{m,\mathrm{O_3}}$ shows that there is a stratospheric clockwise circulation, but that this

is separated from the lower parts of the atmosphere by an anticlockwise circulation at the ϕ' corresponding to the Rossby gyres and misses part of the ozone production regions between 10 and 100 hPa. Therefore, for $70 < \lambda' \leq 110°$, no ozone accumulation is found following the stratospheric overturning circulation. Figure 4.6c again indicates dayside-to-nightside transport of ozone-rich air, with ozone for the mid-λ' gyre ($110 < \lambda' \leq 220°$) being supplied from the ozone production regions between pressures of 0.2 hPa and 20 hPa. Lastly, Figure 4.6d shows that in the final non-gyre range ($220 < \lambda' \leq 320°$) there is a stratospheric overturning circulation transporting ozone-rich air, but this circulation misses part of the ozone production region between 0.3 and 10 hPa and is generally weaker than for the ranges containing the gyres. Furthermore, the air that descends below ~ 10 hPa will meet the equatorial jet, leading to chemical destruction of ozone (due to HO_x-rich air from the dayside) or advection back to the dayside followed by photochemical destruction. Therefore, this λ'-range is not accumulating ozone in the lower part of the atmosphere.

This interpretation of the atmospheric dynamics is supported by an age-of-air tracer experiment. In Figure 4.7, I show the zonally-averaged time evolution of the age-of-air-tracer during the model spin-up period. As a passive tracer, it is only affected by dynamical processes in the UM, including both advection and convection. The age-of-air tracer is initialised at 0 s and provides a measure of the amount of time that has passed since an air parcel was last found in the lowest layers of the atmosphere (below ~ 2 km or 700 hPa). As such, the tracer measures the time it takes a parcel to rise from these lowest layers into the stratosphere. The tracer values are reset to 0 in the lowest layers at every model timestep. With the evolution of the age-of-air tracer over ϕ' in Figure 4.7 I show that air rises over and around the substellar point, already providing much younger air to the dayside troposphere (< 15 km) after 10 days of simulation. After 100 days, I find that most of the troposphere has been replenished with much younger air, except for the nightside gyres between $-60° < \phi' < 0°$. This picture persists after 500 days, showing that the age-of-air tracer in the nightside gyres is fed by older air from the stratosphere. From this experiment, I conclude that the mechanism affects any long-lived tracer, and thus might also be important for the distribution of photochemical hazes (Steinrueck et al., 2021).

I conduct a similar experiment for the ozone tracer, after its constant initialisation at mass mixing ratios of 10^{-9}. Figure 4.8 shows the time evolution of the ozone number density, which can be directly compared to Figure 4.3b. At the start of the simulation (t=1 day), ozone is produced on the dayside hemisphere. After 10 days, the peak in ozone number density has moved to higher altitudes, entering the stratosphere (above ~ 100 hPa). After 100 days of simulation, the planetary ozone layer is seen forming in the stratosphere. The peak has moved up again since the passage of radiation through the atmosphere becomes shorter with more ozone. In the troposphere, the accumulation of ozone in the nightside gyres is visible.

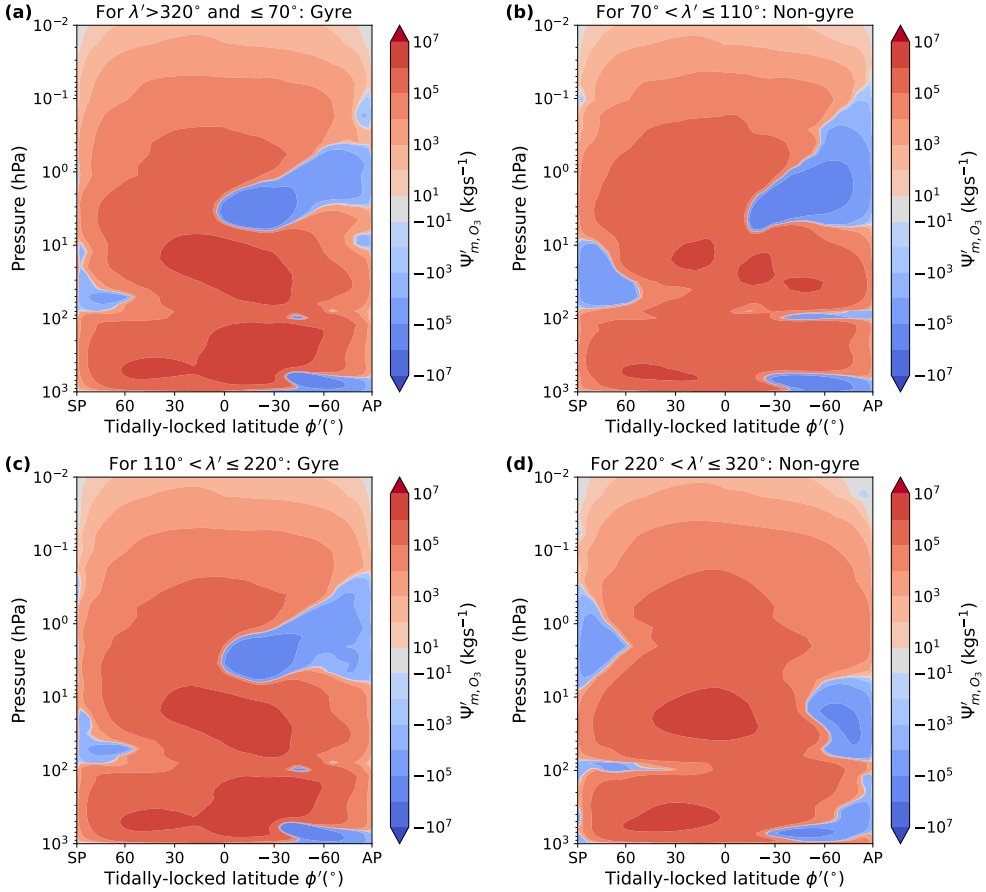

Figure 4.6: The zonal mean meridional ozone mass streamfunction $\Psi'_{m,\mathrm{O_3}}$ (Equation 4.4) in tidally-locked coordinates, for ranges of tidally-locked longitude λ' as shown by the titles of each of the four panels. Panels a and c denote λ'-ranges corresponding to the locations of the ozone accumulation in the Rossby gyres, following the distribution of ozone in Figure 4.3. The λ'-ranges in panels b and d correspond to the regions containing the superrotating jet. As such, panels a and c map out the meridional extent of the transport of ozone-rich air to the nightside.

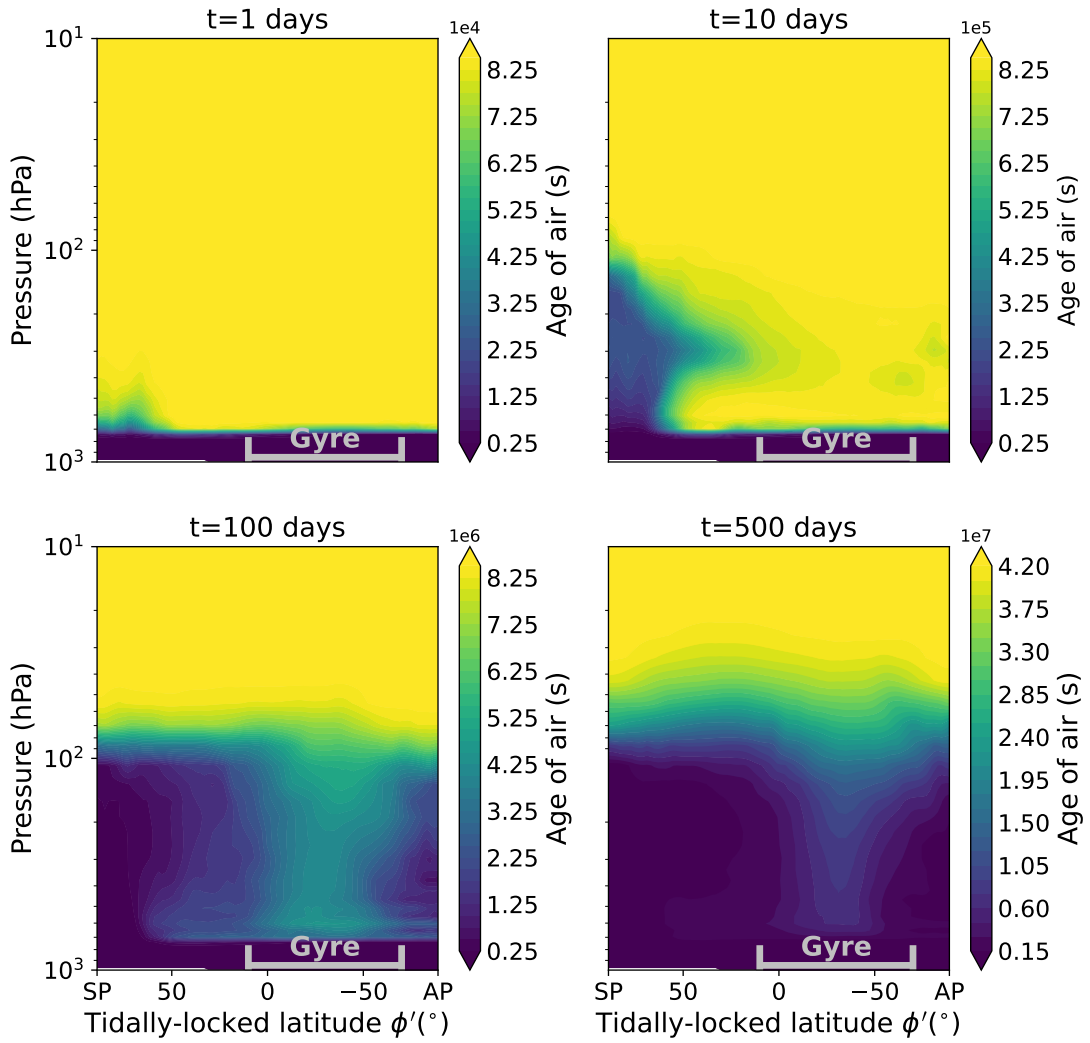

Figure 4.7: Age-of-air tracer during the spin-up of the simulation, showing the mean meridional distribution in tidally-locked coordinates. As a passive tracer, it is only affected by dynamical processes (advective and convective). As such, the age-of-air measures the time it takes a parcel to rise from the lowest atmospheric layers (at $\sim$2 km or 700 hPa) into the stratosphere. The tracer values are reset to 0 in the lowest atmospheric layers at every model timestep. I also show the tidally-locked latitudes corresponding to the nightside gyres in grey.

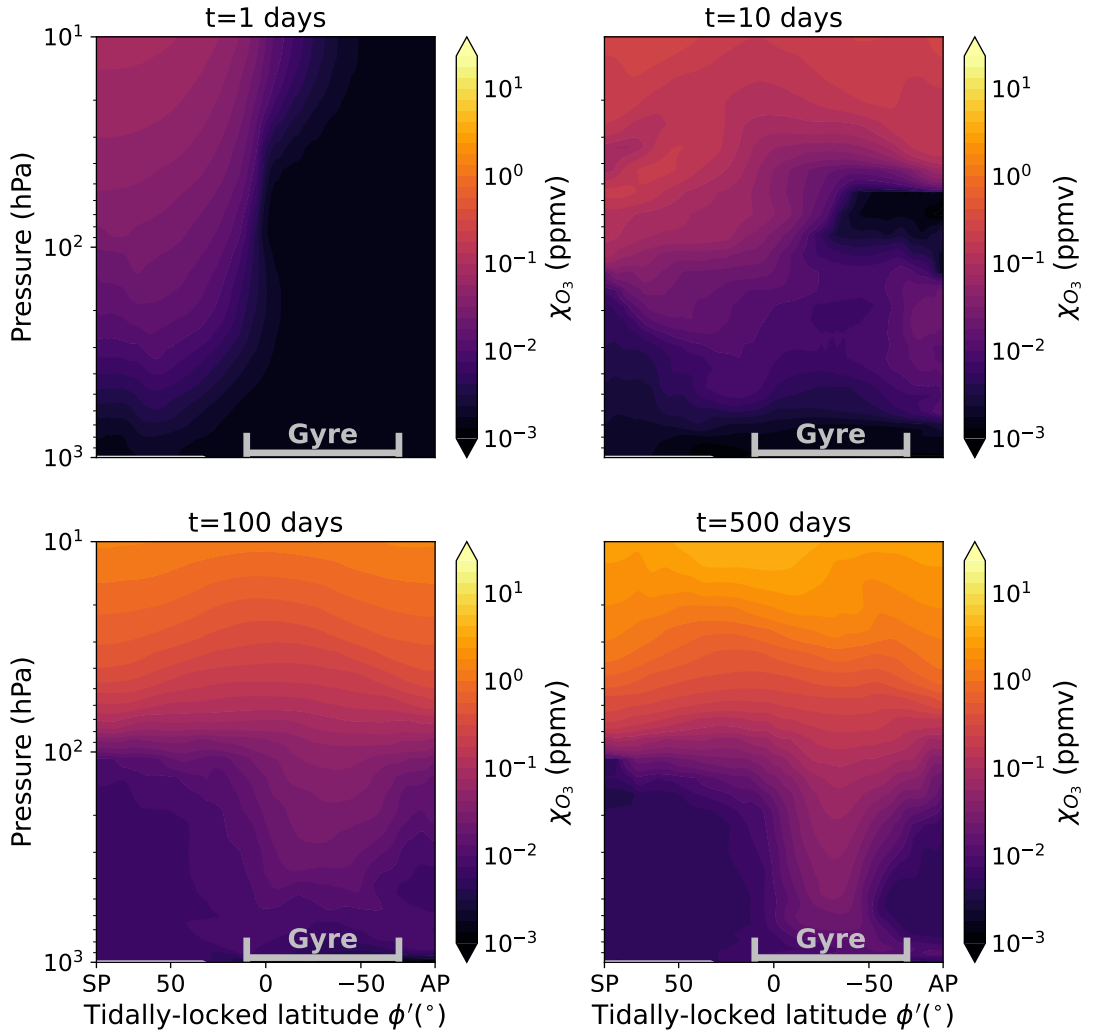

Figure 4.8: Ozone mole fraction during the spin-up of the simulation, showing the mean meridional distribution in tidally-locked coordinates. Similar to Figure 4.7, but now for a chemically active species. I also show the tidally-locked latitudes corresponding to the nightside gyres in grey.

These abundances are similar to those in the lower stratosphere, and the contour levels bend downwards at the gyre locations. This same distribution persists after 500 days, and way beyond the spin-up period as shown in Figure 4.3b. This confirms that after ozone forms on the dayside, the stratospheric circulation drives ozone to the nightside and into the gyres.

To further diagnose the nightside descent of ozone molecules into the gyres, we can define the vertical flux of ozone across pressure or altitude levels as:

$$F_{\mathrm{O_3}} = \int_{P_{max}}^{P_{min}} (w \cdot n_{\mathrm{O_3}}) dP, \tag{4.9}$$

where w is the vertical wind velocity (m s^{-1}) and $n_{\mathrm{O_3}}$ the ozone number density in molecules m^{-3}. Negative values correspond to downward transport and positive values to upward transport of ozone. The integration between pressure levels P_{max} and P_{min} is done to determine the total flux exchange between the stratosphere and troposphere. Using the streamfunctions in Figure 4.5 and the ozone distribution in Figure 4.3b, I determine that downward transport between $\sim$200 and 8 hPa drives the ozone accumulation. Figure 4.9 shows the vertical flux of ozone, integrated over pressures between 190 and 8 hPa. Generally, I find a relatively small but hemisphere-wide upward flux on the dayside. The nightside gyre locations stand out with a relatively strong downward flux. Hence, the ozone that was produced in the stratosphere will be transported downward into the troposphere at the gyre locations. Combining the streamfunctions, the tracer evolution experiments and the vertical ozone flux, I find that the stratospheric overturning circulation provides a connection between the ozone production regions and the nightside gyres, leading to the accumulation of ozone in the latter. To the author's knowledge, this is the first time this connection has been reported.

4.3.3 Dynamical and Chemical Timescales

As outlined in Section 4.2.2, I extract the three wind components and reaction fluxes for the Chapman termination reaction (R1) and rate-limiting step of the dominant HO_x catalytic cycle (R2) to calculate dynamical (τ_u, τ_v, and τ_w) and chemical lifetimes (τ_{Chap} and τ_{HOx}) around the planet. Figure 4.10 shows the different lifetimes at each of the four locations. From Figure 4.10a I conclude that the dynamical lifetimes are shorter than the chemical lifetimes at all four locations, indicating that dynamics can be an important driver of disequilibrium abundances in this pressure range.

In Figure 4.10b I highlight the differences between τ_u and τ_w, for the troposphere ($<$100 hPa) and lower stratosphere (between 100 hPa and 10 hPa), by using the fraction τ_u/τ_w. Vertical transport is the dominant process for $\tau_u/\tau_w > 1$ (right of the vertical line) and horizontal transport for $\tau_u/\tau_w < 1$ (left of the vertical line). Around the substellar point (solid lines), I determine that vertical mixing dominates the troposphere ($\tau_u/\tau_w > 1$) and that zonal mixing (τ_u) starts to take over for P$>$80 hPa. Above this pressure, chemical abundances at the substellar

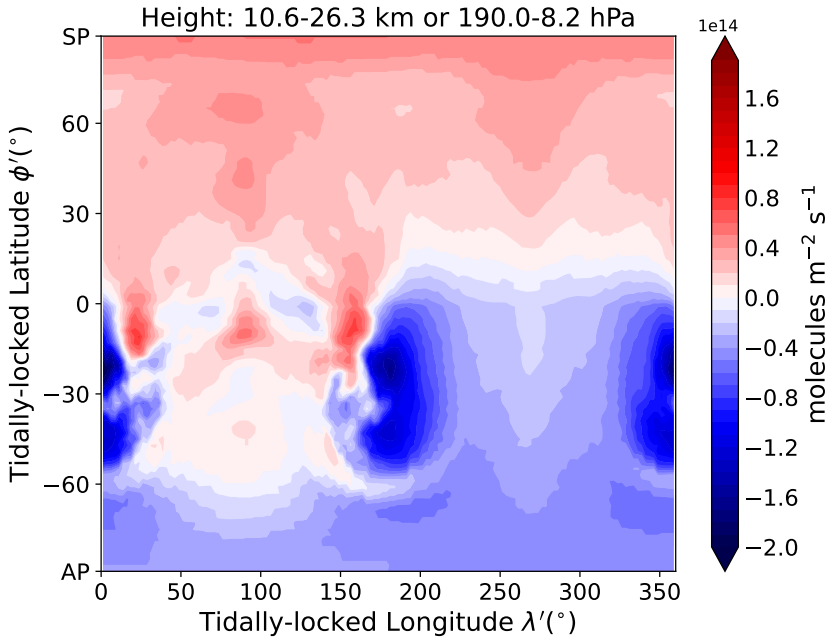

Figure 4.9: Vertical flux of ozone (F_{O_3} in molecules m^{-2} s^{-1}) between P_{max}=190 hPa and P_{min}=8.2 hPa. The predominantly downward exchange at the locations of the Rossby gyres illustrates how the enhanced ozone column densities are driven by the downward motions that are part of the stratospheric dayside-to-nightside circulation.

point can be spread out zonally towards the nightside, connecting with the ozone-producing region that is part of the overturning circulation from Section 4.3.2. At the nightside location of the jet, $\tau_u/\tau_w<1$, and the zonal wind is capable of homogenising any vertically-driven disequilibrium. The circumnavigating jet then leads to the relatively thin ozone column for $70°<\lambda'<110°$ and $220°<\lambda'<320°$ in Figure 4.3 (across all ϕ'). At the locations of the nightside gyres, Figure 4.10b shows that τ_u and τ_w are intermittently the smallest, indicating that both vertical and zonal mixing can drive disequilibrium abundances. However, as mentioned in Section 4.3.2, the edges of the gyres act as mixing barriers. Hence, the zonal transport leads to homogenisation within the gyres. Vertical mixing that is part of the overturning dayside-to-nightside circulation is dominant between ∼200 and 50 hPa at the gyre locations. This vertical mixing drives the observed disequilibrium abundances of tropospheric ozone at the gyre locations, and thus the maximum ozone column densities in Figure 4.3a.

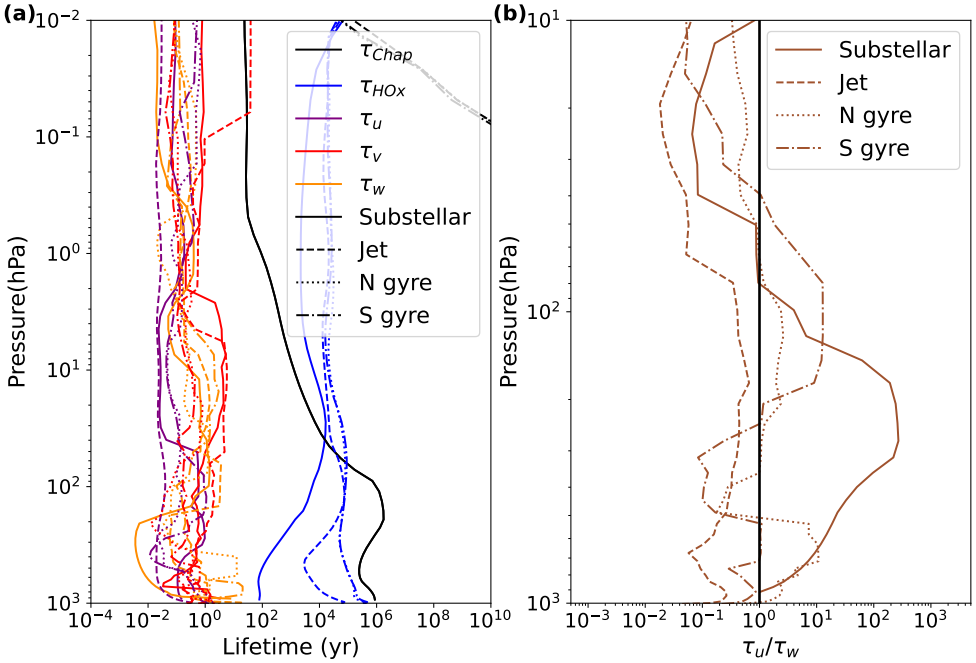

Figure 4.10: Dynamical and chemical lifetimes over four locations in the atmosphere: the substellar point, two regions over the gyres and one region over the nightside jet. (a) τ_u, τ_v and τ_w denote the dynamical lifetime versus zonal, meridional, and vertical transport, respectively. τ_{Chap} and τ_{HOx} show the chemical lifetimes of ozone versus loss by the Chapman termination reaction (R1) and the dominant HO_x catalytic cycle (R2), respectively. From the comparatively long chemical lifetimes, I deduce that dynamical processes control the chemical abundances. (b) The fraction of the zonal to vertical dynamical lifetimes in the lower stratosphere (between 100 hPa and 10 hPa) and troposphere (<100 hPa), along with a vertical line indicating where they are equal ($\tau_u/\tau_w=1$). Vertical transport is the dominant process for $\tau_u/\tau_w>1$ and horizontal transport for $\tau_u/\tau_w<1$.

Table 4.2: Species-weighted streamfunctions $\Psi'_{m,\mathrm{x}}$ in kg s^{-1} averaged over pressure levels corresponding to the troposphere and stratosphere. Shown for ozone and lightning-induced chemistry in the form of HNO_3 and N_2O_5.

	$\Psi'_{m,\mathrm{O_3}}$	$\Psi'_{m,\mathrm{HNO_3}}$	$\Psi'_{m,\mathrm{N_2O_5}}$
Troposphere	9.70×10^{5}	9.47×10^{-1}	4.44×10^{-2}
Lower stratosphere	6.09×10^{5}	6.07×10^{-3}	1.50×10^{-3}

4.3.4 Lightning-induced Chemistry

The impact of the overturning circulation goes beyond the spatial distribution of ozone, as is evident from the distribution of the age-of-air tracer as shown in Figure 4.7. Any tracer, gaseous or non-gaseous phase, can continue to circulate as long as its chemical lifetime exceeds the dynamical timescales. Hence, the overturning circulation is relevant for any so-called long-lived atmospheric tracer. I performed similar analyses using the species-weighted streamfunction as defined in Section 4.2.2 on the distributions of nitric acid (HNO_3) and dinitrogen pentoxide (N_2O_5). Both of these species are signatures of lightning-induced chemistry in these simulations as shown in Chapter 3. They are non-radical species with relatively long chemical lifetimes and are mainly destroyed by photolysis and wet deposition (rainout). In the dayside troposphere, the lifetimes against wet deposition are $\sim10^{-2}-10^{2}$ yr, while higher up in the atmosphere the lifetimes against photolysis are $\sim10-10^{2}$ yr. On the nightside, these loss processes are absent and thus their chemical lifetimes approach infinity.

I calculate $\Psi'_{m,\mathrm{HNO_3}}$ and $\Psi'_{m,\mathrm{N_2O_5}}$ similar to Equation 4.4, and calculate the mean of each of the species-weighted streamfunctions over the troposphere ($>10^{2}$ hPa) and mid-to-lower stratosphere ($1<$P$<10^{2}$ hPa). The results are shown in Table 4.2. The circulation cells weighted by HNO_3 and N_2O_5 are strongest in the troposphere, at ~0.95 and ~0.04 kg s^{-1}, respectively, because of the strong overturning circulation here (see Figure 4.5b). The troposphere is also the region where lightning flashes are predicted to occur and thus where HNO_3, N_2O_5, and their precursors are produced (see Figure 3.12). The factor 10^{6} and 10^{7} difference with the ozone-weighted streamfunction in Table 4.2 is a consequence of the much lower predicted abundances of HNO_3 and N_2O_5. Moving up to the stratosphere, I find that the ozone-weighted streamfunction is similar to the streamfunction in the troposphere, providing the connection to the nightside gyres. For HNO_3 and N_2O_5, the streamfunction is ~30 and 150 times lower in the stratosphere, due to low levels of stratospheric HNO_3 and N_2O_5 with the absence of lightning-induced chemistry at those pressure levels. Because of the lack of stratospheric HNO_3 and N_2O_5, the overturning circulation will not be able to accumulate these species at the locations of the nightside gyres (as is evident in the spatial distribution in Figure 3.13).

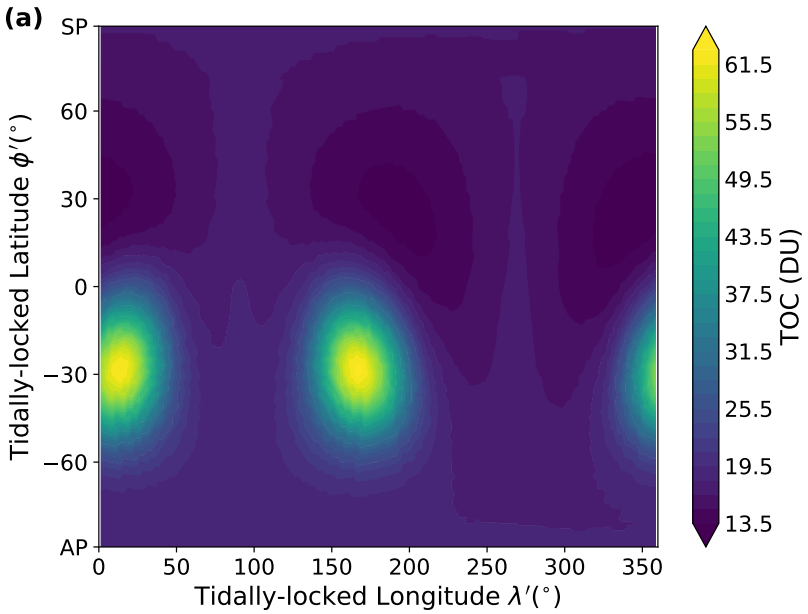

Figure 4.11: Total ozone column density, over 50 orbits of Proxima Centauri b for the 0.01 PAL O_2 case, again showing the spatially variable ozone layer with accumulation at the locations of the nightside Rossby gyres ($-60<\phi'<0$).

4.3.5 0.01 PAL O_2 Simulations

Figure 4.11 shows the ozone column density for a synchronously rotating planet around Proxima Centauri, assuming the atmosphere has 0.01 PAL O_2. I find lower ozone column densities (global average of 20 DU) with decreased O_2 levels, agreeing with a reduced ozone column for Earth around the Sun for decreased O_2 levels (Cooke et al., 2022). Nevertheless, significant spatial variability and the accumulation of ozone in the nightside gyres are still visible, similar to the 1 PAL case in Figure 4.3a. The highest ozone column densities of 63 DU are found at the gyre locations (as compared to 1401 DU in the 1 PAL case). The similarity in the spatial variability to the 1 PAL O_2 atmosphere suggests the existence of a similar circulation-driven mechanism.

To explore the capability of a 0.01 PAL O_2 atmosphere to support a stratospheric dayside-to-nightside circulation, Figure 4.12 shows the time evolution of the ozone mole fraction during part of the spin-up of this simulation. From day 1, ozone starts to form above 100 hPa, and starts to circulate towards the nightside after 10 days. After 100 days, the ozone layer is present between 40 and 3 hPa, and downward movement from the ozone layer at the gyre locations is visible ($-60^\circ<\phi'<0^\circ$). These features are even more pronounced on day 500, and persist afterwards. The vertical distribution and its temporal evolution show that a similar stratospheric dayside-to-nightside circulation followed by subsidence at the gyre locations drives the ozone accumulation over the gyres. Further diagnosis of the mechanism using the streamfunctions and vertical ozone flux (not shown) confirm this picture.

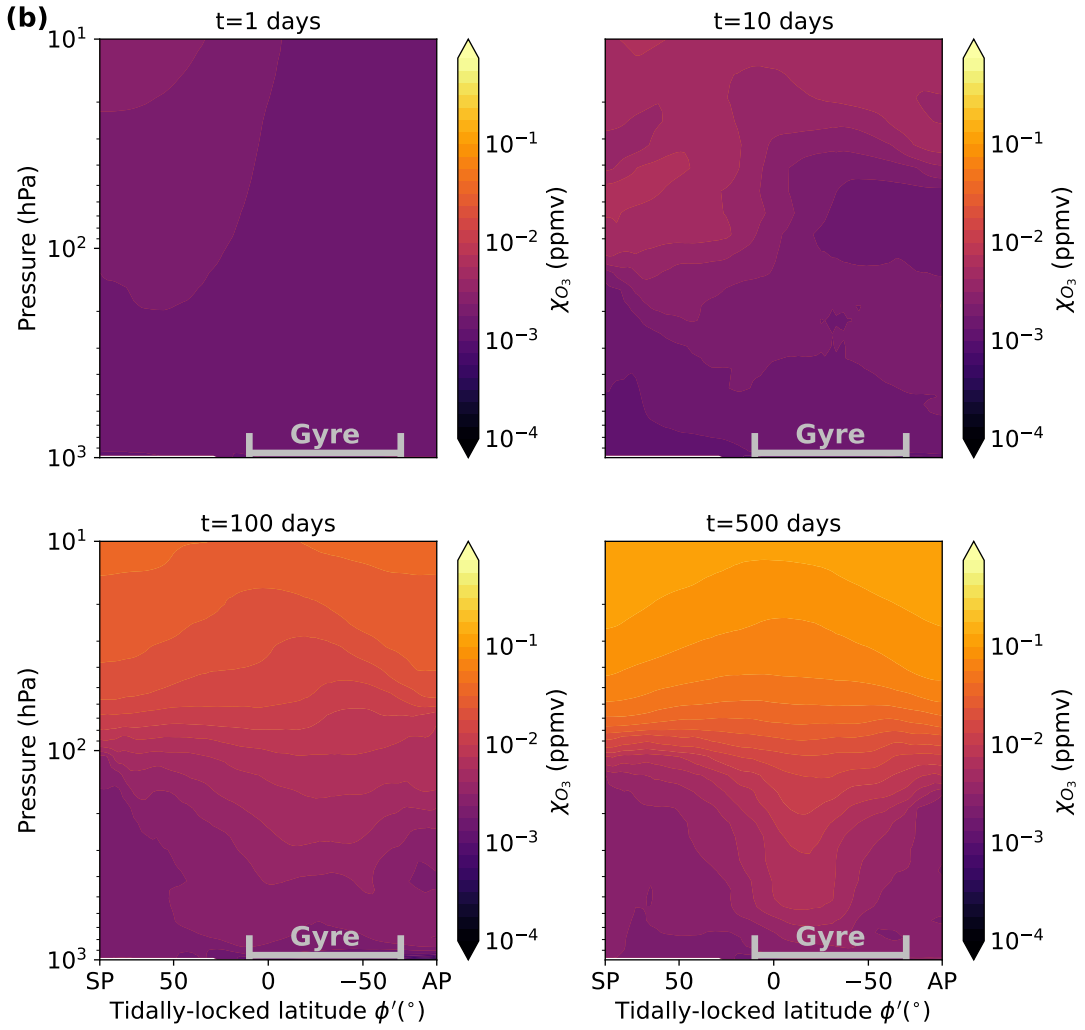

Figure 4.12: Ozone mole fraction during the spin-up of the simulation for the 0.01 PAL O_2 case, showing the mean meridional distribution in tidally-locked coordinates. I also show the tidally-locked latitudes corresponding to the nightside gyres in grey, and can see that the accumulation of ozone here happens in a similar way as in Figure 4.8.

4.4 Discussion

In this section, I start by describing the driving mechanism for the overturning circulation. I then show its impact on other long-lived tracers and discuss relevant temporal variability in the atmospheres of synchronously rotating exoplanets. Lastly, I produce synthetic emission spectra to investigate the observational impact of circulation-driven ozone chemistry.

4.4.1 Driving Mechanism of the Overturning Circulation

The tropospheric overturning circulation for moist, rocky exoplanets in a synchronous orbit is driven by the absorption of incoming stellar radiation and latent heat release on the dayside, and longwave radiative cooling on the nightside (e.g. Showman et al., 2013; Boutle et al., 2017). Wang and Yang (2022) study dry, rocky planets rotating synchronously around an M-dwarf star and find that the overturning circulation is indirectly driven by the stellar radiation, in the form of nightside cooling by CO_2. They find that an overturning circulation forms in a N_2-CO_2 atmosphere, but not in a pure N_2 atmosphere (Wang & Yang, 2022). Prescribed CO_2 distributions from Wang and Yang (2022) show that shortwave (SW) absorption on the planetary dayside only has a limited impact on the overturning circulation. CO_2 can cool an atmosphere when it is found in layers exhibiting a temperature inversion (Wang & Yang, 2022). Enhanced infrared emission from increasing CO_2 levels cools the Earth's stratosphere (Luther et al., 1977; Brasseur & Hitchman, 1988; Langematz et al., 2003; Shine et al., 2003; Fomichev et al., 2007). On synchronously rotating planets, this can induce a downward motion on the nightside that subsequently drives dayside-to-nightside overturning circulation.

Since I focus on the stratosphere, which is relatively dry even for a moist climate of a rocky exoplanet in a synchronous orbit, I can build upon these results in identifying the driving mechanism. The SW atmospheric heating rates in Figure 4.13a show that CO_2 (the green line) acts as an important SW absorber on the dayside. The main absorber in the troposphere is H_2O, whereas CO_2 starts to become dominant above ~ 170 hPa. In line with Wang and Yang (2022), I find that heating due to SW absorption by CO_2 plays a minor role in the troposphere. However, in the stratosphere CO_2 absorption can become important because peak emissions from M dwarfs are emitted at near-infrared (NIR) wavelengths, relatively long as compared to other stars. CO_2 (and H_2O) have strong NIR absorption bands (Selsis et al., 2007; Turbet et al., 2016; Lobo et al., 2023), which explains why CO_2 is the dominant absorbing species above ~ 170 hPa, in contrast to ozone in the Earth's stratosphere. As expected, the total dayside heating rates (solid black line) greatly exceed the nightside values (dashed line), forming a direct driver for the overturning circulation. Additionally, Figure 4.13b shows the longwave (LW) heating rates, with negative values indicating cooling of the atmosphere. The black lines show stronger LW cooling on the nightside as compared to the dayside. Again, CO_2 is mainly responsible for these cooling rates, due to its presence in temperature inversion layers at ~ 100 and ~ 1 hPa. This radiative cooling on the nightside drives a large-scale downwelling which,

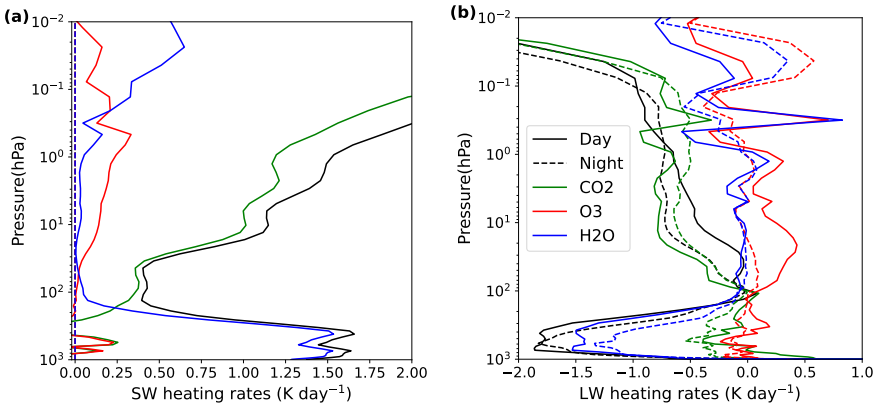

Figure 4.13: Atmospheric heating (and cooling) rates, for (a) the SW radiation and (b) LW radiation. Solid lines show the hemispheric average over the dayside and dashed lines over the nightside. The coloured lines indicate the individual components contributing to the total heating rates in black, showing that CO_2 (green) becomes the dominant contributor to the dayside SW heating rates and that LW cooling is also mainly driven by CO_2.

together with SW heating on the dayside, supports the stratospheric overturning circulation (Edson et al., 2011; Koll & Abbot, 2016; Wang & Yang, 2022), and can explain the ozone maxima at the locations of the nightside gyres. The atmospheric pressure within the gyre is relatively low, analogous to the eye of tropical cyclones (Schubert et al., 2007). Such a pressure gradient naturally induces downward transport at the gyre locations. An important follow-up to this study is to investigate the ozone distribution for a variety of rotation states (see e.g. Carone et al., 2018; Haqq-Misra et al., 2018; Chen et al., 2019) in light of the circulation-driven chemistry proposed here.

4.4.2 Long-lived Atmospheric Tracers

The stratospheric dayside-to-nightside circulation affects other tracers than ozone, as I show with the results for the age-of-air in Section 4.3.2 and the lightning-induced species in Section 4.3.4. In the presence of stellar flares, Ridgway et al. (2023) show that the gyres are depleted in ozone (see their Figure 12). This can also be explained by the stratospheric overturning circulation, since flare-induced chemistry will result in a large amount of nitric oxide (NO) and nitrogen dioxide (NO_2) (together known as the NO_x chemical family) at stratospheric levels (Ridgway et al., 2023). This NO_x can follow the stratospheric overturning circulation from the dayside to the nightside. Once on the nightside, it can be transported downward at the location of the gyres and locally deplete the ozone through the NO_x catalytic cycle (Ridgway et al., 2023), given that flares produce sufficient NO_x.

The impact of the overturning circulation on the distribution of ozone has analogies with studies that simulate tracers in the atmospheres of synchronously rotating hot Jupiters. Parmentier et al. (2013) identified dynamical mixing in hot Jupiter atmospheres as a process leading to cold trapping of condensible species on the planetary nightside. Their experiments involve gravitational settling as a source of these condensed particles, which leads to a gradient of tracer abundance, with fewer particles as we move up through the atmosphere. Upward mixing induced by the large-scale dynamics balances the settling of these particles, preventing the complete depletion of particles and inducing a strong spatial variation in the tracer abundances. The extent of the mechanism depends on the strength of frictional drag (Komacek et al., 2019). The mechanism does not require convection but follows the large-scale atmospheric motions that are ultimately driven by the dayside-nightside heating contrast (Parmentier et al., 2013), as is the case for the circulation-driven ozone distribution discussed here. Another example of a long-lived tracer is photochemical haze, which is also expected to form at stratospheric altitudes (e.g. Arney et al., 2017) and, for synchronously rotating exoplanets, only on the dayside of a planet (e.g. Steinrueck et al., 2021). Steinrueck et al. (2021) show that the 3D distribution of small photochemical hazes (≤ 10 nm) in hot Jupiter atmospheres is also driven by dynamical mixing. The highest tracer abundances are found above the production peak, indicating upwelling on the dayside. Then a divergent flow leads to transport towards the poles and the nightside. On the nightside, the haze particles are then advected downward and get trapped in the mid-latitude gyres (Steinrueck et al., 2021). These dynamically-induced asymmetries can produce distinctions between a planet's terminator regions, as shown for hot Jupiters (Drummond et al., 2020; Steinrueck et al., 2021; Zamyatina et al., 2023). Following up on the results presented here, we will investigate the potential terminator variability of the circulation-driven ozone distribution and its observability.

4.4.3 Time Variability

Besides spatial variability in tracer distributions, simulations of synchronously rotating exoplanets exhibit several modes of temporal variability. The formation of the Rossby gyres is due to the thermal forcing asymmetries (Showman & Polvani, 2010, 2011). Cohen et al. (2023a) show that these gyres oscillate over longitude λ, with the extent depending on the planet's rotation period and thus dynamical state. Planets with a slower rotation rate have longer oscillation periods, resulting in a 157.5-day oscillation for Proxima Centauri b, which was determined from the temporal evolution of the cloud cover (Cohen et al., 2023a). Using a dynamical systems approach, Hochman et al. (2022) compare TRAPPIST-1e in a synchronous orbit to Earth and find that the climate extremes on a synchronously rotating exoplanet are more sensitive to changes in the partial pressure of CO_2.

Since the stellar spectra are constant in time and the planet rotates in a 1:1 resonant orbit without eccentricity and/or obliquity, such variability has to be produced by internal atmospheric variability. Cohen et al. (2023a) show that feedback between cloud cover and the incoming stellar radiation can influence the dynamics and drive zonal movement of the gyres, leading to variations in humidity and cloud cover over time. The accumulation of ozone (Figure 4.3) depends on the gyres so we can expect a corresponding variation in atmospheric ozone. To verify this, in Figure 4.14 I track the temporal evolution of the tidally-locked coordinates corresponding to the maximum in the ozone layer and the minimum in the vertical flux of ozone (F_{O_3}, thus corresponding to the strongest downward flux). Figure 4.14a shows ϕ' and Figure 4.14b λ' corresponding to these extrema, and the approximate extents of the gyres are indicated in yellow. The locations of the maximum ozone column density and minimum vertical flux are not perfectly aligned, because the maximum ozone column density corresponds to a long-term mean location of the gyre and thus depends on vertical fluxes over an extended period. The minimum vertical flux represents a snapshot in time and is also impacted by the upward flux from the gyre (see the red regions in Figure 4.9). From Figure 4.14a, I determine that the maximum ozone column density is generally found at ϕ' corresponding to the gyre locations, with a small meridional variation over time. The minimum F_{O_3} shows more variability in tidally-locked latitude, but the strongest downward flux is generally also located at the gyre locations. In Figure 4.14b, the variations in the tidally-locked longitude λ' over time are visible. The low-λ' gyre typically hosts the maximum ozone column, but there are periods when the mid-λ' gyre hosts the maximum ozone column. The variations in the minimum F_{O_3} broadly align with the maximum in the ozone column density, following the gyre position that has the maximum ozone column at that time. The location of minimum F_{O_3} shows more variability due to its instantaneous nature.

I translate the temporal variability into simulated observables using the Planetary Spectrum Generator (PSG: Villanueva et al., 2018; Villanueva et al., 2022). To simulate an emission spectrum that includes half the planetary dayside and half the nightside, I extract the atmospheric pressure and temperature and mole fractions of relevant chemical species (N_2, O_2, CO_2, H_2O, O_3, N_2O, HNO_3 and N_2O_5) for these locations, take the zonal and meridional averages and compute radiative transfer with PSG. In Figure 4.15 I show the resulting planet-to-star contrast for the JWST-MIRI wavelength range, along with a zoom-in that focuses on the ozone 9.6 μm feature. Using extrema in the gyre positions over time from Figure 4.14, I simulate the emission spectra of Proxima Centauri b for different 6-day intervals and indicate the maximum day in the legend of Figure 4.15. I find variations around the ozone features at 9.6 μm and between 14-16 μm (due to absorption by CO_2, H_2O, and ozone). Hence, the region around 9.6 μm is the place to look for ozone variability. Focusing on the region around 9.6 μm shows that the maximum temporal variations are about 0.5 ppm. Spectroscopic characterisation of these absorption features to the level needed to identify these temporal variations is challenging, as detecting the features themselves would already require many

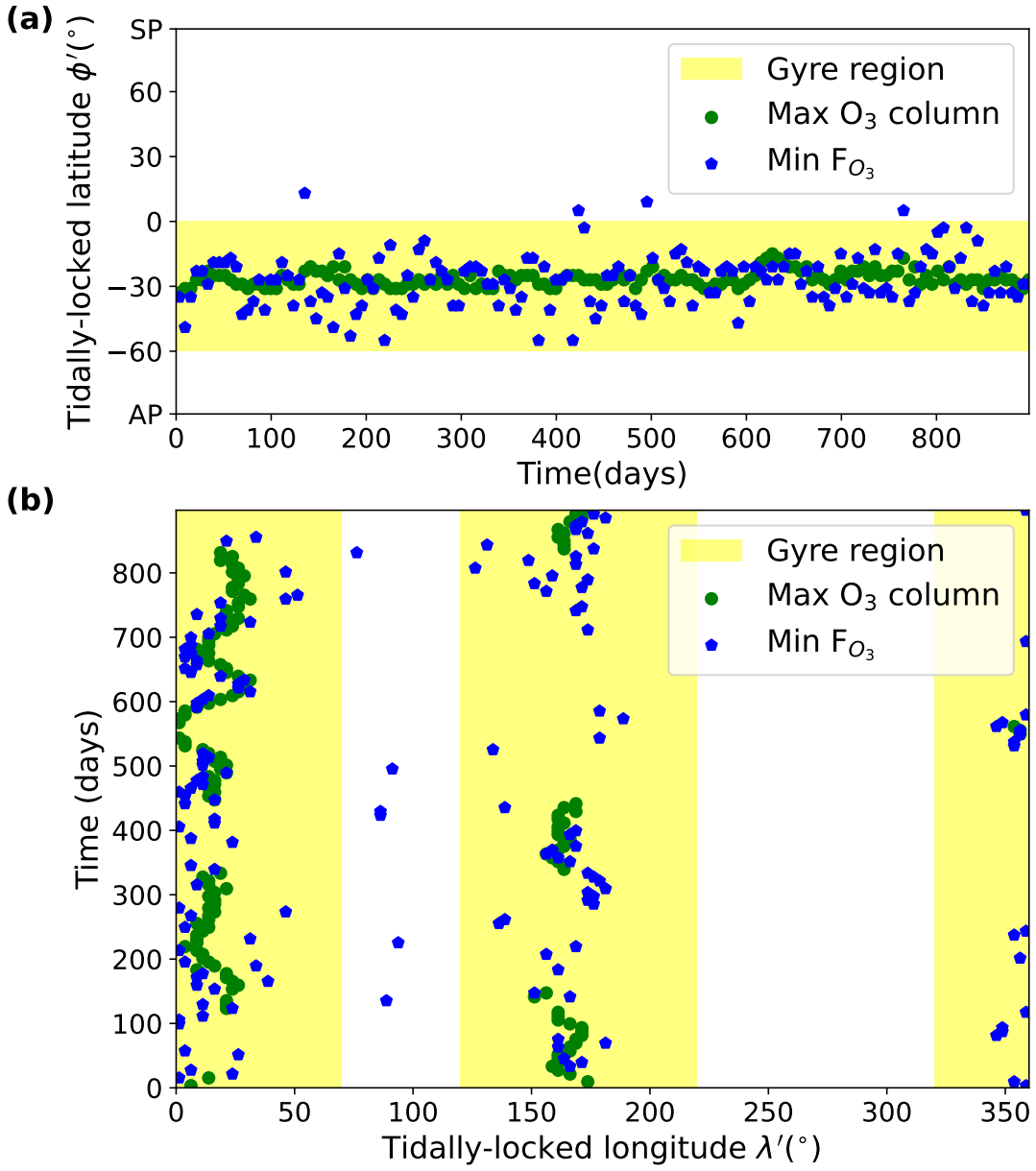

Figure 4.14: Temporal evolution of the locations of extremes in the ozone column density (see Figure 4.3) and vertical ozone flux F_{O_3} as defined in Equation 4.9. I extract the tidally-locked latitude ϕ' and longitude λ' corresponding to the maximum ozone column density (shown as the green dots) and the minimum F_{O_3} (or the strongest downward flux, shown as the blue hexagons), to look for correlations between the two. Panels a and b show the temporal evolution of ϕ' and λ', respectively, and the yellow rectangles indicate the gyre locations.

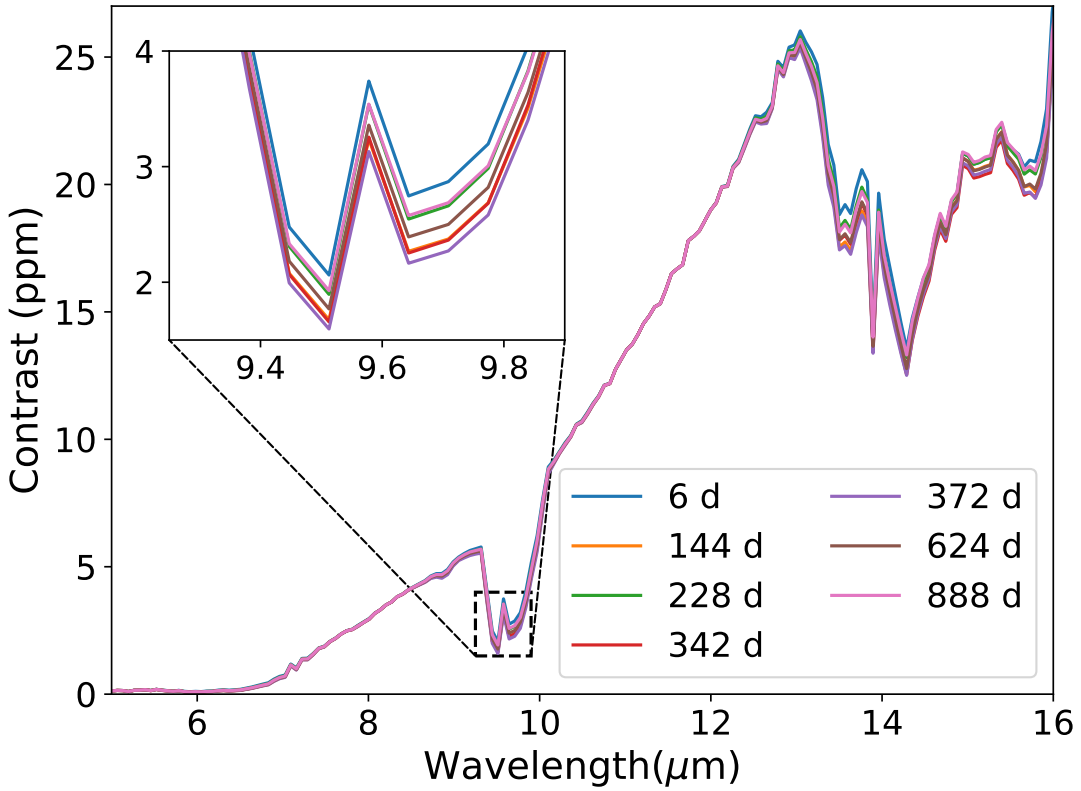

Figure 4.15: Simulated emission spectra of Proxima Centauri b, for a range of 6-day intervals informed by extrema in the gyre locations (Figure 4.14). The legend shows the maximum day corresponding to each of the 6-day intervals. The inset region shows the region corresponding to the 9.6 μm ozone feature in greater detail.

days of co-added observations (Kreidberg & Loeb, 2016). However, the recent photometric observations of the thermal emission from TRAPPIST-1 b with JWST indicate the telescope's capacity to observe favourable terrestrial exoplanets (Greene et al., 2023). Mission concepts such as the Large Interferometer For Exoplanets (Quanz et al., 2022) further utilise the mid-infrared in the characterisation of terrestrial exoplanets and will have to consider the impact of 3D spatial and temporal variability in atmospheric dynamics and chemistry.

The hot Jupiter simulations of passive tracers by Parmentier et al. (2013) also exhibit significant temporal variability. Oscillations in the equatorial jet and variations in the dayside-to-nightside flow produce large local variations, which could again impact the spectroscopic observations of the planets, both when conducting extended observations and when observing the same object at two different points in time.

Another mode of variability in the atmospheres of exoplanets in synchronous orbits around M dwarfs is the Longitudinally Asymmetric Stratospheric wind Oscillation (LASO; Cohen et al., 2022). Since this entails a stratospheric turnover of wind directions, it could be relevant for stratospheric ozone. Analysing ozone mole fractions over time, I find variations in the ozone

mole fractions above $\sim$30 km (or $\sim$3.5 hPa) as a consequence of the LASO. However, these variations occur higher up in the atmosphere than the overturning circulation feeding the gyres and thus do not affect the gyre abundances significantly. Hochman et al. (2022) investigate atmospheric dynamics, atmospheric variability and climate extremes using a dynamical systems approach. As compared to an Earth analogue, they find significantly different spatial variability in the climate extremes for TRAPPIST-1 e, assuming it is synchronously rotating. Varying basic parameters like the partial pressure of CO_2, Hochman et al. (2022) find that the climate and climate extremes on TRAPPIST-1e are more sensitive than the Earth analogue. Importantly, climate variability on synchronously rotating exoplanets may be of a similar level as the variability produced by the seasons on Earth (Hochman et al., 2022), which seems to be supported by the findings on variability in the ozone column densities. Variations in ozone column densities of up to $\pm$8 DU on the dayside and as much as $\pm$30 DU close to the gyres on the nightside are seen, corresponding to their zonal movement as shown in Figure 4.14. Tropospheric ozone over the Earth's northern midlatitudes shows a seasonal variability of 7–8 DU, related to stratosphere-troposphere exchange (Hsu & Prather, 2009). A comprehensive comparison is beyond the scope of this paper, but I plan to explore this further as part of an in-depth investigation of the observability of the circulation-driven ozone distribution.

External drivers of variability in exoplanet atmospheres can also drive temporal variations in spectral features. Stellar flares are a likely cause for planets orbiting M-dwarf stars, and can modulate the abundance of photochemically produced species such as ozone, HO_x, and NO_x (Segura et al., 2010; Scheucher et al., 2018; Chen et al., 2021; Ridgway et al., 2023). Orbital configuration, in particular the eccentricity, can cause variations in the abundance of chemical species over time, as Liu et al. (2023) showed for the water vapour abundance on an Earth-like planet. I leave an expansion of circulation-driven atmospheric chemistry in eccentric orbits for future work. In compact multiplanet systems, planet-planet interactions may produce spin-orbit variations that cause libration of the substellar point (Chen et al., 2023). This libration strongly affects the climate of planets orbiting close to the outer edge of the Habitable Zone and may bring temporal variations in photo- and thermochemistry along. Lastly, impacts of planetesimals can cause loss of atmospheric mass (Schlichting & Mukhopadhyay, 2018) and thereby affect the extent of spectral features. Identifying the effects of each of these external drivers will benefit from understanding internal drivers of atmospheric variability, and vice versa.

4.5 Conclusions

I use a 3D CCM (UM-UKCA) to study the spatial structure of the ozone layer on an exoplanet rotating in a 1:1 spin-orbit resonance around an M-dwarf star, using the parameters corresponding to Proxima Centauri b. The results are relevant for similar M-dwarf orbiting planets, specifically for slowly rotating planets with a strong overturning circulation and a single equatorial jet in the troposphere. I investigate the spatial variability in the ozone layer and specifically the accumulation in two nightside ozone maxima, in the form of maximum ozone columns at the locations of the permanent Rossby gyres. This work builds upon previous studies that have shown that M-dwarf radiation supports the emergence of a global ozone layer.

I show that stratospheric dayside-to-nightside circulation and downward motion over low-pressure nightside gyres can explain the spatial variability in ozone. The photochemistry required to initiate the Chapman mechanism of ozone formation is limited to the dayside hemisphere, given the absence of incoming stellar radiation on the nightside. I find a connection between the ozone production regions on the dayside and the nightside hemisphere, using the transformation to the tidally-locked coordinate system. Meridional streamfunctions that I calculate from the divergent wind component illustrate the existence of a stratospheric dayside-to-nightside overturning circulation. This circulation consists of a single circulation cell characterized by upwelling motion in the ozone production regions, followed by stratospheric dayside-to-nightside transport and downwelling motions at the locations of the nightside gyres. The downwelling motion produces a flux of ozone from the stratosphere into the troposphere, leading to well-defined maxima in the ozone distribution. I find that the stratospheric dayside-to-nightside circulation controls the ozone distribution for both a 1 PAL O_2 and a 0.01 PAL O_2 atmosphere. The circulation-driven ozone chemistry impacts spectroscopic observations, although the impact of temporal variability is limited to sub-ppm levels in emission spectra.

By investigating the impact of the stratospheric overturning circulation on lightning-induced chemical species (also limited to dayside production, but solely in the troposphere), I explain why these species do not show a similar accumulation in the nightside gyres. I show with an age-of-air tracer experiment that the stratospheric overturning circulation also affects other tracer species in the stratosphere, including gaseous chemical tracers and particulate components of photochemical haze, with the only requirement that the dynamical lifetimes are sufficiently short compared to chemical timescales.

I identify hemispheric contrasts in atmospheric heating and cooling rates as the driver for the overturning circulation. Dayside heating can directly drive the overturning circulation, and nightside cooling provides an indirect component by inducing local downward motion. The relatively low atmospheric pressure over the nightside gyres further induces downward motion here. Since the stratosphere is relatively dry, CO_2 absorption is the main contributor to these heating and cooling rates. Ozone absorption also contributes to the rates, but its contribution is weaker than CO_2 since M-dwarf fluxes peak close to absorption bands of CO_2.

For the first time, I find a connection between the ozone-producing dayside of synchronously rotating planets and the simulated ozone maxima on the nightside, covering hemispheric scales and multiple vertical levels in the stratosphere and troposphere. The role of the stratospheric dayside-to-nightside circulation in driving the ozone distribution around the planet illustrates the necessity of 3D model to capture atmospheric processes correctly. Any robust interpretation of spectroscopic observations will need to understand the spatial and temporal variability of chemical species due to such circulation-driven chemistry.

Chapter 5

Observational signatures of 3D atmospheric chemistry for Earth-like exoplanets in spin-orbit resonances.

This Chapter will be submitted for publication as:

Observational signatures of 3D atmospheric chemistry for Earth-like exoplanets in spin-orbit resonances.

Marrick Braam, Paul I. Palmer, Leen Decin, Nathan J. Mayne, James Manners, Sarah Rugheimer

Author contributions: Marrick Braam conceived the science question, performed the simulations and analyses, and wrote the manuscript. Paul Palmer and Leen Decin contributed via regular discussions and advice and provided feedback on the manuscript. Nathan Mayne and James Manners contributed to the development of the model. Sarah Rugheimer contributed to the analysis of the TRAPPIST-1 d climate state. All co-authors provided feedback to the manuscript.

5.1 Introduction

Exoplanet discoveries cover diverse stellar, orbital, and planetary characteristics. Exoplanets are easier to characterise with current observatories around relatively cool stars such as M- and K-type stars, because of observational advantages (Charbonneau & Deming, 2007) and the high occurrence rates of such stars and planets orbiting them (Bochanski et al., 2010; Petigura et al., 2013; Dressing & Charbonneau, 2015). Due to their relatively low luminosity, the circumstellar Habitable Zone (HZ) – the region in which liquid water can exist on a planetary surface (Kasting et al., 1993) – is located close to the star. Consequently, a planet orbiting in the HZ will experience a differential gravitational field inducing strong tidal torques in the planet. The torques affect the planet's rotational angular momentum until a specific frequency is reached in a process called tidal locking (Goldreich & Peale, 1966;

Stephen H Dole, 1970; Barnes, 2017; Pierrehumbert & Hammond, 2019). These frequencies are known as spin-orbit resonances akin to Solar System examples like the Moon's 1:1 spin-orbit resonance around the Earth and Mercury's 3:2 spin-orbit resonance around the Sun. Barnes (2017) find that tidal locking is possible for planets around M-, K-, and G-type stars but might also be a consequence of planet-planet interactions in a multiplanet system.

The timescales associated with tidal locking are short compared to planetary lifetimes (Goldreich & Peale, 1966; Pierrehumbert & Hammond, 2019) for close-in exoplanets, as shown in Figure 1.3. The final state following the process of tidal locking depends on a planet's eccentricity e (Goldreich & Peale, 1966; Dobrovolskis, 2007; Pierrehumbert & Hammond, 2019): a 1:1 spin-orbit resonance or synchronous rotation is the most likely state for planets with $e \lesssim 0.2$, a 3:2 spin-orbit resonance is most likely for $0.2 \lesssim e \lesssim 0.35$. The resulting planetary climates for these two resonances are markedly distinct (e.g. Turbet et al., 2016; Boutle et al., 2017). Higher-order resonances such as 2:1 are possible for planets with $e \gtrsim 0.4$, but the climatic consequences are more subtle. 1:1 spin-orbit resonances lead to a permanent dayside and nightside hemisphere whereas each hemisphere in a 3:2 resonance alternately experiences daytime for a full orbit followed by nighttime for a full orbit.

To explore the habitability of such planetary environments, 3-D General Circulation Models are employed to simulate the main physical processes in a planetary atmosphere and to predict the resulting climate. For planets in 1:1 resonances, these show large temperature differences between the dayside and nightside hemisphere, although atmospheric heat transport can prevent atmospheric collapse (Joshi et al., 1997). The atmospheric circulation of such exoplanets are likely to exhibit distinct regimes depending on a planet's rotation rate, radius, and atmospheric composition (e.g. Merlis & Schneider, 2010; Edson et al., 2011; Carone et al., 2014, 2015, 2016; Kopparapu et al., 2017; Noda et al., 2017; Haqq-Misra et al., 2018), and the regimes are summarized in figure 1 of Carone et al. (2018). The circulation regimes can be diagnosed intuitively using the Rossby deformation radius (determining the maximum extent of zonal overturning circulation) and Rhines length (determining the maximum extent of zonally elongated turbulent structures) (Haqq-Misra et al., 2018). In this study, I consider two distinct circulation regimes:

- The first regime exhibits weak superrotation with a single equatorial jet, planetary-scale turbulent structures, and mainly shows zonal gradients in atmospheric quantities like temperature. This 'Rhines rotator' regime (Haqq-Misra et al., 2018), also known as 'Type II circulation' (Noda et al., 2017), and the 'single jet' regime (Sergeev et al., 2022a).
- The second regime exhibits superrotation in a pair of midlatitude jets and and mainly shows meridional gradients in atmospheric quantities like temperature. This is the 'fast rotator' regime (Haqq-Misra et al., 2018), also known as 'Type IV circulation' (Noda et al., 2017), and the 'double jet' regime (Sergeev et al., 2022a).

Sergeev et al. (2022a) show that a single planet close to a regime transition in terms of its rotation rate can also exhibit different circulation regimes, depending on the initial conditions and model parameterisations.

A 3:2 resonance results in a changing daytime hemisphere for the planet and exhibits meridional gradients in atmospheric quantities, such as large equator-to-pole differences in temperature that exceed the zonal gradients (Turbet et al., 2016; Boutle et al., 2017; Del Genio et al., 2019). Therefore, Del Genio et al. (2019) suggest that – at least in the absence of eccentricity – the circulation is more like that of a slowly rotating Earth (see also Del Genio & Suozzo, 1987), with a meridional circulation of one Hadley cell per hemisphere and westward jets over the midlatitudes. Including eccentricity will cause an irradiation pattern and associated heating concentrated in two hot spots, one for each hemisphere (Dobrovolskis, 2015; Boutle et al., 2017; Colose et al., 2021). Additionally, an eccentric orbit will produce an increase of the mean stellar flux over one orbit as compared to the circular case (Williams & Pollard, 2002; Dressing et al., 2010; Bolmont et al., 2016). Spin-orbit resonances may affect the inner edge of the HZ, as defined by the moist greenhouse limit of the maximum stratospheric water vapour abundances to retain the Earth's oceans (Ingersoll, 1969; Kasting, 1988) or the Simpson-Nakajima limit in outgoing longwave radiation (Simpson, 1928; Nakajima et al., 1992; Goldblatt et al., 2013; Chaverot et al., 2022). However, Colose et al. (2021) find that higher-order resonances have little effect on the inner edge since warming of the planet is accompanied by a drier stratosphere.

For both resonance states, the interplay between atmospheric dynamics, chemistry, and thermodynamics will control the distribution of atmospheric tracers such as clouds and chemical species. Previous work has shown that the distribution of clouds depends on the rotation rate and circulation regime of 1:1 resonant planets (e.g. Komacek & Abbot, 2019; Sergeev et al., 2022a), affecting the planetary climate (Yang et al., 2013; Yang & Abbot, 2014; Kopparapu et al., 2016). Convective clouds cover the dayside of 1:1 resonant planet with zonal variations and a much thinner nightside cloud deck (see figure 3 of Boutle et al., 2017). For 3:2 resonant planets, the cloud cover follows the hot spots in temperature and shows banded structures with meridional variations and a relatively thin high-latitude cloud deck (see figure 10 of Boutle et al., 2017).

The circulation mechanisms also affects the distributions of chemical species for 1:1 resonant planets as shown by simulations using 3D coupled climate-chemistry models or CCMs (see Chapter 3, also Chen et al., 2019, 2021; Ridgway et al., 2023). Even though the production of photochemical species like ozone or lightning-induced chemistry is limited to the dayside, in Chapter 4 I demonstrate that a stratospheric dayside-to-nightside circulation can drive the accumulation of such species on the nightside. Interactive chemistry for a 3:2 resonant orbit has not yet been investigated but, given the meridional gradients in temperature and more Earth-like circulation discussed above, we might expect a mechanism similar to the Brewer-

Dobson circulation, which controls the distributions of species like ozone and water vapour on Earth (e.g. Brewer, 1949; Dobson, 1956; Butchart, 2014). The Brewer-Dobson circulation describes the ascent of chemically enriched air in the tropics, followed by equator-to-pole transport in the stratosphere, and finally descent at higher latitudes. In the case of radiatively active tracers – like clouds, ozone, or water vapour – such circulation mechanisms and the resulting spatial distributions in turn affect the thermal structure of a planetary atmosphere, depending on the spectral energy distribution of the host star (see e.g. Godolt et al., 2015). In turn, such radiative feedbacks can affect the dynamical state of the atmosphere (Hochman et al., 2023; De Luca et al., 2024)

The complex 3D interplay between stellar radiation, planetary orbit, atmospheric dynamics, and (photo)chemistry determines the planetary climate and habitability as well as potential spectroscopic observations. In emission, reflection, or transmission, each of these observations will be affected by 3D spatial variations (Turbet et al., 2016; Boutle et al., 2017; Cooke et al., 2023b). Additionally, a range of temporal variations are predicted by CCM simulations of 1:1 resonant planets and affect observations, including seasonal variations (Cooke et al., 2023b), internal atmospheric variability (see Chapter 4; also Cohen et al., 2022, 2023a; De Luca et al., 2024), or variability due to external causes such as flares or cosmic rays (Segura et al., 2010; Scheucher et al., 2018; Chen et al., 2021; Ridgway et al., 2023). The passage through periastron and apoastron for a planet in an eccentric 3:2 resonant orbit might be another mode of thermal and chemical variation with observational consequences. Emission spectroscopy is particularly useful since 1) it probes the pressure-temperature structure of the atmosphere (Madhusudhan & Seager, 2009), 2) observes a planetary hemisphere at all times, 3) can be done for most of the orbit, and 4) are less impacted by clouds (e.g. Kitzmann et al., 2011).

In this study, I have investigated the 3D interplay between stellar radiation, atmospheric dynamics, and (photo)chemistry for two tidally locked planets around M-stars – nominally Proxima Centauri b (Anglada-Escudé et al., 2016) and TRAPPIST-1 d (Gillon et al., 2017) – simulating both a 1:1 and 3:2 spin-orbit resonance. These exoplanets receive different amounts of stellar radiation and are known to exhibit distinct circulation regimes for a 1:1 resonant orbit, which I will compare with the effects of an eccentric 3:2 resonant orbit. In Section 5.2 I describe the CCM configurations, the calculation of stellar radiation in an eccentric orbit, planetary configurations, and the generation of emission spectra. I report the findings on the orbital effects on 3D atmospheric chemistry in Section 5.3. This Section will also present the observational consequences of spatial and temporal variations in atmospheric chemistry. Finally, I will put the results of this Chapter into context and provide the main conclusions in Section 5.4.

5.2 Methods

This Section begins with an introducion of the 3D CCM. I then describe the main characteristics of both planet configurations (Section 5.2.2) and the general simulation setups (Section 5.2.3). Finally, Section 5.2.4 elaborates on the generation of emission and transmission spectra from the 3D CCM data.

5.2.1 Coupled Climate-Chemistry Model

The 3D CCM consists of the Met Office Unified Model (UM) as the GCM coupled with the UK Chemistry and Aerosol framework (UKCA), as described in Chapter 2. UM-UKCA is used to describe the atmospheric dynamics and chemistry for configurations of Proxima Centauri b and TRAPPIST-1 d. For both cases, I assume an aquaplanet with 1 bar surface pressure and use a horizontal resolution of 2 by 2.5° in latitude and longitude, like in Chapters 3 and 4.

The UM is used in the Global Atmosphere 7.0 configuration (Walters et al., 2019), including the ENDGAME dynamical core to solve the equations of motion (Wood et al., 2014). Parametrized sub-grid processes include convection (mass-flux based on Gregory and Rowntree 1990), water cloud physics (Wilson et al., 2008), turbulent mixing (Lock et al., 2000; Brown et al., 2008) and the emergence of lightning (Price & Rind, 1992; Luhar et al., 2021, see also Chapter 3). Radiative transfer through the atmosphere is treated by the Suite of Community Radiative Transfer codes based on Edwards and Slingo (SOCRATES) scheme (Edwards & Slingo, 1996). The UM is a state-of-the-art model for the prediction of Earth's weather and climate and was in recent years adapted to the study of several types of exoplanets, including terrestrial planets (e.g. Mayne et al., 2014a; Boutle et al., 2017; Lewis et al., 2018; Eager et al., 2020; Yates et al., 2020) but also Mini-Neptunes (e.g. Drummond et al., 2018a) and hot Jupiters (e.g. Mayne et al., 2014b, 2017). Furthermore, the UM was part of the Trappist-1 e Habitable Atmosphere Intercomparison (THAI) project (Fauchez et al., 2022; Sergeev et al., 2022b; Turbet et al., 2022).

The incoming stellar radiation and its passage through the atmosphere as well as the photolysis rates of chemical species will change over time with a dependence on the orbital parameters. The inclusion of positional astronomy within SOCRATES (Edwards & Slingo, 1996; Manners et al., 2021) and UKCA/Fast-JX is based on the description in Smart (1944) and Mueller (1995). As described in Section 2.1.2, the orbital parameters of the planetary system are used to calculate the varying stellar zenith angle (ζ) and normally incoming stellar radiation at the top of the atmosphere (S_{TOA}). In turn, the model calculates the incoming stellar radiation S at any location as:

$$S(t) = S_{TOA}(t) \times \cos(\zeta). \tag{5.1}$$

The equation of time (Mueller, 1995) corrects for the variable length of day due to the eccentric orbits of Proxima Centauri b and TRAPPIST-1 d in a 3:2 resonance.

UKCA is used to simulate the global atmospheric chemical composition and its coupled interaction with the climate and its main components are described in Section 2.2. UKCA includes gas-phase chemistry and uses the UM for large-scale advection, convective transport and boundary layer mixing of the chemical tracers (Morgenstern et al., 2009; O'Connor et al., 2014; Archibald et al., 2020). Additionally, the Fast-JX photolysis scheme is implemented within UKCA, calculating photolysis rates of chemical species in the atmosphere (Wild et al., 2000; Bian & Prather, 2002; Neu et al., 2007; Telford et al., 2013). Fast-JX uses multi-scattering eight-stream radiative transfer – taking into account the varying optical depths of Rayleigh scattering, absorbing gases, clouds, and aerosols – to provide an interactive treatment of photolysis in calculating the 3D distribution of chemical species in the atmosphere. Fast-JX was adapted to enhance its flexibility in terms of stellar radiation in Section 3.2.3. I distribute the stellar flux over the 18 wavelength bins of Fast-JX (covering 177–850 nm), as illustrated in Figures 2.2 and 3.1. During the CCM simulations, I rescale these fluxes to the orbital evolution of a planet, interactively calculating photolysis rates over the planetary orbit. The chemistry included is a reduced version of UKCA's Stratospheric-Tropospheric scheme (StratTrop, Archibald et al., 2020), including the Chapman mechanism of ozone formation, and the hydrogen oxide (HO_x) and nitrogen oxide (NO_x) catalytic cycles. This results in 21 chemical species that are connected by 71 reactions, as elaborated in Section 2.2.5. The atmospheres are initialized at an Earth-like atmospheric composition, using pre-industrial values of N_2, O_2, and CO_2. Water vapour abundances are determined interactively following evaporation from the surface ocean. The atmospheric chemistry is driven by photolysis and the atmospheric thermal structure. Additionally, lightning flashes provide a source of nitrogen oxide to drive the NO_x catalytic cycle, as described in Section 3.2.4.

5.2.2 Planet Configurations

Tidal interactions between the planet and its host star or other planets in the system can change a planet's spin state and orbital eccentricity. This is especially significant for the M-dwarf orbiting planets such as Proxima Centauri b and TRAPPIST-1 d (Shields et al., 2016). For these planets, I configure CCM simulations for two distinct orbital setups to investigate the coupled 3D evolution of the climate and atmospheric chemistry, as shown in Table 5.1. The 1:1 spin-orbit resonant cases represent synchronous rotation resulting in a permanent dayside and nightside hemisphere for a planet and are the most likely orbital states for $e \lesssim 0.2$ (Goldreich & Peale, 1966; Dobrovolskis, 2007). For an eccentricity of $\sim$0.3, there is a 55% chance that the planet orbits in a 3:2 spin-orbit resonance (Dobrovolskis, 2007). Therefore, I also simulate Proxima Centauri b and TRAPPIST-1 d in a 3:2 spin-orbit resonance with e=0.3.

Proxima Centauri b is the nearest known exoplanet to the Solar System orbiting at 0.0485 AU around its M5.5V host star, and was detected by the radial velocity method (Anglada-Escudé et al., 2016). For Proxima Centauri b, the configurations as shown in Table 5.1 are based on those of Boutle et al. (2017) and Chapter 3, with the same stellar irradiance and a spectral energy distribution from the v2.2 composite spectrum for Proxima Centauri from the MUSCLES spectral survey (France et al., 2016; Loyd et al., 2016; Youngblood et al., 2016). Since the planet is non-transiting, we only have a lower limit on the planet mass of $M\sin(i)$=1.27 $M_\oplus$ (Anglada-Escudé et al., 2016), later refined to 1.07 $M_\oplus$ (Faria et al., 2022). Following Turbet et al. (2016), I assume a mass of 1.4 $M_\oplus$ and use Earth's density (5.5 g cm^{-3}) to calculate a radius of 1.1 $R_\oplus$ and surface gravity of 10.9 m s^{-2}. For Proxima Centauri b, I simulate the atmosphere up to an altitude of 85 km (Yates et al., 2020, see also Chapter 3.2), to include stratospheric photochemistry. I use the relation with the scale height H to translate the altitude into a top-of-the-atmosphere pressure P_{TOA} of:

$$P_{\mathrm{TOA}} = P_0 e^{-\frac{z}{H}} = P_0 e^{-\frac{mg}{k_b T} z} = 9.8 \times 10^{-5} \mathrm{hPa}, \tag{5.2}$$

using P_0=1,000 hPa, $m \approx 4.81 \times 10^{-26}$ for an Earth-like atmosphere, g=10.9 m s^{-2}, and T=200 K or H=5,266 m. Given pressures ranges of the Earth's troposphere (1000–100 hPa), stratosphere (100–1 hPa), and mesosphere (1–10^{-3} hPa), I ensure the inclusion of all three layers, important for ozone chemistry (e.g. Seinfeld & Pandis, 2016).

The TRAPPIST-1 (M8V star) system was detected by Gillon et al. (2017) using the transit method. The luminosity of the host star is equal to 5.53×10^{-4} $L_\odot$ (Ducrot et al., 2020; Agol et al., 2021) and the spectral energy distribution is specified in the v2.3 composite spectrum from the Mega-MUSCLES survey as shown in Wilson et al. (2021). Both are rescaled to the orbit of planet d during the simulation. Planet d orbits around its star in 4.050 days on a semi-major axis of 0.02227 AU (Agol et al., 2021) near the inner edge of the liquid water Habitable Zone (Turbet et al., 2018). Its density and gravity are lower than Earth's at 4.4 g cm^{-3} and 6.12 m s^{-2}, respectively. The lower gravity increases the atmospheric scale height to 9,379 m. Rewriting Equation 5.2 to solve for z at the top-of-the-atmosphere for TRAPPIST-1 d, I find that a model top of 150 km is needed to include the same pressure levels as the simulations for Proxima Centauri b. However, in this case simulations were unstable (likely due to very strong high-altitude winds). A model top of 120 km ($P_{\mathrm{TOA}} = 3 \times 10^{-3}$ hPa according to Equation 5.2) results in stable simulations and still probes stratospheric processes, in particular photochemistry.

I deliberately simulate Proxima Centauri b and TRAPPIST-1 d in this study. For a 1:1 spin-orbit resonance, Proxima Centauri b falls into the Rhines rotator regime and TRAPPIST-1 d into the fast rotator regime, as described in Section 5.1 (see also Carone et al., 2018; Haqq-Misra et al., 2018). I simulate both circulation regimes to probe the effects on atmospheric chemistry using the parameters in the first and third column of Table 5.1.

Table 5.1: Orbital and planetary parameters for the setups for Proxima Centauri b (PCb) and TRAPPIST-1 d (T1d).

Parameter	PCb 1:1	PCb 3:2	T1d 1:1	T1d 3:2
Semi-major axis (AU)	0.0485		0.02227	
Stellar luminosity ($L_\odot$	1.52×10^{-3}		4.32×10^{-4}	
Irradiance at 1 AU (W m^{-2})	2.074		0.588	
Orbital Period (days)	11.186		4.050	
Radius ($R_\oplus$)	1.1		0.788	
Surface gravity (m s^{-2})	10.9		6.12	
Rotation rate (rad s^{-1})	6.501×10^{-6}	9.7517×10^{-6}	1.7958×10^{-5}	2.6937×10^{-5}
Eccentricity	0	0.3	0	0.3
Obliquity	0	0	0	0
Model top (km)	85	85	120	120

Using Equation 2.15, the stellar luminosity of 5.53×10^{-4} $L_\odot$ for TRAPPIST-1 (Ducrot et al., 2020; Agol et al., 2021) can be converted to an irradiance of 1518 W m^{-2} at the orbital distance of TRAPPIST-1 d. This irradiance exceeds what Earth receives from the Sun (1361 W m^{-2}) and induces a runaway greenhouse state within 1060 days, as also reported by Wolf (2017) and Turbet et al. (2020). For the aim of investigating 3D effects on the atmospheric chemistry for this planet in the fast rotator regime, I artificially reduce the luminosity of TRAPPIST-1 by $\sim$22% to 4.32×10^{-4} $L_\odot$, resulting in a reduced irradiance for TRAPPIST-1 d of 1186 W m^{-2}. Figure 5.1 compares the climatic evolution between the reduced irradiance (T1d reduced S_{TOA}) and true irradiance (T1d true S_{TOA}) simulations of TRAPPIST-1 d in a 1:1 spin-orbit resonance. The runaway climate state for the true irradiance is visible in multiple diagnostics from the simulation. The global mean surface temperature in panel a increases by 60 K in the first 1060 days and panel b shows that a radiative disbalance of 64 W m^{-2} is left for the true irradiance setup after these 1060 days. The reduced irradiance at TRAPPIST-1 d results in global temperatures that are 45 K lower and reaches radiative balance after about 2000 days. The true irradiance simulation also reaches the Simpson-Nakajima limit in outgoing radiation of 282 W m^{-2} (Simpson, 1928; Nakajima et al., 1992; Goldblatt & Watson, 2012), as shown by the black dashed line in panel c. The vertically integrated water vapour column density (hereafter H_2O(g) column) in panel d increases substantially to 2.3×10^{28} molec m^{-2} and stratospheric water vapour mixing ratios exceed the threshold for a runaway greenhouse (Kasting, 1988). For the reduced irradiance at TRAPPIST-1 d I find a global mean water vapour column ten times smaller and mixing ratios well below the runaway limit. Hence, the artificial reduction of the irradiance of TRAPPIST-1 d prevents a runaway greenhouse effect and will be used in the remainder of this study.

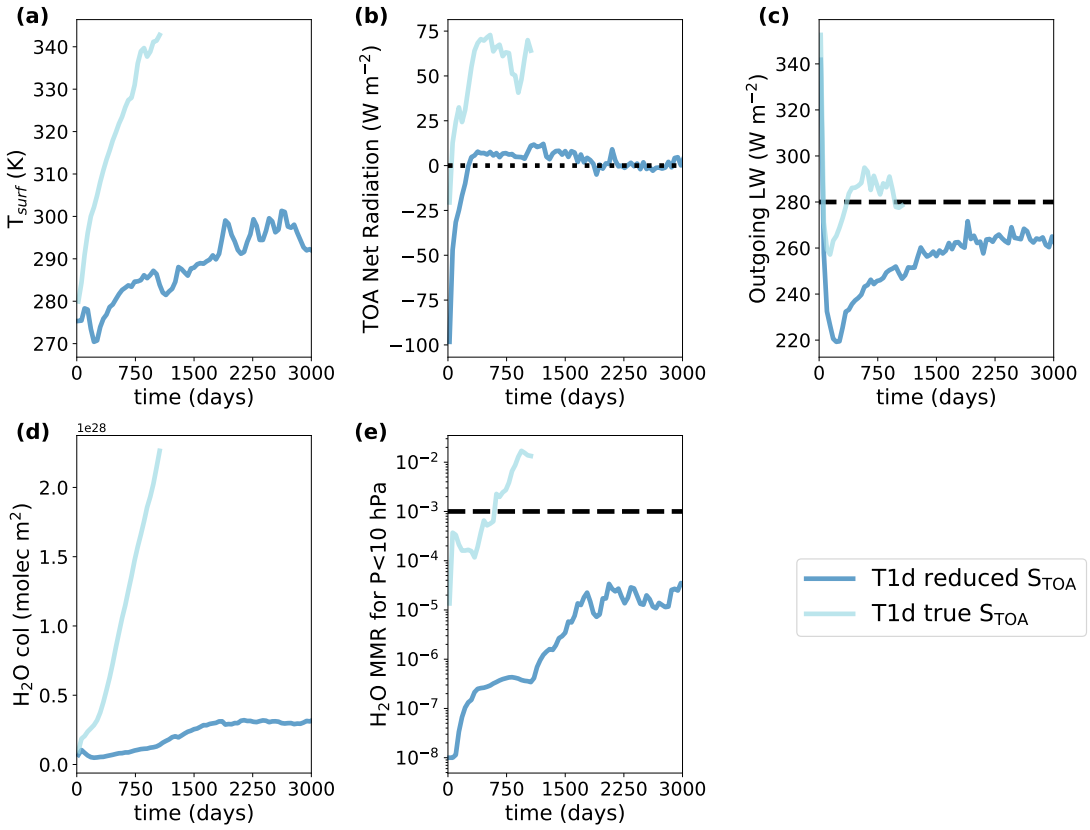

Figure 5.1: Temporal evolution of global mean climatological diagnostics, including (a) the surface temperature, (b) the balance between incoming and outgoing radiation at the top-of-the-atmosphere, (c) the outgoing radiation, (d) the vertically integrated water vapour column density, and (e) the stratospheric water vapour mixing ratios. The results are shown for TRAPPIST-1 d receiving an irradiance of 1186 W m^{-2} (T1d reduced S_{TOA}) and 1518 W m^{-2} (T1d true S_{TOA}). The dotted black line in panel b indicates radiative balance. The dashed black line in panel c shows the Simpson-Nakajima limit in outgoing longwave radiation for a runaway greenhouse effect according to Goldblatt and Watson (2012) and the dashed black line in panel e the threshold in stratospheric water vapour abundances following Kasting (1988).

Current radial velocity measurements of Proxima Centauri b indicate upper limits on the eccentricity of 0.35 (Anglada-Escudé et al., 2016) and 0.29 (Jenkins et al., 2019), with a likely value of 0.25 (Brown, 2017). Given this eccentricity the planet might orbit in a 3:2 spin-orbit resonance (Dobrovolskis, 2007). To study the impact of this higher resonance on the climate, habitability, and atmospheric chemistry, I configure the planet with an increased rotation rate that covers 1.5π radian in one orbital period (see the PCb 3:2 case in Table 5.1). Due to the eccentricity, the planet's distance from the host star varies between 0.046–0.0485 AU.

Planet-planet interactions can induce eccentricities in multiplanet systems (e.g. Barnes, 2017). The planets around TRAPPIST-1 orbit in a tightly packed resonant chain and all have eccentricities $<$0.1 (Gillon et al., 2017; Luger et al., 2017; Grimm et al., 2018). However, studies of the tidal dynamics in the TRAPPIST-1 system indicate that planets d, e, and f may have been captured in 3:2 resonance during their evolution (Makarov et al., 2018). Additionally, planets similar to TRAPPIST-1 d in terms of the host star and circulation regime may exist in a 3:2 spin-orbit resonance. Therefore, I also configure TRAPPIST-1 d in a 3:2 resonant orbit with an increased rotation rate and eccentricity of 0.3 (see the T1d 3:2 case in Table 5.1). The planet's distance from the host star varies between 0.0213–0.0223 AU. Generally, the results apply to similar exoplanets in terms of the host star, orbital configuration, atmospheric composition, and circulation regime.

5.2.3 Simulation Setups

I spin up each of the models from the initial atmospheric state as defined in Section 5.2.1 to a steady state, determined by a slope approaching zero in the time evolution of key atmospheric variables. The stabilisation of the surface temperature and radiative balance at the top of the atmosphere determine the dynamical steady state that takes about 2,000 Earth days (hereafter, just days). Using ozone as a long-lived species (with chemical lifetimes of $>$25 years, see Section 4.3.3), the chemical steady state was determined by stabilisation of the ozone column density and mole fraction (the amount of ozone compared to total amount of air), and takes about 4,000 days. After the spin-up and an additional 2,000–3,000 days, I use 600 days of simulation for the 1:1 resonant cases (corresponding to 50 and 150 orbits for Proxima Centauri b and TRAPPIST-1 d, respectively) to determine the climatologies and steady state conditions. I use 120 days of daily output for the analysis of the 3:2 resonant orbits. For all setups, I also use the first 1,000 simulation days to diagnose the atmospheric circulation and its effect on 3D distributions of atmospheric tracers. Lastly, I use daily outputs of the steady states for each case to produce emission spectra at different timesteps, as described in the next section.

5.2.4 Planetary Spectrum Generator

I use the NASA Planetary Spectrum Generator (PSG: Villanueva et al., 2018; Villanueva et al., 2022), an online radiative transfer tool, to explore the effect of 3D spatial variations in atmospheric properties on emission spectra. The PSG GlobES[1] 3D mapping tool translates the simulated 3D data into synthetic spectra. I include CCM output for 3D distributions of temperature, pressure, water clouds, ice clouds, and gaseous chemical compounds H_2O, O_3, NO, NO_2, N_2O, HNO_3. Additionally, I take constant vertical abundance profiles of N_2, O_2, and CO_2 into account, following the CCM assumptions (see Section 5.2.1). The application of GlobES follows Fauchez et al. (2022), based on publicly available scripts designed for the UM[2] that were complemented to also handle output from the UM-UKCA framework [3]. Since emission spectra are affected by the whole observed disk of the planet, PSG weights the projected area of each latitude-longitude bin and uses a layer-by-layer pseudo-spherical ray-tracing algorithm to perform the radiative transfer calculations across the whole disk. The spectra from each latitude-longitude bin are then combined into one observed spectrum, taking the observing geometry into account. The full details of these calculations can be found in Villanueva et al. (2022). Molecular absorptions are taken from the latest HITRAN database updates (Gordon et al., 2022). The radiative transfer also accounts for collision-induced absorption (CIA) by CO_2-CO_2, H_2O-H_2O, H_2O-N_2, and N_2-N_2 pairs and for aerosol properties following Mie theory.

From an observer's perspective, the observed hemisphere and thus the 3D distribution of atmospheric properties change as a planet moves through its orbit (see e.g. Olson et al., 2018), depending both on the orbital phase and inclination. Therefore, the combined time-dependence of the CCM simulations and the orbital phase angle of the planet is an important factor in generating synthetic observables. For Proxima Centauri b, the orbital inclination is unknown. Kane et al. (2017) address the dependent mass and inclination of Proxima Centauri b and determine that the planet is $\sim$85% likely to be terrestrial, corresponding to a relatively high inclination (through the $M\ sin(i)$=1.27 $M_\oplus$ dependence). For a mass of about 1.4 $M_\oplus$ I then deduce an inclination of 70° for the generation of emission spectra, implying that the orbit is not fully face-on but that we can nevertheless probe a planetary disk throughout the full orbital phase.

From the CCM simulations, I take the instantaneous output on a daily basis for 12 days to cover a full orbit of synthetic emission spectra. Given Proxima Centauri b's orbital period of 11.186 days, I cover the orbit in phase angle steps of 32.1831° per day. The orbital phase angles corresponding to the 12 simulation days are shown in Table 5.2. I use the same phase angles to cover one orbit for the 3:2 resonance, but since the planet no longer rotates syn-

1. https://psg.gsfc.nasa.gov/apps/globes.php
2. https://github.com/nasapsg/globes
3. https://github.com/marrickb/eccent_3dchem_PSJ

Table 5.2: Orbital phase angles to cover a full orbit for Proxima Centauri b in a 1:1 and 3:2 resonant orbit. For the 3:2 resonance, the substellar point changes as a function of time as specified by the substellar longitude.

Days	Phase angle (°)	Substellar longitude 3:2 (°)
1	102.94	0
2	135.12	16.09
3	167.31	32.18
4	199.49	48.27
5	231.67	64.36
6	263.85	80.45
7	296.04	96.54
8	328.22	112.63
9	0.40	128.72
10	32.59	144.81
11	64.77	160.90
12	96.95	176.99

chronously, the substellar longitude also changes as a function of time. For a 3:2 resonance, this corresponds to a shift of 180 ° per orbit or 180° per day, so that the daytime hemisphere changes for every orbit. Therefore, a stellar day would technically take 22.4 days, but the variations are covered in only 12 days. The substellar longitude for all 12 days is also shown in Table 5.2. Both the phase angles and substellar longitude are given to PSG to calculate the emission spectra.

TRAPPIST-1 d has tight constraints on an orbital inclination of 89.75°, indicating practically an edge-on orbit (Gillon et al., 2017). Hence, we can observe transmission spectra during the primary transit and emission spectra when the planet is out of transit, and most easily when the planet is furthest away from the star (around orbital phase angles of 90 and 270°). Given TRAPPIST-1 d's orbital period of 4.050 days, the planet orbital rotation corresponds to 88.889° per day. To probe temporal variations in the emission spectra generated from 3D data, I again take the instantaneous output from the CCM simulation. I calculate emission spectra every two days, since this corresponds out-of-transit days with small variations in the exact orbital phase angle due to the 177° shift every two days. The exact phase angles are shown in Table 5.3. I cover 6 orbits (or 12 phase angles) around the host star in days 0–22 and add another orbit with days 36 and 38 since these are closest to phase angles 90 and 270°, producing a total of 14 emission spectra. Additionally, I simulate transmission spectra during two transits (on day 37 and day 118) to probe variability between these. The results for TRAPPIST-1 d in a 3:2 resonance will not be translated into simulated emission spectra, as the atmosphere is unstable due to a runaway greenhouse (see Section 5.3).

Table 5.3: Orbital phase angles to simulate emission spectra for seven orbits and transmission spectra during two different transits for TRAPPIST-1 d in a 1:1 resonance.

Emission	
Days	Phase angle (°)
0	130.00
2	307.78
4	125.56
6	303.33
8	121.11
10	298.89
12	116.67
14	294.44
16	112.22
18	290.90
20	107.78
22	285.55
36	90.00
38	267.77
Transmission	
37	178.89
118	178.89

5.3 Results

I first compare the planetary climates and resulting ozone distributions for the four simulations in Sections 5.3.1 and 5.3.2. I identify the dominant chemical processes in the simulations in Section 5.3.3, before discussing the time evolution of the 3:2 resonant case. Each simulation has a distinct interplay with atmospheric circulation that I describe in Section 5.3.5. In Section 5.3.6, I present simulated observables based on my 3D simulations. For the true irradiance that TRAPPIST-1 d receives, the planet will transition into a runaway greenhouse state (see Section 5.2.2) and thus the results are not necessarily valid for TRAPPIST-1 d as we currently know it. Nevertheless, the 3D distributions and dominant circulation mechanisms apply more generally to planets that receive a slightly lower irradiance but are similar in terms of the host star, orbital configuration, atmospheric composition, and circulation regime.

5.3.1 Planetary Climates

The planetary climate for a 1:1 resonant Proxima Centauri b with an Earth-like atmospheric composition has been investigated extensively (e.g. Turbet et al., 2016; Boutle et al., 2017), focusing on the dayside-nightside distinctions. For the sake of the discussion and for the comparison with TRAPPIST-1 d, I show the temporal mean distribution of the surface temperature from the CCM simulations in Figure 5.2. The global mean temperature is 229 K and goes from as low as 156 K in the nightside gyres (see also Section 4.3) up to a maximum of 288 K. Taking

means for the dayside and nightside hemisphere, I find a hemispheric difference of 67 K. The distribution looks similar to that of Turbet et al. (2016) and Boutle et al. (2017). Importantly, the wind vectors indicate the single equatorial jet that characterises the circulation regime of Proxima Centauri b (see e.g. Carone et al., 2018).

TRAPPIST-1 d orbits closer to its host star, leading to generally warmer surface temperatures with a global mean of 289 K. The nightside minima are 255 K and the temperature peaks close to the substellar point at 318 K. The white lines show that most of the dayside and about half of the nightside hemisphere are above the freezing point of water (273.15 K), as compared to just $\sim$45% of Proxima Centauri b's dayside hemisphere. The circulation of TRAPPIST-1 d is dominated by two midlatitude jets. Comparing both planets, Proxima Centauri b mainly indicates a zonal gradient in temperature whereas TRAPPIST-1 d shows a meridional gradient in temperature. This also leads to a reduced dayside-nightside hemispheric difference of 19 K for TRAPPIST-1 d.

When simulating both planets in a 3:2 spin-orbit resonance, the substellar point is no longer fixed. Instead, the substellar point shifts by 180° for every orbit around the star. Figure 5.3 shows how the 3:2 resonance impacts the surface temperature for Proxima Centauri b. The planet has two warm regions, one centred at 0° and one at 180° longitude. Hemispheric differences in temperature between the 0° and 180° hemisphere are only 5 K (Figure 5.3a) and -4 K (Figure 5.3b) depending on the timestep, indicating the enhanced homogeneity across the planet as compared to the 1:1 resonant planets. I show the surface temperature for daytime on the 0° hemisphere in Figure 5.3a and for daytime on the 180° hemisphere in Figure 5.3b. Both timesteps go from a minimum of 217 K to maximum 298 K, with a global mean surface temperature of 270 K, a 17% increase compared to the 1:1 resonance. The general warming in moving from the 1:1 to the 3:2 resonance is also evident from the white contour lines showing that about half of each hemisphere is above the freezing point of water.

The warming effect of the 3:2 resonance is even more pronounced for TRAPPIST-1 d, for which I show temporal averages for days 40–80 and 5600–5640 in Figures 5.4a and 5.4b, respectively. During days 40–80, only the poles are below the freezing point of water and the global mean temperature has risen to 294 K. Two relatively hot regions are still distinguishable centred at 0° and 180° longitude. During days 5600–5640 the temperature of TRAPPIST-1 d globally exceeds the freezing point of water with a mean of 333 K (a 15% increase compared to the 1:1 resonance). After this period, the model becomes unstable.

To diagnose the instability, I plot the time evolution of the global mean surface temperature along with the H_2O(g) column in Figure 5.5. The H_2O(g) column steadily increases with the increased surface temperature, due to a shifted balance of more evaporation of surface water versus condensation in the atmosphere. The 15% increase in temperature compared to the 1:1 resonance (denoted by the triangles) is accompanied by a six-fold increase in the H_2O(g) column. The continuous increase in water vapour will induce further greenhouse warming

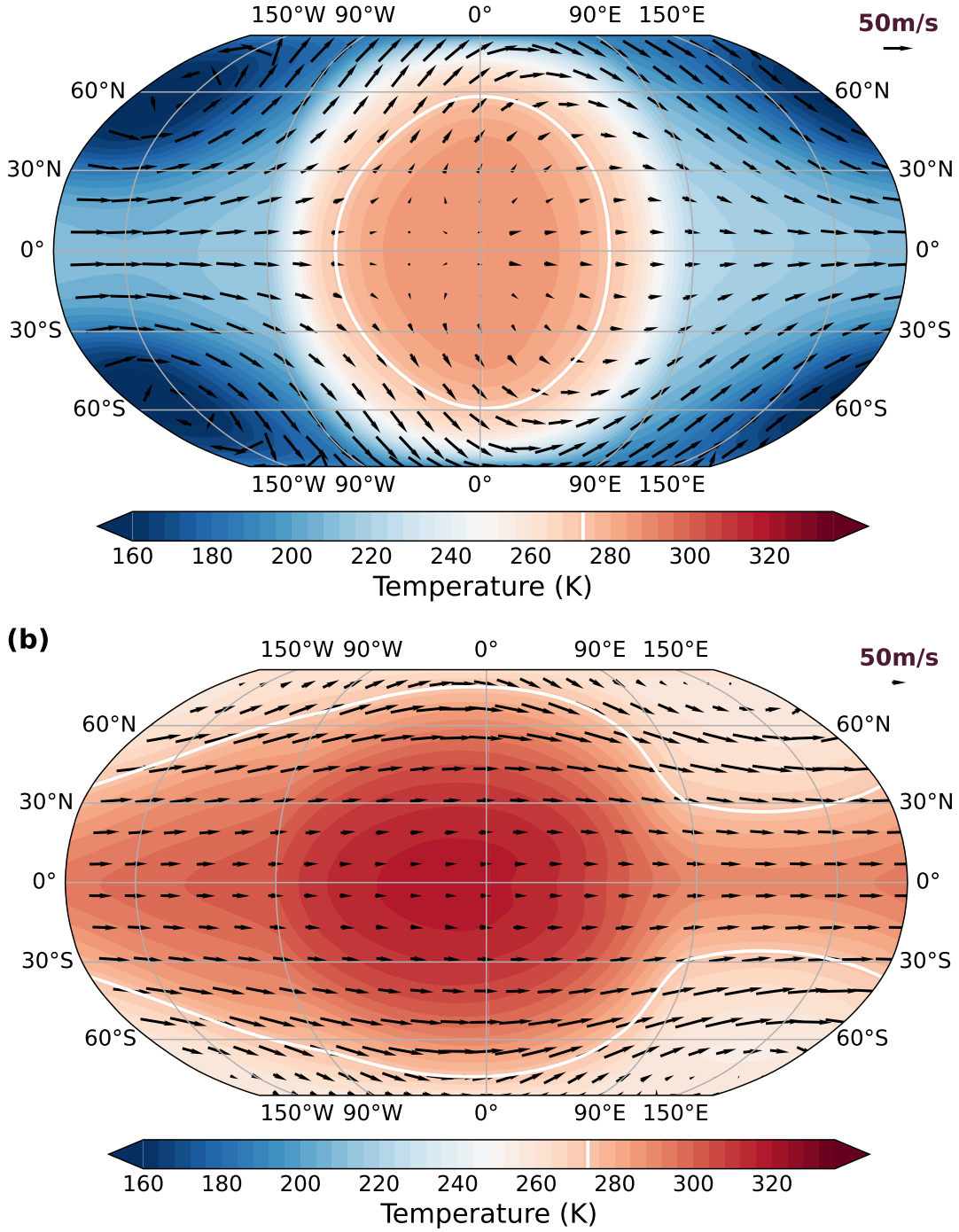

Figure 5.2: Temporal mean surface temperature over 600 days for (a) Proxima Centauri b and (b) TRAPPIST-1 d, both orbiting in a 1:1 spin-orbit resonance. The substellar point (SP) is located at $(\phi, \lambda) = (0°, 0°)$. Overplotted are the horizontal wind vectors at P$\approx$250 hPa and 75 hPa, showing both the equatorial jet for Proxima Centauri b and the two mid-latitude jets for TRAPPIST-1 d. The white contour lines indicate surface temperatures of 273.15 K, and therefore the regions that can sustain liquid water.

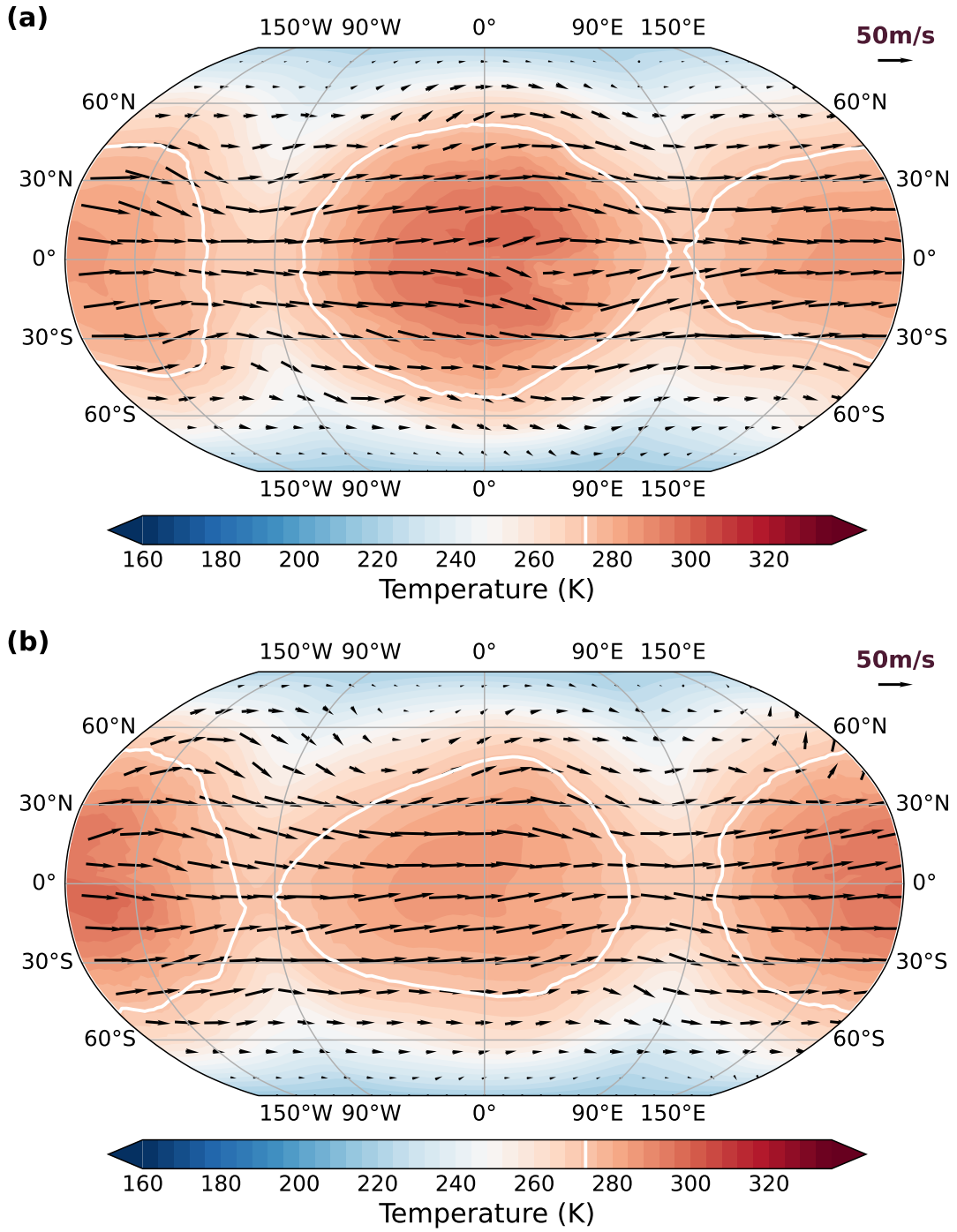

Figure 5.3: Mean surface temperature for Proxima Centauri b in a 3:2 resonance for (a) daytime on the 0° hemisphere and (b) daytime on the 180° hemisphere.

through the strong mid-infrared absorption by water vapour, which in turn drives a stronger shift towards more evaporation, and this process will continue iteratively causing TRAPPIST-1 d in a 3:2 spin-orbit resonance to reach the moist greenhouse limit (e.g. Simpson, 1928; Nakajima et al., 1992; Goldblatt et al., 2013; Chaverot et al., 2022). Since the model has failed to reach a steady state, I will not describe the atmospheric chemistry in further detail for the case of TRAPPIST-1 d in a 3:2 resonance.

5.3.2 Ozone Columns

In Figure 5.6a I show the vertically integrated ozone column density (hereafter ozone column) for Proxima Centauri b, which also shows zonal variations in line with the surface temperature distribution in Figure 5.2a. The global mean ozone column is 387 DU (1 DU$=2.687 \times 10^{20}$ molecules m^{-2}), ranging from a minimum dayside value of 262 DU to a maximum of 1466 DU at the location of the nightside gyres. The 3D distribution is driven by a stratospheric dayside-to-nightside circulation, as shown in Chapter 4.

The simulation of TRAPPIST-1 d instead shows meridional variations in the ozone column (Figure 5.6b), with a relatively small equatorial ozone column (minimum of 33 DU) and a maximum column of 110 DU at high latitudes. The global average is 47 DU, much lower than Proxima Centauri b due to a different incoming stellar flux distribution driving photolysis and due to ozone destruction processes that will be further discussed in Section 5.3.3. The spatial distribution is similar to the global distribution of the ozone column on Earth, despite a difference in magnitude (Earth's ozone ranges from 200–500 DU). This indicates a change in stratospheric circulation driving the 3D ozone distribution as compared to Proxima Centauri b, which I will further investigate in Section 5.3.5.

Proxima Centauri b in a 3:2 resonance also exhibits meridional variations in the ozone column as shown in Figure 5.7, again qualitatively matching the gradients in surface temperature. Comparing Figures 5.7a and 5.7b, the smallest ozone column is found on the dayside hemisphere, which is at 0° and 180° in Figures 5.7a and 5.7b, respectively. Both timesteps have a global mean ozone column of 773 DU, but vary in their minima of 625 DU (a) and 610 DU (b) and maxima of 1157 DU (a) and 1137 DU (b). Compared to the 1:1 resonant orbit, Proxima Centauri b in a 3:2 resonance shows a much smaller spread in ozone column values, along with an increased global mean. This indicates that there is more homogeneity across the planet for a 3:2 resonance. The spatial distribution of the ozone column is circulation-driven, as I will show in Section 5.3.5. However, the 3:2 resonant orbit induces variability that is visible in the global extrema of both timesteps and, when comparing Figures 5.7a and 5.7b, on each hemisphere separately. I will further explore this variability in Section 5.3.4.

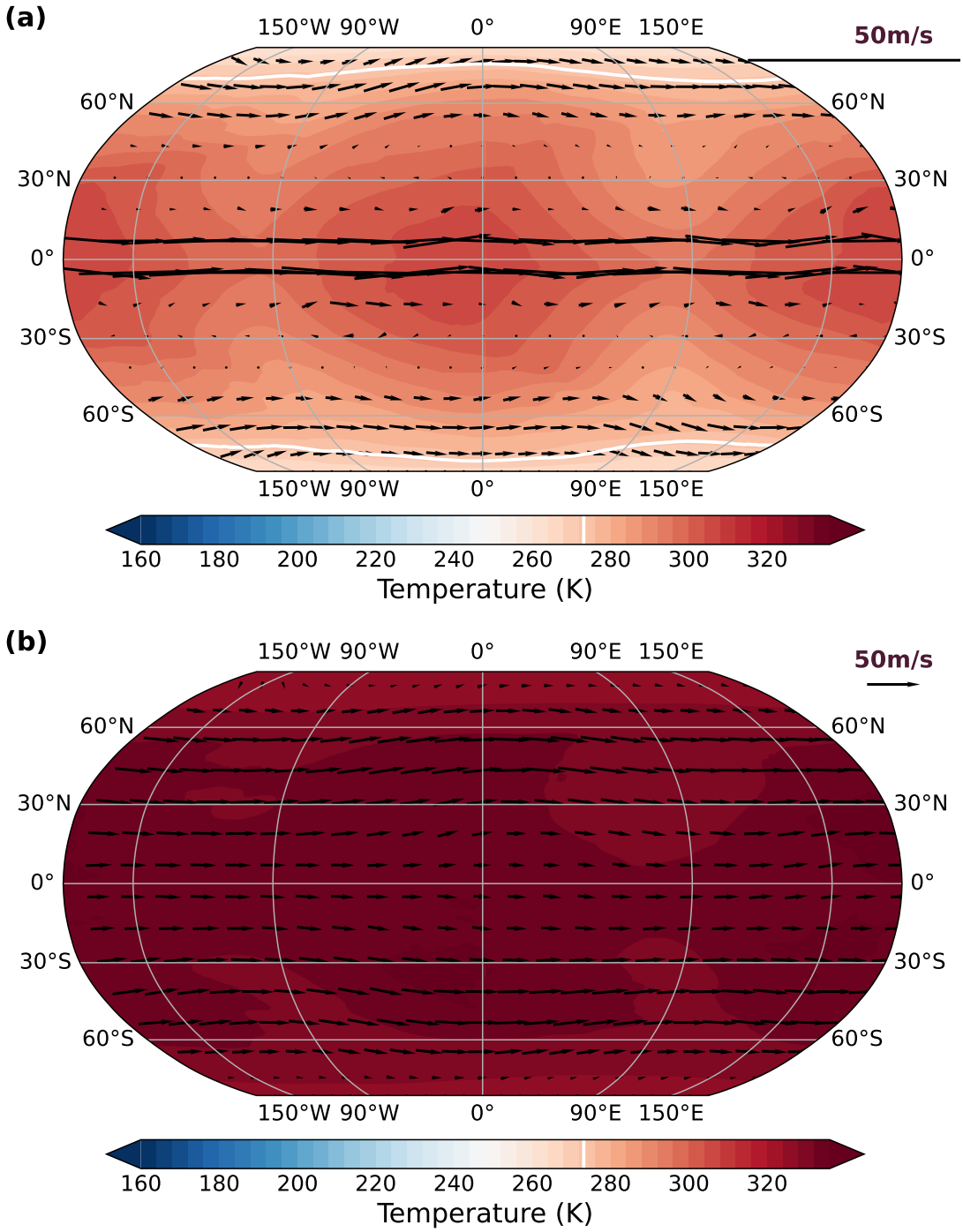

Figure 5.4: Temporal mean surface temperature for TRAPPIST-1 d in a 3:2 resonance for (a) days 40–80 and (b) 5600–5640. In panel (a) the changing dayside hemisphere in a 3:2 resonance is visible with two hotspots centred at longitudes 0 and 180°, but panel (b) shows that the global surface warms significantly over the course of the simulation.

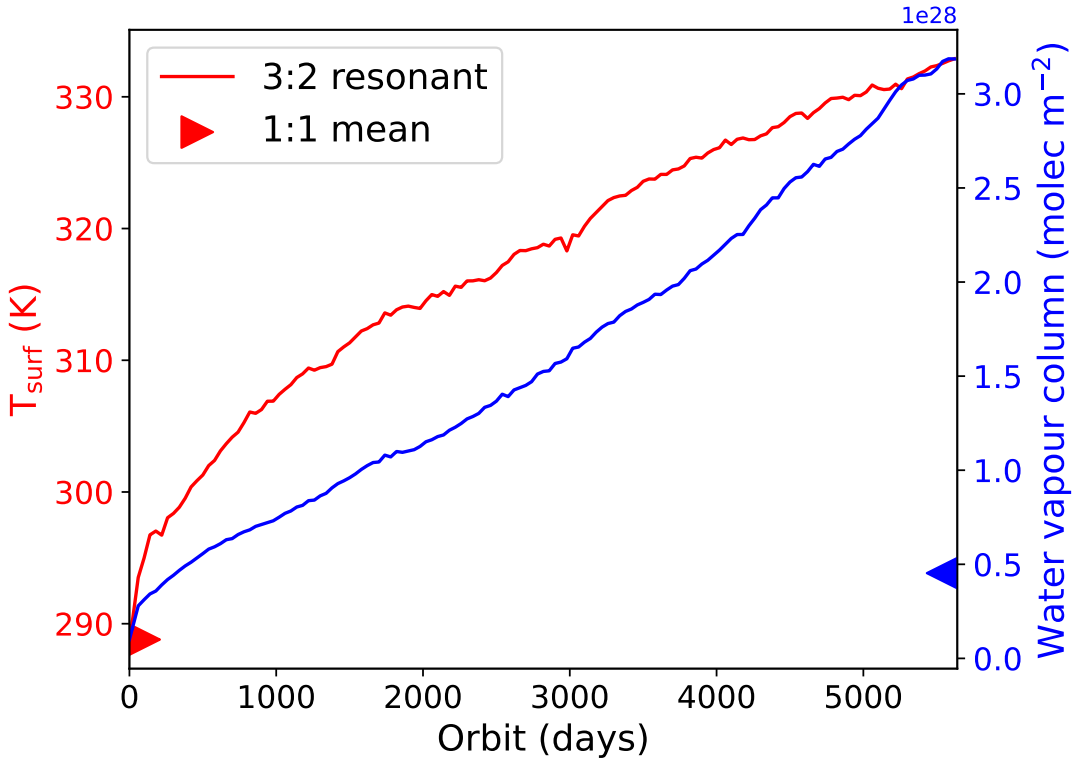

Figure 5.5: Temporal evolution of the surface temperature (red) and vertically integrated column of water vapour (blue) for TRAPPIST-1 d in a 3:2 resonance. Both the surface temperature and water vapour column keep increasing, indicating that the planet approaches the moist greenhouse limit. For reference, the average temperature and water vapour column for the 1:1 resonance are shown as the red and blue triangles.

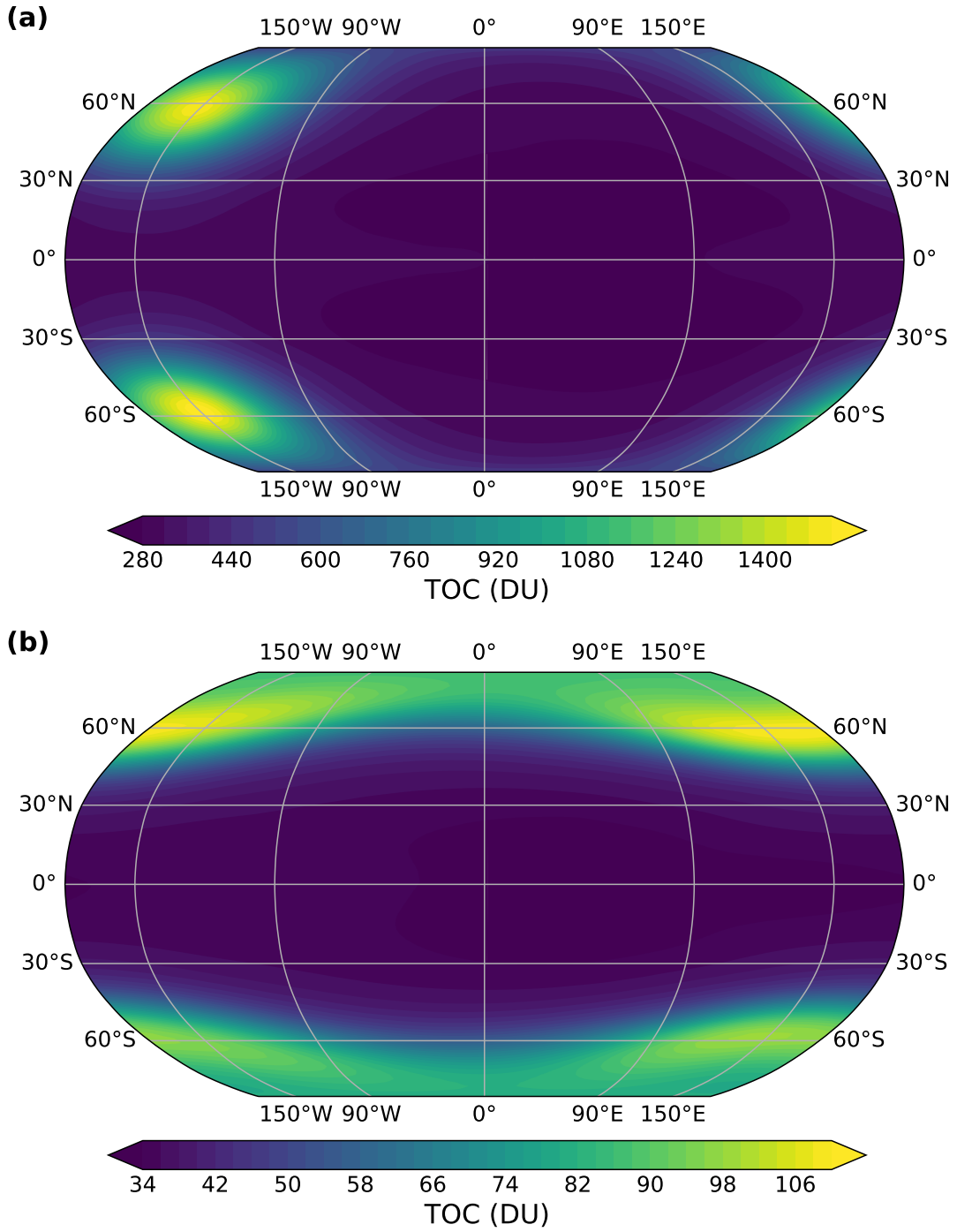

Figure 5.6: Mean over 600 days of the vertically integrated ozone column density for (a) Proxima Centauri b and (b) TRAPPIST-1 d, both orbiting in a 1:1 spin-orbit resonance.

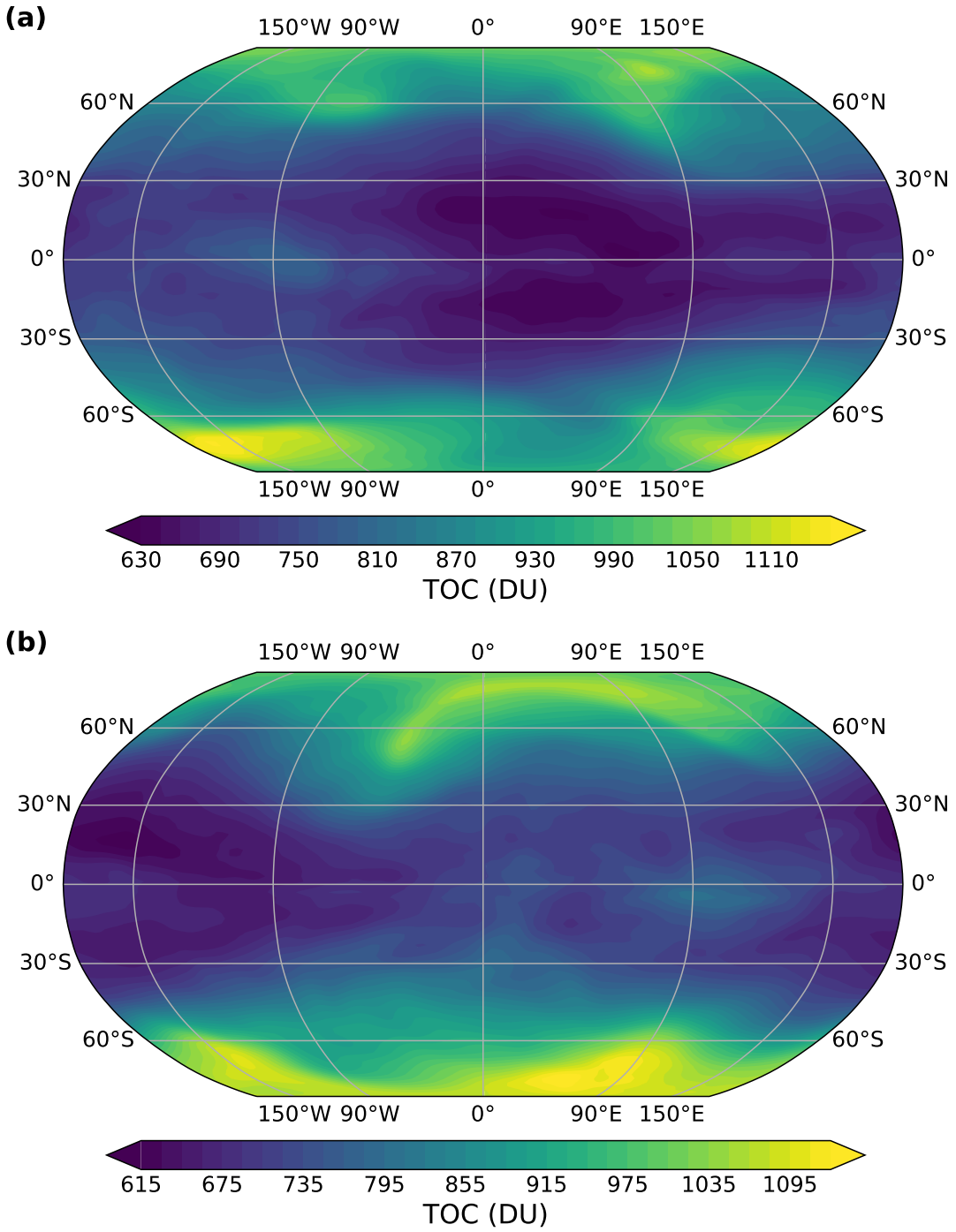

Figure 5.7: Mean vertically integrated ozone column density for Proxima Centauri b in a 3:2 resonance for (a) daytime on the 0° hemisphere and (b) daytime on the 180° hemisphere.

5.3.3 Comparing the Dominant Chemical Processes

Three chemical mechanisms are of key importance to explain the abundance of ozone molecules in an Earth-like atmospheric composition (for previous work in the context of M-dwarf radiation, see e.g. Chapter 3 and Segura et al., 2003; Rugheimer et al., 2015a; Yates et al., 2020; Ridgway et al., 2023). First, the photolysis of O_2 drives the Chapman mechanism of ozone formation (Chapman, 1930):

$$O_2 + h\nu \longrightarrow O(^3P) + O(^3P), \quad \text{(R1)}$$
$$O(^3P) + O_2 + M \longrightarrow O_3 + M, \quad \text{(R2)}$$
$$O_3 + h\nu \longrightarrow O_2 + O(^3P), \quad \text{(R3)}$$
$$O_3 + h\nu \longrightarrow O_2 + O(^1D), \quad \text{(R4)}$$
$$O_3 + O(^3P) \longrightarrow O_2 + O_2. \quad \text{(R5)}$$

Reaction R1 initiates the production of ozone and Reaction R5 represents the termination step by destroying ozone. Reactions R2–R4 describe the rapid interchange between $O(^1D)$, $O(^3P)$, O_2, and ozone. Once formed, ozone can then be destroyed by a number of catalytic cycles (Bates & Nicolet, 1950; Crutzen, 1970; Johnston, 1971; Grenfell et al., 2006), that are commonly grouped as the HO_x(=H+OH+HO_2) and NO_x(=NO+NO_2) cycles, presenting the other main chemical mechanisms. An example of such a catalytic cycle is:

$$OH + O_3 \longrightarrow HO_2 + O_2, \quad \text{(R6)}$$
$$\underline{HO_2 + O(^3P) \longrightarrow OH + O_2}, \quad \text{(R7)}$$
$$\text{Net: } O_3 + O(^3P) \longrightarrow 2O_2.$$

Hence, the net reaction shows that ozone is destroyed without consuming the catalyst (HO_x) species that remain available for another round of ozone destruction. The cycle is initiated by the production of OH from the photolysis or oxidation of water vapour:

$$H_2O + h\nu \longrightarrow OH + H, \quad \text{(R8)}$$
$$H_2O + O(^1D) \longrightarrow 2OH, \quad \text{(R9)}$$

and the cycle is terminated when HO_x species react to destroy themselves:

$$OH + HO_2 \longrightarrow H_2O + O_2. \quad \text{(R10)}$$

The rate-limiting step in this specific cycle is Reaction R7 in the lower atmosphere or reaction R6 in the upper atmosphere (see Section 3.3). Hence, the rate of these specific reactions determine the strength of the catalytic cycle and thus the amount of ozone destruction. The rate associated with Reaction R10 is generally between 100–1000 times slower than that of Reactions R6 or R7, implying that one OH molecule can participate in 100–1000 catalytic cycles before being destroyed itself. These rate calculations are shown explicitly for Proxima Centauri b in a 1:1 resonance in Section 3.3.3 and specifically Figure 3.6. In the rest of this section, I will analyse the vertical distribution of ozone in the simulations for Proxima Centauri b and TRAPPIST-1 d by comparing the abundances of key chemical species and the most important reactions for the formation and destruction of ozone.

Figure 5.8 shows the hemispheric mean vertical distributions of the air temperature, liquid and ice cloud abundances, and the mole fractions χ_i of chemical species *i* as indicated by the title of each panel. The air temperatures in Figure 5.8a illustrate the distinct atmospheric pressure-temperature structure for Proxima Centauri b on one hand (navy and blue lines) and TRAPPIST-1 d on the other (red and maroon lines). TRAPPIST-1 d is warmer for the full vertical extent of the atmosphere, with a tropopause at substantially lower pressures ($\sim$100 hPa for Proxima Centauri b and $\sim$20 hPa for TRAPPIST-1 d). For 1:1 resonant orbits of both planets, Figure 5.8a shows hemispheric contrasts in temperature for P>100 hPa, comparing the solid lines (0° hemisphere) and dashed lines (180° hemisphere), in contrast to homogeneity for the 3:2 resonances. Once more, a 3:2 resonant orbit results in a warmer planet for almost all vertical layers compared to a 1:1 resonance.

The distribution of water vapour in Figure 5.8b illustrates that a 3:2 resonant orbit leads to a much wetter atmosphere than a 1:1 resonant orbit. The atmosphere of TRAPPIST-1 d in a 3:2 resonance is particularly wet, with the planet seemingly approaching the moist greenhouse limit as discussed in Section 5.3.1. This limit corresponds to a water-dominated stratosphere (Kopparapu et al., 2013), when mole fractions exceed $\chi_{H_2O}>10^{-3}$ (Kasting, 1988). Figure 5.8b shows that TRAPPIST-1 d in a 3:2 resonance exceeds this threshold for all vertical levels. Comparing the two planets in a 1:1 resonance, TRAPPIST-1 d's atmosphere contains much more water vapour for P$>$5 hPa, whereas its atmosphere is drier for P$<$5 hPa. The extended liquid water and ice cloud structures (Panels 5.8c and 5.8d) seem to deplete the atmosphere of TRAPPIST-1 d of water vapour before it can reach the higher layers.

For the remaining gas-phase chemical compounds shown in panels e-i of Figure 5.8, I omit the case of TRAPPIST-1 d in a 3:2 resonance because of its unstable climate state. The vertical distribution of ozone in Figure 5.8e shows that the balance between photochemical production and chemical destruction leads to more net ozone for Proxima Centauri b, with a structure depending on the spin-orbit resonance. Ozone peaks at $\chi_{O_3}\simeq 10$ ppm for Proxima

Centauri b and $\chi_{O_3} \simeq 1$ ppm for TRAPPIST-1 d. The 3:2 resonance shows similar profiles for both hemispheres. Hemispheric differences are visible in both 1:1 resonances, corresponding distinctly to the zonal variations for Proxima Centauri b (Figure 5.6a) but strongly affected by the meridional variations for TRAPPIST-1 d (Figure 5.6b).

The vertical profiles of OH and HO_2 in panels f and g of Figure 5.8 demonstrate that, despite the smaller amounts of water vapour in Proxima Centauri b's lower atmosphere (P>5 hPa), OH and HO_2 levels are higher due to differences in HOx production (via H_2O photolysis in R8 and oxidation in R9) and destruction mechanisms, that I will further describe below. The oxidation also needs the presence of $O(^1D)$ from ozone photolysis (R4) to proceed.

The profiles of NO in Figure 5.8h indicate substantially higher NO in the simulations of TRAPPIST-1 d. Since NO in the lower atmosphere is mainly produced by lightning discharges (see Chapter 3), this indicates a much higher lightning activity and subsequent chemical impact for TRAPPIST-1 d compared to Proxima Centauri b. The tall cloud structures for TRAPPIST-1 d (Figure 5.8c and d) support this idea, as the lightning flash rates in my simulation are parameterised in terms of cloud-top heights (described in Section 3.2.4), and lead to strong NO emissions for P>8 hPa. I compare the associated lightning flash rates (LFRs) in Figure 5.9. For 1:1 resonant planets, peaks in LFR are found close to the substellar point (0° latitude and longitude), producing the hemispheric differences in NO as shown in Figure 5.8h. For the 3:2 resonant planet, I find that LFR peaks are found on both the 0° and 180° longitude hemispheres, corresponding to the temperature hotspots in Figure 5.3 and explaining the homogeneous profile of NO in Figure 5.8h. LFRs for TRAPPIST-1 d are over two orders of magnitude larger than Proxima Centauri b, explaining the dominant role that lightning-induced NO_x plays in this simulation. NO_3 is also enhanced for TRAPPIST-1 d (panel i), particularly in the 180° hemisphere for P< hPa. Its long lifetime on nighttime hemispheres in the absence of stellar radiation explains the accumulation on the nightside (180°) hemispheres of the 1:1 resonant planets. For P>100 hPa, Proxima Centauri b in a 3:2 resonance reaches similar NO_3 levels as the TRAPPIST-1 d nightside hemisphere, but this is confined to higher atmospheric pressures. These large abundances signify the nighttime accumulation on a 3:2 resonant exoplanet. Both hemispheres show the same profiles because I average over multiple timesteps and thus over changing daytime hemispheres.

To support the interpretation of chemical abundance distributions, I plot the hemispheric means of a selection of reaction rates in Figure 5.10. These describe the three main mechanisms for ozone chemistry, including Reaction R1 (Figure 5.10a) and R5 (Figure 5.10b) of the Chapman mechanism, the initiation reactions (R8 and R9, Figure 5.10c and 5.10d) and rate-limiting steps (Figure 5.10e–g) for the HO_x catalytic cycles, and the rate-limiting steps (Figure 5.10h and 5.10f) for the NO_x catalytic cycles.

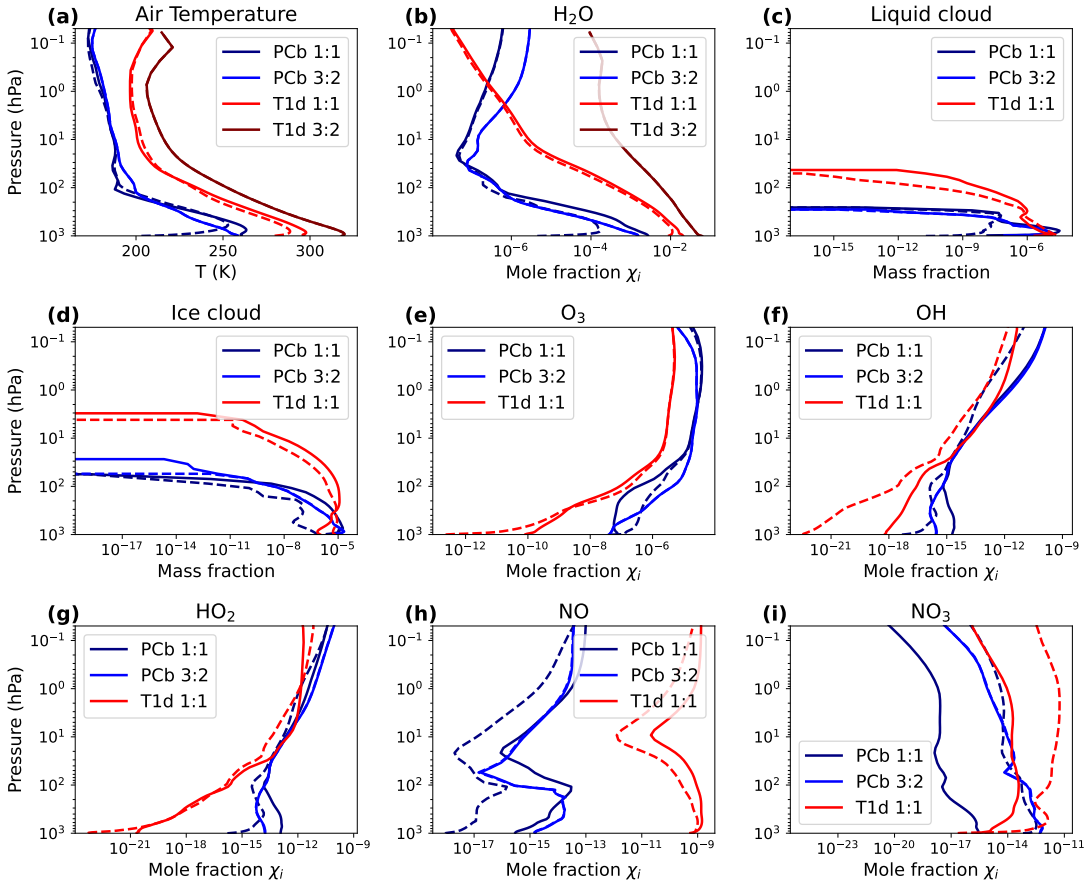

Figure 5.8: Hemispheric means of the vertical distribution of air temperature, liquid and ice cloud abundances, and mole fractions χ_i of chemical species i related to ozone formation in each of the four simulations. Each plot has a title corresponding to the variable or chemical species shown. Solid lines indicate the mean over the 0° hemisphere and dashed lines the mean over the 180° hemisphere, representing the dayside and nightside in 1:1 resonant orbits. The vertical distributions illustrate important differences between the Proxima Centauri b (PCb) and TRAPPIST-1 d (T1d) setups as well as differences between 1:1 and 3:2 spin-orbit resonances.

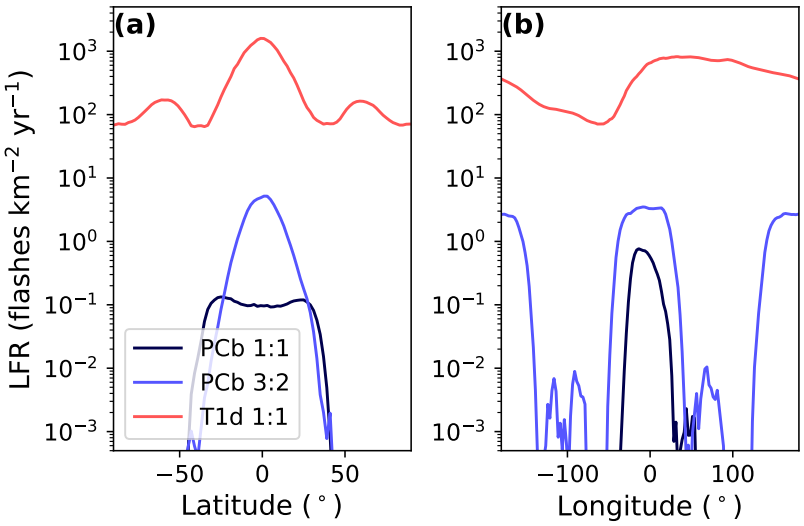

Figure 5.9: Simulated lightning flash rates for Proxima Centauri in a 1:1 resonance (PCb 1:1) and a 3:2 resonance (PCb 3:2) and TRAPPIST-1 d in a 1:1 resonance. The zonal-mean meridional distribution in panel a and meridional-mean zonal distribution in panel b demonstrate that lightning flashes are contained to the dayside hemisphere for 1:1 resonant planets and are found on both hemispheres for 3:2 resonant planets.

From Figure 5.10a I infer that O_2 photolysis rates are higher for Proxima Centauri b throughout most of the atmosphere, following from the higher incoming UV flux (see Figure 2.2) and producing a larger amount of ozone through the Chapman mechanism (Reactions R1–R5). However, for P$>$100 hPa TRAPPIST-1 d has stronger O_2 photolysis rates due to a lower amount of overhead ozone (see Figure 5.8e) absorbing incoming radiation at the relevant wavelengths ($\lambda<$240 nm). Additionally, nightside photolysis rates for 1:1 resonant orbits are 3–6 orders of magnitude lower than on the dayside (see also Yates et al., 2020). The Chapman termination reaction in Figure 5.10b follows the ozone profiles (Figure 5.8e) and also has higher rates for Proxima Centauri b. The termination reaction represents the dominant destruction mechanism between 1–40 hPa since it exceeds all other ozone destruction reactions at these levels. Note that the Chapman termination reaction also indicates lower nightside rates, because of its dependence on O(^{3}P) whose abundance depends on photochemistry.

The photolysis and oxidation of water vapour (Figures 5.10c–d) drive the production of OH, determining the OH profile (Figure 5.8f) and initiating the HO_x catalytic cycles of ozone destruction. H_2O photolysis dominates HO_x production for P$<$10 hPa, which is faster for Proxima Centauri b due to higher H_2O abundances and enhanced radiation in the Schumann-Runge bands ($\lambda<$202 nm, see Figure 3.1). H_2O oxidation dominates for P$>$10 hPa, depending on H_2O (lower for PCb) and O_3 (lower for T1d) abundances. Figure 5.10c shows that R9 is stronger for T1d between 10–400 hPa, whereas OH levels are generally lower for P$>$10 hPa. The much higher NO_x abundances (e.g., Figures 5.8h-i) present an additional sink for HO_x in

the form of:

$$NO_2 + OH + M \longrightarrow HNO_3 + M. \quad \text{(R11)}$$

The importance of this reaction as a sink for NO_x species was also shown in Section 3.3.5 and part of the reaction mechanism in Figure 3.11. Similar to reactions R12 and R14 of the current Chapter (see Figure 5.10h-i), R11 is much faster for TRAPPIST-1 d, destroying HO_x in the lower atmosphere.

The rate-limiting steps in different HO_x cycles (Figures 5.10e–g) are generally stronger for the Proxima Centauri b simulations, which also follows from the higher rates of H_2O photolysis and oxidation.

For TRAPPIST-1 d, Figures 5.10h–i show that the rate-limiting steps of NO_x cycles are much faster than those of the HO_x cycles, following the enhanced production of NO by lightning discharges (Figure 5.8h). Hence, for P$>$100 hPa, ozone destruction is dominated by the following NO_x cycle:

$$NO + O_3 \longrightarrow NO_2 + O_2, \quad \text{(R12)}$$
$$NO_2 + O_3 \longrightarrow NO_3 + O_2, \quad \text{(R13)}$$
$$\underline{NO_3 + h\nu \longrightarrow NO + O_2,} \quad \text{(R14)}$$
$$\text{Net: } 2O_3 \longrightarrow 3O_2.$$

For 0.2 hPa$<$P$<$100 hPa, ozone destruction tends to be dominated by:

$$NO + O_3 \longrightarrow NO_2 + O_2, \quad \text{(R15)}$$
$$\underline{NO_2 + O(^3P) \longrightarrow NO + O_2}, \quad \text{(R16)}$$
$$\text{Net: } O_3 + O(^3P) \longrightarrow 2O_2.$$

In summary, in terms of decreasing P (or increasing altitude), ozone destruction for Proxima Centauri b is controlled by HO_x cycling (panel 5.10e), the Chapman mechanism (panel 5.10d), and again HO_x cycling (panels 5.10f–g). Ozone destruction on TRAPPIST-1 d is instead controlled by NO_x cycling (panels 5.10i–h), indicating a much more prominent role for lightning-induced chemistry on TRAPPIST-1 d.

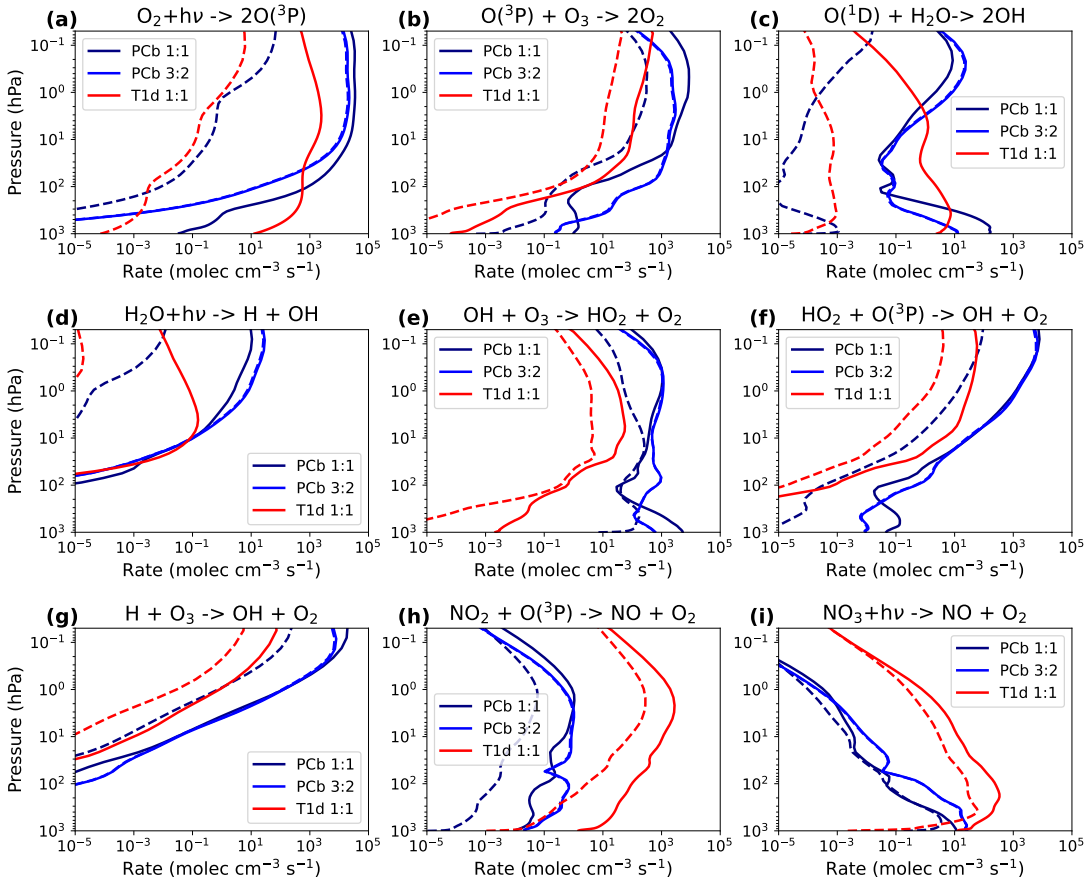

Figure 5.10: Hemispheric means of the vertical distribution of selected reaction rates in each of the four simulations. Each plot title indicates the to the chemical reaction shown, for the stable simulations of Proxima Centauri b (PCb) and TRAPPIST-1 d (T1d). Solid lines indicate the mean over the 0° hemisphere and dashed lines the mean over the 180° hemisphere, representing the dayside and nightside in 1:1 resonant orbits. The reactions were selected to include the Chapman mechanism of ozone formation (panel a and b), the HO_x catalytic cycles (panel c-g), and the NO_x catalytic cycles (panel h and i).

5.3.4 Temporal Evolution of the 3:2 Resonance

The 3:2 spin-orbit resonance for Proxima Centauri displays variability in the global mean values and spatial distributions of temperature (Figures 5.3a and 5.3b) and ozone column (Figures 5.7a and 5.7b). I confirm this variability in Figure 5.11, focusing on the temporal evolution of four key properties of the planet: the incoming stellar radiation at the top of the atmosphere (S_{TOA}), the surface temperature, the H_2O(g) column, and the ozone column. For each property, I calculate the mean of the global region (black), the 0° hemisphere centred at 0° latitude and longitude (orange), and the 180° hemisphere centred at 180° latitude and 0° longitude (blue).

S_{TOA} in Figure 5.11a illustrates the change in the dayside hemisphere: at the first periastron (dotted grey lines), S_{TOA} peaks on the 0° hemisphere and at the second periastron, S_{TOA} peaks on the 180° hemisphere. When the planet is at periastron, there is no incoming radiation on the nighttime hemisphere and thus $S_{TOA}=0$. This day-night cycle keeps repeating over the orbital evolution. The passages of apoastron (dashed grey lines) represent a minimum in the global mean S_{TOA}. The fluctuations in the global mean S_{TOA} exhibit the effect of the orbital eccentricity affecting the star-planet separation.

The varying amount of incoming radiation affects the surface temperature, as shown in Figure 5.11b. The peaks in surface temperature occur just after periastron passage, whereas the lowest surface temperatures occur after apoastron passage, for the global and the hemispheric means. The time lag between S_{TOA} and temperature extremes indicates the response time of the atmosphere to a change in radiation. Global mean temperature varies by up to 1.7 K (0.5% compared to the global mean) due to the eccentric orbit. Hemispheric variations can reach up to 8 K between daytime peaks and nighttime dips. For the 1:1 resonant orbit, hemispheric differences in temperature can be as high as 67 K (see Figure 5.2a). Hence, this again shows enhanced homogeneity across the planet for a 3:2 resonant orbit.

The H_2O(g) column in Figure 5.11c broadly follows the trends of the surface temperature, although the H_2O(g) column extremes have a slightly longer timelag after the periastron and apoastron passages. As described in Section 5.3.1, increased global temperatures lead to enhanced evaporation of water vapour from the surface ocean, explaining the additional lag in H_2O(g) column variations. The maximum H_2O(g) column of 3.2×10^{26} molecules cm^{-2} occurs during the daytime, about three days after periastron, and is 48% higher than the time-averaged global mean. The hemispheric mean H_2O(g) column then declines steeply down to its minimum (41% below the time-averaged global mean) during the nighttime. A temporary flattening of this decline in the H_2O(g) column is observed around apoastron, when the daytime is centred at 270° longitude, perfectly in the middle of the two hemispheres defined with centres at 0 and 180° longitude. During apoastron passage, a markedly different atmospheric circulation affects either hemisphere. The temporal evolution of the vertical wind (not shown) indicates a sudden decrease in the efficiency of the overturning circulation,

affecting the H_2O(g) column. Besides the day-night cycle in H_2O(g) column, Figure 5.11c demonstrates a periastron-apoastron cycle in the global mean H_2O column (black line) with up to 12% higher and 8% lower H_2O(g) column levels shortly after periastron and apoastron, respectively.

The global ozone column (Figure 5.11d) fluctuates by only $\sim$0.2 DU in the periastron-apoastron cycle, since the column density represents an integrated quantity that is most sensitive to the atmospheric layers with the highest air density and thus the lower atmosphere below the ozone production regions (see Figure 4.4). Considering only the levels above 18 km or 80 hPa (not shown), I find a maximum ozone column after periastron and minimum after apoastron, with variations of up to 10 DU between them that result from fluctuations in photochemistry and thus incoming radiation. By probing the ozone column at the surface, as shown here, I can connect hemispheric variations to dynamically-driven chemistry (following Chapter 4) and show the impact of the dominant chemical destruction processes in the troposphere (at P>100 hPa). Daytime-nighttime cycles are visible: ozone accumulates on the (changing) nighttime hemisphere with mean ozone columns that are up to 41 DU higher (5.3%) than the global mean, whereas daytime ozone is depleted by up to $-$5.3% as compared to the global mean.

The amount of H_2O and its photolysis determine the strength of the HO_x catalytic cycle, dominating ozone destruction in the troposphere during the daytime (see Section 5.3.3). Therefore, the daytime hemisphere – where the ozone column dips and the H_2O(g) column peaks – illustrates a matching but opposite trend in ozone and H_2O(g) columns when comparing Figures 5.11c and 5.11d. When the H_2O(g) column peaks, there is a stronger potential for HO_x-catalysed ozone destruction, evident from the dip in the ozone column. Nighttime ozone faces a lower H_2O(g) column and thus lower destruction rates. The matching trend is also evident from the plateauing behaviour at apoastron passage, which is seen for both ozone and H_2O(g) columns, albeit in opposite manner. The nighttime ozone exceeds the global mean value at all times and mirrors the temporal evolution of the daytime ozone, which indicates the dynamical connection between the daytime and nighttime hemisphere that I will explore in the next Section.

5.3.5 Dynamically-driven 3D Distributions

The zonal-mean meridional distribution of χ_{O_3} (coloured contours in Figure 5.12) confirms the ozone column distributions as described in Section 5.3.2. The contour lines in Figure 5.12 represent the age-of-air tracer, an inert tracer (no chemical or radiative interaction, purely dynamical) that counts the time that has passed since an air parcel was last in the lowest layers of the atmosphere (z$<$2 km or P$>$700 hPa). In this way, the age-of-air tracer can probe atmospheric dynamics and exchange between the troposphere and stratosphere.

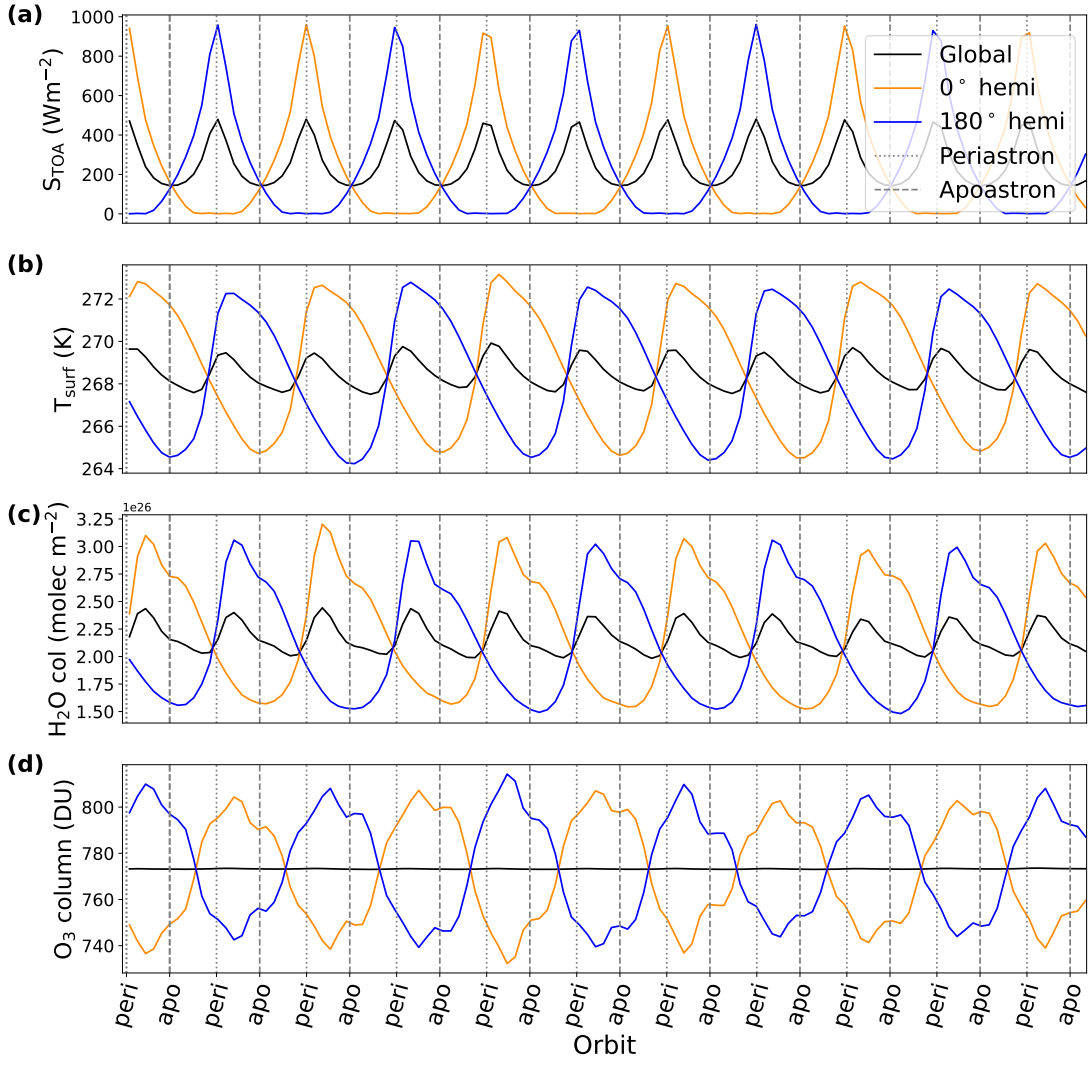

Figure 5.11: Temporal evolution of incoming stellar radiation at the top of the atmosphere (S_{TOA}, panel a), surface temperature (b), and vertically integrated water vapour (c) and ozone column densities (d) on Proxima Centauri b in a 3:2 resonance over 120 days, corresponding to almost 11 orbits. Orange and blue lines indicate the 0° and 180° hemispheres, respectively. The global average values are shown as the black line. From the peaks in S_{TOA}, I identify the periastron and apoastron passages, denoted as the dotted and dashed grey vertical lines and specified on the x-axis. From periastron to the next periastron, Proxima Centauri b completes one orbit around its host star, for a total of almost 11 orbits shown here.

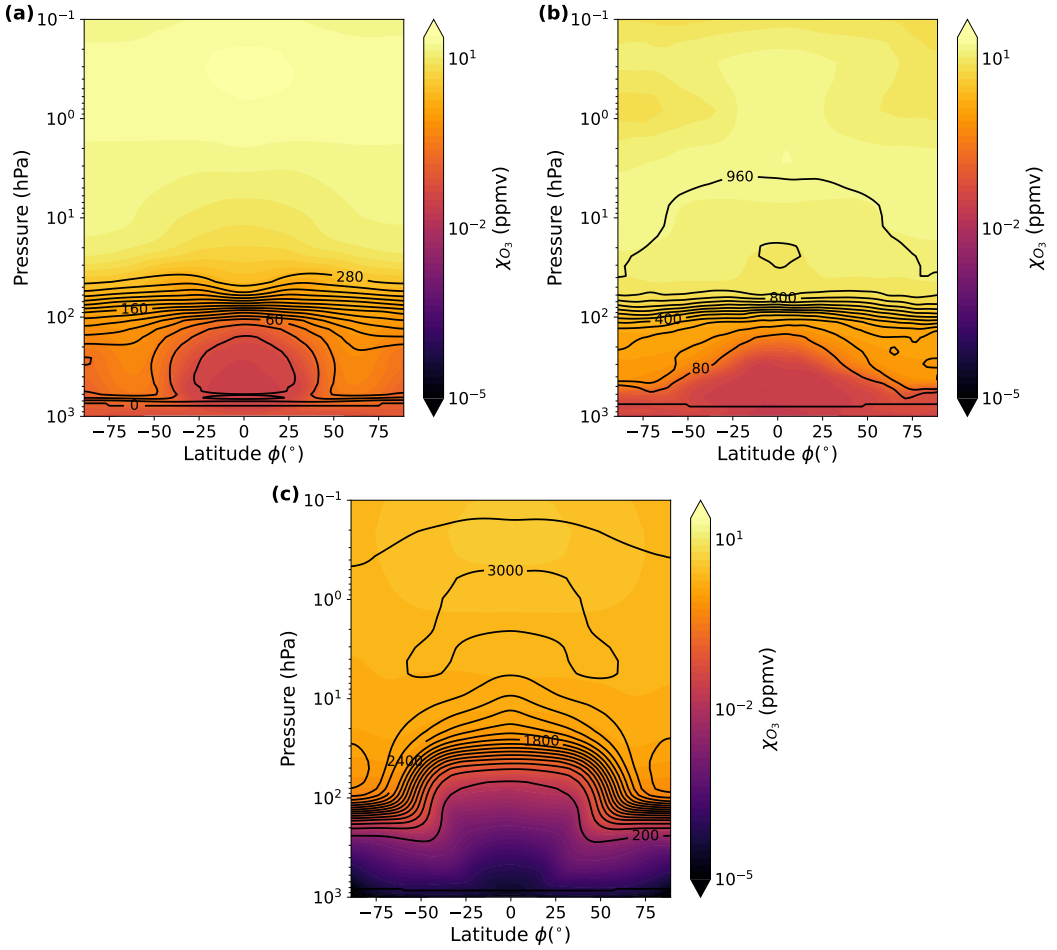

Figure 5.12: Zonal-mean meridional distribution of the mole fraction χ_{O_3} for (a) Proxima Centauri b in a 1:1 resonance, (b) Proxima Centauri b in a 3:2 resonance, and (c) TRAPPIST-1 d in a 1:1 resonance. Overplotted black contour lines correspond to the age-of-air tracer in days, to diagnose atmospheric circulation. The age-of-air tracer is is initialized at 0 s everywhere and reset whenever a parcel of air reaches the lowest atmospheric layers (below $\sim$2 km or P$>$700 hPa). In this way, the age-of-air tracer measures the amount of time since an air parcel was last found in the lowest layers of the atmosphere, probing the main features of the atmospheric circulation.

The main photochemical production regions of ozone are in the stratosphere during the daytime. For Proxima Centauri b, this corresponds to P$<$90 hPa for the 1:1 resonance and P$<$20 hPa for the 3:2 resonance, since radiation penetrates deeper into the atmosphere on the permanent dayside for a 1:1 resonant orbit (shown in Figure 5.10a). Following the dayside production on a 1:1 resonant Proxima Centauri b close to ϕ=0°, χ_{O_3} spreads to higher latitudes where it subsides down to $\sim$30 hPa (Figure 5.12a). For pressures exceeding $\sim$600 hPa, regional enhancements are visible between $-80<\phi<-40°$ and $40<\phi<80°$: these represent the gyre accumulation as shown in Figure 5.6a. Since I show the zonal mean the zonal variations are lost, but the enhancements are still caused by the nightside accumulation over the gyre regions. The black contour lines in Figure 5.12a show that the gyre regions consist of relatively old air as compared to the tropospheric surroundings, indicating that the gyres are connected to the older stratospheric air overhead. In Chapter 4 I show that a stratospheric dayside-to-nightside circulation drives this connection.

The high-latitude ozone column is also enhanced for a 3:2 resonant orbit, although now globally as shown in Figure 5.7. χ_{O_3} in Figure 5.12b confirms this spatial distribution, with enhanced χ_{O_3} at high latitudes for pressures as high as $\sim$600 hPa. The age-of-air distribution shows that older, ozone-rich air subsides at these high latitudes, producing the enhanced ozone columns. Hence, following the daytime production of ozone in the equatorial region (around ϕ=0° for all longitudes), this indicates the existence of a stratospheric equator-to-pole circulation that drives the ozone-rich air from low to high latitudes. The meridional circulation system has similarities to the Brewer-Dobson Circulation that describes the transport of ozone from its equatorial production regions to high latitudes on Earth (Brewer, 1949; Dobson, 1956; Butchart, 2014).

TRAPPIST-1 d shows qualitatively similar meridional variations in the ozone column (Figure 5.6b). The vertical distributions of χ_{O_3} and the age-of-air tracer in Figure 5.12c confirm this picture, although the ozone layer and age-of-air contourlines have shifted upwards in the atmosphere relatively to the results for Proxima Centauri b. In this case, photochemical production of ozone mainly occurs in the equatorial regions for P$<$30 hPa, followed again by equator-to-pole circulation that drives the buildup of ozone at higher latitudes. Again, the meridional circulation system shows similarities to the Brewer-Dobson Circulation on Earth (Brewer, 1949; Dobson, 1956; Butchart, 2014).

5.3.6 Observational Prospects

I translate the 3D data into synthetic observables using the PSG GlobES tool (Villanueva et al., 2018; Villanueva et al., 2022), as described in Section 5.2.4. I use the phase angles in Tables 5.2 and 5.3 to cover the 1:1 resonant cases. Additionally, I take the changing substellar longitude for the 3:2 resonant orbit of Proxima Centauri b into account to include a changing daytime hemisphere, also following Table 5.2.

The observed hemisphere and the corresponding distribution of surface temperature as a function of phase angle and substellar longitude are shown in Figure 5.13 for Proxima Centauri b 1:1 resonant (top), Proxima Centauri b 3:2 resonant (middle), and TRAPPIST-1 d 1:1 resonant (bottom). Due to the orbital inclination, we can cover a full phase for Proxima Centauri b. For TRAPPIST-1 d we can observe emission spectra for small variations in phase angle around 90° and 270°. Additionally, Figure 5.13 shows distinct spatial distributions: there are clear hemispheric differences in surface temperature over phase angles for the 1:1 resonant cases, whereas the 3:2 case is much more homogeneous.

Figure 5.14 shows emission spectra for the three planet configurations as a function of phase angle and focused on the proposed spectral range for the Large Interferometer for Exoplanets (LIFE) mission concept (Quanz et al., 2022). It should be noted that the spectrum shows the contrast between the planet and stellar radiation. The planet's thermal radiation alone shows peak wavelengths of 11.1–13.5 μm for Proxima Centauri b in a 1:1 resonance and around 11.2 μm for the 3:2 resonance, connecting well with the planetary temperatures. The thermal emission from the warmer TRAPPIST-1 d peaks at 10.7 μm.

For Proxima Centauri b in a 1:1 resonance, substantial spectral variations are visible in Figure 5.14a depending on the observed orbital phase (Figure 5.13a). The most prominent variations are driven by the observed temperature distribution (8–9.5 and 10–13.6 μm) and water vapour abundances (16.3–18.5 μm). Smaller variations of up to $\sim$4 ppm are seen for the ozone feature around 9.6 μm and water vapour features between 7–8 μm. The CO_2 feature covering 14–16.3 μm is constant over time because of its fixed abundance in the simulations and also affects the emission features between 16–18 μm. The highest contrasts are seen for the 32° and 0° phase angles, for which we observe most of the warm dayside hemisphere. The smallest contrasts correspond to the nightside views at phase angles of 167° and 200°. All other phase angles lead to intermediate contrasts. Hence, a synchronously rotating planet provides a cycle of observed contrast levels in an emission spectrum as the planet completes an orbit, varying by up to 20 ppm between 12–13 μm and up to 36 ppm between 16.3–18.5 μm.

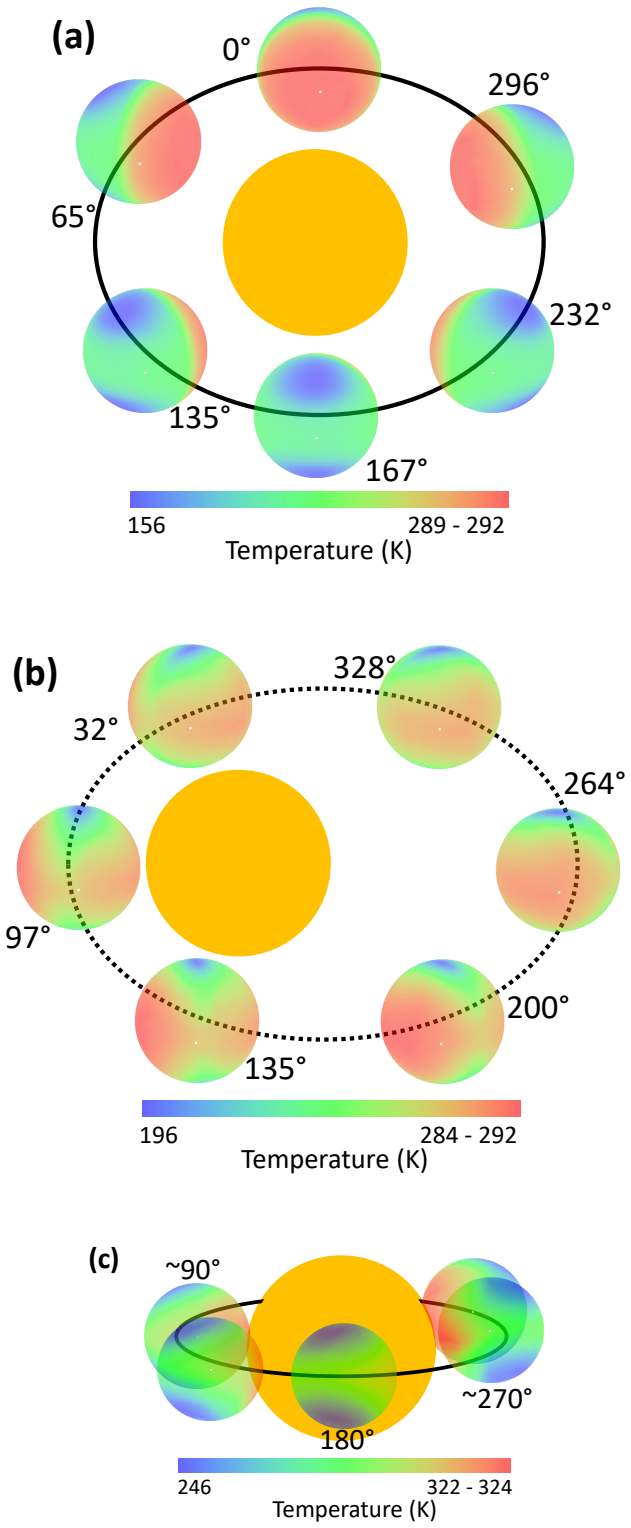

Figure 5.13: Orbital evolution (not to scale) of phase angles and corresponding surface temperature distributions on emission disks as observed by a distant observer. Proxima Centauri b at an orbital inclination of 70° is shown in (a) a 1:1 spin-orbit resonance and (b) a 3:2 resonance. Panel (c) shows TRAPPIST-1 d in a 1:1 spin-orbit resonance with an orbital inclination of 90° and includes the primary transit. Temperature maps denote variable ranges for each panel.

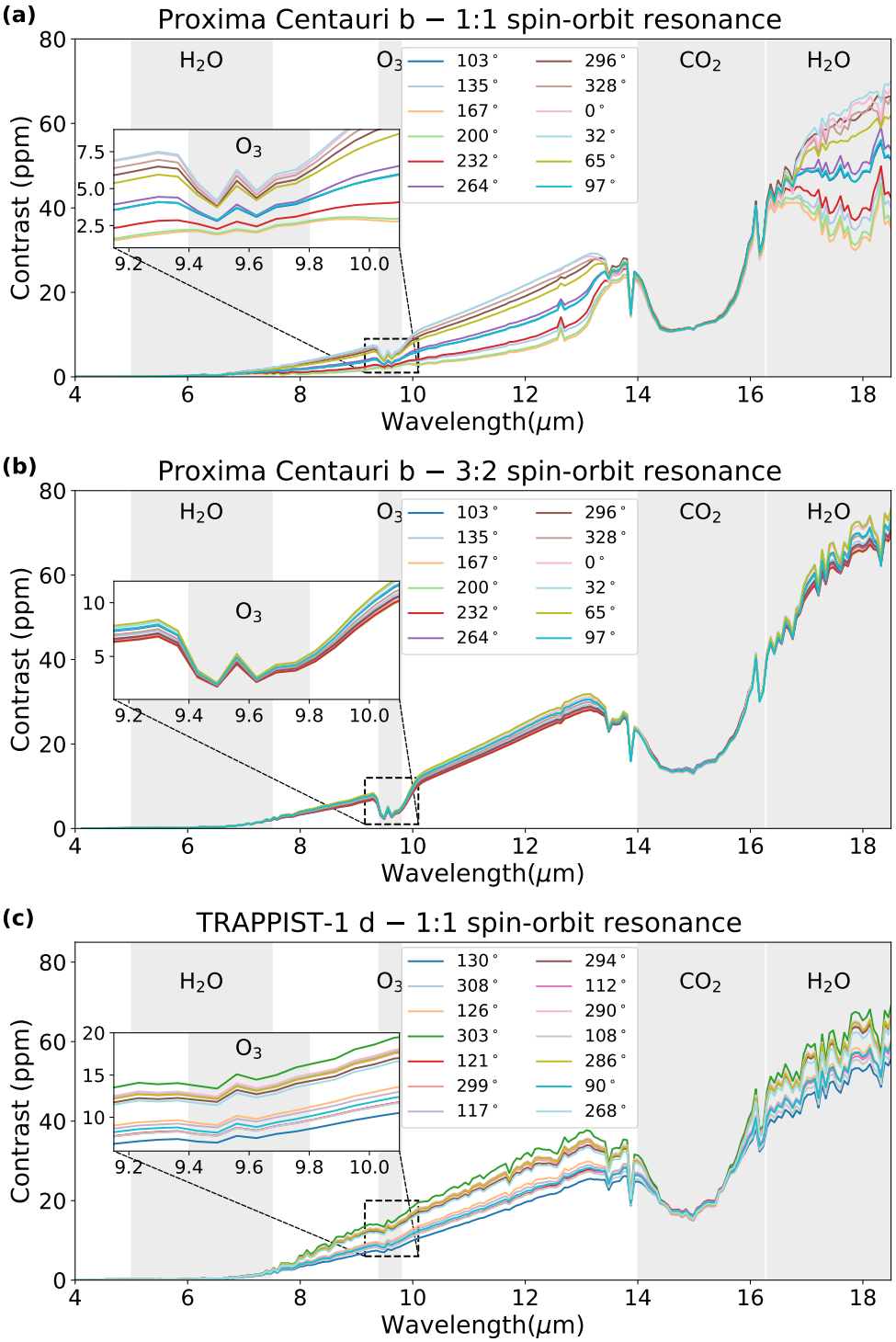

Figure 5.14: Synthetic emission spectra using different orbital phase angles for (a) Proxima Centauri b in a 1:1 resonant orbit, (b) Proxima Centauri b in a 3:2 resonant orbit, and (c) TRAPPIST-1 d in a 1:1 resonant orbit. Colours represent the orbital phase and the corresponding timestep of the simulation, using daily output (see Table 5.2). I use PSG with the GlobES 3D mapping tool to translate 3D CCM data into synthetic emission spectra.

Moving to Proxima Centauri b in a 3:2 resonant orbit, Figure 5.14b shows that the increased global homogeneity (Figure 5.13b) basically removes all of the phase angle variations in the emission spectrum. Further investigation also reveals that ice clouds mute spectral features particularly between 7–9 μm and 10–13.6 μm. The broad structure of the dominant opacity sources (water vapour, ozone, CO_2) remains similar to the 1:1 case, with contrast levels up to 7 ppm higher than the highest contrasts for the 1:1 case (spectra for 0° and 32° phase angles in Figure 5.14a). The ozone features around 9.6 μm are slightly deeper due to the enhanced global ozone column (see Section 5.3.2). The lack of temporal variability in the 3:2 resonant orbit presents a discriminant to determine whether a planet orbits in a 1:1 or a 3:2 resonance around its host star. Phase curves that focus on the ozone feature see a persistent feature for a 3:2 resonance and will see its disappearance for a 1:1 resonance. The same distinction is seen for any of the wavelengths corresponding to the water vapour features.

For TRAPPIST-1 d, the hemispheric variations in temperature are once again substantial (Figure 5.13c). However, due to the orbital inclination we can only probe a limited range of phase angles in emission, prohibiting us from seeing the variability over a full orbit. For phase angles between 90–130° and 268–308°, I predict variations of up to 14 ppm in Figure 5.14c, mostly between 8–14 μm and 16.3–18.5 μm. The ozone feature at 9.6 μm is muted, due to its considerably lower abundances for TRAPPIST-1 d (Figure 5.8e). Additionally, overlapping features from the ice cloud deck partially mute the ozone feature and also impact the regions between 7–9 μm and 10–13.6 μm, given the relatively high mass fraction and vertical extent of ice clouds (for P$>$3 hPa, see Figure 5.8d). Ice clouds are enhanced on the dayside hemisphere and therefore vary in their impact as a function of orbital phase angle.

Several more subtle distinctions probe the atmospheric pressure-temperature structure when comparing specific spectral bands for CO_2 (at 12.6 μm) and H_2O (at 18.3 μm) across the three planets. Infrared emission features originate in the regions of high optical depth and depend on both the abundances and the temperature difference of the absorbing and emitting layers (e.g. Madhusudhan & Seager, 2009; Rugheimer et al., 2013). If the region of high optical depth is in the cooler parts of the atmosphere, this generates a weaker thermal signal than that of the hotter part of the atmosphere. Hence, if temperature decreases with decreasing pressure, we see absorption features. Conversely, in case of a temperature inversion, we see emission features. Proxima Centauri b in a 1:1 resonance shows absorption features for the CO_2 and H_2O feature when we mainly probe the dayside hemisphere (e.g. for 0° and 32° in Figure 5.14a). However, when we probe most of the nightside hemisphere (e.g. for 167° and 200° in Figure 5.14a), both features become emission features, indicating a different vertical temperature profile between the dayside and nightside hemisphere. The distinction is not visible in Figure 5.8a due to the time-averaging, but on a daily output the nightside hemisphere exhibits a temperature inversion between pressures 0.1 hPa and 0.01 hPa, which is absent from the dayside hemisphere. The homogeneity of the 3:2 resonant orbit removes

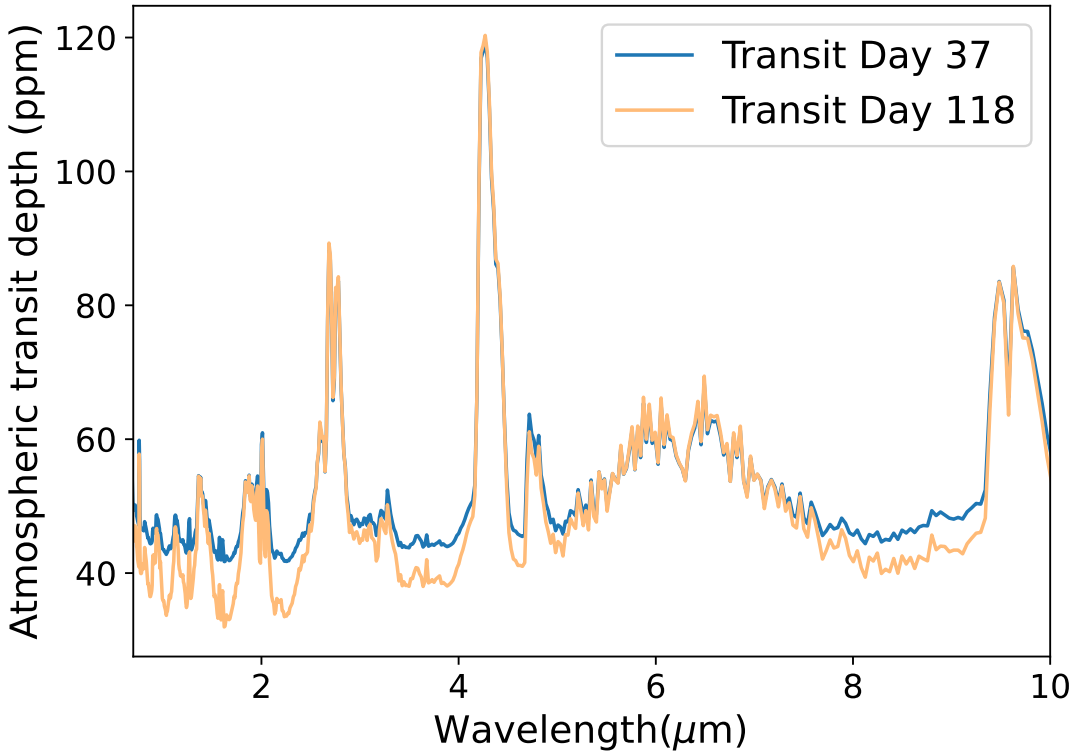

Figure 5.15: Synthetic transmission spectra for TRAPPIST-1 d in a 1:1 resonant orbit. Two simulation days corresponding to different transits are compared, as specified in Table 5.3.

this dayside-nightside distinction in the pressure-temperature profile and thus both the CO_2 features are absorbing over a full orbit. For TRAPPIST-1 d in a 1:1 resonance, the CO_2 feature (12.6 μm) remains an emission feature for the full orbit, whereas the water feature at 18.3 μm remains absorbing. Figure 5.8a illustrates a temperature inversion in the upper layers of the atmosphere (P$<$0.4hPa). In these layers, H_2O abundances are low (see Figure 5.8b) and therefore the H_2O absorption features originate deeper in the atmosphere. On the other hand, the vertically uniform CO_2 abundances of 391 ppm provide a large opacity even in the upper atmosphere and under the influence of the temperature inversion produce emission features.

Figure 5.15 shows the simulated transmission spectra of TRAPPIST-1 d. The atmospheric transit depth corresponds to the stellar flux lost specifically due to the transit of the planetary atmosphere. CO_2 ($\sim$2, 2.8 and 4.3 μm), H_2O ($\sim$5.5–8 μm), and ozone ($\sim$4.7 and 9.6 μm) show absorption features varying between 20–80 ppm. Small differences of up to 10 ppm distinguish the two simulated transits due to temporal variability in the cloud deck.

5.4 Discussion and Conclusion

Motivated by the range of possible exoplanet environments in terms of the host star, orbital configuration, and planetary parameters, I employ a 3D CCM to investigate the complex interplay between stellar radiation, atmospheric dynamics, and (photochemistry) for Proxima Centauri b and TRAPPIST-1 d, two of the most promising candidates for habitable environments around M-dwarfs. These and similar exoplanets are likely tidally locked to their host star (Goldreich & Peale, 1966; Barnes, 2017), in either a 1:1 or 3:2 spin-orbit resonance depending on eccentricity. In a 1:1 spin-orbit resonance, GCM simulations predict dayside-nightside differences and distinct regimes of atmospheric circulation for these planets (e.g. Carone et al., 2018), with the existence of an equatorial jet for Proxima Centauri b and a pair of midlatitude jets for TRAPPIST-1 d. The changing daytime hemisphere in an eccentric 3:2 spin-orbit resonance produces two hot spots along with meridional differences in e.g. the temperature that are more like Earth and present a more homogeneous atmosphere (e.g. Boutle et al., 2017). I identify the main mechanisms controlling the atmospheric chemistry for both planets in a 1:1 and 3:2 spin-orbit resonance, and for the latter setup present the first simulations of interactive (photo)chemistry. The orbital configurations impact the habitability of the planetary surface and observability of chemical species in the atmosphere.

5.4.1 Climate

For the true irradiance received by TRAPPIST-1 d, the planet transitions into a runaway greenhouse state regardless of the spin-orbit resonance. To still quantify the 3D effects on atmospheric chemistry for a planet in the fast rotator circulation regime, I artificially reduce the irradiance by $\sim$22% to ensure a stable climate for a 1:1 spin-orbit resonance (see Figure 5.1). I find that both planets in a 1:1 resonance exhibit stable climates, with $\sim$25% (Proxima Centauri b) and $\sim$75% (TRAPPIST-1 d) of the planetary surface above the freezing point of water. Simulating a 3:2 resonance with an eccentricity of 0.3 results in general warming for both planets. The eccentric orbit increases the mean flux over one orbit as compared to the circular case (see also Williams & Pollard, 2002; Dressing et al., 2010; Bolmont et al., 2016) and the changing location of the substellar point means that the stabilizing cloud feedback that cools 1:1 resonant planets (Yang et al., 2013; Kopparapu et al., 2016) is less effective. Nevertheless, Proxima Centauri b exhibits a stable planetary climate with two habitable regions, one centred at 0° latitude and longitude and one at 0° latitude and 180° longitude (Turbet et al., 2016; Boutle et al., 2017; Del Genio et al., 2019). TRAPPIST-1 d in a 3:2 resonance reaches the moist greenhouse limit (Kasting, 1988) with a wet stratosphere and a sixfold increase in H_2O (g) column as compared to the 1:1 resonance. Hence, the planet is no longer in a stable climate state. Colose et al. (2021) already studied the effects of the 3:2 spin-orbit resonance on the inner edge of the HZ. Contrary to my results, they find that their simulations do not generally result in wet stratospheres and therefore do not necessarily reach the limit. Liu

et al. (2023) do find a wetter stratosphere for Earth with an eccentricity of 0.4 as compared to a circular orbit. I suggest a model intercomparison project focusing on the impact of spin-orbit resonances on habitability as future work. The most recent update for the Gaia parallax and bolometric luminosity calculation of TRAPPIST-1 (Sanghi et al., 2023) should be used in further climate simulations of planets in this system and for determining the location of the inner HZ boundary.

5.4.2 Chemistry

Comparing the 3D distributions of ozone confirms the dependence of (photo)chemistry on an interplay between the stellar radiation, orbital configuration, and atmospheric circulation. The incoming stellar radiation and its wavelength dependence determine the different photochemical balance of ozone between Proxima Centauri b and TRAPPIST-1 d (see Kozakis et al., 2022). For the 1:1 resonant planets, a dependence on the circulation state was also suggested by Chen et al. (2019) for a range of orbital periods and stellar temperatures. On Earth, the Brewer-Dobson circulation transports ozone to the poles and controls the spatial distribution of ozone (Brewer, 1949; Dobson, 1956; Butchart, 2014). In Chapter 4, I show that the spatial distribution of ozone on Proxima Centauri b in a 1:1 resonance is controlled by a stratospheric dayside-to-nightside circulation mechanism, resulting in the zonal asymmetry as shown in Figure 5.6a. For the 3:2 resonance (Figure 5.7) and TRAPPIST-1 d in a 1:1 resonance (Figure 5.6b) I find meridional variations in the ozone column. Age-of-air tracer experiments suggest that a stratospheric equator-to-pole circulation mechanism similar to the Brewer-Dobson circulation causes the spatial distribution.

I explain the differences in vertical ozone profiles (Figure 5.8e) by comparing the dominant chemical processes in the simulations. The production of ozone fundamentally depends on the incoming UV flux (as shown in detail by e.g. Selsis et al., 2002; Segura et al., 2003; Grenfell et al., 2007; Grenfell et al., 2014; Kozakis et al., 2022). A low total amount of UV flux produces little ozone with barely discernible absorption features in synthetic spectra (Grenfell et al., 2007), which is the case for my simulation of TRAPPIST-1 d. On the other hand, high UV fluxes will be absorbed by ozone and significantly heat the stratosphere, in turn diminishing the strength of the ozone features in emission spectra (Kozakis et al., 2022) and thus making it harder to detect the 9.6 μm features in Figure 5.14. Proxima Centauri b seems to receive the right amount of radiation for significant ozone formation without substantial stratospheric heating, like the M7-orbiting exoplanet from Grenfell et al. (2014). For Proxima Centauri b, HO_x cycles dominate ozone destruction in the troposphere and upper stratosphere, in line with Yates et al. (2020) and Braam et al. (2022). TRAPPIST-1 d has a substantially stronger NO_x production due to its tall cloud structures (Figure 5.8c and d) and associated higher lightning flash rates. Therefore, NO_x cycling dominates ozone destruction in most of the atmosphere and emphasizes the role of lightning on atmospheric chemistry and the

interpretation of biosignatures (Ardaseva et al., 2017, see also Chapter 3). The difference in lightning flash rates between both planets motivates future work on lightning in diverse exoplanet configurations. Catalytic cycling of ozone is also sensitive to the amount of UV flux (e.g. Grenfell et al., 2014), which is especially important considering the impact of flares on atmospheric chemistry around M-type stars (e.g. Chen et al., 2021; Ridgway et al., 2023). The trade-off between UV driving ozone formation and stratospheric heating and the subsequent impact on atmospheric dynamics (De Luca et al., 2024) needs to be further explored using 3D models.

For Proxima Centauri b, HO_x cycles dominate ozone destruction in the troposphere and upper stratosphere, in line with Yates et al. (2020) and Chapter 3. TRAPPIST-1 d has a substantially stronger NO_x production due to its tall cloud structures (Figure 5.8c and d) and associated higher lightning flash rates. Therefore, NO_x cycling dominates ozone destruction in most of the atmosphere and emphasizes the role of lightning on atmospheric chemistry and the interpretation of biosignatures (Ardaseva et al., 2017, see Chapter 3). The difference in lightning flash rates between both planets motivates future work on lightning in diverse exoplanet configurations. Catalytic cycling of ozone is also sensitive to the amount of UV flux (e.g. Grenfell et al., 2014), which is especially important considering the impact of flares on atmospheric chemistry around M-type stars (e.g. Chen et al., 2021; Ridgway et al., 2023). The trade-off between UV driving ozone formation and stratospheric heating and the subsequent impact on atmospheric dynamics (De Luca et al., 2024) needs to be further explored using 3D models.

Further analysis of the 3:2 spin-orbit resonance reveals daytime-nighttime cycles as well as periastron-apoastron cycles in temperature, H_2O (g) column, and O_3 column, ultimately driven by variations in the incoming stellar radiation. I find that extrema in temperature, H_2O (g) column, and ozone column follow periastron and periastron passages with a brief time-lag, denoting the response time of the atmosphere to radiation changes. Especially H_2O cycles are prominent, with hemispheric changes up to 48% and eccentricity changes up to 12% as compared to the time-averaged global mean H_2O (g) column. Global mean ozone fluctuations due to eccentricity are small at $\sim$0.2 DU due to the relatively long chemical lifetime of ozone for Proxima Centauri b conditions (see Yates et al., 2020, and Section 4.3.3). However, the daytime-nighttime cycle with ozone accumulation during the nighttime are clearly visible with hemispheric enhancements and depletion of up to 41 DU (5.3%) as compared to the time-averaged global mean. The daytime-nighttime cycle illustrates the strong dependence of the ozone distribution on the coupling of photochemistry and atmospheric dynamics (see also Chapter 4). The mean hotspot temperatures (within the white lines in Figure 5.3) consistently

exceed 280 K, in accordance with Boutle et al. (2017). They also showed that, for this eccentric orbit, the mean flux approximation does not hold (Bolmont et al., 2016). To further unveil the characteristics of the dynamic atmosphere in a 3:2 spin-orbit resonance, I suggest the application of dynamical systems metrics (e.g. Hochman et al., 2022, 2023).

5.4.3 Observability

I report several potential 3D spatial and temporal effects on emission spectra, using the PSG GlobES tool (Villanueva et al., 2018; Villanueva et al., 2022) to comprehensively generate synthetic spectra from my 3D simulations whilst varying the observed 3D geometry with the orbital phase angle. For Proxima Centauri b and TRAPPIST-1 d in a 1:1 resonance, variations in the pressure-temperature profile as well as horizontal and vertical variations in H_2O and ozone abundances cause spectral fluctuations of up to 36 ppm for Proxima Centauri b. Despite only probing a small fraction of the TRAPPIST-1 d orbit due to its inclination (see Figure 5.13c), I still predict spectral fluctuations of up to 14 ppm. The more homogeneous atmosphere of Proxima Centauri b in a 3:2 resonance diminishes spectral variations as a function of orbital phase, as also shown by Turbet et al. (2016) and Boutle et al. (2017). The presence or absence of these spectral fluctuations then presents a discriminant between a 1:1 or 3:2 spin-orbit resonance. The ozone feature at 9.6 μm provides an additional window to probe with time-resolved emission spectra or a phase curve, that we can only predict and interpret using 3D CCM simulations. Given the uncertainties for JWST observations of TRAPPIST-1 b and c (Greene et al., 2023; Zieba et al., 2023), these likely disappear under current noise levels of the observations, but the time-averaged 1-D profiles still depend on the 3D nature of atmospheres.

However, the spectra in Figure 5.14 were deliberately generated for the proposed wavelength range of the LIFE mission concept (Quanz et al., 2022). Given the extremely small angular separation of the planet, TRAPPIST-1 d will likely not be detectable with LIFE (Carrión-González et al., 2023). Nevertheless, the results are valid for similar exoplanets in terms of size and atmospheric pressure that also exhibit the fast rotator circulation regime. On the other hand, spectral features for Proxima Centauri b are expected to be visible after observing for only about a day (Defrère et al., 2018), making this planet a prime target for the LIFE mission (Angerhausen et al., 2024). LIFE has the capability to detect P-T profiles on Earth as an exoplanet with constant chemical abundance profiles (Konrad et al., 2022). Alei et al. (2022) extend the analysis to the changing atmospheric conditions through Earth's history, finding biases in retrieved P-T profiles. Mettler et al. (2024) find similar biases in the P-T profiles using disk-integrated Earth observations, but suggest these are due to the assumption of

constant abundance profiles in the retrievals as compared to non-constant abundance profiles in generating synthetic spectra. As I describe here, the temporal and spatial variations in the P-T profile are a complex interplay between the radiative, thermal, dynamical, and chemical state of the atmosphere that can only be explored using 3D CCM simulations.

The main spectral features of chemical species such as CO_2, H_2O, O_3, and CH_4 can be detected by LIFE to determine the atmospheric composition of terrestrial exoplanets, for the baseline LIFE requirements of spectral resolution R=50 and signal-to-noise ratio S/N=10, though O_3 and CH_4 benefit from enhanced S/N=20 (Alei et al., 2022; Konrad et al., 2022; Mettler et al., 2024). Using real disk and time-averaged Earth observations, Mettler et al. (2023) find that the mid-infrared spectrum of Earth as an exoplanet will vary as a function of season and viewing geometry. Variations in temperature or planetary albedo should be detectable with LIFE for the baseline R and S/N requirements (Mettler et al., 2024), but varying abundances of chemical species with season or viewing geometry are currently muted by retrieval uncertainties (Mettler et al., 2024). However, as Mettler et al. (2024) also note, these retrieval results are biased by simplifying assumptions such as cloud-free atmospheres or vertically constant abundance profiles, with work underway to mitigate these. Variations with season or viewing geometry are planet-specific and, as I show here, zonal asymmetries in a 1:1 spin-orbit resonance result in more dramatic spectral variations as compared to the meridional asymmetries on a 3:2 spin-orbit resonant exoplanet or on Earth. Therefore, an in-depth investigation of the observability of the spectral variations in Figure 5.14 with LIFE is currently being conducted for various combinations of S/N and R.

Chapter 6

Discussion

6.1 Summary of Results

Rocky exoplanets orbiting in the HZ of relatively cool M- and K-type stars are likely tidally locked to their host star with spin-orbit resonance depending on the orbital eccentricity. In this thesis, I have studied the atmospheres of such exoplanets and addressed a variety of potential drivers of disequilibrium chemistry, assuming an Earth-like atmospheric composition. A sophisticated 3D CCM – consisting of the Met Office Unified Model and the UK Chemistry and Aerosols framework – was used to comprehensively simulate the physical and chemical processes in the planetary atmosphere and their implications for habitability. Here, I summarize the main findings of this thesis, connecting them to the aims of the thesis as stated in Section 1.8.

How do the variations in quiescent stellar spectra drive 3D photochemistry in the atmospheres of tidally locked exoplanets?

Using the latest available data for the stellar spectrum of Proxima Centauri from the MUSCLES spectral library, I have improved upon earlier simulations of the atmospheric chemistry on Proxima Centauri b by Yates et al. (2020), who used a simulated spectrum for Proxima Centauri b from the BT-Settl library. In Chapter 3, I demonstrated that the MUSCLES spectrum for Proxima Centauri results in enhanced ozone formation and a tenfold increase in ozone column densities on Proxima Centauri b as compared to Yates et al. (2020). The higher total amount of UV flux and a larger FUV/NUV ratio (0.012 for the MUSCLES spectrum versus 2.92×10^{-6} for the BT-Settl spectrum) explain the difference in ozone abundances. In Chapter 5, I add simulations for TRAPPIST-1 d, using the composite stellar spectrum from the Mega-MUSCLES survey for TRAPPIST-1 (Wilson et al., 2021). For this spectrum, I find an FUV/NUV ratio of 0.0018, explaining decreased ozone production as compared to the MUSCLES spectrum for Proxima Centauri b. The total UV flux for $\lambda<$400 nm is lower than both the MUSCLES and BT-Settl spectrum of Proxima Centauri, further explaining the weak

ozone production on TRAPPIST-1 d. In the 1:1 resonant cases, photochemistry is limited to the dayside hemisphere, but photochemical products such as ozone show significant spatial variability with, for example, accumulation on the nightside of Proxima Centauri b as shown in Chapter 3.

What is the potential for lightning formation on tidally locked exoplanets, and how does this energetic (disequilibrium) process affect atmospheric chemistry in 3D?

For the same setup configuration for Proxima Centauri b, I then investigated the potential for lightning initiation on tidally locked exoplanets, specifically those orbiting in a 1:1 spin-orbit resonance. Using a parametrization of lightning flash rates in terms of cloud-top height – commonly applied in studies of Earth's climate and chemistry – I found that vigorous convection over and around the substellar point drives the formation of tall convective cloud structures, providing the right conditions for lightning initiation. I found LFRs up to 0.16 flashes km^{-2} yr^{-1} around the substellar point, lower than observed continental LFRs on Earth (global average of 3.4 flashes km^{-2} yr^{-1} as calculated from LIS/OTD data Cecil et al. 2014) but comparable to oceanic rates far away from landmasses (0.11–0.57 flashes km^{-2} yr^{-1}). The spatially asymmetric distribution of lightning flashes enriches the dayside atmosphere below $\sim$20 km in NO_x, providing enhanced catalytic cycling of ozone at these altitudes. Following its dayside production, NO_x is then advected to the nightside of the planet by the large-scale circulation. In the absence of photochemistry, NO_x reacts further to form the more complex NO_y species. Due to their long lifetime in the absence of photolysis, they act as reservoir species on the planet's nightside.

How do 3D circulation patterns affect the atmospheric chemistry on tidally locked exoplanets and can these explain spatially varying ozone layers as previously predicted?

In Chapter 4, I further investigated the spatial variability in the 3D distribution of ozone, as reported in Chapter 3. My simulations and the earlier ones by Yates et al. (2020) showed that ozone accumulates on the nightside hemisphere. Ozone production requires the photolysis of molecular oxygen and is thus limited to the dayside of the planet. This indicates dynamical connections between the dayside and nightside hemispheres, which I diagnosed by applying a transformation from the traditional geographic coordinate system to a tidally locked coordinate system (Koll & Abbot, 2015; Hammond & Lewis, 2021). The circulation on 1:1 resonant exoplanets is driven by the dayside-nightside contrast in irradiation, driving an overturning circulation with dayside upwelling and nightside downwelling, which in turn generates planetary-scale Rossby and Kelvin waves that feed a superrotating jet and produce a pair of cyclonic gyres on the nightside (Showman et al., 2013). In Chapter 4, I identified a stratospheric dayside-to-nightside circulation mechanism that advects ozone from its dayside production regions towards the nightside, where it subsides and accumulates at the locations of the gyres. Age-of-air tracer experiments showed that the circulation mechanism does not

just affect ozone, but can affect any tracer (chemical compounds or aerosols), as long as 1) the dynamical timescales are shorter than chemical timescales and 2) there is a dayside stratospheric production mechanism. Hence, the circulation mechanism is not very effective for the 3D distribution of the (tropospheric) lightning-induced species, as reported in Chapter 3.

What are the effects of distinct spin-orbit resonances on planetary climate and atmospheric chemistry?

Chapter 5 begins with a thorough comparison of the planetary climate and atmospheric chemistry for two exoplanets exhibiting distinct circulation regimes, simulating both a 1:1 and an eccentric 3:2 spin-orbit resonance. TRAPPIST-1 d reaches the runaway greenhouse limit for the true irradiance regardless of the spin-orbit resonance. An artificial reduction of the irradiance by $\sim$22% ensures a stable climate for a 1:1 spin-orbit resonance (see Figure 5.1) and allows an investigation of 3D atmospheric chemistry for a planet in this circulation regime. I found that both Proxima Centauri b and TRAPPIST-1 d exhibit stable climate regimes for a 1:1 resonance, with $\sim$25% and $\sim$75% of the planetary surface above the freezing temperature of water, respectively. For an eccentric 3:2 resonance, I predicted the warming of the surface for both planets. The warming is explained by an increase of the mean stellar flux over one eccentric orbit as compared to a circular one and a less effective stabilising cloud radiative feedback compared to the 1:1 resonance due to the changing substellar longitude. Proxima Centauri b exhibits a stable climate, with two habitable regions centred at 0° and 180° longitude. The warming induces the runaway greenhouse effect for TRAPPIST-1 d, diagnosed through a wet stratosphere, a sixfold increase in the vertically integrated H_2O (g) column density, and passing the threshold of the Simpson-Nakajima limit in outgoing planetary radiation.

The 3-D ozone distributions for the set of simulations in Chapter 5 illustrate the dependence of (photo)chemistry on the interplay between stellar radiation, orbital configuration, and atmospheric circulation. The respective stellar fluxes determine the different ozone abundances for Proxima Centauri b and TRAPPIST-1 d. The spatial distribution with longitudinal gradients on Proxima Centauri b is controlled by a stratospheric dayside-to-nightside circulation as shown in Chapter 4. For Proxima Centauri b in a 3:2 resonant and TRAPPIST-1 d in a 1:1 resonant orbit, I instead found longitudinal gradients in the ozone column densities. Again using age-of-air tracer experiments, I showed that these distributions are driven by an equator-to-pole stratospheric circulation with similarities to the Brewer-Dobson circulation that controls the ozone distribution on Earth. I found distinctions in the dominant destruction mechanisms: HO_x catalytic cycles primarily destroy ozone in Proxima Centauri b's atmosphere, whereas NO_x catalytic cycling dominates ozone destruction for TRAPPIST-1 d. Stronger H_2O photolysis

and oxidation produce more HO_x on Proxima Centauri b, whereas LFRs on TRAPPIST-1 d are orders of magnitude higher, driving enhanced NO_x production and catalytic cycling as well as interactions with HO_x species. This demonstrates the range of 3D processes affecting atmospheric chemistry and how they can differ from planet to planet.

In turn, these orbit- and planet-dependent 3D processes affect the strength of ozone spectral features and determine the spatial and temporal variations in emission spectra, as will be further elaborated in the final question of this Section. On Earth, the amount and distribution of ozone protects surface life from harmful radiation, which is even more important given the enhanced UV radiation and presence of stellar flares around M-dwarfs (Rugheimer et al., 2015b). In Section 3.4.1, I find that the ozone layer protects the surface of Proxima Centauri b from harmful UV radiation, allowing only 15% of the incoming stellar UV radiation ($\lambda < 32$ nm) to reach the surface. We also found that flares can enhance the ozone column density, reducing the potential harmful effects of the next flare (Ridgway et al., 2023). On the other hand, direct contact with near-surface ozone damages life on Earth (Zhang et al., 2019). Hence, understanding the 3D distribution of ozone and its temporal variation is potentially a key component of planetary habitability. Whilst photochemistry and flares mainly drive chemistry in the upper atmosphere, lightning is a key driver of disequilibrium chemistry in the troposphere, with a potential role in prebiotic synthesis in the reduced atmosphere of the Early Earth (Miller, 1953) and exoplanets in general (Rimmer & Rugheimer, 2019). Therefore, the 3D distribution and resulting chemical effects of lightning can teach us about the prebiotic potential of exoplanet environments.

How does 3D atmospheric chemistry evolve for an eccentric orbit and does this produce any variability?

For the 3:2 spin-orbit resonance of Proxima Centauri b, I identified daytime-nighttime cycles and periastron-apoastron cycles in hemispheric mean surface temperature, H_2O (g) column densities, and ozone column densities. These cycles are ultimately driven by the variations in incoming stellar radiation due to the planet's rotation and eccentric orbit. The extrema in both cycles follow with a brief time lag after periastron and apoastron, corresponding to the atmospheric response time. Daytime-nighttime cycles show hemispheric variations of up to 48% and 5.3% for H_2O (g) and ozone column densities as compared to the global and temporal mean. Periastron-apoastron cycles are less pronounced at 12% and 0.05% for H_2O and ozone, respectively. The weaker ozone cycles are explained by its relatively long chemical lifetime damping out photochemically driven variations.

What traces do these 3D effects in atmospheric chemistry leave in synthetic spectra and will they be tractable in future observations?

Throughout Chapters 3 4, and 5, I have produced synthetic spectra of the planetary atmospheres to determine the prospects of observing the various 3D effects. For Proxima Centauri b and similar planets, lightning-induced NO_x species are too low in abundance and located too deep in the atmosphere to leave any observable features in transmission spectra. The enhanced lightning-induced NO_x for TRAPPIST-1 d and similar planets presents a possible opportunity here. I then focused on the thermal radiation from the planets themselves in emission spectra. I used the NASA PSG GlobES tool (Villanueva et al., 2018; Villanueva et al., 2022) to account for 3D spatial and temporal variations in meteorological and chemical parameters in the generation of emission spectra. The spectra were computed as a function of the orbital phase angle, considering the orbital evolution and observed geometry. For the 1:1 resonant simulations of Proxima Centauri b and TRAPPIST-1 d, the emission spectra show fluctuations in chemical signatures of up to 36 ppm and 14 ppm, respectively. The 9.6 μm ozone features fluctuate by 6–9 ppm. The 3:2 resonance for Proxima Centauri b results in a more homogeneous atmosphere as a function of orbital phase angle, reducing most spectral fluctuations and presenting a potential discriminant from the 1:1 resonance.

6.2 Implications

The results in this thesis for distinct planetary environments emphasize the complex 3D nature of planetary atmospheres and the plethora of processes that can drive or affect disequilibrium atmospheric chemistry. The analysis of the impact of an individual process is helpful and often required to build an intuitive understanding but, in reality, there is a complex interplay between all these physical and chemical processes – stellar radiation, orbital dynamics, atmospheric dynamics, the hydrological cycle including cloud formation, lightning initiation, and (photo)chemistry – that can only be understood with sophisticated 3D models. Whilst detections of potential biosignatures on rocky exoplanets may be reported in the coming years, any reliable interpretation of these biosignature detections will fundamentally depend on the planetary environment and will thus require context from 3D simulations.

In Chapters 3 and 5, I show that the magnitude of ozone production depends on the total amount and spectral distribution of stellar UV radiation. On the other hand, too much radiation in turn heats the stratosphere, with the potential to diminish chemical signatures in emission spectra. Proxima Centauri b, in particular, seems to be in the sweet spot of incoming stellar radiation that drives significant ozone production but not too intense stratospheric heating (Grenfell et al., 2014). The stellar radiation from TRAPPIST-1 leads to weak ozone production on planet d, but as Wilson et al. (2021) note, the NUV stellar radiation is based on a semi-empirical model using the measured emission lines fixed to an arbitrary continuum. To

better understand planetary environments, we need to accurately understand the stellar UV radiation, particularly for M-type stars with their associated flares. A recent study to which I contributed showed that flares drive enhanced ozone formation (Ridgway et al., 2023), potentially reducing the atmospheric impact of the next stellar flare.

Lightning initiates catalytic NO_x cycles and the evaporation of surface water followed by photolysis or oxidation initiates catalytic HO_x cycles to destroy ozone. LFRs are relatively low for the conditions on Proxima Centauri b, but for TRAPPIST-1 d simulated LFRs range from 70–1000 flashes $km^{-2}yr^{-1}$. The lightning initiation follows the extent of cloud formation and thus is strongly influenced by irradiation, thermodynamics, orbital configuration, and atmospheric dynamics. These results show that lightning is a strong function of the planetary environment and that its 3D impact needs to be considered on an individual basis, especially when we start interpreting potential biosignatures.

I have demonstrated in Chapter 5 that the orbital configuration determines the distribution of stellar radiation and thus the circulation regime of the planetary atmosphere. The comparison between 1:1 resonances for Proxima Centauri b and TRAPPIST-1 d shows that this determines the spatial distribution of chemical species, producing either latitudinal or longitudinal variations in the vertically integrated column densities. The nightside gyre locations are not fixed but vary with longitude over time (as shown in Chapter 4), producing an internal mode of atmospheric variability in H_2O (see also Cohen et al., 2023a) and ozone abundances (De Luca et al., 2024). The 3:2 resonances with eccentricity provide external modes of variability through the daytime-nighttime and periastron-apoastron cycles. These cycles affect the atmospheric dynamics and chemistry, but also indicate cycles in temperature and precipitation that are thought to be essential for the origin of life on a planet (Pearce et al., 2017). The existence of such cycles is also dependent on various 3D processes.

The atmospheric dynamics of the planets, ultimately due to asymmetric heating by the incoming stellar radiation, is essential to understanding the distributions of atmospheric tracers (including chemical species and aerosols such as clouds and hazes) for any orbital configuration. I show the value of age-of-air tracer experiments to probe the dynamics in terrestrial exoplanet atmospheres in Chapters 4 and 5. The first application of tidally locked coordinates to the study of atmospheric chemistry in Chapter 4 helped unveil the key role of dayside-to-nightside circulation mechanisms in the stratosphere for ozone (and other tracers) on 1:1 resonant exoplanets. Such approaches build upon decades of research into climate-dynamics-chemistry interactions in the Earth System modelling community, highlighting the importance of close connections between Earth System science and exoplanet science. In a subsequent paper that was co-authored by me, we further unveil the climate-dynamics-chemistry interactions at play by combining CCM simulations with dynamical systems theory (De Luca et al., 2024, building upon Hochman et al., 2022, 2023). These results demonstrate that interactive ozone enhances variability in the compound dynamics of temperature and

wind speeds. Furthermore, we find a correlation between variability in the extent and location of the nightside ozone columns and the dynamical systems theory metrics of dynamical stability (co-persistence and co-dimension De Luca et al., 2024). We find an enhanced ozone column for dynamically unstable atmospheric states in terms of temperature and wind speeds and a diminished ozone column for dynamically stable states. This once again illustrates the coupled interplay of climate, atmospheric dynamics, and chemistry, strengthening the findings in Chapter 4 of this thesis. Ozone is particularly suited to probe these connections since it is both radiatively active and depends on photochemical production mechanisms. However, depending on the stellar and planetary environment many other molecules with rotational-vibrational transitions will be radiatively active and affected by photochemistry, like the triatomic molecules H_2O, CO_2, HCN, NO_2, and N_2O, but also molecules such as CH_4 and NH_3.

Contrasting the TRAPPIST-1 d simulations in Chapter 5 shows the sensitivity of planetary climates to the orbital configuration using a reduced irradiance. I find a stable climate state and a runaway climate for a 1:1 and an eccentric 3:2 spin-orbit resonance, respectively, indicating a connection between the inner edge of the HZ (see Section 1.6) and the spin-orbit resonance. This climate-orbit connection is more sensitive than those found by Colose et al. (2021), who find relatively dry stratospheres for higher-order resonances in contrast to wet stratospheres in this study. The different findings warrant further investigation but nevertheless, my results show the importance of understanding the orbital configuration and its connection to the 3D planetary climate and atmospheric chemistry in our quest for habitable exoplanets. The additional radiative feedback from interactive chemistry (e.g. ozone as a greenhouse gas, or H_2O destruction due to chemistry) can either speed up or prevent the runaway scenario, with similar impacts from the potential presence of aerosols following haze parameterisations from Mak et al. (2023) and Mak et al. (2024).

The spectral fluctuations that I found in Chapter 5 for the 1:1 resonant planets depend on both the observing geometry and the 3D distribution of chemical species. The predicted discriminant from the more homogeneous 3:2 resonant atmosphere will have to be considered when looking for seasonally varying biosignatures (Schwieterman et al., 2018). Whilst the spectral fluctuations most likely disappear below the noise levels for current observations using JWST, future missions such as LIFE or HWO will be able to probe individual features as well as spatial and temporal fluctuations in those features. Previous predictions and retrievals for LIFE emphasize the critical role of vertically varying profiles of pressure-temperature and chemical abundances to avoid biases in the retrievals (Alei et al., 2022; Konrad et al., 2022; Mettler et al., 2024), on top of the considered horizontal variations. Such 3D variations and potential spectral fluctuations can only be predicted and interpreted using complex 3D CCMs, emphasizing an important role for CCM simulations in developing the science objectives for such observatories.

6.3 Suggestions for future work

6.3.1 Atmospheric Chemistry

I conclude this thesis with suggestions for future research. In Chapters 3, 4, and 5, I have identified several drivers of disequilibrium chemistry in the atmospheres of exoplanets orbiting M-dwarfs, whilst emphasizing that these depend on the host star and orbital configuration. Lightning-induced chemistry should be further studied with CCM simulations for a diverse set of exoplanets. Based on the high LFRs on TRAPPIST-1 d I find that the NO_x catalytic cycle dominates ozone destruction, suggesting an important role for biosignature interpretation that is planet-specific. Reactive halogen gases such as chlorine (Cl) and bromine (Br) provide additional catalytic cycles destroying ozone on Earth (Seinfeld & Pandis, 2016), both at low latitudes and over the poles in the presence of Polar Stratospheric Clouds (PSCs: Tritscher et al., 2021). The low temperatures and dry air over the nightside gyres of exoplanets in 1:1 spin-orbit resonances are reminiscent of the polar stratosphere on Earth with an unexplored potential to form PSCs and initiate additional ozone destruction. This thesis assumes tabulated dry deposition velocities but UKCA can be used to interactively calculate dry deposition (see O'Connor et al., 2014) with a potential impact on disequilibrium chemistry and ozone in particular. The obliquity of a planet drives seasonality (e.g. Olson et al., 2018) and additional cycles like those presented in Chapter 5 and further CCM simulations are needed to investigate its effect on 3D atmospheric chemistry and its ability to mimic seasonally varying biosignatures. This thesis considers neutral chemistry, but atoms and molecules in planetary atmospheres may be ionised by photoionisation, lightning ionisation, impact ionisation, or charge exchange processes with stellar winds. The presence of ionised compounds can lead to atmospheric escape (e.g. Tian, 2015a) and affects the atmospheric chemistry and planetary climate (e.g. Airapetian et al., 2020). Because of the inherent 3D nature of these processes, future 3D modeling will have to incorporate them.

Ozone is a fascinating species due to its participation in the photochemical and radiative balance of a planetary atmosphere, leading to climate-dynamics-chemistry interactions as discovered in Chapters 4 and 5 for planets around M-dwarfs before being further investigated in De Luca et al. (2024). Despite a strong ozone production on Proxima Centauri b, its stratospheric presence on planets around M-dwarfs does not heat the stratosphere as strongly as seen on Earth or predicted for other planets around G- or F-type stars (Godolt et al., 2015). This implies a sensitivity of the climate-dynamics-chemistry interactions to the stellar spectral energy distribution, motivating further investigations for planets around MKGF stars and whenever improved observations of stellar spectra become available. Moreover – as suggested in Section 6.2 – many other photochemically active species have rotational-vibrational transitions (e.g. H_2O, CO_2, HCN, NO_2, N_2O, CH_4, NH_3) and thus have the ability to induce climate-dynamics-chemistry interactions. The CCM presented includes interactions due to H_2O, NO_2, and N_2O, but enhanced sources for the latter two species will be required to induce

noticeable climate-dynamics-chemistry interactions (e.g., biogenic emissions Schwieterman et al., 2018). In the simulations of this thesis, CO_2 is included as a fixed abundance and CH_4 is set to zero. Both can be included in the interactive chemistry calculations but their photolysis is mainly driven by radiation at $\lambda < 177$ nm, making the climate-dynamics-chemistry interactions hard to capture with this CCM due to the cutoff at 177 nm (see Section 2.2.2). Future work with a chemistry module that is more flexible for non-oxygenated atmospheres – as presented in Ridgway et al. (2023) – will be directed to the study of these interactions. NH_3 and HCN would be essential parts of these studies, as also shown by 1D photochemical modelling (Rimmer & Rugheimer, 2019).

Whilst the parametrization of LFRs in terms of cloud-top height is based on the fundamental laws of electricity (Vonnegut, 1963), it is empirically tuned to match observed LFRs on Earth (Williams, 1985; Price & Rind, 1992; Luhar et al., 2021). Other parametrizations of lightning initiation exist: in terms of convective precipitation and mass flux (Allen & Pickering, 2002), convective available potential energy (Williams & Stanfill, 2002; Stolz et al., 2017), or upward ice flux (McCaul et al., 2009; Finney et al., 2014). Recently, Balduin et al. (2023) developed a simple parametrization in terms of pressure, temperature, vertical wind, and grain charges to study the potential for lightning in protoplanetary disks, indicating applicability in a variety of environmental settings. A comparison of different parametrizations is currently being conducted (Sergeev et al. (inc. Braam), in prep.) and can be used as a basis for future studies of lightning-induced chemistry in exoplanet atmospheres.

The adaptation of Earth System Models to the study of exoplanets naturally starts with an atmospheric composition similar to modern Earth, opening a variety of 3D physical and chemical processes that can be explored for exoplanets, as shown in this thesis. However, the Earth's atmospheric composition has evolved considerably over geological timescales (Lyons et al., 2014; Zahnle et al., 2020; Cooke et al., 2022), with associated 3D climate interactions (Eager-Nash et al., 2023, e.g.). On the Early Earth, prebiotic chemistry is thought to have started in reducing environmental conditions. 1-D photochemical modelling studies of reducing atmospheric chemistry on Early Earth and exoplanets illustrate the dependence on environmental conditions (Zahnle, 1986; Airapetian et al., 2016; Rimmer & Rugheimer, 2019; Pearce et al., 2022). 3D simulations of atmospheric (photo)chemistry in reducing conditions are, as of yet, unexplored. We are currently laying the foundations for these 3D simulations by testing and developing suitable chemical networks.

Connecting with the conditions driving prebiotic chemistry, especially the 3:2 spin-orbit resonant exoplanet simulations in this thesis demonstrate radiative, temperature, and chemical cycles (see Chapter 5). Along with wet-dry cycles following precipitation (Pearce et al., 2017), such cycles have been proposed as essential requirements for prebiotic synthesis. 3D CCM simulations can predict the long-term behaviour of such cycles and provide essential input for studies of prebiotic synthesis on exoplanets.

6.3.2 Habitability

The climate-chemistry interactions that are presented in this thesis can be further explored by comparisons between simulations of interactive chemistry versus static atmospheric conditions. In this way, we can determine the planetary and stellar environments for which the presence of species like ozone affects the surface temperatures and thus planetary habitability, including the spatial and temporal variations due to interactive chemistry. An expansion of the habitability concept involves the protection from harmful surface UV radiation that a planetary ozone layer provides (Ridgway et al., 2023). Again, this needs to be explored for a range of exoplanet configurations. Model intercomparison projects like the THAI project (Fauchez et al., 2022; Sergeev et al., 2022b; Turbet et al., 2022) increase the confidence and validity of our exoplanet simulations and need to be performed for photochemical models. The 1D Photochemical Intercomparison for Exoplanets (PIE) is currently being conducted and may be followed by a 3D CCM intercomparison.

The connection between the inner edge of the HZ and spin-orbit resonances needs to be investigated for other spin-orbit resonances and more orbital configurations. Given the reduced irradiance that is required to keep TRAPPIST-1 d in a stable climate state, the inner HZ boundary for the TRAPPIST system is probably located somewhere between the orbits of planets d and e. We are currently analysing an ensemble of simulations to better quantify this sensitivity, varying the orbital distance, spin-orbit resonance, eccentricity, climate-chemistry interactions (individually simulating the radiative impacts of ozone, H_2O, and N_2O), and the presence of a constant aerosol layer. These results will improve our definition of the inner HZ boundary in the TRAPPIST-1 system and shed light on the ability of TRAPPIST-1 d and e to retain an atmosphere of Earth-like composition. The initial findings suggest that the eccentricity in higher-order resonances is the driving factor for the runaway greenhouse state. Chemical feedbacks only delay the inevitable runaway and a constant aerosol layer seems to speed up the warming process. Incorporating the latest determination of the bolometric luminosity of TRAPPIST-1 (Sanghi et al., 2023) will further refine the location of the inner HZ boundary.

The dependence of climate on the spin-orbit resonance that this thesis reports contrasts with Colose et al. (2021), who find that higher-order resonances do not imply a wetter stratosphere and, thus, planets are less prone to a runaway greenhouse effect. On the other hand, Liu et al. (2023) simulate Earth's climate for varying eccentricity and report a wetter stratosphere and increased temperatures for higher eccentricities, agreeing with my finding that eccentricity drives a warmer climate. Possible explanations for the differences include the model description and strength of vertical mixing and the location of the tropopause, both affecting the

exchange between the troposphere and stratosphere. A model intercomparison project can clarify these differences. Since differing stratospheric water vapour mixing ratios should affect observations (see Section 5.3.6), this intercomparison can quantify observational differences between the climate states and their sensitivity to eccentricity.

Opportunities exist to quantify the effects of 3D interactive photochemistry on HZ boundaries. Including CO_2 photolysis in a 3D CCM might prevent atmospheric collapse of a CO_2-rich atmosphere on the nightside of a 1:1 resonant exoplanet (e.g. Wordsworth, 2015). On the other hand, H_2O photolysis might remove H_2O as a greenhouse gas and reduce the greenhouse effect from H_2O.

6.3.3 Observability

The simulated observational effects of 3D chemistry seem to disappear below the JWST noise floor but offer a promising outlook for emission spectroscopy with the LIFE mission concept, at least for Proxima Centauri b. The observability of the chemical features and their temporal variations are currently being tested by adding simulated noise to the spectra in Figure 5.14 using the LIFEsim instrument simulator (Dannert et al., 2022). Predicting LIFE's observing capabilities has so far followed a logical order, from 1D simulations of Earth as an exoplanet (Konrad et al., 2022), to diverse exoplanet scenarios in 1D (Alei et al., 2022), to using 3D Earth observations (Mettler et al., 2022; Mettler et al., 2023, 2024). The next step would be to test the observability of the 3D variations for a tidally locked M-dwarf exoplanet as presented in this thesis. In the case of abiotic O_2 produced from CO_2 photolysis on planets orbiting M-dwarfs (Domagal-Goldman et al., 2014; Tian et al., 2014; Harman et al., 2015), an O_2 detection (direct or inferred from ozone) would be accompanied by CO spectral features (Harman et al., 2015; Schwieterman et al., 2018). Simulations with interactive CO_2 chemistry, as proposed in Section 6.3.1, should investigate the 3D variations of CO along with its observational consequences. Besides LIFE, NASA is developing the HWO mission to study reflected light from terrestrial exoplanets and ground-based future observatories like the ELT will also have the potential to probe terrestrial atmospheres, perhaps requiring a few modifications (Vaughan et al., 2024). Understanding the observability of the presence or absence of 3D variations will be essential in designing the science goals and interpretation of data from these future observatories.

Bibliography

Abe, Y., Abe-Ouchi, A., Sleep, N. H., & Zahnle, K. J. (2011). Habitable Zone Limits for Dry Planets. *Astrobiology*, *11*(5), 443–460. https://doi.org/10.1089/ast.2010.0545

Agol, E., Dorn, C., Grimm, S. L., Turbet, M., Ducrot, E., Delrez, L., Gillon, M., Demory, B.-O., Burdanov, A., Barkaoui, K., Benkhaldoun, Z., Bolmont, E., Burgasser, A., Carey, S., Wit, J. d., Fabrycky, D., Foreman-Mackey, D., Haldemann, J., Hernandez, D. M., … Grootel, V. V. (2021). Refining the Transit-timing and Photometric Analysis of TRAPPIST-1: Masses, Radii, Densities, Dynamics, and Ephemerides. *The Planetary Science Journal*, *2*(1), 1. https://doi.org/10.3847/PSJ/abd022

Airapetian, V. S., Glocer, A., Gronoff, G., Hébrard, E., & Danchi, W. (2016). Prebiotic chemistry and atmospheric warming of early Earth by an active young Sun. *Nature Geoscience*, *9*(6), 452–455. https://doi.org/10.1038/ngeo2719

Airapetian, V. S., Barnes, R., Cohen, O., Collinson, G. A., Danchi, W. C., Dong, C. F., Genio, A. D. D., France, K., Garcia-Sage, K., Glocer, A., Gopalswamy, N., Grenfell, J. L., Gronoff, G., Güdel, M., Herbst, K., Henning, W. G., Jackman, C. H., Jin, M., Johnstone, C. P., … Yamashiki, Y. (2020). Impact of space weather on climate and habitability of terrestrial-type exoplanets. *International Journal of Astrobiology*, *19*(2), 136–194. https://doi.org/10.1017/S1473550419000132

Airapetian, V. S., Glocer, A., Khazanov, G. V., Loyd, R. O. P., France, K., Sojka, J., Danchi, W. C., & Liemohn, M. W. (2017). How Hospitable Are Space Weather Affected Habitable Zones? The Role of Ion Escape. *The Astrophysical Journal*, *836*(1), L3. https://doi.org/10.3847/2041-8213/836/1/L3

Alei, E., Konrad, B. S., Angerhausen, D., Grenfell, J. L., Mollière, P., Quanz, S. P., Rugheimer, S., & Wunderlich, F. (2022). Large Interferometer For Exoplanets (LIFE) - V. Diagnostic potential of a mid-infrared space interferometer for studying Earth analogs. *Astronomy & Astrophysics*, *665*, A106. https://doi.org/10.1051/0004-6361/202243760

Allen, D., Pickering, K. E., Bucsela, E., Van Geffen, J., Lapierre, J., Koshak, W., & Eskes, H. (2021a). Observations of Lightning NOx Production From Tropospheric Monitoring Instrument Case Studies Over the United States. *Journal of Geophysical Research: Atmospheres*, *126*(10), e2020JD034174. https://doi.org/10.1029/2020JD034174

Allen, D. J., & Pickering, K. E. (2002). Evaluation of lightning flash rate parameterizations for use in a global chemical transport model. *Journal of Geophysical Research: Atmospheres*, *107*(D23), ACH 15–1–ACH 15–21. https://doi.org/10.1029/2002JD002066

Allen, D. J., Pickering, K. E., Lamsal, L., Mach, D. M., Quick, M. G., Lapierre, J., Janz, S., Koshak, W., Kowalewski, M., & Blakeslee, R. (2021b). Observations of Lightning NOx Production From GOES-R Post Launch Test Field Campaign Flights. *Journal of Geophysical Research: Atmospheres*, *126*(8), e2020JD033769. https://doi.org/10.1029/2020JD033769

Amundsen, D. S., Baraffe, I., Tremblin, P., Manners, J., Hayek, W., Mayne, N. J., & Acreman, D. M. (2014). Accuracy tests of radiation schemes used in hot Jupiter global circulation models. *Astronomy & Astrophysics*, *564*, A59. https://doi.org/10.1051/0004-6361/201323169

Amundsen, D. S., Mayne, N. J., Baraffe, I., Manners, J., Tremblin, P., Drummond, B., Smith, C., Acreman, D. M., & Homeier, D. (2016). The UK Met Office global circulation model with a sophisticated radiation scheme applied to the hot Jupiter HD 209458b. *Astronomy & Astrophysics*, *595*, A36. https://doi.org/10.1051/0004-6361/201629183

Amundsen, D. S., Tremblin, P., Manners, J., Baraffe, I., & Mayne, N. J. (2017). Treatment of overlapping gaseous absorption with the correlated-k method in hot Jupiter and brown dwarf atmosphere models. *Astronomy & Astrophysics*, *598*, A97. https://doi.org/10.1051/0004-6361/201629322

Angerhausen, D., Pidhorodetska, D., Leung, M., Hansen, J., Alei, E., Dannert, F., Kammerer, J., Quanz, S. P., Schwieterman, E. W., & initiative, T. L. (2024). Large Interferometer For Exoplanets (LIFE). XII. The Detectability of Capstone Biosignatures in the Mid-infrared—Sniffing Exoplanetary Laughing Gas and Methylated Halogens [Publisher: The American Astronomical Society]. *The Astronomical Journal*, *167*(3), 128. https://doi.org/10.3847/1538-3881/ad1f4b

Anglada-Escudé, G., Amado, P. J., Barnes, J., Berdiñas, Z. M., Butler, R. P., Coleman, G. A. L., de la Cueva, I., Dreizler, S., Endl, M., Giesers, B., Jeffers, S. V., Jenkins, J. S., Jones, H. R. A., Kiraga, M., Kürster, M., López-González, M. J., Marvin, C. J., Morales, N., Morin, J., … Zechmeister, M. (2016). A terrestrial planet candidate in a temperate orbit around Proxima Centauri. *Nature*, *536*(7617), 437–440. https://doi.org/10.1038/nature19106

Aplin, K. L. (2006). Atmospheric Electrification in the Solar System. *Surveys in Geophysics*, *27*(1), 63–108. https://doi.org/10.1007/s10712-005-0642-9

Arakawa, A. (2004). The Cumulus Parameterization Problem: Past, Present, and Future. *Journal of Climate*, *17*(13), 2493–2525. https://doi.org/10.1175/1520-0442(2004)017<2493:RATCPP>2.0.CO;2

Archibald, A. T., O'Connor, F. M., Abraham, N. L., Archer-Nicholls, S., Chipperfield, M. P., Dalvi, M., Folberth, G. A., Dennison, F., Dhomse, S. S., Griffiths, P. T., Hardacre, C., Hewitt, A. J., Hill, R. S., Johnson, C. E., Keeble, J., Köhler, M. O., Morgenstern, O., Mulcahy, J. P., Ordóñez, C., ... Zeng, G. (2020). Description and evaluation of the UKCA stratosphere–troposphere chemistry scheme (StratTrop vn 1.0) implemented in UKESM1. *Geoscientific Model Development*, *13*(3), 1223–1266. https://doi.org/https://doi.org/10.5194/gmd-13-1223-2020

Ardaseva, A., Rimmer, P. B., Waldmann, I., Rocchetto, M., Yurchenko, S. N., Helling, C., & Tennyson, J. (2017). Lightning chemistry on Earth-like exoplanets. *Monthly Notices of the Royal Astronomical Society*, *470*(1), 187–196. https://doi.org/10.1093/mnras/stx1012

Arney, G., Domagal-Goldman, S. D., Meadows, V. S., Wolf, E. T., Schwieterman, E., Charnay, B., Claire, M., Hébrard, E., & Trainer, M. G. (2016). The Pale Orange Dot: The Spectrum and Habitability of Hazy Archean Earth. *Astrobiology*, *16*(11), 873–899. https://doi.org/10.1089/ast.2015.1422

Arney, G. N., Meadows, V. S., Domagal-Goldman, S. D., Deming, D., Robinson, T. D., Tovar, G., Wolf, E. T., & Schwieterman, E. (2017). Pale Orange Dots: The Impact of Organic Haze on the Habitability and Detectability of Earthlike Exoplanets. *The Astrophysical Journal*, *836*(1), 49. https://doi.org/10.3847/1538-4357/836/1/49

Bacmeister, J. T., & Stephens, G. L. (2011). Spatial statistics of likely convective clouds in CloudSat data. *Journal of Geophysical Research: Atmospheres*, *116*(D4). https://doi.org/10.1029/2010JD014444

Balduin, T., Woitke, P., Jørgensen, U. G., Thi, W.-F., & Narita, Y. (2023). Size-dependent charging of dust particles in protoplanetary disks - Can turbulence cause charge separation and lightning? *Astronomy & Astrophysics*, *678*, A192. https://doi.org/10.1051/0004-6361/202346442

Banerjee, A., Archibald, A. T., Maycock, A. C., Telford, P., Abraham, N. L., Yang, X., Braesicke, P., & Pyle, J. A. (2014). Lightning NOx, a key chemistry–climate interaction: Impacts of future climate change and consequences for tropospheric oxidising capacity. *Atmospheric Chemistry and Physics*, *14*(18), 9871–9881. https://doi.org/10.5194/acp-14-9871-2014

Baraffe, I., Homeier, D., Allard, F., & Chabrier, G. (2015). New evolutionary models for pre-main sequence and main sequence low-mass stars down to the hydrogen-burning limit. *Astronomy & Astrophysics*, *577*, A42. https://doi.org/10.1051/0004-6361/201425481

Barnes, R. (2017). Tidal locking of habitable exoplanets. *Celestial Mechanics and Dynamical Astronomy*, *129*(4), 509–536. https://doi.org/10.1007/s10569-017-9783-7

Bates, D. R., & Nicolet, M. (1950). The photochemistry of atmospheric water vapor. *Journal of Geophysical Research (1896-1977)*, *55*(3), 301–327. https://doi.org/10.1029/JZ055i003p00301

Bean, J. L., Raymond, S. N., & Owen, J. E. (2021). The Nature and Origins of Sub-Neptune Size Planets. *Journal of Geophysical Research: Planets*, *126*(1), e2020JE006639. https://doi.org/10.1029/2020JE006639

Bian, H., & Prather, M. J. (2002). Fast-J2: Accurate Simulation of Stratospheric Photolysis in Global Chemical Models. *Journal of Atmospheric Chemistry*, *41*(3), 281–296. https://doi.org/10.1023/A:1014980619462

Boccippio, D. J. (2002). Lightning Scaling Relations Revisited. *Journal of the Atmospheric Sciences*, *59*(6), 1086–1104. https://doi.org/10.1175/1520-0469(2002)059<1086:LSRR>2.0.CO;2

Bochanski, J. J., Hawley, S. L., Covey, K. R., West, A. A., Reid, I. N., Golimowski, D. A., & Ivezić, Z. (2010). THE LUMINOSITY AND MASS FUNCTIONS OF LOW-MASS STARS IN THE GALACTIC DISK. II. THE FIELD. *The Astronomical Journal*, *139*(6), 2679. https://doi.org/10.1088/0004-6256/139/6/2679

Bolmont, E., Libert, A.-S., Leconte, J., & Selsis, F. (2016). Habitability of planets on eccentric orbits: Limits of the mean flux approximation. *Astronomy & Astrophysics*, *591*, A106. https://doi.org/10.1051/0004-6361/201628073

Bönisch, H., Engel, A., Birner, T., Hoor, P., Tarasick, D. W., & Ray, E. A. (2011). On the structural changes in the Brewer-Dobson circulation after 2000. *Atmospheric Chemistry and Physics*, *11*(8), 3937–3948. https://doi.org/10.5194/acp-11-3937-2011

Borucki, W. J., Mc Kenzie, R. L., McKay, C. P., Duong, N. D., & Boac, D. S. (1985). Spectra of simulated lightning on Venus, Jupiter, and Titan. *Icarus*, *64*(2), 221–232. https://doi.org/10.1016/0019-1035(85)90087-9

Boutle, I. A., Eyre, J. E. J., & Lock, A. P. (2014). Seamless Stratocumulus Simulation across the Turbulent Gray Zone. *Monthly Weather Review*, *142*(4), 1655–1668. https://doi.org/10.1175/MWR-D-13-00229.1

Boutle, I. A., Mayne, N. J., Drummond, B., Manners, J., Goyal, J., Hugo Lambert, F., Acreman, D. M., & Earnshaw, P. D. (2017). Exploring the climate of Proxima B with the Met Office Unified Model. *Astronomy & Astrophysics*, *601*, A120. https://doi.org/10.1051/0004-6361/201630020

Braam, M., Palmer, P. I., Decin, L., Ridgway, R. J., Zamyatina, M., Mayne, N. J., Sergeev, D. E., & Abraham, N. L. (2022). Lightning-induced chemistry on tidally-locked Earth-like exoplanets. *Monthly Notices of the Royal Astronomical Society*, *517*(2), 2383–2402. https://doi.org/10.1093/mnras/stac2722

Braam, M., Palmer, P. I., Decin, L., Cohen, M., & Mayne, N. J. (2023). Stratospheric dayside-to-nightside circulation drives the 3D ozone distribution on synchronously rotating rocky exoplanets. *Monthly Notices of the Royal Astronomical Society*, *526*(1), 263–278. https://doi.org/10.1093/mnras/stad2704

Brasseur, G., & Hitchman, M. H. (1988). Stratospheric Response to Trace Gas Perturbations: Changes in Ozone and Temperature Distributions. *Science*, *240*(4852), 634–637. https://doi.org/10.1126/science.240.4852.634

Brewer, A. W. (1949). Evidence for a world circulation provided by the measurements of helium and water vapour distribution in the stratosphere. *Quarterly Journal of the Royal Meteorological Society*, *75*(326), 351–363. https://doi.org/10.1002/qj.49707532603

Brown, A. R., Beare, R. J., Edwards, J. M., Lock, A. P., Keogh, S. J., Milton, S. F., & Walters, D. N. (2008). Upgrades to the Boundary-Layer Scheme in the Met Office Numerical Weather Prediction Model. *Boundary-Layer Meteorology*, *128*(1), 117–132. https://doi.org/10.1007/s10546-008-9275-0

Brown, R. A. (2017). On the Eccentricity of Proxima b. *The Astrophysical Journal*, *844*(2), 100. https://doi.org/10.3847/1538-4357/aa621a

Brune, W. H., McFarland, P. J., Bruning, E., Waugh, S., MacGorman, D., Miller, D. O., Jenkins, J. M., Ren, X., Mao, J., & Peischl, J. (2021). Extreme oxidant amounts produced by lightning in storm clouds. *Science*, *372*(6543), 711–715. https://doi.org/10.1126/science.abg0492

Bucsela, E. J., Pickering, K. E., Allen, D. J., Holzworth, R. H., & Krotkov, N. A. (2019). Midlatitude Lightning NOx Production Efficiency Inferred From OMI and WWLLN Data. *Journal of Geophysical Research: Atmospheres*, *124*(23), 13475–13497. https://doi.org/10.1029/2019JD030561

Burrows, J. P., Richter, A., Dehn, A., Deters, B., Himmelmann, S., Voigt, S., & Orphal, J. (1999). ATMOSPHERIC REMOTE-SENSING REFERENCE DATA FROM GOME—2. TEMPERATURE-DEPENDENT ABSORPTION CROSS SECTIONS OF O3 IN THE 231–794NM RANGE. *Journal of Quantitative Spectroscopy and Radiative Transfer*, *61*(4), 509–517. https://doi.org/10.1016/S0022-4073(98)00037-5

Butchart, N. (2014). The Brewer-Dobson circulation. *Reviews of Geophysics*, *52*(2), 157–184. https://doi.org/10.1002/2013RG000448

Carone, L., Keppens, R., & Decin, L. (2014). Connecting the dots: A versatile model for the atmospheres of tidally locked Super-Earths. *Monthly Notices of the Royal Astronomical Society*, *445*(1), 930–945. https://doi.org/10.1093/mnras/stu1793

Carone, L., Keppens, R., & Decin, L. (2015). Connecting the dots – II. Phase changes in the climate dynamics of tidally locked terrestrial exoplanets. *Monthly Notices of the Royal Astronomical Society*, *453*(3), 2412–2437. https://doi.org/10.1093/mnras/stv1752

Carone, L., Keppens, R., & Decin, L. (2016). Connecting the dots – III. Nightside cooling and surface friction affect climates of tidally locked terrestrial planets. *Monthly Notices of the Royal Astronomical Society*, *461*(2), 1981–2002. https://doi.org/10.1093/mnras/stw1265

Carone, L., Keppens, R., Decin, L., & Henning, T. (2018). Stratosphere circulation on tidally locked ExoEarths. *Monthly Notices of the Royal Astronomical Society*, *473*(4), 4672–4685. https://doi.org/10.1093/mnras/stx2732

Carrión-González, Ó., Kammerer, J., Angerhausen, D., Dannert, F., Muñoz, A. G., Quanz, S. P., Absil, O., Beichman, C. A., Girard, J. H., Mennesson, B., Meyer, M. R., & Stapelfeldt, K. R. (2023). Large Interferometer For Exoplanets (LIFE) - X. Detectability of currently known exoplanets and synergies with future IR/O/UV reflected-starlight imaging missions [Publisher: EDP Sciences]. *Astronomy & Astrophysics*, *678*, A96. https://doi.org/10.1051/0004-6361/202347027

Carver, G. D., Brown, P. D., & Wild, O. (1997). The ASAD atmospheric chemistry integration package and chemical reaction database. *Computer Physics Communications*, *105*(2), 197–215. https://doi.org/10.1016/S0010-4655(97)00056-8

Cecil, D. J., Buechler, D. E., & Blakeslee, R. J. (2014). Gridded lightning climatology from TRMM-LIS and OTD: Dataset description. *Atmospheric Research*, *135-136*, 404–414. https://doi.org/10.1016/j.atmosres.2012.06.028

Chameides, W. L., Stedman, D. H., Dickerson, R. R., Rusch, D. W., & Cicerone, R. J. (1977). NOx Production in Lightning. *Journal of the Atmospheric Sciences*, *34*(1), 143–149. https://doi.org/10.1175/1520-0469(1977)034<0143:NPIL>2.0.CO;2

Chameides, W. L., & Walker, J. C. G. (1981). Rates of fixation by lightning of carbon and nitrogen in possible primitive atmospheres. *Origins of life*, *11*(4), 291–302. https://doi.org/10.1007/BF00931483

Chapman, S. (1930). XXXV. On ozone and atomic oxygen in the upper atmosphere. *The London, Edinburgh, and Dublin Philosophical Magazine and Journal of Science*, *10*(64), 369–383.

Charbonneau, D., & Deming, D. (2007, June). The Dynamics-Based Approach to Studying Terrestrial Exoplanets. https://doi.org/10.48550/arXiv.0706.1047

Chaverot, G., Turbet, M., Bolmont, E., & Leconte, J. (2022). How does the background atmosphere affect the onset of the runaway greenhouse? *Astronomy & Astrophysics*, *658*, A40. https://doi.org/10.1051/0004-6361/202142286

Chen, H., Wolf, E. T., Kopparapu, R., Domagal-Goldman, S., & Horton, D. E. (2018). Biosignature Anisotropy Modeled on Temperate Tidally Locked M-dwarf Planets. *The Astrophysical Journal*, *868*(1), L6. https://doi.org/10.3847/2041-8213/aaedb2

Chen, H., Wolf, E. T., Zhan, Z., & Horton, D. E. (2019). Habitability and Spectroscopic Observability of Warm M-dwarf Exoplanets Evaluated with a 3D Chemistry-Climate Model. *The Astrophysical Journal*, *886*(1), 16. https://doi.org/10.3847/1538-4357/ab4f7e

Chen, H., Zhan, Z., Youngblood, A., Wolf, E. T., Feinstein, A. D., & Horton, D. E. (2021). Persistence of flare-driven atmospheric chemistry on rocky habitable zone worlds. *Nature Astronomy*, *5*(3), 298–310. https://doi.org/10.1038/s41550-020-01264-1

Chen, H., Li, G., Paradise, A., & Kopparapu, R. K. (2023). Sporadic Spin-orbit Variations in Compact Multiplanet Systems and Their Influence on Exoplanet Climate. *The Astrophysical Journal Letters*, *946*(2), L32. https://doi.org/10.3847/2041-8213/acbd33

Childs, A. C., Martin, R. G., & Livio, M. (2022). Life on Exoplanets in the Habitable Zone of M Dwarfs? *The Astrophysical Journal Letters*, *937*(2), L41. https://doi.org/10.3847/2041-8213/ac9052

Chipperfield, M., Kinnison, D., Bekki, S., Bruhl, C., Canty, T., Cionni, I., Dhomse, S., Froidevaux, L., Fuller, R., Muller, R., Prather, M., Salawitch, R., Santee, M., Tian, W., & Tilmes, S. (2010). Chapter 6 - Stratospheric Chemistry in SPARC Report No. 5 on the Evaluation of Chemistry-Climate Models. *Chapter 6 - Stratospheric Chemistry in SPARC Report No. 5 on the Evaluation of Chemistry-Climate Models*. Retrieved May 17, 2021, from https://escholarship.org/uc/item/9060v2sw

Chyba, C. F. (1990). Impact delivery and erosion of planetary oceans in the early inner Solar System. *Nature*, *343*(6254), 129–133. https://doi.org/10.1038/343129a0

Clark, S. K., Ward, D. S., & Mahowald, N. M. (2017). Parameterization-based uncertainty in future lightning flash density. *Geophysical Research Letters*, *44*(6), 2893–2901. https://doi.org/10.1002/2017GL073017

Cohen, M., Bollasina, M. A., Palmer, P. I., Sergeev, D. E., Boutle, I. A., Mayne, N. J., & Manners, J. (2022). Longitudinally Asymmetric Stratospheric Oscillation on a Tidally Locked Exoplanet. *The Astrophysical Journal*, *930*(2), 152. https://doi.org/10.3847/1538-4357/ac625d

Cohen, M., Bollasina, M. A., Sergeev, D. E., Palmer, P. I., & Mayne, N. J. (2023a). Traveling Planetary-scale Waves Cause Cloud Variability on Tidally Locked Aquaplanets. *The Planetary Science Journal*, *4*(4), 68. https://doi.org/10.3847/PSJ/acc9c4

Cohen, M., Kosar, B., Halford, A., Ringuette, R., Silva, C. d., Bortnik, J., Cohen, M., Smith, D., Dwyer, J., Morales, C., Mcharg, M., Derr, J., Kolmasova, I., Mailyan, B., Albrecht, R., Smith, J., Liu, N., Lang, T., Trostel, J., … Lay, E. (2023b). The Impacts of Lightning Beyond the Troposphere. *Bulletin of the American Astronomical Society*, *55*. https://doi.org/10.3847/25c2cfeb.1cd28060

Colose, C. M., Haqq-Misra, J., Wolf, E. T., Genio, A. D. D., Barnes, R., Way, M. J., & Ruedy, R. (2021). Effects of Spin–Orbit Resonances and Tidal Heating on the Inner Edge of the Habitable Zone. *The Astrophysical Journal*, *921*(1), 25. https://doi.org/10.3847/1538-4357/ac135c

Cooke, G. J., Marsh, D. R., Walsh, C., Black, B., & Lamarque, J.-F. (2022). A revised lower estimate of ozone columns during Earth's oxygenated history. *Royal Society Open Science*, *9*(1), 211165. https://doi.org/10.1098/rsos.211165

Cooke, G. J., Marsh, D. R., Walsh, C., & Youngblood, A. (2023a). Degenerate Interpretations of O3 Spectral Features in Exoplanet Atmosphere Observations Due to Stellar UV Uncertainties: A 3D Case Study with TRAPPIST-1 e [Publisher: The American Astronomical Society]. *The Astrophysical Journal*, *959*(1), 45. https://doi.org/10.3847/1538-4357/ad0381

Cooke, G. J., Marsh, D. R., Walsh, C., Rugheimer, S., & Villanueva, G. L. (2023b). Variability due to climate and chemistry in observations of oxygenated Earth-analogue exoplanets. *Monthly Notices of the Royal Astronomical Society*, *518*(1), 206–219. https://doi.org/10.1093/mnras/stac2604

Crutzen, P. J. (1970). The influence of nitrogen oxides on the atmospheric ozone content. *Quarterly Journal of the Royal Meteorological Society*, *96*(408), 320–325. https://doi.org/https://doi.org/10.1002/qj.49709640815

Dannert, F. A., Ottiger, M., Quanz, S. P., Laugier, R., Fontanet, E., Gheorghe, A., Absil, O., Dandumont, C., Defrère, D., Gascón, C., Glauser, A. M., Kammerer, J., Lichtenberg, T., Linz, H., & Loicq, J. (2022). Large Interferometer For Exoplanets (LIFE) - II. Signal simulation, signal extraction, and fundamental exoplanet parameters from single-epoch observations. *Astronomy & Astrophysics*, *664*, A22. https://doi.org/10.1051/0004-6361/202141958

Davies, T., Cullen, M. J. P., Malcolm, A. J., Mawson, M. H., Staniforth, A., White, A. A., & Wood, N. (2005). A new dynamical core for the Met Office's global and regional modelling of the atmosphere [_eprint: https://onlinelibrary.wiley.com/doi/pdf/10.1256/qj.04.101]. *Quarterly Journal of the Royal Meteorological Society*, *131*(608), 1759–1782. https://doi.org/10.1256/qj.04.101

De Luca, P., Braam, M., Komacek, T. D., & Hochman, A. (2024). The impact of Ozone on Earth-like exoplanet climate dynamics: The case of Proxima Centauri b. *Monthly Notices of the Royal Astronomical Society*, stae1199. https://doi.org/10.1093/mnras/stae1199

Defrère, D., Léger, A., Absil, O., Garcia Munoz, A., Grenfell, J. L., Godolt, M., Loicq, J., Kammerer, J., Quanz, S., Rauer, H., Schifano, L., & Tian, F. (2018). Characterizing the atmosphere of Proxima b with a space-based mid-infrared nulling interferometer [Conference Name: Optical and Infrared Interferometry and Imaging VI Place: eprint: arXiv:1807.09996 ADS Bibcode: 2018SPIE10701E..1HD], *10701*, 107011H. https://doi.org/10.1117/12.2312839

Del Genio, A. D., & Suozzo, R. J. (1987). A Comparative Study of Rapidly and Slowly Rotating Dynamical Regimes in a Terrestrial General Circulation Model. *Journal of the Atmospheric Sciences*, *44*(6), 973–986. https://doi.org/10.1175/1520-0469(1987)044<0973:ACSORA>2.0.CO;2

Del Genio, A. D., Way, M. J., Amundsen, D. S., Aleinov, I., Kelley, M., Kiang, N. Y., & Clune, T. L. (2019). Habitable Climate Scenarios for Proxima Centauri b with a Dynamic Ocean. *Astrobiology*, *19*(1), 99–125. https://doi.org/10.1089/ast.2017.1760

de Pater, I., & Lissauer, J. J. (2015). *Planetary Sciences* (I. de Pater & J. J. Lissauer, Eds.; 2nd ed.). Cambridge University Press. https://doi.org/10.1017/CBO9781316165270

Des Marais, D. J., Harwit, M. O., Jucks, K. W., Kasting, J. F., Lin, D. N. C., Lunine, J. I., Schneider, J., Seager, S., Traub, W. A., & Woolf, N. J. (2002). Remote sensing of planetary properties and biosignatures on extrasolar terrestrial planets. *Astrobiology*, *2*(2), 153–181. https://doi.org/10.1089/15311070260192246

Dessler, A. E., Palm, S. P., & Spinhirne, J. D. (2006). Tropical cloud-top height distributions revealed by the Ice, Cloud, and Land Elevation Satellite (ICESat)/Geoscience Laser Altimeter System (GLAS). *Journal of Geophysical Research: Atmospheres*, *111*(D12). https://doi.org/10.1029/2005JD006705

de Wit, J., Wakeford, H. R., Gillon, M., Lewis, N. K., Valenti, J. A., Demory, B.-O., Burgasser, A. J., Burdanov, A., Delrez, L., Jehin, E., Lederer, S. M., Queloz, D., Triaud, A. H. M. J., & Van Grootel, V. (2016). A combined transmission spectrum of the Earth-sized exoplanets TRAPPIST-1 b and c. *Nature*, *537*(7618), 69–72. https://doi.org/10.1038/nature18641

de Wit, J., Wakeford, H. R., Lewis, N. K., Delrez, L., Gillon, M., Selsis, F., Leconte, J., Demory, B.-O., Bolmont, E., Bourrier, V., Burgasser, A. J., Grimm, S., Jehin, E., Lederer, S. M., Owen, J. E., Stamenković, V., & Triaud, A. H. M. J. (2018). Atmospheric reconnaissance of the habitable-zone Earth-sized planets orbiting TRAPPIST-1. *Nature Astronomy*, *2*(3), 214–219. https://doi.org/10.1038/s41550-017-0374-z

Diamond-Lowe, H., Berta-Thompson, Z., Charbonneau, D., & Kempton, E. M.-R. (2018). Ground-based Optical Transmission Spectroscopy of the Small, Rocky Exoplanet GJ 1132b. *The Astronomical Journal*, *156*(2), 42. https://doi.org/10.3847/1538-3881/aac6dd

Dobrovolskis, A. R. (2007). Spin states and climates of eccentric exoplanets. *Icarus*, *192*(1), 1–23. https://doi.org/10.1016/j.icarus.2007.07.005

Dobrovolskis, A. R. (2015). Insolation patterns on eccentric exoplanets. *Icarus*, *250*, 395–399. https://doi.org/10.1016/j.icarus.2014.12.017

Dobson, G. M. B. (1956). Origin and distribution of the polyatomic molecules in the atmosphere. *Proceedings of the Royal Society of London. Series A. Mathematical and Physical Sciences*, *236*(1205), 187–193. https://doi.org/10.1098/rspa.1956.0127

Domagal-Goldman, S. D., Segura, A., Claire, M. W., Robinson, T. D., & Meadows, V. S. (2014). ABIOTIC OZONE AND OXYGEN IN ATMOSPHERES SIMILAR TO PREBIOTIC EARTH. *The Astrophysical Journal*, *792*(2), 90. https://doi.org/10.1088/0004-637X/792/2/90

Dressing, C. D., Spiegel, D. S., Scharf, C. A., Menou, K., & Raymond, S. N. (2010). HABITABLE CLIMATES: THE INFLUENCE OF ECCENTRICITY. *The Astrophysical Journal*, *721*(2), 1295. https://doi.org/10.1088/0004-637X/721/2/1295

Dressing, C. D., & Charbonneau, D. (2013). THE OCCURRENCE RATE OF SMALL PLANETS AROUND SMALL STARS. *The Astrophysical Journal*, *767*(1), 95. https://doi.org/10.1088/0004-637X/767/1/95

Dressing, C. D., & Charbonneau, D. (2015). THE OCCURRENCE OF POTENTIALLY HABITABLE PLANETS ORBITING M DWARFS ESTIMATED FROM THE FULL KEPLER DATASET AND AN EMPIRICAL MEASUREMENT OF THE DETECTION SENSITIVITY. *The Astrophysical Journal*, *807*(1), 45. https://doi.org/10.1088/0004-637X/807/1/45

Drummond, B., Tremblin, P., Baraffe, I., Amundsen, D. S., Mayne, N. J., Venot, O., & Goyal, J. (2016). The effects of consistent chemical kinetics calculations on the pressure-temperature profiles and emission spectra of hot Jupiters. *Astronomy & Astrophysics*, *594*, A69. https://doi.org/10.1051/0004-6361/201628799

Drummond, B., Mayne, N. J., Baraffe, I., Tremblin, P., Manners, J., Amundsen, D. S., Goyal, J., & Acreman, D. (2018a). The effect of metallicity on the atmospheres of exoplanets with fully coupled 3D hydrodynamics, equilibrium chemistry, and radiative transfer. *Astronomy & Astrophysics*, *612*, A105. https://doi.org/10.1051/0004-6361/201732010

Drummond, B., Mayne, N. J., Manners, J., Carter, A. L., Boutle, I. A., Baraffe, I., Hébrard, É., Tremblin, P., Sing, D. K., Amundsen, D. S., & Acreman, D. (2018b). Observable Signatures of Wind-driven Chemistry with a Fully Consistent Three-dimensional Radiative Hydrodynamics Model of HD 209458b. *The Astrophysical Journal Letters*, *855*(2), L31. https://doi.org/10.3847/2041-8213/aab209

Drummond, B., Hebrard, E., Mayne, N. J., Venot, O., Ridgway, R. J., Changeat, Q., Tsai, S.-m., Manners, J., Tremblin, P., Abraham, N. L., Sing, D., & Kohary, K. (2020). Implications of three-dimensional chemical transport in hot Jupiter atmospheres: Results from a consistently coupled chemistry-radiation-hydrodynamics model. *Astronomy & Astrophysics*, *636*, A68. https://doi.org/10.1051/0004-6361/201937153

Ducrot, E., Gillon, M., Delrez, L., Agol, E., Rimmer, P., Turbet, M., Günther, M. N., Demory, B.-O., Triaud, A. H. M. J., Bolmont, E., Burgasser, A., Carey, S. J., Ingalls, J. G., Jehin, E., Leconte, J., Lederer, S. M., Queloz, D., Raymond, S. N., Selsis, F., ... Wit, J. d. (2020). TRAPPIST-1: Global results of the Spitzer Exploration Science Program Red Worlds [Publisher: EDP Sciences]. *Astronomy & Astrophysics*, *640*, A112. https://doi.org/10.1051/0004-6361/201937392

Eager, J. K., Reichelt, D. J., Mayne, N. J., Lambert, F. H., Sergeev, D. E., Ridgway, R. J., Manners, J., Boutle, I. A., Lenton, T. M., & Kohary, K. (2020). Implications of different stellar spectra for the climate of tidally-locked Earth-like exoplanets. *Astronomy & Astrophysics*, *639*, A99. https://doi.org/10.1051/0004-6361/202038089

Eager-Nash, J. K., Mayne, N. J., Nicholson, A. E., Prins, J. E., Young, O. C. F., Daines, S. J., Sergeev, D. E., Lambert, F. H., Manners, J., Boutle, I. A., Wolf, E. T., Kamp, I. E. E., Kohary, K., & Lenton, T. M. (2023). 3D Climate Simulations of the Archean Find That Methane has a Strong Cooling Effect at High Concentrations [_eprint: https://onlinelibrary.wiley.com/doi/pdf/10.1029/2022JD037544]. *Journal of Geophysical Research: Atmospheres*, *128*(6), e2022JD037544. https://doi.org/10.1029/2022JD037544

Edson, A., Lee, S., Bannon, P., Kasting, J. F., & Pollard, D. (2011). Atmospheric circulations of terrestrial planets orbiting low-mass stars. *Icarus*, *212*(1), 1–13. https://doi.org/10.1016/j.icarus.2010.11.023

Edwards, B., Changeat, Q., Mori, M., Anisman, L. O., Morvan, M., Yip, K. H., Tsiaras, A., Al-Refaie, A., Waldmann, I., & Tinetti, G. (2020). Hubble WFC3 Spectroscopy of the Habitable-zone Super-Earth LHS 1140 b. *The Astronomical Journal*, *161*(1), 44. https://doi.org/10.3847/1538-3881/abc6a5

Edwards, J. M., & Slingo, A. (1996). Studies with a flexible new radiation code. I: Choosing a configuration for a large-scale model. *Quarterly Journal of the Royal Meteorological Society*, *122*(531), 689–719. https://doi.org/https://doi.org/10.1002/qj.49712253107

Esentürk, E., Abraham, N. L., Archer-Nicholls, S., Mitsakou, C., Griffiths, P., Archibald, A., & Pyle, J. (2018). Quasi-Newton methods for atmospheric chemistry simulations: Implementation in UKCA UM vn10.8. *Geoscientific Model Development*, *11*(8), 3089–3108. https://doi.org/10.5194/gmd-11-3089-2018

Etten-Bohm, M., Yang, J., Schumacher, C., & Jun, M. (2021). Evaluating the Relationship Between Lightning and the Large-Scale Environment and its Use for Lightning Prediction in Global Climate Models. *Journal of Geophysical Research: Atmospheres*, *126*(5), e2020JD033990. https://doi.org/10.1029/2020JD033990

Eyring, V., Arblaster, J. M., Cionni, I., Sedláček, J., Perlwitz, J., Young, P. J., Bekki, S., Bergmann, D., Cameron-Smith, P., Collins, W. J., Faluvegi, G., Gottschaldt, K.-D., Horowitz, L. W., Kinnison, D. E., Lamarque, J.-F., Marsh, D. R., Saint-Martin, D., Shindell, D. T., Sudo, K., … Watanabe, S. (2013). Long-term ozone changes and associated climate impacts in CMIP5 simulations. *Journal of Geophysical Research: Atmospheres*, *118*(10), 5029–5060. https://doi.org/10.1002/jgrd.50316

Faria, J. P., Mascareño, A. S., Figueira, P., Silva, A. M., Damasso, M., Demangeon, O., Pepe, F., Santos, N. C., Rebolo, R., Cristiani, S., Adibekyan, V., Alibert, Y., Allart, R., Barros, S. C. C., Cabral, A., D'Odorico, V., Marcantonio, P. D., Dumusque, X., Ehrenreich, D., … Osorio, M. R. Z. (2022). A candidate short-period sub-Earth orbiting Proxima Centauri [Publisher: EDP Sciences]. *Astronomy & Astrophysics*, *658*, A115. https://doi.org/10.1051/0004-6361/202142337

Fauchez, T. J., Turbet, M., Sergeev, D. E., Mayne, N. J., Spiga, A., Sohl, L., Saxena, P., Deitrick, R., Gilli, G., Domagal-Goldman, S. D., Forget, F., Consentino, R., Barnes, R., Haqq-Misra, J., Way, M. J., Wolf, E. T., Olson, S., Crouse, J. S., Janin, E., ... Bouldin, N. (2021). TRAPPIST Habitable Atmosphere Intercomparison (THAI) Workshop Report. *The Planetary Science Journal*, *2*(3), 106. https://doi.org/10.3847/PSJ/abf4df

Fauchez, T. J., Villanueva, G. L., Sergeev, D. E., Turbet, M., Boutle, I. A., Tsigaridis, K., Way, M. J., Wolf, E. T., Domagal-Goldman, S. D., Forget, F., Haqq-Misra, J., Kopparapu, R. K., Manners, J., & Mayne, N. J. (2022). The TRAPPIST-1 Habitable Atmosphere Intercomparison (THAI). III. Simulated Observables—the Return of the Spectrum. *The Planetary Science Journal*, *3*(9), 213. https://doi.org/10.3847/PSJ/ac6cf1

Faulk, S., Mitchell, J., & Bordoni, S. (2017). Effects of Rotation Rate and Seasonal Forcing on the ITCZ Extent in Planetary Atmospheres. *Journal of the Atmospheric Sciences*, *74*(3), 665–678. https://doi.org/10.1175/JAS-D-16-0014.1

Feng, Y. K., Robinson, T. D., Fortney, J. J., Lupu, R. E., Marley, M. S., Lewis, N. K., Macintosh, B., & Line, M. R. (2018). Characterizing Earth Analogs in Reflected Light: Atmospheric Retrieval Studies for Future Space Telescopes. *The Astronomical Journal*, *155*(5), 200. https://doi.org/10.3847/1538-3881/aab95c

Finney, D. L., Doherty, R. M., Wild, O., Huntrieser, H., Pumphrey, H. C., & Blyth, A. M. (2014). Using cloud ice flux to parametrise large-scale lightning. *Atmospheric Chemistry and Physics*, *14*(23), 12665–12682. https://doi.org/10.5194/acp-14-12665-2014

Finney, D. L., Doherty, R. M., Wild, O., Stevenson, D. S., MacKenzie, I. A., & Blyth, A. M. (2018). A projected decrease in lightning under climate change. *Nature Climate Change*, *8*(3), 210–213. https://doi.org/10.1038/s41558-018-0072-6

Fomichev, V. I., Jonsson, A. I., Grandpré, J. d., Beagley, S. R., McLandress, C., Semeniuk, K., & Shepherd, T. G. (2007). Response of the Middle Atmosphere to CO2 Doubling: Results from the Canadian Middle Atmosphere Model. *Journal of Climate*, *20*(7), 1121–1144. https://doi.org/10.1175/JCLI4030.1

Forget, F., & Leconte, J. (2014). Possible climates on terrestrial exoplanets. *Philosophical Transactions of the Royal Society A: Mathematical, Physical and Engineering Sciences*, *372*(2014), 20130084. https://doi.org/10.1098/rsta.2013.0084

France, K., Loyd, R. O. P., Youngblood, A., Brown, A., Schneider, P. C., Hawley, S. L., Froning, C. S., Linsky, J. L., Roberge, A., Buccino, A. P., Davenport, J. R. A., Fontenla, J. M., Kaltenegger, L., Kowalski, A. F., Mauas, P. J. D., Miguel, Y., Redfield, S., Rugheimer, S., Tian, F., ... Weisenburger, K. L. (2016). THE MUSCLES TREASURY SURVEY. I. MOTIVATION AND OVERVIEW*. *The Astrophysical Journal*, *820*(2), 89. https://doi.org/10.3847/0004-637X/820/2/89

Fressin, F., Torres, G., Charbonneau, D., Bryson, S. T., Christiansen, J., Dressing, C. D., Jenkins, J. M., Walkowicz, L. M., & Batalha, N. M. (2013). THE FALSE POSITIVE RATE OF KEPLER AND THE OCCURRENCE OF PLANETS. *The Astrophysical Journal*, *766*(2), 81. https://doi.org/10.1088/0004-637X/766/2/81

Frierson, D. M. W., Held, I. M., & Zurita-Gotor, P. (2006). A Gray-Radiation Aquaplanet Moist GCM. Part I: Static Stability and Eddy Scale. *Journal of the Atmospheric Sciences*, *63*(10), 2548–2566. https://doi.org/10.1175/JAS3753.1

Fulton, B. J., Petigura, E. A., Howard, A. W., Isaacson, H., Marcy, G. W., Cargile, P. A., Hebb, L., Weiss, L. M., Johnson, J. A., Morton, T. D., Sinukoff, E., Crossfield, I. J. M., & Hirsch, L. A. (2017). The California-Kepler Survey. III. A Gap in the Radius Distribution of Small Planets*. *The Astronomical Journal*, *154*(3), 109. https://doi.org/10.3847/1538-3881/aa80eb

Gaillard, F., Bouhifd, M. A., Füri, E., Malavergne, V., Marrocchi, Y., Noack, L., Ortenzi, G., Roskosz, M., & Vulpius, S. (2021). The Diverse Planetary Ingassing/Outgassing Paths Produced over Billions of Years of Magmatic Activity. *Space Science Reviews*, *217*(1), 22. https://doi.org/10.1007/s11214-021-00802-1

Ganzeveld, L., & Lelieveld, J. (1995). Dry deposition parameterization in a chemistry general circulation model and its influence on the distribution of reactive trace gases. *Journal of Geophysical Research: Atmospheres*, *100*(D10), 20999–21012. https://doi.org/10.1029/95JD02266

Gao, P., Hu, R., Robinson, T. D., Li, C., & Yung, Y. L. (2015). STABILITY OF CO2 ATMOSPHERES ON DESICCATED M DWARF EXOPLANETS. *The Astrophysical Journal*, *806*(2), 249. https://doi.org/10.1088/0004-637X/806/2/249

Garcia, L. J., Moran, S. E., Rackham, B. V., Wakeford, H. R., Gillon, M., Wit, J. d., & Lewis, N. K. (2022). HST/WFC3 transmission spectroscopy of the cold rocky planet TRAPPIST-1h. *Astronomy & Astrophysics*, *665*, A19. https://doi.org/10.1051/0004-6361/202142603

Garcia-Sage, K., Glocer, A., Drake, J. J., Gronoff, G., & Cohen, O. (2017). On the Magnetic Protection of the Atmosphere of Proxima Centauri b. *The Astrophysical Journal*, *844*(1), L13. https://doi.org/10.3847/2041-8213/aa7eca

Garraffo, C., Drake, J. J., & Cohen, O. (2016). THE SPACE WEATHER OF PROXIMA CENTAURI b. *The Astrophysical Journal*, *833*(1), L4. https://doi.org/10.3847/2041-8205/833/1/L4

Geisler, J. E. (1981). A Linear Model of the Walker Circulation. *Journal of the Atmospheric Sciences*, *38*(7), 1390–1400. https://doi.org/10.1175/1520-0469(1981)038<1390:ALMOTW>2.0.CO;2

Giannakopoulos, C., Chipperfield, M. P., Law, K. S., & Pyle, J. A. (1999). Validation and intercomparison of wet and dry deposition schemes using 210Pb in a global three-dimensional off-line chemical transport model. *Journal of Geophysical Research: Atmospheres*, *104*(D19), 23761–23784. https://doi.org/10.1029/1999JD900392

Gill, A. E. (1980). Some simple solutions for heat-induced tropical circulation. *Quarterly Journal of the Royal Meteorological Society*, *106*(449), 447–462. https://doi.org/10.1002/qj.49710644905

Gillon, M., Triaud, A. H. M. J., Demory, B.-O., Jehin, E., Agol, E., Deck, K. M., Lederer, S. M., de Wit, J., Burdanov, A., Ingalls, J. G., Bolmont, E., Leconte, J., Raymond, S. N., Selsis, F., Turbet, M., Barkaoui, K., Burgasser, A., Burleigh, M. R., Carey, S. J., ... Queloz, D. (2017). Seven temperate terrestrial planets around the nearby ultracool dwarf star TRAPPIST-1. *Nature*, *542*(7642), 456–460. https://doi.org/10.1038/nature21360

Gladstone, G. R., Stern, S. A., Ennico, K., Olkin, C. B., Weaver, H. A., Young, L. A., Summers, M. E., Strobel, D. F., Hinson, D. P., Kammer, J. A., Parker, A. H., Steffl, A. J., Linscott, I. R., Parker, J. W., Cheng, A. F., Slater, D. C., Versteeg, M. H., Greathouse, T. K., Retherford, K. D., ... THE NEW HORIZONS SCIENCE TEAM. (2016). The atmosphere of Pluto as observed by New Horizons. *Science*, *351*(6279), aad8866. https://doi.org/10.1126/science.aad8866

Godolt, M., Grenfell, J. L., Hamann-Reinus, A., Kitzmann, D., Kunze, M., Langematz, U., von Paris, P., Patzer, A. B. C., Rauer, H., & Stracke, B. (2015). 3D climate modeling of Earth-like extrasolar planets orbiting different types of host stars. *Planetary and Space Science*, *111*, 62–76. https://doi.org/10.1016/j.pss.2015.03.010

Goldblatt, C., & Watson, A. J. (2012). The runaway greenhouse: Implications for future climate change, geoengineering and planetary atmospheres. *Philosophical Transactions of the Royal Society A: Mathematical, Physical and Engineering Sciences*, *370*(1974), 4197–4216. https://doi.org/10.1098/rsta.2012.0004

Goldblatt, C., Robinson, T. D., Zahnle, K. J., & Crisp, D. (2013). Low simulated radiation limit for runaway greenhouse climates. *Nature Geoscience*, *6*(8), 661–667. https://doi.org/10.1038/ngeo1892

Goldreich, P. (1966). Final spin states of planets and satellites. *The Astronomical Journal*, *71*, 1. https://doi.org/10.1086/109844

Goldreich, P., & Soter, S. (1966). Q in the solar system. *Icarus*, *5*(1), 375–389. https://doi.org/10.1016/0019-1035(66)90051-0

Goldreich, P., & Peale, S. (1966). Spin-orbit coupling in the solar system. *The Astronomical Journal*, *71*, 425. https://doi.org/10.1086/109947

Gordon, I. E., Rothman, L. S., Hargreaves, R. J., Hashemi, R., Karlovets, E. V., Skinner, F. M., Conway, E. K., Hill, C., Kochanov, R. V., Tan, Y., Wcisło, P., Finenko, A. A., Nelson, K., Bernath, P. F., Birk, M., Boudon, V., Campargue, A., Chance, K. V., Coustenis, A., ... Yurchenko, S. N. (2022). The HITRAN2020 molecular spectroscopic database. *Journal of Quantitative Spectroscopy and Radiative Transfer*, *277*, 107949. https://doi.org/10.1016/j.jqsrt.2021.107949

Greaves, J. S., Richards, A. M. S., Bains, W., Rimmer, P. B., Sagawa, H., Clements, D. L., Seager, S., Petkowski, J. J., Sousa-Silva, C., Ranjan, S., Drabek-Maunder, E., Fraser, H. J., Cartwright, A., Mueller-Wodarg, I., Zhan, Z., Friberg, P., Coulson, I., Lee, E., & Hoge, J. (2021). Phosphine gas in the cloud decks of Venus. *Nature Astronomy*, *5*(7), 655–664. https://doi.org/10.1038/s41550-020-1174-4

Greene, T. P., Bell, T. J., Ducrot, E., Dyrek, A., Lagage, P.-O., & Fortney, J. J. (2023). Thermal Emission from the Earth-sized Exoplanet TRAPPIST-1 b using JWST. *Nature*, 1–2. https://doi.org/10.1038/s41586-023-05951-7

Gregory, D., & Rowntree, P. R. (1990). A Mass Flux Convection Scheme with Representation of Cloud Ensemble Characteristics and Stability-Dependent Closure. *Monthly Weather Review*, *118*(7), 1483–1506. https://doi.org/10.1175/1520-0493(1990)118<1483:AMFCSW>2.0.CO;2

Grenfell, J. L., Gebauer, S., v. Paris, P., Godolt, M., & Rauer, H. (2014). Sensitivity of biosignatures on Earth-like planets orbiting in the habitable zone of cool M-dwarf Stars to varying stellar UV radiation and surface biomass emissions. *Planetary and Space Science*, *98*, 66–76. https://doi.org/10.1016/j.pss.2013.10.006

Grenfell, J. L., Lehmann, R., Mieth, P., Langematz, U., & Steil, B. (2006). Chemical reaction pathways affecting stratospheric and mesospheric ozone. *Journal of Geophysical Research: Atmospheres*, *111*(D17). https://doi.org/10.1029/2004JD005713

Grenfell, J. L., Stracke, B., von Paris, P., Patzer, B., Titz, R., Segura, A., & Rauer, H. (2007). The response of atmospheric chemistry on earthlike planets around F, G and K Stars to small variations in orbital distance. *Planetary and Space Science*, *55*(5), 661–671. https://doi.org/10.1016/j.pss.2006.09.002

Grimm, S. L., Demory, B.-O., Gillon, M., Dorn, C., Agol, E., Burdanov, A., Delrez, L., Sestovic, M., Triaud, A. H. M. J., Turbet, M., Bolmont, É., Caldas, A., de Wit, J., Jehin, E., Leconte, J., Raymond, S. N., Van Grootel, V., Burgasser, A. J., Carey, S., ... Queloz, D. (2018). The nature of the TRAPPIST-1 exoplanets. *Astronomy & Astrophysics*, *613*, A68. https://doi.org/10.1051/0004-6361/201732233

Gupta, A., & Schlichting, H. E. (2019). Sculpting the valley in the radius distribution of small exoplanets as a by-product of planet formation: The core-powered mass-loss mechanism. *Monthly Notices of the Royal Astronomical Society*, *487*(1), 24–33. https://doi.org/10.1093/mnras/stz1230

Haagen-Smit, A. J. (1952). Chemistry and Physiology of Los Angeles Smog. *Industrial & Engineering Chemistry*, *44*(6), 1342–1346. https://doi.org/10.1021/ie50510a045

Hammond, M., Tsai, S.-M., & Pierrehumbert, R. T. (2020). The Equatorial Jet Speed on Tidally Locked Planets. I. Terrestrial Planets. *The Astrophysical Journal*, *901*(1), 78. https://doi.org/10.3847/1538-4357/abb08b

Hammond, M., & Lewis, N. T. (2021). The rotational and divergent components of atmospheric circulation on tidally locked planets. *Proceedings of the National Academy of Sciences*, *118*(13), e2022705118. https://doi.org/10.1073/pnas.2022705118

Han, Y., Luo, H., Wu, Y., Zhang, Y., & Dong, W. (2021). Cloud ice fraction governs lightning rate at a global scale. *Communications Earth & Environment*, *2*(1), 1–9. https://doi.org/10.1038/s43247-021-00233-4

Haqq-Misra, J., & Kopparapu, R. K. (2015). Geothermal heating enhances atmospheric asymmetries on synchronously rotating planets. *Monthly Notices of the Royal Astronomical Society*, *446*(1), 428–438. https://doi.org/10.1093/mnras/stu2052

Haqq-Misra, J., Wolf, E. T., Joshi, M., Zhang, X., & Kopparapu, R. K. (2018). Demarcating circulation regimes of synchronously rotating terrestrial planets within the habitable zone. *The Astrophysical Journal*, *852*(2), 67. https://doi.org/10.3847/1538-4357/aa9f1f

Harman, C. E., Schwieterman, E. W., Schottelkotte, J. C., & Kasting, J. F. (2015). ABIOTIC O_2 LEVELS ON PLANETS AROUND F, G, K, AND M STARS: POSSIBLE FALSE POSITIVES FOR LIFE? *The Astrophysical Journal*, *812*(2), 137. https://doi.org/10.1088/0004-637X/812/2/137

Harman, C. E., Felton, R., Hu, R., Domagal-Goldman, S. D., Segura, A., Tian, F., & Kasting, J. F. (2018). Abiotic O_2 Levels on Planets around F, G, K, and M Stars: Effects of Lightning-produced Catalysts in Eliminating Oxygen False Positives. *The Astrophysical Journal*, *866*(1), 56. https://doi.org/10.3847/1538-4357/aadd9b

Helling, C. (2019). Exoplanet Clouds. *Annual Review of Earth and Planetary Sciences*, *47*(1), 583–606. https://doi.org/10.1146/annurev-earth-053018-060401

Helling, C., Jardine, M., Diver, D., & Witte, S. (2013). Dust cloud lightning in extraterrestrial atmospheres. *Planetary and Space Science*, *77*, 152–157. https://doi.org/10.1016/j.pss.2012.07.003

Heng, K., Frierson, D. M. W., & Phillipps, P. J. (2011). Atmospheric circulation of tidally locked exoplanets: II. Dual-band radiative transfer and convective adjustment. *Monthly Notices of the Royal Astronomical Society*, *418*(4), 2669–2696. https://doi.org/10.1111/j.1365-2966.2011.19658.x

Heng, K., & Showman, A. P. (2015). Atmospheric Dynamics of Hot Exoplanets. *Annual Review of Earth and Planetary Sciences*, *43*, 509–540. https://doi.org/10.1146/annurev-earth-060614-105146

Heng, K., Lyons, J. R., & Tsai, S.-M. (2016). ATMOSPHERIC CHEMISTRY FOR ASTROPHYSICISTS: A SELF-CONSISTENT FORMALISM AND ANALYTICAL SOLUTIONS FOR ARBITRARY C/O. *The Astrophysical Journal*, *816*(2), 96. https://doi.org/10.3847/0004-637X/816/2/96

Hess, S. L., Ryan, J. A., Tillman, J. E., Henry, R. M., & Leovy, C. B. (1980). The annual cycle of pressure on Mars measured by Viking Landers 1 and 2. *Geophysical Research Letters*, *7*(3), 197–200. https://doi.org/10.1029/GL007i003p00197

Hochman, A., Luca, P. D., & Komacek, T. D. (2022). Greater Climate Sensitivity and Variability on TRAPPIST-1e than Earth. *The Astrophysical Journal*, *938*(2), 114. https://doi.org/10.3847/1538-4357/ac866f

Hochman, A., Komacek, T. D., & De Luca, P. (2023, July). Analogous response of temperate terrestrial exoplanets and Earth's climate dynamics to greenhouse gas supplement. https://doi.org/10.48550/arXiv.2307.01983

Hodosán, G., Helling, C., Asensio-Torres, R., Vorgul, I., & Rimmer, P. B. (2016). Lightning climatology of exoplanets and brown dwarfs guided by Solar System data. *Monthly Notices of the Royal Astronomical Society*, *461*(4), 3927–3947. https://doi.org/10.1093/mnras/stw1571

Howard, A. W., Marcy, G. W., Bryson, S. T., Jenkins, J. M., Rowe, J. F., Batalha, N. M., Borucki, W. J., Koch, D. G., Dunham, E. W., Gautier, T. N., Cleve, J. V., Cochran, W. D., Latham, D. W., Lissauer, J. J., Torres, G., Brown, T. M., Gilliland, R. L., Buchhave, L. A., Caldwell, D. A., … MacQueen, P. J. (2012). PLANET OCCURRENCE WITHIN 0.25 AU OF SOLAR-TYPE STARS FROM KEPLER*. *The Astrophysical Journal Supplement Series*, *201*(2), 15. https://doi.org/10.1088/0067-0049/201/2/15

Hsu, D. C., Ford, E. B., Ragozzine, D., & Ashby, K. (2019). Occurrence Rates of Planets Orbiting FGK Stars: Combining Kepler DR25, Gaia DR2, and Bayesian Inference. *The Astronomical Journal*, *158*(3), 109. https://doi.org/10.3847/1538-3881/ab31ab

Hsu, J., & Prather, M. J. (2009). Stratospheric variability and tropospheric ozone. *Journal of Geophysical Research: Atmospheres*, *114*(D6). https://doi.org/10.1029/2008JD010942

Hu, R., Seager, S., & Bains, W. (2012). PHOTOCHEMISTRY IN TERRESTRIAL EXOPLANET ATMOSPHERES. I. PHOTOCHEMISTRY MODEL AND BENCHMARK CASES. *The Astrophysical Journal*, *761*(2), 166. https://doi.org/10.1088/0004-637X/761/2/166

Hu, Y., & Yang, J. (2014). Role of ocean heat transport in climates of tidally locked exoplanets around M dwarf stars. *Proceedings of the National Academy of Sciences*, *111*(2), 629–634. https://doi.org/10.1073/pnas.1315215111

Ida, S., & Lin, D. N. C. (2004). Toward a Deterministic Model of Planetary Formation. I. A Desert in the Mass and Semimajor Axis Distributions of Extrasolar Planets. *The Astrophysical Journal*, *604*(1), 388. https://doi.org/10.1086/381724

Ikoma, M., & Hori, Y. (2012). IN SITU ACCRETION OF HYDROGEN-RICH ATMOSPHERES ON SHORT-PERIOD SUPER-EARTHS: IMPLICATIONS FOR THE KEPLER-11 PLANETS. *The Astrophysical Journal*, *753*(1), 66. https://doi.org/10.1088/0004-637X/753/1/66

Ingersoll, A. P. (1969). The Runaway Greenhouse: A History of Water on Venus. *Journal of the Atmospheric Sciences*, *26*(6), 1191–1198. https://doi.org/10.1175/1520-0469(1969)026<1191:TRGAHO>2.0.CO;2

Isaksen, I. S. A., Granier, C., Myhre, G., Berntsen, T. K., Dalsøren, S. B., Gauss, M., Klimont, Z., Benestad, R., Bousquet, P., Collins, W., Cox, T., Eyring, V., Fowler, D., Fuzzi, S., Jöckel, P., Laj, P., Lohmann, U., Maione, M., Monks, P., ... Wuebbles, D. (2009). Atmospheric composition change: Climate–Chemistry interactions. *Atmospheric Environment*, *43*(33), 5138–5192. https://doi.org/10.1016/j.atmosenv.2009.08.003

Jenkins, J. S., Harrington, J., Challener, R. C., Kurtovic, N. T., Ramirez, R., Peña, J., McIntyre, K. J., Himes, M. D., Rodríguez, E., Anglada-Escudé, G., Dreizler, S., Ofir, A., Peña Rojas, P. A., Ribas, I., Rojo, P., Kipping, D., Butler, R. P., Amado, P. J., Rodríguez-López, C., ... Murgas, F. (2019). Proxima Centauri b is not a transiting exoplanet. *Monthly Notices of the Royal Astronomical Society*, *487*, 268–274. https://doi.org/10.1093/mnras/stz1268

Johnston, H. (1971). Reduction of Stratospheric Ozone by Nitrogen Oxide Catalysts from Supersonic Transport Exhaust [Publisher: American Association for the Advancement of Science]. *Science*, *173*(3996), 517–522. https://doi.org/10.1126/science.173.3996.517

Joshi, M. M., Haberle, R. M., & Reynolds, R. T. (1997). Simulations of the Atmospheres of Synchronously Rotating Terrestrial Planets Orbiting M Dwarfs: Conditions for Atmospheric Collapse and the Implications for Habitability. *Icarus*, *129*(2), 450–465. https://doi.org/10.1006/icar.1997.5793

Joshi, M. M., Elvidge, A. D., Wordsworth, R., & Sergeev, D. (2020). Earth's Polar Night Boundary Layer as an Analog for Dark Side Inversions on Synchronously Rotating Terrestrial Exoplanets. *The Astrophysical Journal*, *892*(2), L33. https://doi.org/10.3847/2041-8213/ab7fb3

Joshi, M. M. (2003). Climate Model Studies of Synchronously Rotating Planets. *Astrobiology*, *3*(2), 415–427. https://doi.org/10.1089/153110703769016488

Joshi, M. M., & Haberle, R. M. (2012). Suppression of the Water Ice and Snow Albedo Feedback on Planets Orbiting Red Dwarf Stars and the Subsequent Widening of the Habitable Zone. *Astrobiology*, *12*(1), 3–8. https://doi.org/10.1089/ast.2011.0668

Kaltenegger, L. (2017). How to Characterize Habitable Worlds and Signs of Life. *Annual Review of Astronomy and Astrophysics*, *55*(1), 433–485. https://doi.org/10.1146/annurev-astro-082214-122238

Kane, S. R., Gelino, D. M., & Turnbull, M. C. (2017). ON THE ORBITAL INCLINATION OF PROXIMA CENTAURI b. *The Astronomical Journal*, *153*(2), 52. https://doi.org/10.3847/1538-3881/153/2/52

Kasting, J. F., & Donahue, T. M. (1980). The evolution of atmospheric ozone [_eprint: https://onlinelibrary.wiley.com/doi/pdf/10.1029/JC085iC06p03255]. *Journal of Geophysical Research: Oceans*, *85*(C6), 3255–3263. https://doi.org/10.1029/JC085iC06p03255

Kasting, J. F. (1988). Runaway and moist greenhouse atmospheres and the evolution of Earth and Venus. *Icarus*, *74*(3), 472–494. https://doi.org/10.1016/0019-1035(88)90116-9

Kasting, J. F., Whitmire, D. P., & Reynolds, R. T. (1993). Habitable Zones around Main Sequence Stars. *Icarus*, *101*(1), 108–128. https://doi.org/10.1006/icar.1993.1010

Kasting, J. F., & Catling, D. (2003). Evolution of a Habitable Planet. *Annual Review of Astronomy and Astrophysics*, *41*(1), 429–463. https://doi.org/10.1146/annurev.astro.41.071601.170049

Kirk, J., Stevenson, K. B., Fu, G., Lustig-Yaeger, J., Moran, S. E., Peacock, S., Alam, M. K., Batalha, N. E., Bennett, K. A., Gonzalez-Quiles, J., López-Morales, M., Lothringer, J. D., MacDonald, R. J., May, E. M., Mayorga, L. C., Rustamkulov, Z., Sing, D. K., Sotzen, K. S., Valenti, J. A., & Wakeford, H. R. (2024). JWST/NIRCam Transmission Spectroscopy of the Nearby Sub-Earth GJ 341b. *The Astronomical Journal*, *167*(3), 90. https://doi.org/10.3847/1538-3881/ad19df

Kitzmann, D., Patzer, A. B. C., Paris, P. v., Godolt, M., & Rauer, H. (2011). Clouds in the atmospheres of extrasolar planets - II. Thermal emission spectra of Earth-like planets influenced by low and high-level clouds. *Astronomy & Astrophysics*, *531*, A62. https://doi.org/10.1051/0004-6361/201014343

Koll, D. D. B., & Abbot, D. S. (2015). DECIPHERING THERMAL PHASE CURVES OF DRY, TIDALLY LOCKED TERRESTRIAL PLANETS. *The Astrophysical Journal*, *802*(1), 21. https://doi.org/10.1088/0004-637X/802/1/21

Koll, D. D. B., & Abbot, D. S. (2016). Temperature Structure and Atmospheric Circulation of Dry Tidally Locked Rocky Exoplanets. *The Astrophysical Journal*, *825*, 99. https://doi.org/10.3847/0004-637X/825/2/99

Komacek, T. D., & Abbot, D. S. (2019). The Atmospheric Circulation and Climate of Terrestrial Planets Orbiting Sun-like and M Dwarf Stars over a Broad Range of Planetary Parameters. *The Astrophysical Journal*, *871*(2), 245. https://doi.org/10.3847/1538-4357/aafb33

Komacek, T. D., Showman, A. P., & Parmentier, V. (2019). Vertical Tracer Mixing in Hot Jupiter Atmospheres. *The Astrophysical Journal*, *881*(2), 152. https://doi.org/10.3847/1538-4357/ab338b

Konrad, B. S., Alei, E., Quanz, S. P., Angerhausen, D., Carrión-González, O., Fortney, J. J., Grenfell, J. L., Kitzmann, D., Mollière, P., Rugheimer, S., & Wunderlich, F. (2022). Large Interferometer For Exoplanets (LIFE) - III. Spectral resolution, wavelength range, and sensitivity requirements based on atmospheric retrieval analyses of an exo-Earth. *Astronomy & Astrophysics*, *664*, A23. https://doi.org/10.1051/0004-6361/202141964

Kopparapu, R. K., Ramirez, R., Kasting, J. F., Eymet, V., Robinson, T. D., Mahadevan, S., Terrien, R. C., Domagal-Goldman, S., Meadows, V., & Deshpande, R. (2013). HABITABLE ZONES AROUND MAIN-SEQUENCE STARS: NEW ESTIMATES. *The Astrophysical Journal*, *765*(2), 131. https://doi.org/10.1088/0004-637X/765/2/131

Kopparapu, R. K., Wolf, E. T., Arney, G., Batalha, N. E., Haqq-Misra, J., Grimm, S. L., & Heng, K. (2017). Habitable Moist Atmospheres on Terrestrial Planets near the Inner Edge of the Habitable Zone around M Dwarfs. *The Astrophysical Journal*, *845*(1), 5. https://doi.org/10.3847/1538-4357/aa7cf9

Kopparapu, R. K., Arney, G., Haqq-Misra, J., Lustig-Yaeger, J., & Villanueva, G. (2021). Nitrogen Dioxide Pollution as a Signature of Extraterrestrial Technology. *The Astrophysical Journal*, *908*(2), 164. https://doi.org/10.3847/1538-4357/abd7f7

Kopparapu, R. k., Wolf, E. T., Haqq-Misra, J., Yang, J., Kasting, J. F., Meadows, V., Terrien, R., & Mahadevan, S. (2016). THE INNER EDGE OF THE HABITABLE ZONE FOR SYNCHRONOUSLY ROTATING PLANETS AROUND LOW-MASS STARS USING GENERAL CIRCULATION MODELS. *The Astrophysical Journal*, *819*(1), 84. https://doi.org/10.3847/0004-637X/819/1/84

Kozakis, T., Mendonça, J. M., & Buchhave, L. A. (2022). Is ozone a reliable proxy for molecular oxygen? I. The O2-O3 relationship for Earth-like atmospheres. *Astronomy & Astrophysics*. https://doi.org/10.1051/0004-6361/202244164

Kramm, U., Nettelmann, N., Fortney, J. J., Neuhäuser, R., & Redmer, R. (2012). Constraining the interior of extrasolar giant planets with the tidal Love number k2 using the example of HAT-P-13b [ADS Bibcode: 2012A&A...538A.146K]. *Astronomy and Astrophysics*, *538*, A146. https://doi.org/10.1051/0004-6361/201118141

Kreidberg, L., Bean, J. L., Désert, J.-M., Line, M. R., Fortney, J. J., Madhusudhan, N., Stevenson, K. B., Showman, A. P., Charbonneau, D., McCullough, P. R., Seager, S., Burrows, A., Henry, G. W., Williamson, M., Kataria, T., & Homeier, D. (2014). A Precise Water Abundance Measurement for the Hot Jupiter WASP-43b. *The Astrophysical Journal Letters*, *793*(2), L27. https://doi.org/10.1088/2041-8205/793/2/L27

Kreidberg, L., & Loeb, A. (2016). PROSPECTS FOR CHARACTERIZING THE ATMOSPHERE OF PROXIMA CENTAURI b. *The Astrophysical Journal Letters*, *832*(1), L12. https://doi.org/10.3847/2041-8205/832/1/L12

Kreidberg, L., Koll, D. D. B., Morley, C., Hu, R., Schaefer, L., Deming, D., Stevenson, K. B., Dittmann, J., Vanderburg, A., Berardo, D., Guo, X., Stassun, K., Crossfield, I., Charbonneau, D., Latham, D. W., Loeb, A., Ricker, G., Seager, S., & Vanderspek, R. (2019). Absence of a thick atmosphere on the terrestrial exoplanet LHS 3844b. *Nature*, *573*(7772), 87–90. https://doi.org/10.1038/s41586-019-1497-4

Krissansen-Totton, J., Olson, S., & Catling, D. C. (2018). Disequilibrium biosignatures over Earth history and implications for detecting exoplanet life. *Science Advances*, *4*(1), eaao5747. https://doi.org/10.1126/sciadv.aao5747

Kunimoto, M., & Matthews, J. M. (2020). Searching the Entirety of Kepler Data. II. Occurrence Rate Estimates for FGK Stars. *The Astronomical Journal*, *159*(6), 248. https://doi.org/10.3847/1538-3881/ab88b0

Langematz, U., Kunze, M., Krüger, K., Labitzke, K., & Roff, G. L. (2003). Thermal and dynamical changes of the stratosphere since 1979 and their link to ozone and CO2 changes. *Journal of Geophysical Research: Atmospheres*, *108*(D1), ACL 9–1–ACL 9–13. https://doi.org/10.1029/2002JD002069

Lewis, N. T., Lambert, F. H., Boutle, I. A., Mayne, N. J., Manners, J., & Acreman, D. M. (2018). The Influence of a Substellar Continent on the Climate of a Tidally Locked Exoplanet. *The Astrophysical Journal*, *854*(2), 171. https://doi.org/10.3847/1538-4357/aaad0a

Libby-Roberts, J. E., Berta-Thompson, Z. K., Diamond-Lowe, H., Gully-Santiago, M. A., Irwin, J. M., Kempton, E. M.-R., Rackham, B. V., Charbonneau, D., Désert, J.-M., Dittmann, J. A., Hofmann, R., Morley, C. V., & Newton, E. R. (2022). The Featureless HST/WFC3 Transmission Spectrum of the Rocky Exoplanet GJ 1132b: No Evidence for a Cloud-free Primordial Atmosphere and Constraints on Starspot Contamination. *The Astronomical Journal*, *164*(2), 59. https://doi.org/10.3847/1538-3881/ac75de

Lichtenberg, T., Schaefer, L. K., Nakajima, M., & Fischer, R. A. (2023). Geophysical Evolution During Rocky Planet Formation. *534*, 907. https://doi.org/10.48550/arXiv.2203.10023

Lim, O., Benneke, B., Doyon, R., MacDonald, R. J., Piaulet, C., Artigau, E., Coulombe, L.-P., Radica, M., L'Heureux, A., Albert, L., Rackham, B. V., Wit, J. d., Salhi, S., Roy, P.-A., Flagg, L., Fournier-Tondreau, M., Taylor, J., Cook, N. J., Lafrenière, D., … Darveau-Bernier, A. (2023). Atmospheric Reconnaissance of TRAPPIST-1 b with JWST/NIRISS: Evidence for Strong Stellar Contamination in the Transmission Spectra. *The Astrophysical Journal Letters*, *955*(1), L22. https://doi.org/10.3847/2041-8213/acf7c4

Lincowski, A. P., Lustig-Yaeger, J., & Meadows, V. S. (2019). Observing Isotopologue Bands in Terrestrial Exoplanet Atmospheres with the James Webb Space Telescope: Implications for Identifying Past Atmospheric and Ocean Loss. *The Astronomical Journal*, *158*, 26. https://doi.org/10.3847/1538-3881/ab2385

Lines, S., Mayne, N. J., Boutle, I. A., Manners, J., Lee, E. K. H., Helling, C., Drummond, B., Amundsen, D. S., Goyal, J., Acreman, D. M., Tremblin, P., & Kerslake, M. (2018). Simulating the cloudy atmospheres of HD 209458 b and HD 189733 b with the 3D Met Office Unified Model. *Astronomy & Astrophysics*, *615*, A97. https://doi.org/10.1051/0004-6361/201732278

Liu, B., Marsh, D., Walsh, C., & Cooke, G. (2023). Higher Water Loss on Earth-like Exoplanets in Eccentric Orbits. *Monthly Notices of the Royal Astronomical Society*, *524*(1), 1491–1502. https://doi.org/10.1093/mnras/stad1828

Liu, C., Cecil, D. J., Zipser, E. J., Kronfeld, K., & Robertson, R. (2012). Relationships between lightning flash rates and radar reflectivity vertical structures in thunderstorms over the tropics and subtropics. *Journal of Geophysical Research: Atmospheres*, *117*(D6). https://doi.org/10.1029/2011JD017123

Lobo, A. H., Shields, A. L., Palubski, I. Z., & Wolf, E. (2023). Terminator Habitability: The Case for Limited Water Availability on M-dwarf Planets. *The Astrophysical Journal*, *945*(2), 161. https://doi.org/10.3847/1538-4357/aca970

Lock, A. P., Brown, A. R., Bush, M. R., Martin, G. M., & Smith, R. N. B. (2000). A New Boundary Layer Mixing Scheme. Part I: Scheme Description and Single-Column Model Tests. *Monthly Weather Review*, *128*(9), 3187–3199. https://doi.org/10.1175/1520-0493(2000)128<3187:ANBLMS>2.0.CO;2

Lopez, E. D., & Fortney, J. J. (2013). THE ROLE OF CORE MASS IN CONTROLLING EVAPORATION: THE KEPLER RADIUS DISTRIBUTION AND THE KEPLER-36 DENSITY DICHOTOMY. *The Astrophysical Journal*, *776*(1), 2. https://doi.org/10.1088/0004-637X/776/1/2

Lovelock, J. E. (1965). A physical basis for life detection experiments. *Nature*, *207*(997), 568–570. https://doi.org/10.1038/207568a0

Loyd, R. O. P., France, K., Youngblood, A., Schneider, C., Brown, A., Hu, R., Linsky, J., Froning, C. S., Redfield, S., Rugheimer, S., & Tian, F. (2016). The MUSCLES Treasury Survey. III. X-Ray to Infrared Spectra of 11 M and K Stars Hosting Planets. *The Astrophysical Journal*, *824*, 102. https://doi.org/10.3847/0004-637X/824/2/102

Luger, R., & Barnes, R. (2015). Extreme Water Loss and Abiotic O2 Buildup on Planets Throughout the Habitable Zones of M Dwarfs. *Astrobiology*, *15*(2), 119–143. https://doi.org/10.1089/ast.2014.1231

Luger, R., Sestovic, M., Kruse, E., Grimm, S. L., Demory, B.-O., Agol, E., Bolmont, E., Fabrycky, D., Fernandes, C. S., Van Grootel, V., Burgasser, A., Gillon, M., Ingalls, J. G., Jehin, E., Raymond, S. N., Selsis, F., Triaud, A. H. M. J., Barclay, T., Barentsen, G., … Queloz, D. (2017). A seven-planet resonant chain in TRAPPIST-1. *Nature Astronomy*, *1*(6), 1–8. https://doi.org/10.1038/s41550-017-0129

Luhar, A. K., Galbally, I. E., Woodhouse, M. T., & Abraham, N. L. (2021). Assessing and improving cloud-height-based parameterisations of global lightning flash rate, and their impact on lightning-produced NO_{<i>x</i>} and tropospheric composition in a chemistry–climate model. *Atmospheric Chemistry and Physics*, *21*(9), 7053–7082. https://doi.org/10.5194/acp-21-7053-2021

Lustig-Yaeger, J., Meadows, V. S., & Lincowski, A. P. (2019). The Detectability and Characterization of the TRAPPIST-1 Exoplanet Atmospheres with JWST. *The Astronomical Journal*, *158*(1), 27. https://doi.org/10.3847/1538-3881/ab21e0

Lustig-Yaeger, J., Fu, G., May, E. M., Ceballos, K. N. O., Moran, S. E., Peacock, S., Stevenson, K. B., Kirk, J., López-Morales, M., MacDonald, R. J., Mayorga, L. C., Sing, D. K., Sotzen, K. S., Valenti, J. A., Redai, J. I. A., Alam, M. K., Batalha, N. E., Bennett, K. A., Gonzalez-Quiles, J., . . . Wakeford, H. R. (2023). A JWST transmission spectrum of the nearby Earth-sized exoplanet LHS 475 b. *Nature Astronomy*, *7*(11), 1317–1328. https://doi.org/10.1038/s41550-023-02064-z

Luther, F. M., Wuebbles, D. J., & Chang, J. S. (1977). Temperature feedback in a stratospheric model. *Journal of Geophysical Research (1896-1977)*, *82*(31), 4935–4942. https://doi.org/10.1029/JC082i031p04935

Lyons, T. W., Reinhard, C. T., & Planavsky, N. J. (2014). The rise of oxygen in Earth's early ocean and atmosphere. *Nature*, *506*(7488), 307–315. https://doi.org/10.1038/nature13068

Madhusudhan, N., & Seager, S. (2009). A TEMPERATURE AND ABUNDANCE RETRIEVAL METHOD FOR EXOPLANET ATMOSPHERES. *The Astrophysical Journal*, *707*(1), 24. https://doi.org/10.1088/0004-637X/707/1/24

Mak, M. T., Mayne, N. J., Sergeev, D. E., Manners, J., Eager-Nash, J. K., Arney, G., Hébrard, E., & Kohary, K. (2023). 3D Simulations of the Archean Earth Including Photochemical Haze Profiles. *Journal of Geophysical Research: Atmospheres*, *128*(20), e2023JD039343. https://doi.org/10.1029/2023JD039343

Mak, M. T., Sergeev, D., Mayne, N., Banks, N., Eager-Nash, J., Manners, J., Arney, G., Hebrard, E., & Kohary, K. (2024, March). 3D simulations of TRAPPIST-1e with varying CO2, CH4 and haze profiles. https://doi.org/10.48550/arXiv.2403.06928

Makarov, V. V. (2012). CONDITIONS OF PASSAGE AND ENTRAPMENT OF TERRESTRIAL PLANETS IN SPIN-ORBIT RESONANCES [Publisher: The American Astronomical Society]. *The Astrophysical Journal*, *752*(1), 73. https://doi.org/10.1088/0004-637X/752/1/73

Makarov, V. V., Berghea, C. T., & Efroimsky, M. (2018). Spin-orbital Tidal Dynamics and Tidal Heating in the TRAPPIST-1 Multiplanet System. *The Astrophysical Journal*, *857*(2), 142. https://doi.org/10.3847/1538-4357/aab845

Manners, J., Edwards, J. M., Hill, P., & Thelen, J.-C. (2021). SOCRATES (Suite Of Community RAdiative Transfer codes based on Edwards and Slingo) Technical Guide. https://code.metoffice.gov.uk/trac/socrates

Mao, J., Zhao, T., Keller, C. A., Wang, X., McFarland, P. J., Jenkins, J. M., & Brune, W. H. (2021). Global Impact of Lightning-Produced Oxidants. *Geophysical Research Letters*, *48*(21), e2021GL095740. https://doi.org/10.1029/2021GL095740

Masson-Delmotte, V., Zhai, P., Pirani, A., Connors, S. L., Péan, C., Berger, S., Caud, N., Chen, Y., Goldfarb, L., Gomis, M. I., Huang, M., Leitzell, K., Lonnoy, E., Matthews, J. B. R., Maycock, T. K., Waterfield, T., Yelekçi, Ö., Yu, R., & Zhou, B. (Eds.). (2021). *Climate Change 2021: The Physical Science Basis. Contribution of Working Group I to the Sixth Assessment Report of the Intergovernmental Panel on Climate Change*. Cambridge University Press. https://doi.org/10.1017/9781009157896

May, E. M., Taylor, J., Komacek, T. D., Line, M. R., & Parmentier, V. (2021). Water Ice Cloud Variability and Multi-epoch Transmission Spectra of TRAPPIST-1e. *The Astrophysical Journal Letters*, *911*(2), L30. https://doi.org/10.3847/2041-8213/abeeff

May, E. M., MacDonald, R. J., Bennett, K. A., Moran, S. E., Wakeford, H. R., Peacock, S., Lustig-Yaeger, J., Highland, A. N., Stevenson, K. B., Sing, D. K., Mayorga, L. C., Batalha, N. E., Kirk, J., López-Morales, M., Valenti, J. A., Alam, M. K., Alderson, L., Fu, G., Gonzalez-Quiles, J., ... Sotzen, K. S. (2023). Double Trouble: Two Transits of the Super-Earth GJ 1132 b Observed with JWST NIRSpec G395H. *The Astrophysical Journal Letters*, *959*(1), L9. https://doi.org/10.3847/2041-8213/ad054f

Mayne, N. J., Baraffe, I., Acreman, D. M., Smith, C., Wood, N., Amundsen, D. S., Thuburn, J., & Jackson, D. R. (2014a). Using the UM dynamical cores to reproduce idealised 3-D flows. *Geoscientific Model Development*, *7*(6), 3059–3087. https://doi.org/10.5194/gmd-7-3059-2014

Mayne, N. J., Drummond, B., Debras, F., Jaupart, E., Manners, J., Boutle, I. A., Baraffe, I., & Kohary, K. (2019). The Limits of the Primitive Equations of Dynamics for Warm, Slowly Rotating Small Neptunes and Super Earths. *The Astrophysical Journal*, *871*(1), 56. https://doi.org/10.3847/1538-4357/aaf6e9

Mayne, N. J., Baraffe, I., Acreman, D. M., Smith, C., Browning, M. K., Amundsen, D. S., Wood, N., Thuburn, J., & Jackson, D. R. (2014b). The unified model, a fully-compressible, non-hydrostatic, deep atmosphere global circulation model, applied to hot Jupiters: ENDGame for a HD 209458b test case. *Astronomy & Astrophysics*, *561*, A1. https://doi.org/10.1051/0004-6361/201322174

Mayne, N. J., Debras, F., Baraffe, I., Thuburn, J., Amundsen, D. S., Acreman, D. M., Smith, C., Browning, M. K., Manners, J., & Wood, N. (2017). Results from a set of three-dimensional numerical experiments of a hot Jupiter atmosphere. *Astronomy & Astrophysics*, *604*, A79. https://doi.org/10.1051/0004-6361/201730465

Mayor, M., & Queloz, D. (1995). A Jupiter-mass companion to a solar-type star. *nat*, *378*(6555), 355–359. https://doi.org/10.1038/378355a0

McCaul, E. W., Goodman, S. J., LaCasse, K. M., & Cecil, D. J. (2009). Forecasting Lightning Threat Using Cloud-Resolving Model Simulations. *Weather and Forecasting*, *24*(3), 709–729. https://doi.org/10.1175/2008WAF2222152.1

Meadows, V. S., & Barnes, R. K. (2018). Factors Affecting Exoplanet Habitability. In H. J. Deeg & J. A. Belmonte (Eds.), *Handbook of Exoplanets* (pp. 2771–2794). Springer International Publishing. https://doi.org/10.1007/978-3-319-55333-7_57

Merlis, T. M., & Schneider, T. (2010). Atmospheric Dynamics of Earth-Like Tidally Locked Aquaplanets. *Journal of Advances in Modeling Earth Systems*, *2*(4). https://doi.org/10.3894/JAMES.2010.2.13

Mettler, J.-N., Quanz, S. P., Helled, R., Olson, S. L., & Schwieterman, E. W. (2022, October). *Earth as an Exoplanet: II. Earth's Time-Variable Thermal Emission and its Atmospheric Seasonality of Bio-Indicators* (tech. rep.). Retrieved October 12, 2022, from https://ui.adsabs.harvard.edu/abs/2022arXiv221005414M

Mettler, J.-N., Quanz, S. P., Helled, R., Olson, S. L., & Schwieterman, E. W. (2023). Earth as an Exoplanet. II. Earth's Time-variable Thermal Emission and Its Atmospheric Seasonality of Bioindicators. *The Astrophysical Journal*, *946*(2), 82. https://doi.org/10.3847/1538-4357/acbe3c

Mettler, J.-N., Konrad, B. S., Quanz, S. P., & Helled, R. (2024). Earth as an Exoplanet. III. Using Empirical Thermal Emission Spectra as an Input for Atmospheric Retrieval of an Earth-twin Exoplanet. *The Astrophysical Journal*, *963*(1), 24. https://doi.org/10.3847/1538-4357/ad198b

Miller, S. L. (1953). A Production of Amino Acids under Possible Primitive Earth Conditions. *Science, New Series*, *117*(3046), 528–529. http://www.jstor.org/stable/1680569

Miyazaki, K., Eskes, H. J., Sudo, K., & Zhang, C. (2014). Global lightning NO_x production estimated by an assimilation of multiple satellite data sets. *Atmospheric Chemistry and Physics*, *14*(7), 3277–3305. https://doi.org/10.5194/acp-14-3277-2014

Moran, S. E., Stevenson, K. B., Sing, D. K., MacDonald, R. J., Kirk, J., Lustig-Yaeger, J., Peacock, S., Mayorga, L. C., Bennett, K. A., López-Morales, M., May, E. M., Rustamkulov, Z., Valenti, J. A., Redai, J. I. A., Alam, M. K., Batalha, N. E., Fu, G., Gonzalez-Quiles, J., Highland, A. N., ... Wakeford, H. R. (2023). High Tide or Riptide on the Cosmic Shoreline? A Water-rich Atmosphere or Stellar Contamination for the Warm Super-Earth GJ 486b from JWST Observations. *The Astrophysical Journal Letters*, *948*(1), L11. https://doi.org/10.3847/2041-8213/accb9c

Mordasini, C., Alibert, Y., Benz, W., & Naef, D. (2009). Extrasolar planet population synthesis - II. Statistical comparison with observations. *Astronomy & Astrophysics*, *501*(3), 1161–1184. https://doi.org/10.1051/0004-6361/200810697

Morgenstern, O., Braesicke, P., O'Connor, F. M., Bushell, A. C., Johnson, C. E., Osprey, S. M., & Pyle, J. A. (2009). Evaluation of the new UKCA climate-composition model – Part 1: The stratosphere. *Geoscientific Model Development*, *2*(1), 43–57. https://doi.org/ https://doi.org/10.5194/gmd-2-43-2009

Moses, J. I. (2014). Chemical kinetics on extrasolar planets. *Philosophical Transactions of the Royal Society A: Mathematical, Physical and Engineering Sciences*, *372*(2014), 20130073. https://doi.org/10.1098/rsta.2013.0073

Mueller, M. (1995). Equation of Time - Problem in Astronomy. *Acta Physica Polonica A 88 Supplement*, *S-49*.

Murray, L. T. (2016). Lightning NOxand Impacts on Air Quality. *Current Pollution Reports*, *2*(2), 115–133. https://doi.org/10.1007/s40726-016-0031-7

Nakajima, S., Hayashi, Y.-Y., & Abe, Y. (1992). A Study on the "Runaway Greenhouse Effect" with a One-Dimensional Radiative–Convective Equilibrium Model. *Journal of the Atmospheric Sciences*, *49*(23), 2256–2266. https://doi.org/10.1175/1520-0469(1992)049<2256:ASOTGE>2.0.CO;2

Navarro-González, R., McKay, C. P., & Mvondo, D. N. (2001). A possible nitrogen crisis for Archaean life due to reduced nitrogen fixation by lightning. *Nature*, *412*(6842), 61–64. https://doi.org/10.1038/35083537

Neu, J. L., Prather, M. J., & Penner, J. E. (2007). Global atmospheric chemistry: Integrating over fractional cloud cover. *Journal of Geophysical Research: Atmospheres*, *112*(D11). https://doi.org/https://doi.org/10.1029/2006JD008007

Nixon, M. C., & Madhusudhan, N. (2022). Aura-3D: A Three-dimensional Atmospheric Retrieval Framework for Exoplanet Transmission Spectra. *The Astrophysical Journal*, *935*(2), 73. https://doi.org/10.3847/1538-4357/ac7c09

Nna Mvondo, D., Navarro-González, R., McKay, C. P., Coll, P., & Raulin, F. (2001). Production of nitrogen oxides by lightning and coronae discharges in simulated early earth, venus and mars environments. *Advances in Space Research*, *27*(2), 217–223. https://doi.org/10.1016/S0273-1177(01)00050-3

Noda, S., Ishiwatari, M., Nakajima, K., Takahashi, Y. O., Takehiro, S., Onishi, M., Hashimoto, G. L., Kuramoto, K., & Hayashi, Y. .-. (2017). The circulation pattern and day-night heat transport in the atmosphere of a synchronously rotating aquaplanet: Dependence on planetary rotation rate. *Icarus*, *282*, 1–18. https://doi.org/10.1016/j.icarus.2016.09.004

Noyelles, B., Frouard, J., Makarov, V. V., & Efroimsky, M. (2014). Spin–orbit evolution of Mercury revisited. *Icarus*, *241*, 26–44. https://doi.org/10.1016/j.icarus.2014.05.045

O'Connor, F. M., Johnson, C. E., Morgenstern, O., Abraham, N. L., Braesicke, P., Dalvi, M., Folberth, G. A., Sanderson, M. G., Telford, P. J., Voulgarakis, A., Young, P. J., Zeng, G., Collins, W. J., & Pyle, J. A. (2014). Evaluation of the new UKCA climate-composition model – Part 2: The Troposphere. *Geoscientific Model Development*, *7*(1), 41–91. https://doi.org/10.5194/gmd-7-41-2014

Olson, S. L., Schwieterman, E. W., Reinhard, C. T., Ridgwell, A., Kane, S. R., Meadows, V. S., & Lyons, T. W. (2018). Atmospheric Seasonality as an Exoplanet Biosignature. *The Astrophysical Journal Letters*, *858*(2), L14. https://doi.org/10.3847/2041-8213/aac171

O'Malley-James, J. T., & Kaltenegger, L. (2017). UV surface habitability of the TRAPPIST-1 system. *Monthly Notices of the Royal Astronomical Society: Letters*, *469*(1), L26–L30. https://doi.org/10.1093/mnrasl/slx047

Owen, J. E., & Wu, Y. (2013). KEPLER PLANETS: A TALE OF EVAPORATION. *The Astrophysical Journal*, *775*(2), 105. https://doi.org/10.1088/0004-637X/775/2/105

Owens, A. J., Hales, C. H., Filkin, D. L., Miller, C., Steed, J. M., & Jesson, J. P. (1985). A coupled one-dimensional radiative-convective, chemistry-transport model of the atmosphere: 1. Model structure and steady state perturbation calculations. *Journal of Geophysical Research: Atmospheres*, *90*(D1), 2283–2311. https://doi.org/10.1029/JD090iD01p02283

Paradise, A., Fan, B. L., Menou, K., & Lee, C. (2021). Climate diversity in the solar-like habitable zone due to varying background gas pressure. *Icarus*, *358*, 114301. https://doi.org/10.1016/j.icarus.2020.114301

Parmentier, V., Showman, A. P., & Lian, Y. (2013). 3D mixing in hot Jupiters atmospheres - I. Application to the day/night cold trap in HD 209458b. *Astronomy & Astrophysics*, *558*, A91. https://doi.org/10.1051/0004-6361/201321132

Pearce, B. K. D., Pudritz, R. E., Semenov, D. A., & Henning, T. K. (2017). Origin of the RNA world: The fate of nucleobases in warm little ponds. *Proceedings of the National Academy of Sciences*, *114*(43), 11327–11332. https://doi.org/10.1073/pnas.1710339114

Pearce, B. K. D., Molaverdikhani, K., Pudritz, R. E., Henning, T., & Cerrillo, K. E. (2022). Toward RNA Life on Early Earth: From Atmospheric HCN to Biomolecule Production in Warm Little Ponds [Publisher: The American Astronomical Society]. *The Astrophysical Journal*, *932*(1), 9. https://doi.org/10.3847/1538-4357/ac47a1

Petigura, E. A., Howard, A. W., & Marcy, G. W. (2013). Prevalence of Earth-size planets orbiting Sun-like stars. *Proceedings of the National Academy of Sciences*, *110*(48), 19273–19278. https://doi.org/10.1073/pnas.1319909110

Piaulet, C., Benneke, B., Almenara, J. M., Dragomir, D., Knutson, H. A., Thorngren, D., Peterson, M. S., Crossfield, I. J. M., M. -R. Kempton, E., Kubyshkina, D., Howard, A. W., Angus, R., Isaacson, H., Weiss, L. M., Beichman, C. A., Fortney, J. J., Fossati, L., Lammer, H., McCullough, P. R., ... Wong, I. (2023). Evidence for the volatile-rich composition of a 1.5-Earth-radius planet. *Nature Astronomy*, *7*(2), 206–222. https://doi.org/10.1038/s41550-022-01835-4

Pierrehumbert, R. T. (2010a). A Palette of Climates for Gliese 581g. *The Astrophysical Journal*, *726*(1), L8. https://doi.org/10.1088/2041-8205/726/1/L8

Pierrehumbert, R. T. (2010b, December). *Principles of Planetary Climate*. Cambridge University Press.

Pierrehumbert, R. T., & Hammond, M. (2019). Atmospheric Circulation of Tide-Locked Exoplanets. *Annual Review of Fluid Mechanics*, *51*(1), 275–303. https://doi.org/10.1146/annurev-fluid-010518-040516

Pluriel, W. (2023). Hot Exoplanetary Atmospheres in 3D. *Remote Sensing*, *15*(3). https://doi.org/https://doi.org/10.3390/rs15030635

Pont, F., Sing, D. K., Gibson, N. P., Aigrain, S., Henry, G., & Husnoo, N. (2013). The prevalence of dust on the exoplanet HD 189733b from Hubble and Spitzer observations. *Monthly Notices of the Royal Astronomical Society*, *432*(4), 2917–2944. https://doi.org/10.1093/mnras/stt651

Price, C., & Rind, D. (1992). A simple lightning parameterization for calculating global lightning distributions. *Journal of Geophysical Research: Atmospheres*, *97*(D9), 9919–9933. https://doi.org/https://doi.org/10.1029/92JD00719

Price, C., & Rind, D. (1993). What determines the cloud-to-ground lightning fraction in thunderstorms? *Geophysical Research Letters*, *20*(6), 463–466. https://doi.org/10.1029/93GL00226

Price, C., & Rind, D. (1994). Modeling Global Lightning Distributions in a General Circulation Model. *Monthly Weather Review*, *122*(8), 1930–1939. https://doi.org/10.1175/1520-0493(1994)122<1930:MGLDIA>2.0.CO;2

Proedrou, E., & Hocke, K. (2016). Characterising the three-dimensional ozone distribution of a tidally locked Earth-like planet. *Earth, Planets and Space*, *68*(1), 96. https://doi.org/10.1186/s40623-016-0461-x

Proedrou, E., Hocke, K., & Wurz, P. (2016). The middle atmospheric circulation of a tidally locked Earth-like planet and the role of the sea surface temperature. *Progress in Earth and Planetary Science*, *3*(1), 22. https://doi.org/10.1186/s40645-016-0098-1

Quanz, S. P., Ottiger, M., Fontanet, E., Kammerer, J., Menti, F., Dannert, F., Gheorghe, A., Absil, O., Airapetian, V. S., Alei, E., Allart, R., Angerhausen, D., Blumenthal, S., Buchhave, L. A., Cabrera, J., Carrión-González, Ó., Chauvin, G., Danchi, W. C., Dandumont, C., ... Wyatt, M. C. (2022). Large Interferometer For Exoplanets (LIFE) - I. Improved exoplanet detection yield estimates for a large mid-infrared space-interferometer mission. *Astronomy & Astrophysics*, *664*, A21. https://doi.org/10.1051/0004-6361/202140366

Rackham, B. V., Apai, D., & Giampapa, M. S. (2018). The Transit Light Source Effect: False Spectral Features and Incorrect Densities for M-dwarf Transiting Planets. *The Astrophysical Journal*, *853*(2), 122. https://doi.org/10.3847/1538-4357/aaa08c

Rakov, V. A., & Uman, M. A. (2003, August). *Lightning: Physics and Effects*. Cambridge University Press.

Ramanathan, V., Callis, L., Cess, R., Hansen, J., Isaksen, I., Kuhn, W., Lacis, A., Luther, F., Mahlman, J., Reck, R., & Schlesinger, M. (1987). Climate-chemical interactions and effects of changing atmospheric trace gases. *Reviews of Geophysics*, *25*(7), 1441–1482. https://doi.org/10.1029/RG025i007p01441

Renaud, J. P., Henning, W. G., Saxena, P., Neveu, M., Bagheri, A., Mandell, A., & Hurford, T. (2021). Tidal Dissipation in Dual-body, Highly Eccentric, and Nonsynchronously Rotating Systems: Applications to Pluto–Charon and the Exoplanet TRAPPIST-1e. *The Planetary Science Journal*, *2*(1), 4. https://doi.org/10.3847/PSJ/abc0f3

Ribas, I., Guinan, E. F., Güdel, M., & Audard, M. (2005). Evolution of the Solar Activity over Time and Effects on Planetary Atmospheres. I. High-Energy Irradiances (1-1700 å). *The Astrophysical Journal*, *622*(1), 680. https://doi.org/10.1086/427977

Ribas, I., Bolmont, E., Selsis, F., Reiners, A., Leconte, J., Raymond, S. N., Engle, S. G., Guinan, E. F., Morin, J., Turbet, M., Forget, F., & Anglada-Escudé, G. (2016). The habitability of Proxima Centauri b - I. Irradiation, rotation and volatile inventory from formation to the present. *Astronomy & Astrophysics*, *596*, A111. https://doi.org/10.1051/0004-6361/201629576

Ribas, I., Gregg, M. D., Boyajian, T. S., & Bolmont, E. (2017). The full spectral radiative properties of Proxima Centauri. *Astronomy & Astrophysics*, *603*, A58. https://doi.org/10.1051/0004-6361/201730582

Ridgway, R. J., Zamyatina, M., Mayne, N. J., Manners, J., Lambert, F. H., Braam, M., Drummond, B., Hébrard, E., Palmer, P. I., & Kohary, K. (2023). 3D modelling of the impact of stellar activity on tidally locked terrestrial exoplanets: Atmospheric composition and habitability. *Monthly Notices of the Royal Astronomical Society*, *518*(2), 2472–2496. https://doi.org/10.1093/mnras/stac3105

Rimmer, P. B., & Helling, C. (2016). A CHEMICAL KINETICS NETWORK FOR LIGHTNING AND LIFE IN PLANETARY ATMOSPHERES. *The Astrophysical Journal Supplement Series*, *224*(1), 9. https://doi.org/10.3847/0067-0049/224/1/9

Rimmer, P. B., & Rugheimer, S. (2019). Hydrogen cyanide in nitrogen-rich atmospheres of rocky exoplanets. *Icarus*, *329*, 124–131. https://doi.org/10.1016/j.icarus.2019.02.020

Rio, C., Del Genio, A. D., & Hourdin, F. (2019). Ongoing Breakthroughs in Convective Parameterization. *Current Climate Change Reports*, *5*(2), 95–111. https://doi.org/10.1007/s40641-019-00127-w

Rogers, L. A. (2015). MOST 1.6 EARTH-RADIUS PLANETS ARE NOT ROCKY. *The Astrophysical Journal*, *801*(1), 41. https://doi.org/10.1088/0004-637X/801/1/41

Rugheimer, S., Kaltenegger, L., Segura, A., Linsky, J., & Mohanty, S. (2015a). EFFECT OF UV RADIATION ON THE SPECTRAL FINGERPRINTS OF EARTH-LIKE PLANETS ORBITING M STARS. *The Astrophysical Journal*, *809*(1), 57. https://doi.org/10.1088/0004-637X/809/1/57

Rugheimer, S., Segura, A., Kaltenegger, L., & Sasselov, D. (2015b). UV SURFACE ENVIRONMENT OF EARTH-LIKE PLANETS ORBITING FGKM STARS THROUGH GEOLOGICAL EVOLUTION [Publisher: The American Astronomical Society]. *The Astrophysical Journal*, *806*(1), 137. https://doi.org/10.1088/0004-637X/806/1/137

Rugheimer, S., Kaltenegger, L., Zsom, A., Segura, A., & Sasselov, D. (2013). Spectral Fingerprints of Earth-like Planets Around FGK Stars. *Astrobiology*, *13*(3), 251–269. https://doi.org/10.1089/ast.2012.0888

Rushby, A. J., Shields, A. L., Wolf, E. T., Laguë, M., & Burgasser, A. (2020). The Effect of Land Albedo on the Climate of Land-dominated Planets in the TRAPPIST-1 System. *The Astrophysical Journal*, *904*(2), 124. https://doi.org/10.3847/1538-4357/abbe04

Sagan, C., Thompson, W. R., Carlson, R., Gurnett, D., & Hord, C. (1993). A search for life on Earth from the Galileo spacecraft. *Nature*, *365*(6448), 715–721. https://doi.org/10.1038/365715a0

Sander, R., & Crutzen, P. J. (1996). Model study indicating halogen activation and ozone destruction in polluted air masses transported to the sea. *Journal of Geophysical Research: Atmospheres*, *101*(D4), 9121–9138. https://doi.org/10.1029/95JD03793

Sanghi, A., Liu, M. C., Best, W. M. J., Dupuy, T. J., Siverd, R. J., Zhang, Z., Hurt, S. A., Magnier, E. A., Aller, K. M., & Deacon, N. R. (2023). The Hawaii Infrared Parallax Program. VI. The Fundamental Properties of 1000+ Ultracool Dwarfs and Planetary-mass Objects Using Optical to Mid-infrared Spectral Energy Distributions and Comparison to BT-Settl and ATMO 2020 Model Atmospheres [Publisher: The American Astronomical Society]. *The Astrophysical Journal*, *959*(1), 63. https://doi.org/10.3847/1538-4357/acff66

Scalo, J., Kaltenegger, L., Segura, A., Fridlund, M., Ribas, I., Kulikov, Y. N., Grenfell, J. L., Rauer, H., Odert, P., Leitzinger, M., Selsis, F., Khodachenko, M. L., Eiroa, C., Kasting, J., & Lammer, H. (2007). M Stars as Targets for Terrestrial Exoplanet Searches And Biosignature Detection. *Astrobiology*, *7*(1), 85–166. https://doi.org/10.1089/ast.2006.0125

Scheucher, M., Grenfell, J. L., Wunderlich, F., Godolt, M., Schreier, F., & Rauer, H. (2018). New Insights into Cosmic-Ray-induced Biosignature Chemistry in Earth-like Atmospheres. *The Astrophysical Journal*, *863*(1), 6. https://doi.org/10.3847/1538-4357/aacf03

Schlichting, H. E., & Mukhopadhyay, S. (2018). Atmosphere Impact Losses. *Space Science Reviews*, *214*(1), 34. https://doi.org/10.1007/s11214-018-0471-z

Schubert, W. H., Rozoff, C. M., Vigh, J. L., McNoldy, B. D., & Kossin, J. P. (2007). On the distribution of subsidence in the hurricane eye. *Quarterly Journal of the Royal Meteorological Society*, *133*(624), 595–605. https://doi.org/10.1002/qj.49

Schumann, U., & Huntrieser, H. (2007). The global lightning-induced nitrogen oxides source. *Atmospheric Chemistry and Physics*, *7*(14), 3823–3907. https://doi.org/10.5194/acp-7-3823-2007

Schwieterman, E. W., Kiang, N. Y., Parenteau, M. N., Harman, C. E., DasSarma, S., Fisher, T. M., Arney, G. N., Hartnett, H. E., Reinhard, C. T., Olson, S. L., Meadows, V. S., Cockell, C. S., Walker, S. I., Grenfell, J. L., Hegde, S., Rugheimer, S., Hu, R., & Lyons, T. W. (2018). Exoplanet Biosignatures: A Review of Remotely Detectable Signs of Life. *Astrobiology*, *18*(6), 663–708. https://doi.org/10.1089/ast.2017.1729

Seager, S., & Sasselov, D. D. (2000). Theoretical Transmission Spectra during Extrasolar Giant Planet Transits. *apj*, *537*(2), 916–921. https://doi.org/10.1086/309088

Seager, S., Bains, W., & Hu, R. (2013). BIOSIGNATURE GASES IN H2-DOMINATED ATMOSPHERES ON ROCKY EXOPLANETS. *The Astrophysical Journal*, 19.

Seager, S. (2013). Exoplanet Habitability. *Science*, *340*(6132), 577–581. https://doi.org/10.1126/science.1232226

Segura, A., Krelove, K., Kasting, J. F., Sommerlatt, D., Meadows, V., Crisp, D., Cohen, M., & Mlawer, E. (2003). Ozone Concentrations and Ultraviolet Fluxes on Earth-Like Planets Around Other Stars. *Astrobiology*, *3*(4), 689–708. https://doi.org/10.1089/153110703322736024

Segura, A., Kasting, J. F., Meadows, V., Cohen, M., Scalo, J., Crisp, D., Butler, R. A., & Tinetti, G. (2005). Biosignatures from Earth-Like Planets Around M Dwarfs. *Astrobiology*, *5*(6), 706–725. https://doi.org/10.1089/ast.2005.5.706

Segura, A., Walkowicz, L. M., Meadows, V., Kasting, J., & Hawley, S. (2010). The Effect of a Strong Stellar Flare on the Atmospheric Chemistry of an Earth-like Planet Orbiting an M Dwarf. *Astrobiology*, *10*(7), 751–771. https://doi.org/10.1089/ast.2009.0376

Seinfeld, J. H., & Pandis, S. N. (2016, April). *Atmospheric Chemistry and Physics: From Air Pollution to Climate Change*. John Wiley & Sons.

Selsis, F., Despois, D., & Parisot, J.-P. (2002). Signature of life on exoplanets: Can darwin produce false positive detections? *Astronomy & Astrophysics*, *388*(3), 985–1003. https://doi.org/10.1051/0004-6361:20020527

Selsis, F., Kasting, J. F., Levrard, B., Paillet, J., Ribas, I., & Delfosse, X. (2007). Habitable planets around the star Gliese 581? *Astronomy & Astrophysics*, *476*(3), 1373–1387. https://doi.org/10.1051/0004-6361:20078091

Selsis, F., Wordsworth, R. D., & Forget, F. (2011). Thermal phase curves of nontransiting terrestrial exoplanets - I. Characterizing atmospheres. *Astronomy & Astrophysics*, *532*, A1. https://doi.org/10.1051/0004-6361/201116654

Sergeev, D. E., Lambert, F. H., Mayne, N. J., Boutle, I. A., Manners, J., & Kohary, K. (2020). Atmospheric Convection Plays a Key Role in the Climate of Tidally Locked Terrestrial Exoplanets: Insights from High-resolution Simulations. *The Astrophysical Journal*, *894*(2), 84. https://doi.org/10.3847/1538-4357/ab8882

Sergeev, D. E., Lewis, N. T., Lambert, F. H., Mayne, N. J., Boutle, I. A., Manners, J., & Kohary, K. (2022a). Bistability of the Atmospheric Circulation on TRAPPIST-1e. *The Planetary Science Journal*, *3*(9), 214. https://doi.org/10.3847/PSJ/ac83be

Sergeev, D. E., Fauchez, T. J., Turbet, M., Boutle, I. A., Tsigaridis, K., Way, M. J., Wolf, E. T., Domagal-Goldman, S. D., Forget, F., Haqq-Misra, J., Kopparapu, R. K., Lambert, F. H., Manners, J., & Mayne, N. J. (2022b). The TRAPPIST-1 Habitable Atmosphere Intercomparison (THAI). II. Moist Cases—The Two Waterworlds. *The Planetary Science Journal*, *3*(9), 212. https://doi.org/10.3847/PSJ/ac6cf2

Shields, A. L., Meadows, V. S., Bitz, C. M., Pierrehumbert, R. T., Joshi, M. M., & Robinson, T. D. (2013). The Effect of Host Star Spectral Energy Distribution and Ice-Albedo Feedback on the Climate of Extrasolar Planets. *Astrobiology*, *13*(8), 715–739. https://doi.org/10.1089/ast.2012.0961

Shields, A. L., Ballard, S., & Johnson, J. A. (2016). The habitability of planets orbiting M-dwarf stars. *Physics Reports*, *663*, 1–38. https://doi.org/10.1016/j.physrep.2016.10.003

Shine, K. P., Bourqui, M. S., Forster, P. M. d. F., Hare, S. H. E., Langematz, U., Braesicke, P., Grewe, V., Ponater, M., Schnadt, C., Smith, C. A., Haigh, J. D., Austin, J., Butchart, N., Shindell, D. T., Randel, W. J., Nagashima, T., Portmann, R. W., Solomon, S., Seidel, D. J., ... Schwarzkopf, M. D. (2003). A comparison of model-simulated trends in stratospheric temperatures. *Quarterly Journal of the Royal Meteorological Society*, *129*(590), 1565–1588. https://doi.org/10.1256/qj.02.186

Showman, A. P., & Guillot, T. (2002). Atmospheric circulation and tides of "51 Pegasus b-like" planets. *Astronomy & Astrophysics*, *385*, 166–180. https://doi.org/10.1051/0004-6361:20020101

Showman, A. P., & Polvani, L. M. (2010). The Matsuno-Gill model and equatorial superrotation. *Geophysical Research Letters*, *37*(18). https://doi.org/10.1029/2010GL044343

Showman, A. P., & Polvani, L. M. (2011). EQUATORIAL SUPERROTATION ON TIDALLY LOCKED EXOPLANETS. *The Astrophysical Journal*, *738*(1), 71. https://doi.org/10.1088/0004-637X/738/1/71

Showman, A. P., Wordsworth, R. D., Merlis, T. M., & Kaspi, Y. (2013). Atmospheric Circulation of Terrestrial Exoplanets. In *Comparative Climatology of Terrestrial Planets* (Vol. 1). University of Arizona Press. Retrieved May 12, 2021, from https://muse.jhu.edu/chapter/1207491

Simpson, S. G. C. (1928). *Some studies in terrestrial radiation*. Edward Stanford.

Smart, W. M. (1944). *Text-book on Spherical Astronomy*. The University Press.

Snellen, I. A. G., Kok, R. J. d., Poole, R. l., Brogi, M., & Birkby, J. (2013). FINDING EXTRATERRESTRIAL LIFE USING GROUND-BASED HIGH-DISPERSION SPECTROSCOPY. *The Astrophysical Journal*, *764*(2), 182. https://doi.org/10.1088/0004-637X/764/2/182

Snellen, I. A. G., de Kok, R. J., de Mooij, E. J. W., & Albrecht, S. (2010). The orbital motion, absolute mass and high-altitude winds of exoplanet HD 209458b. *Nature*, *465*(7301), 1049–1051. https://doi.org/10.1038/nature09111

Sorteberg, A., & Hov, O. (1996). Two parametrizations of the dry deposition exchange for SO2 and NH3 in a numerical model. *Atmospheric Environment*, *30*(10), 1823–1840. https://doi.org/10.1016/1352-2310(95)00381-9

Sossi, P. A., Burnham, A. D., Badro, J., Lanzirotti, A., Newville, M., & O'Neill, H. S. (2020). Redox state of Earth's magma ocean and its Venus-like early atmosphere. *Science Advances*, *6*(48), eabd1387. https://doi.org/10.1126/sciadv.abd1387

Southworth, J., Mancini, L., Madhusudhan, N., Mollière, P., Ciceri, S., & Henning, T. (2017). Detection of the Atmosphere of the 1.6 $M_{\oplus}$ Exoplanet GJ 1132 b. *The Astronomical Journal*, *153*(4), 191. https://doi.org/10.3847/1538-3881/aa6477

Steinrueck, M. E., Showman, A. P., Lavvas, P., Koskinen, T., Tan, X., & Zhang, X. (2021). 3D simulations of photochemical hazes in the atmosphere of hot Jupiter HD 189733b. *Monthly Notices of the Royal Astronomical Society*, *504*(2), 2783–2799. https://doi.org/10.1093/mnras/stab1053

Stephen H Dole. (1970). *Habitable planets for man*. American Elsevier Publishing Company.

Stevens, D. J., & Gaudi, B. S. (2013). A Posteriori Transit Probabilities. *Publications of the Astronomical Society of the Pacific*, *125*(930), 933. https://doi.org/10.1086/672572

Stolz, D. C., Rutledge, S. A., Pierce, J. R., & van den Heever, S. C. (2017). A global lightning parameterization based on statistical relationships among environmental factors, aerosols, and convective clouds in the TRMM climatology. *Journal of Geophysical Research: Atmospheres*, *122*(14), 7461–7492. https://doi.org/10.1002/2016JD026220

Stolz, D. C., Bilsback, K. R., Pierce, J. R., & Rutledge, S. A. (2021). Evaluating Empirical Lightning Parameterizations in Global Atmospheric Models. *Journal of Geophysical Research: Atmospheres*, *126*(4), e2020JD033695. https://doi.org/10.1029/2020JD033695

Swain, M. R., Estrela, R., Roudier, G. M., Sotin, C., Rimmer, P. B., Valio, A., West, R., Pearson, K., Huber-Feely, N., & Zellem, R. T. (2021). Detection of an Atmosphere on a Rocky Exoplanet. *The Astronomical Journal*, *161*(5), 213. https://doi.org/10.3847/1538-3881/abe879

Tabataba-Vakili, F., Grenfell, J. L., Grießmeier, J.-M., & Rauer, H. (2016). Atmospheric effects of stellar cosmic rays on Earth-like exoplanets orbiting M-dwarfs. *Astronomy & Astrophysics*, *585*, A96. https://doi.org/10.1051/0004-6361/201425602

Teal, D. J., Kempton, E. M.-R., Bastelberger, S., Youngblood, A., & Arney, G. (2022). Effects of UV stellar spectral uncertainty on the chemistry of terrestrial atmospheres. *arXiv:2201.08805 [astro-ph]*. Retrieved January 24, 2022, from http://arxiv.org/abs/2201.08805

Telford, P. J., Abraham, N. L., Archibald, A. T., Braesicke, P., Dalvi, M., Morgenstern, O., O'Connor, F. M., Richards, N. A. D., & Pyle, J. A. (2013). Implementation of the Fast-JX Photolysis scheme (v6.4) into the UKCA component of the MetUM chemistry-climate model (v7.3). *Geoscientific Model Development*, *6*(1), 161–177. https://doi.org/10.5194/gmd-6-161-2013

Tian, F. (2015a). Atmospheric Escape from Solar System Terrestrial Planets and Exoplanets [Publisher: Annual Reviews]. *Annual Review of Earth and Planetary Sciences*, *43*(Volume 43, 2015), 459–476. https://doi.org/10.1146/annurev-earth-060313-054834

Tian, F. (2015b). History of water loss and atmospheric O2 buildup on rocky exoplanets near M dwarfs. *Earth and Planetary Science Letters*, *432*, 126–132. https://doi.org/10.1016/j.epsl.2015.09.051

Tian, F., France, K., Linsky, J. L., Mauas, P. J. D., & Vieytes, M. C. (2014). High stellar FUV/NUV ratio and oxygen contents in the atmospheres of potentially habitable planets. *Earth and Planetary Science Letters*, *385*, 22–27. https://doi.org/10.1016/j.epsl.2013.10.024

Tritscher, I., Pitts, M. C., Poole, L. R., Alexander, S. P., Cairo, F., Chipperfield, M. P., Grooß, J.-U., Höpfner, M., Lambert, A., Luo, B., Molleker, S., Orr, A., Salawitch, R., Snels, M., Spang, R., Woiwode, W., & Peter, T. (2021). Polar Stratospheric Clouds: Satellite Observations, Processes, and Role in Ozone Depletion. *Reviews of Geophysics*, *59*(2), e2020RG000702. https://doi.org/10.1029/2020RG000702

Tsai, S.-M., Malik, M., Kitzmann, D., Lyons, J. R., Fateev, A., Lee, E., & Heng, K. (2021). A Comparative Study of Atmospheric Chemistry with VULCAN. *The Astrophysical Journal*, *923*(2), 264. https://doi.org/10.3847/1538-4357/ac29bc

Turbet, M., Leconte, J., Selsis, F., Bolmont, E., Forget, F., Ribas, I., Raymond, S. N., & Anglada-Escudé, G. (2016). The habitability of Proxima Centauri b - II. Possible climates and observability. *Astronomy & Astrophysics*, *596*, A112. https://doi.org/10.1051/0004-6361/201629577

Turbet, M., Bolmont, E., Leconte, J., Forget, F., Selsis, F., Tobie, G., Caldas, A., Naar, J., & Gillon, M. (2018). Modeling climate diversity, tidal dynamics and the fate of volatiles on TRAPPIST-1 planets. *Astronomy & Astrophysics*, *612*, A86. https://doi.org/10.1051/0004-6361/201731620

Turbet, M., Bolmont, E., Bourrier, V., Demory, B.-O., Leconte, J., Owen, J., & Wolf, E. T. (2020). A Review of Possible Planetary Atmospheres in the TRAPPIST-1 System. *Space Science Reviews*, *216*(5), 100. https://doi.org/10.1007/s11214-020-00719-1

Turbet, M., Fauchez, T. J., Sergeev, D. E., Boutle, I. A., Tsigaridis, K., Way, M. J., Wolf, E. T., Domagal-Goldman, S. D., Forget, F., Haqq-Misra, J., Kopparapu, R. K., Lambert, F. H., Manners, J., Mayne, N. J., & Sohl, L. (2022). The TRAPPIST-1 Habitable Atmosphere Intercomparison (THAI). I. Dry Cases—The Fellowship of the GCMs. *The Planetary Science Journal*, *3*(9), 211. https://doi.org/10.3847/PSJ/ac6cf0

Vallis, G. K. (2017, June). *Atmospheric and Oceanic Fluid Dynamics*. Cambridge University Press.

Vasavada, A. R., & Showman, A. P. (2005). Jovian atmospheric dynamics: An update after Galileo and Cassini. *Reports on Progress in Physics*, *68*(8), 1935. https://doi.org/10.1088/0034-4885/68/8/R06

Vaughan, S. R., Birkby, J. L., Thatte, N., Carlotti, A., Houllé, M., Pereira-Santaella, M., Clarke, F., Vigan, A., Lin, Z., & Kaltenegger, L. (2024). Behind the mask: Can HARMONI@ELT detect biosignatures in the reflected light of Proxima b? *Monthly Notices of the Royal Astronomical Society*, *528*(2), 3509–3522. https://doi.org/10.1093/mnras/stae242

Villanueva, G. L., Smith, M. D., Protopapa, S., Faggi, S., & Mandell, A. M. (2018). Planetary Spectrum Generator: An accurate online radiative transfer suite for atmospheres, comets, small bodies and exoplanets. *Journal of Quantitative Spectroscopy and Radiative Transfer*, *217*, 86–104. https://doi.org/10.1016/j.jqsrt.2018.05.023

Villanueva, G. L., Liuzzi, G., Faggi, S., Protopapa, S., Kofman, V., Fauchez, T., Stone, S. W., & Mandell, A. M. (2022, January). *Fundamentals of the Planetary Spectrum Generator*. Retrieved April 28, 2022, from https://ui.adsabs.harvard.edu/abs/2022fpsg.book.....V

von Glasow, R., Bobrowski, N., & Kern, C. (2009). The effects of volcanic eruptions on atmospheric chemistry. *Chemical Geology*, *263*(1), 131–142. https://doi.org/10.1016/j.chemgeo.2008.08.020

Vonnegut, B. (1963). Some Facts and Speculations Concerning the Origin and Role of Thunderstorm Electricity. In D. Atlas, D. R. Booker, H. Byers, R. H. Douglas, T. Fujita, D. C. House, F. H. Ludlum, J. S. Malkus, C. W. Newton, Y. Ogura, R. A. Schleusener, B. Vonnegut & R. T. Williams (Eds.), *Severe Local Storms* (pp. 224–241). American Meteorological Society. https://doi.org/10.1007/978-1-940033-56-3_11

Walker, J. C. G., Hays, P. B., & Kasting, J. F. (1981). A negative feedback mechanism for the long-term stabilization of Earth's surface temperature. *Journal of Geophysical Research: Oceans*, *86*(C10), 9776–9782. https://doi.org/https://doi.org/10.1029/JC086iC10p09776

Walters, D., Baran, A. J., Boutle, I., Brooks, M., Earnshaw, P., Edwards, J., Furtado, K., Hill, P., Lock, A., Manners, J., Morcrette, C., Mulcahy, J., Sanchez, C., Smith, C., Stratton, R., Tennant, W., Tomassini, L., Van Weverberg, K., Vosper, S., ... Zerroukat, M. (2019). The Met Office Unified Model Global Atmosphere 7.0/7.1 and JULES Global Land 7.0 configurations. *Geoscientific Model Development*, *12*(5), 1909–1963. https://doi.org/https://doi.org/10.5194/gmd-12-1909-2019

Wang, S., & Yang, J. (2022). Atmospheric Overturning Circulation on Dry, Tidally Locked Rocky Planets Is Mainly Driven by Radiative Cooling. *The Planetary Science Journal*, *3*(7), 171. https://doi.org/10.3847/PSJ/ac6d65

Webster, C. R., Mahaffy, P. R., Atreya, S. K., Moores, J. E., Flesch, G. J., Malespin, C., McKay, C. P., Martinez, G., Smith, C. L., Martin-Torres, J., Gomez-Elvira, J., Zorzano, M.-P., Wong, M. H., Trainer, M. G., Steele, A., Archer, D., Sutter, B., Coll, P. J., Freissinet, C., ... Vasavada, A. R. (2018). Background levels of methane in Mars' atmosphere show strong seasonal variations. *Science*, *360*(6393), 1093–1096. https://doi.org/10.1126/science.aaq0131

White, A. A., & Bromley, R. A. (1995). Dynamically consistent, quasi-hydrostatic equations for global models with a complete representation of the Coriolis force. *Quarterly Journal of the Royal Meteorological Society*, *121*(522), 399–418. https://doi.org/10.1002/qj.49712152208

White, A. A., Hoskins, B. J., Roulstone, I., & Staniforth, A. (2005). Consistent approximate models of the global atmosphere: Shallow, deep, hydrostatic, quasi-hydrostatic and non-hydrostatic. *Quarterly Journal of the Royal Meteorological Society*, *131*(609), 2081–2107. https://doi.org/10.1256/qj.04.49

Wild, O., & Prather, M. J. (2000). Excitation of the primary tropospheric chemical mode in a global three-dimensional model. *Journal of Geophysical Research: Atmospheres*, *105*(D20), 24647–24660. https://doi.org/10.1029/2000JD900399

Wild, O., Zhu, X., & Prather, M. J. (2000). Fast-J: Accurate Simulation of In- and Below-Cloud Photolysis in Tropospheric Chemical Models. *Journal of Atmospheric Chemistry*, *37*(3), 245–282. https://doi.org/10.1023/A:1006415919030

Williams, D. M., & Pollard, D. (2002). Earth-like worlds on eccentric orbits: Excursions beyond the habitable zone. *International Journal of Astrobiology*, *1*(1), 61–69. https://doi.org/10.1017/S1473550402001064

Williams, E., & Stanfill, S. (2002). The physical origin of the land–ocean contrast in lightning activity. *Comptes Rendus Physique*, *3*(10), 1277–1292. https://doi.org/10.1016/S1631-0705(02)01407-X

Williams, E., Chan, T., & Boccippio, D. (2004). Islands as miniature continents: Another look at the land-ocean lightning contrast. *Journal of Geophysical Research: Atmospheres*, *109*(D16). https://doi.org/10.1029/2003JD003833

Williams, E. R. (1985). Large-scale charge separation in thunderclouds. *Journal of Geophysical Research: Atmospheres*, *90*(D4), 6013–6025. https://doi.org/https://doi.org/10.1029/JD090iD04p06013

Wilson, D. R., & Ballard, S. P. (1999). A microphysically based precipitation scheme for the UK meteorological office unified model. *Quarterly Journal of the Royal Meteorological Society*, *125*(557), 1607–1636. https://doi.org/10.1002/qj.49712555707

Wilson, D. R., Bushell, A. C., Kerr-Munslow, A. M., Price, J. D., & Morcrette, C. J. (2008). PC2: A prognostic cloud fraction and condensation scheme. I: Scheme description. *Quarterly Journal of the Royal Meteorological Society*, *134*(637), 2093–2107. https://doi.org/https://doi.org/10.1002/qj.333

Wilson, D. J., Froning, C. S., Duvvuri, G. M., France, K., Youngblood, A., Schneider, P. C., Berta-Thompson, Z., Brown, A., Buccino, A. P., Hawley, S., Irwin, J., Kaltenegger, L., Kowalski, A., Linsky, J., Loyd, R. O. P., Miguel, Y., Pineda, J. S., Redfield, S., Roberge, A., … Vieytes, M. (2021). The Mega-MUSCLES Spectral Energy Distribution of TRAPPIST-1. *The Astrophysical Journal*, *911*(1), 18. https://doi.org/10.3847/1538-4357/abe771

Woitke, P., Helling, C., Hunter, G. H., Millard, J. D., Turner, G. E., Worters, M., Blecic, J., & Stock, J. W. (2018). Equilibrium chemistry down to 100 K. Impact of silicates and phyllosilicates on the carbon to oxygen ratio. *aap*, *614*, A1. https://doi.org/10.1051/0004-6361/201732193

Wolf, E. T. (2017). Assessing the Habitability of the TRAPPIST-1 System Using a 3D Climate Model. *The Astrophysical Journal Letters*, *839*(1), L1. https://doi.org/10.3847/2041-8213/aa693a

Wolf, E. T., Shields, A. L., Kopparapu, R. K., Haqq-Misra, J., & Toon, O. B. (2017). Constraints on Climate and Habitability for Earth-like Exoplanets Determined from a General Circulation Model. *The Astrophysical Journal*, *837*(2), 107. https://doi.org/10.3847/1538-4357/aa5ffc

Wolf, E. T., Kopparapu, R., Haqq-Misra, J., & Fauchez, T. J. (2022). ExoCAM: A 3D Climate Model for Exoplanet Atmospheres [Publisher: IOP Publishing]. *The Planetary Science Journal*, *3*(1), 7. https://doi.org/10.3847/PSJ/ac3f3d

Wolszczan, A., & Frail, D. A. (1992). A planetary system around the millisecond pulsar PSR1257 + 12. *Nature*, *355*(6356), 145–147. https://doi.org/10.1038/355145a0

Wood, N., Staniforth, A., White, A., Allen, T., Diamantakis, M., Gross, M., Melvin, T., Smith, C., Vosper, S., Zerroukat, M., & Thuburn, J. (2014). An inherently mass-conserving semi-implicit semi-Lagrangian discretization of the deep-atmosphere global non-hydrostatic equations. *Quarterly Journal of the Royal Meteorological Society*, *140*(682), 1505–1520. https://doi.org/https://doi.org/10.1002/qj.2235

Wordsworth, R., Schaefer, L. K., & Fischer, R. A. (2018). Redox Evolution via Gravitational Differentiation on Low-mass Planets: Implications for Abiotic Oxygen, Water Loss, and Habitability. *The Astronomical Journal*, *155*, 195. https://doi.org/10.3847/1538-3881/aab608

Wordsworth, R. (2015). ATMOSPHERIC HEAT REDISTRIBUTION AND COLLAPSE ON TIDALLY LOCKED ROCKY PLANETS. *The Astrophysical Journal*, *806*(2), 180. https://doi.org/10.1088/0004-637X/806/2/180

Wordsworth, R., & Pierrehumbert, R. (2014). ABIOTIC OXYGEN-DOMINATED ATMOSPHERES ON TERRESTRIAL HABITABLE ZONE PLANETS. *The Astrophysical Journal Letters*, *785*(2), L20. https://doi.org/10.1088/2041-8205/785/2/L20

Wordsworth, R., & Kreidberg, L. (2022). Atmospheres of Rocky Exoplanets. *Annual Review of Astronomy and Astrophysics*, *60*(1), 159–201. https://doi.org/10.1146/annurev-astro-052920-125632

Yang, J., Cowan, N. B., & Abbot, D. S. (2013). STABILIZING CLOUD FEEDBACK DRAMATICALLY EXPANDS THE HABITABLE ZONE OF TIDALLY LOCKED PLANETS. *The Astrophysical Journal*, *771*(2), L45. https://doi.org/10.1088/2041-8205/771/2/L45

Yang, J., & Abbot, D. S. (2014). A LOW-ORDER MODEL OF WATER VAPOR, CLOUDS, AND THERMAL EMISSION FOR TIDALLY LOCKED TERRESTRIAL PLANETS. *The Astrophysical Journal*, *784*(2), 155. https://doi.org/10.1088/0004-637X/784/2/155

Yang, J., Leconte, J., Wolf, E. T., Goldblatt, C., Feldl, N., Merlis, T., Wang, Y., Koll, D. D. B., Ding, F., Forget, F., & Abbot, D. S. (2016). Differences in Water Vapor Radiative Transfer among 1D Models Can Significantly Affect the Inner Edge of the Habitable Zone [Publisher: IOP ADS Bibcode: 2016ApJ...826..222Y]. *The Astrophysical Journal*, *826*, 222. https://doi.org/10.3847/0004-637X/826/2/222

Yates, J. S., Palmer, P. I., Manners, J., Boutle, I., Kohary, K., Mayne, N., & Abraham, L. (2020). Ozone chemistry on tidally locked M dwarf planets. *Monthly Notices of the Royal Astronomical Society*, *492*(2), 1691–1705. https://doi.org/10.1093/mnras/stz3520

Young, A. T. (1973). Are the clouds of venus sulfuric acid? *Icarus*, *18*(4), 564–582. https://doi.org/10.1016/0019-1035(73)90059-6

Youngblood, A., France, K., Loyd, R. O. P., Linsky, J. L., Redfield, S., Schneider, P. C., Wood, B. E., Brown, A., Froning, C., Miguel, Y., Rugheimer, S., & Walkowicz, L. (2016). The MUSCLES Treasury Survey. II. Intrinsic LY-alpha and Extreme Ultraviolet Spectra of K and M Dwarfs with Exoplanets*. *The Astrophysical Journal*, *824*, 101. https://doi.org/10.3847/0004-637X/824/2/101

Yung, Y. L., Allen, M., & Pinto, J. P. (1984). Photochemistry of the atmosphere of Titan: Comparison between model and observations. *Astrophysical Journal Supplement Series*, *55*(3), 465–506. Retrieved April 28, 2022, from https://resolver.caltech.edu/CaltechAUTHORS:20140909-090508298

Yung, Y. L., & DeMore, W. B. (1999). *Photochemistry of Planetary Atmospheres*. Oxford University Press.

Zahnle, K. J. (1986). Photochemistry of methane and the formation of hydrocyanic acid (HCN) in the Earth's early atmosphere. *Journal of Geophysical Research: Atmospheres*, *91*(D2), 2819–2834. https://doi.org/10.1029/JD091iD02p02819

Zahnle, K. J., & Walker, J. C. G. (1982). The evolution of solar ultraviolet luminosity. *Reviews of Geophysics*, *20*(2), 280–292. https://doi.org/10.1029/RG020i002p00280

Zahnle, K. J., Lupu, R., Catling, D. C., & Wogan, N. (2020). Creation and Evolution of Impact-generated Reduced Atmospheres of Early Earth. *The Planetary Science Journal*, *1*(1), 11. https://doi.org/10.3847/PSJ/ab7e2c

Zamyatina, M., Hébrard, E., Drummond, B., Mayne, N. J., Manners, J., Christie, D. A., Tremblin, P., Sing, D. K., & Kohary, K. (2023). Observability of signatures of transport-induced chemistry in clear atmospheres of hot gas giant exoplanets. *Monthly Notices of the Royal Astronomical Society*, *519*(2), 3129–3153. https://doi.org/10.1093/mnras/stac3432

Zarka, P., Farrell, W. M., Kaiser, M. L., Blanc, E., & Kurth, W. S. (2004). Study of solar system planetary lightning with LOFAR. *Planetary and Space Science*, *52*(15), 1435–1447. https://doi.org/10.1016/j.pss.2004.09.011

Zeldovich, Y. B., Frank-Kamenetskii, D., & Sadovnikov, P. (1947). *Oxidation of nitrogen in combustion*. Publishing House of the Acad of Sciences of USSR.

Zhang, J. (, Wei, Y., & Fang, Z. (2019). Ozone Pollution: A Major Health Hazard Worldwide [Publisher: Frontiers]. *Frontiers in Immunology*, *10*. https://doi.org/10.3389/fimmu.2019.02518

Zhang, Y., & Yang, J. (2020). How Does Background Air Pressure Influence the Inner Edge of the Habitable Zone for Tidally Locked Planets in a 3D View? *The Astrophysical Journal*, *901*(2), L36. https://doi.org/10.3847/2041-8213/abb87f

Zhou, L., Ma, B., Wang, Y., & Zhu, Y. (2022). Hubble WFC3 Spectroscopy of the Rocky Planet L 98–59 b: No Evidence for a Cloud-free Primordial Atmosphere. *The Astronomical Journal*, *164*(5), 203. https://doi.org/10.3847/1538-3881/ac8fe9

Zhou, L., Ma, B., Wang, Y.-H., & Zhu, Y.-N. (2023). Hubble WFC3 Spectroscopy of the Terrestrial Planets L 98–59 c and d: No Evidence for a Clear Hydrogen Dominated Primary Atmosphere. *Research in Astronomy and Astrophysics*, *23*(2), 025011. https://doi.org/10.1088/1674-4527/acaceb

Zieba, S., Kreidberg, L., Ducrot, E., Gillon, M., Morley, C., Schaefer, L., Tamburo, P., Koll, D. D. B., Lyu, X., Acuña, L., Agol, E., Iyer, A. R., Hu, R., Lincowski, A. P., Meadows, V. S., Selsis, F., Bolmont, E., Mandell, A. M., & Suissa, G. (2023). No thick carbon dioxide atmosphere on the rocky exoplanet TRAPPIST-1 c. *Nature*, *620*(7975), 746–749. https://doi.org/10.1038/s41586-023-06232-z